

ANJANA ASHOK, M.SC.

TARGETED SEARCHES FOR
CONTINUOUS GRAVITATIONAL WAVES

TARGETED SEARCHES FOR
CONTINUOUS GRAVITATIONAL WAVES

Von der QUEST-Leibniz-Forschungsschule
der Gottfried Wilhelm Leibniz Universität
Hannover

zur Erlangung des Grades

Doktorin der Naturwissenschaften
- Dr. rer. nat.-

genehmigte Dissertation von

ANJANA ASHOK, M.SC.
geboren am 29. Juni 1994
in Calicut, Indien

2023

Anjana Ashok, M.Sc. : *Targeted Searches for
continuous gravitational waves* © 2023

REFERENTIN:

Prof. Dr. Maria Alessandra Papa
Max-Planck-Institut für Gravitationsphysik,
(Albert-Einstein-Institut), Hannover, Germany
Leibniz Universität, Hannover, Germany,
University of Wisconsin-Milwaukee, United States of America

KORREFERENTEN:

Prof. Dr. Irene Di Palma
Università di Roma "La Sapienza", Rome, Italy

Prof. Dr. Maura McLaughlin
West Virginia University, United States of America

INSTITUT:

Max-Planck-Institut für Gravitationsphysik,
(Albert-Einstein-Institut), Hannover, Germany

TAG DER PROMOTION:

23. Mai 2023

ABSTRACT

Gravitational waves are a consequence of Albert Einstein's General theory of relativity, which he put forward in 1916. One hundred years later, in 2015, a gravitational wave signal from two merging black holes was detected by the Advanced LIGO detectors. Now, the Advanced LIGO detectors have recorded about a hundred such signals from the merging of compact objects in binary systems.

Rotating neutron stars with a non-axisymmetric distribution of their mass present a perfect candidate for emitting gravitational waves continuously. Such continuous gravitational waves are several orders of magnitude weaker than those emitted by merging binary systems. Not surprisingly, these continuous gravitational wave signals have not yet been detected in the Advanced LIGO data. Efforts to make a detection of such a signal are going on. This thesis presents such a search for continuous gravitational waves.

Pulsars are neutron stars from which electromagnetic emissions have been observed, most commonly in the radio wavelength. These observations provide useful information about the neutron star, including its location in the sky and spin parameters. With this knowledge, we search for the continuous gravitational wave from that specific neutron star – thus targeting a source. Such targeted searches probe a small region of the signal parameter space and hence can afford a fully coherent search in data from all observations of the detectors. This makes targeted searches the most sensitive search strategy.

In this thesis, we present two different methods to search for continuous gravitational wave signals from pulsars. Using these methods, we target newly discovered, fast-spinning pulsars, a majority of them in binary systems. These pulsars have been targeted for continuous gravitational wave emission for the first time in this work. We do not detect a continuous gravitational wave signal from any of the targets. The non-detection of a signal can be translated into constraints on the mass distortions of the pulsar, parameterized by its 'ellipticity'. Our constraints on the ellipticities of these pulsars, using data from all the observation runs of Advanced LIGO detectors, are some of the lowest and lie in the regime of astrophysically interesting values for the parameter.

Keywords: *Continuous gravitational waves, neutron stars, pulsars, ellipticity, LIGO, Data analysis*

ZUSAMMENFASSUNG

Gravitationswellen sind eine direkte Konsequenz der 1916 von Albert Einstein aufgestellten Allgemeinen Relativitätstheorie. Hundert Jahre später, im Jahr 2015, wurde ein Gravitationswellensignal von zwei verschmelzenden schwarzen Löchern von den Advanced LIGO-Detektoren detektiert. Inzwischen haben die Detektoren etwa hundert solcher Signale von verschmelzenden kompakten Doppelsternen aufgezeichnet.

Rotierende Neutronensterne sind aufgrund der nicht achsensymmetrischen Verteilung ihrer Masse ein perfekter Kandidat für die kontinuierliche Ausstrahlung von Gravitationswellen. Solche kontinuierlichen Gravitationswellen sind um mehrere Größenordnungen schwächer als die, die von verschmelzenden Doppelsternsystemen ausgestrahlt werden. Es überrascht deshalb nicht, dass diese kontinuierlichen Gravitationswellensignale noch nicht detektiert wurden. Die Bemühungen um den Nachweis eines solchen Signals sind jedoch im Gange. Die vorliegende Arbeit beschäftigt sich mit der Suche nach kontinuierlichen Gravitationswellen.

Pulsare sind Neutronensterne, die im elektromagnetischen Bereich, meist als Radiowellen, beobachtet werden. Diese Beobachtungen liefern nützliche Informationen über den Neutronenstern, einschließlich seiner Position am Himmel und seiner Spinparameter. Die Informationen können genutzt werden, um gezielt nach der kontinuierlichen Gravitationswelle eines bestimmten Neutronensterns zu suchen. Solche gezielten Suchen untersuchen lediglich einen kleinen Bereich des Signalparameterraums und ermöglichen dadurch eine vollständig kohärente Suche in allen Daten der Detektoren. Dies macht die gezielte Suche zur empfindlichsten Suchstrategie.

Zwei verschiedene Methoden zur Suche nach kontinuierlichen Gravitationswellensignalen von Pulsaren werden in dieser Arbeit vorgestellt. Sie zielen auf neu entdeckte, schnell drehende Pulsare ab, von denen sich die meisten in Doppelsternsystemen befinden. Diese Pulsare wurden im Rahmen dieser Arbeit zum ersten Mal auf kontinuierliche Gravitationswellenemission untersucht. Wir konnten von keinem der Ziele ein kontinuierliches Gravitationswellensignal nachweisen. Die Nichtentdeckung eines Signals kann in Grenzwerte der Deformation eines Pulsars übersetzt werden, die durch seine 'Elliptizität' bestimmt wird. Unsere Grenzwerte für die Elliptizität dieser Pulsare, die aus Daten aller Beobachtungsreihen der LIGO-Detektoren gewonnen wurden, gehören zu den niedrigsten bisher ermittelten und liegen im Bereich der astrophysikalisch interessantesten Werte für diesen Parameter.

Schlagerworte: *Kontinuierliche Gravitationswellen, Neutronensterne, Pulsare, Elliptizität, LIGO, Datenanalyse*

CONTENTS

1	INTRODUCTION	1
2	GRAVITATIONAL WAVES	5
2.1	Einstein's theory of Gravitation	5
2.1.1	Linearised weak field equations	6
2.2	Sources of gravitational waves	9
2.2.1	Quadrupole formula	10
2.2.2	Astrophysical sources of gravitational waves	11
2.3	Measurement of Gravitational waves	12
2.3.1	Interaction of gravitational waves with test particles	12
2.3.2	Gravitational wave detectors - The Advanced LIGO	14
2.4	Current status of gravitational wave astronomy	19
3	CONTINUOUS GRAVITATIONAL WAVES	23
3.1	Gravitational waves from rotating objects like neutron stars	23
3.2	Astrophysical Sources of Continuous Gravitational Waves	27
3.3	Signal model	28
3.4	Search Strategies	30
3.4.1	Targeted searches	30
3.4.2	Directed searches	32
3.4.3	All-sky searches	33
4	PULSARS	35
4.1	Known pulsars	35
4.2	Types of Pulsars in this thesis	37
4.3	Pulsar Timing	38
4.4	Pulsar physics relevant to gravitational wave searches	43
4.4.1	Spin evolution	43
4.4.2	Proper motion	43
4.5	Pulsars and gravitational waves	45
5	METHOD I - TEMPLATED SEARCHES USING THE MULTI-DETECTOR \mathcal{F} -STATISTIC	47
5.1	Search parameters	48
5.1.1	Reference time	48
5.1.2	Doppler parameters	48
5.1.3	Amplitude parameters	49
5.2	Data	50
5.3	Single template search	52
5.4	Band search	53
5.4.1	Bandwidth	53

5.4.2	Search resolution	54
5.4.3	Search	57
5.5	Upper Limits	58
5.6	Ending note	59
6	METHOD II - A NEW BAYESIAN METHOD FOR TARGETED SEARCHES FOR CONTINUOUS GRAVITATIONAL WAVES	61
6.1	Method	61
6.1.1	Bayesian Inference	61
6.1.2	Likelihood function	62
6.1.3	Priors	67
6.1.4	Software Implementation	68
6.1.5	Inferences	69
6.2	Tests	69
6.2.1	Recovery of fake signals	69
6.2.2	PP Plots	70
6.3	Discussion	71
7	RESULTS	73
7.1	Introduction	73
7.2	PSR J1653-0158	75
7.2.1	Data Choices	75
7.2.2	The search	79
7.3	PSR J0154+1833	81
7.3.1	Search In O1O2	82
7.3.2	Search In only O3a	82
7.3.3	Search In O1O2O3a	83
7.4	PSR J0824+0028	86
7.4.1	Search In O1O2	88
7.4.2	Search In only O3a	89
7.4.3	Search In O1O2O3a	92
7.5	PSR J0509+0856	95
7.5.1	Search In O1O2	95
7.5.2	Search In only O3a	96
7.5.3	Search In O1O2O3a	98
7.6	PSR J0732+2314	100
7.6.1	Search In O1O2	100
7.6.2	Search In only O3a	101
7.6.3	Search In O1O2O3a	104
7.7	PSR J0709+0458	106
7.7.1	Search In O1O2	107
7.7.2	Search In only O3a	107
7.7.3	Search In O1O2O3a	110

7.8	PSR J1411+2551	113
7.8.1	Search In O ₁ O ₂	114
7.8.2	Search In only O _{3a}	115
7.8.3	Search In O ₁ O ₂ O _{3a}	117
7.9	PSR J2204+2700	119
7.9.1	Search In O ₁ O ₂	119
7.9.2	Search In only O _{3a}	119
7.9.3	Search In O ₁ O ₂ O _{3a}	121
7.10	Combined Analysis for ARECIBO Pulsars	124
7.11	PSR J1526-2744	127
7.11.1	Bayesian results	132
7.12	J1139-6247	134
7.13	J0744-2525	136
7.14	J0418+6635	137
7.15	J1335-5656	139
7.16	J2034+3632	141
7.17	J1649-3012	142
8	SUMMARY AND CONCLUSIONS	145
8.1	On Methods	146
8.2	On Results	148
8.2.1	Upper limits on gravitational wave emission	148
8.2.2	Ellipticities	149
8.3	On the scope of targeted continuous wave searches	151
8.4	Closing Note	152
	Appendix	154
A	APPENDIX TO CHAPTER 2	157
A.1	Curvature in linearised gravity	157
A.2	Trace of $\bar{h}^{\mu\nu}$	158
A.3	Einstein's Equation in terms of $\bar{h}_{\mu\nu}$	159
	Bibliography	161
	Publications	169
	Curriculum Vitae	209
	Acknowledgments	210

LIST OF FIGURES

- Figure 2.1 Effect of the two polarisations of gravitational waves travelling along the z axis on a ring of test particles lying perpendicular to their path. (a) the ring of particles before the wave reaches them (b) effect produced by the h_+ polarisation (c) effect of the h_\times polarisation. Figure from [Schutz \(1985\)](#) 10
- Figure 2.2 Two test particles lying at rest at $\tau = 0$ in the x - y plane with the time axis along the vertical. 14
- Figure 2.3 The effect of the plus polarisation of gravitational waves in changing the arm lengths of the detector shown in red. The signal evolution over time is shown in the top figure. Figure credit: [Abbott et al. \(2009\)](#) 15
- Figure 2.4 Schematic diagram of LIGO interferometer. Figure credit: [Abbott et al. \(2016\)](#) 15
- Figure 2.5 Noise budget of Advanced-LIGO detector. Figure credit: [Aasi et al. \(2015\)](#) 17
- Figure 2.6 First harmonic violin mode region in H1 (red) and L1 (blue) during O1. The y -axis is the average Amplitude Spectral Density during O1. Figure credit: [Covas et al. \(2018\)](#) 18
- Figure 2.7 The first ever detection of gravitational waves GW150914. Figure credit: [Abbott et al. \(2016\)](#) 19
- Figure 2.8 Masses of observed black holes and neutron stars so far. Figure credit: LIGO-Virgo/Aaron Geller/Northwestern 20
- Figure 2.9 Sources, sensitive frequencies and strains for current and future detectors. Figure credit: gwplotter.com, [Moore et al. \(2015\)](#). Note that a more realistic sensitivity curve for Pulsar Timing Arrays can be found, for example, in [Hazboun et al. \(2019\)](#). 21
- Figure 3.1 The principal axes (x'_1, x'_2, x'_3) rotate with the rigid body and the fixed frame is (x_1, x_2, x_3) . 24
- Figure 3.2 Doppler modulation due to Earth's motion during O1 on the frequency of continuous wave signal from PSR J0154+1833. The gaps in the curve correspond to gaps in the time when data was collected. 28
- Figure 3.3 Geometry of continuous wave signal reception and analysis, showing the source, detector on Earth and SSB. The various frames of reference needed in the description are also shown. Figure Credit: [Miroslav Shaltev \(2013\)](#) 29

- Figure 3.4 Upper limits on h_0 for ≈ 200 pulsars using O3 data. The stars show 95% confident upper limits on the amplitudes of h_0 . Figure Credit - [Abbott et al. \(2022\)](#) 32
- Figure 3.5 90% confidence upper limits on h_0 for continuous waves from the neutron star in the supernova remnant G347.3 for signal frequencies between 20-400Hz in O2 data. Figure from [Ming et al. \(2022\)](#) 33
- Figure 3.6 90% confidence upper limits on h_0 for continuous waves all sky search in public O3 data. Figure from [Steltner et al. \(2023\)](#). The different searches in this plot probe slightly different parameter spaces. 34
- Figure 4.1 The rotating neutron star is modelled as a lighthouse to explain pulsed emission. The bottom panel shows the evolution of the pulse as the beam of radiation rotates with the neutron star. Credit: Animation designed by Michael Kramer 35
- Figure 4.2 Population of known pulsars (3308) as of 20th August 2023 in the ATNF Catalog. The pulsars to the right of the red line lie in the sensitive frequency range of Advanced LIGO detectors. Credit: [Manchester et al. \(2005\)](#) 36
- Figure 4.3 The Arecibo telescope has now been decommissioned following irreparable damage to the antenna. Credit: Nature, News dated 2 December 2020 37
- Figure 4.4 Main stages in a pulsar timing observation. Credit: [Lorimer \(2008\)](#) 39
- Figure 4.5 Pulse dispersion in the Parkes observation of pulsar B1356-60. Credit: [Lorimer \(2008\)](#) 39
- Figure 4.6 Pulse profile for nine pulsars discovered by [Clark et al. \(2023\)](#). The black and red curves show the pulse profiles observed in two wavelengths, the L-band (856-1712MHz) and Ultra High Frequency (544-1088MHz) band of the MeerKAT telescope. 41
- Figure 4.7 Gamma-ray timing solution for PSR J1526-2744 provided by [Clark et al. \(2023\)](#). 42
- Figure 4.8 Geometry of an eccentric orbit of a Pulsar. 42
- Figure 4.9 The transverse motion of the pulsar adds an extra distance to the curve of constant distance to the SSB. The pulse of light from it has to travel an ever-increasing distance causing the observed spin period to be different from the intrinsic spin period. 44
- Figure 6.1 Recovery of a high SNR fake signal using the pipeline. 70
- Figure 6.2 PP plot for weak signal regime with h_0 priors in $[10^{-29}, 10^{-27}]$ 71
- Figure 7.1 Time intervals of radio observation and gravitational wave observation for the pulsars in Section 7.3 to 7.9 74

- Figure 7.2 Time averaged ASD of the detectors in 1Hz around 1016.4 Hz, the signal frequency of J1653-0158 in O1 data. 75
- Figure 7.3 Time averaged ASD of the detectors in 1Hz around 1016.4 Hz, the signal frequency of J1653-0158 in O2 data. 76
- Figure 7.4 Time-frequency maps (time along x-axis and frequency along y-axis) of the noise near the signal frequency of J1653 in (i) H1 during O1 in top left, (ii) H1 during O2 in the top right and (iii) L1 during O2 in the bottom panel. The disturbances are not present in the same frequency bins at all times. 76
- Figure 7.5 Noise in the signal frequency of J1653 in L1 detector during O2. (i) ASD in the signal frequency bin during the times of the observation (ii) middle stretch of O2 highlighted in red (iii) distribution of noise power in the middle stretch after removing fluctuations (iv) final stretch of O2 data (without fluctuations) on which running mean is computed. 77
- Figure 7.6 Data choices for L1 data in O2 run for the search for J1653. The running mean is in green, and the threshold is in cyan. 78
- Figure 7.7 Band search results for J1653-0158. Normalised Histogram of the loudest $2\mathcal{F}$ in 0.1mHz slice, obtained from a search in real data and search in Gaussian noise, in semi-log scale. 80
- Figure 7.8 95% confidence upper limits on the gravitational wave amplitude in a 2 Hz band around twice the rotation frequency of PSR J1653-0158. The x-axis shows the start frequency of the sub-bands and the bars indicate a conservative estimate of the uncertainty on the upper limit values. The "spike" does not indicate a detection: it is due to disturbance in L1 around ≈ 1016.32 Hz. 80
- Figure 7.9 Distribution of $2\mathcal{F}$ in a 3.4 Hz region around the signal frequency of J0154+1833 in O1O2 data. The dashed-grey line shows the $2\mathcal{F}$ value returned in the targeted search. The p-values of this $2\mathcal{F}$ result calculated with respect to different distributions are denoted by 'p_v' in these plots. The different distributions are (i) a central χ^2 distribution of 4 degrees of freedom which is the theoretical distribution of $2\mathcal{F}$ in Gaussian noise, plotted in green (ii) search results from simulated Gaussian noise as a blue histogram (iii) search results from off-source real data as a red histogram (iv) the best fitting χ^2 distribution for the results from Gaussian noise, 'nc' stands for the non-centrality parameter. 83
- Figure 7.10 Upper limit sigmoid fit for J0154+1833 in O1O2 data. The grey dashed line stands for the 95% upper limit. The dash-dotted line shows the 90% upper limit. 84

Figure 7.11	O1O2 data h_0 upper limits in 10 mHz frequency subband searched, based on the most significant result in that 10 mHz subband.	84
Figure 7.12	Distribution of $2\mathcal{F}$ in a 3.4Hz region around the signal frequency of J0154+1833 in O3 data	85
Figure 7.13	p-values of the band search results for J0154+1833 in O3 data	85
Figure 7.14	Upper limit sigmoid fit for J0154+1833 for O3 data	86
Figure 7.15	Distribution of $2\mathcal{F}$ in a 3.4Hz region around the signal frequency of J0154+1833 in O1O2O3 data	86
Figure 7.16	p-values of the band search results for J0154+1833 in O1O2O3 data	87
Figure 7.17	Upper limit sigmoid fit for J0154+1833 in O1O2O3 data	87
Figure 7.18	Distribution of $2\mathcal{F}$ in a 0.8Hz region around the signal frequency of J0824+0028 in O1O2 data	88
Figure 7.19	Upper limit sigmoid fit for J0824+0028 for O1O2 data	89
Figure 7.20	Upper limit sigmoid fit with restricted prior on $\cos \iota$ for J0824+0028 in O1O2 data	89
Figure 7.21	O1O2 data h_0 upper limits in 10 mHz frequency subband searched, based on the most significant result in that 10 mHz subband.	90
Figure 7.22	Distribution of $2\mathcal{F}$ in a 0.8Hz region around the signal frequency of J0824+0028 in O3 data	90
Figure 7.23	p-values of the band search results for J0824+0028 in O3 data	91
Figure 7.24	Upper limit sigmoid fit for J0824+0028 for O3 data	91
Figure 7.25	Upper limit sigmoid fit with restricted prior on $\cos \iota$ for J0824+0028 for O3 data	92
Figure 7.26	Distribution of $2\mathcal{F}$ in a 0.8 Hz region around the signal frequency of J0824+0028 in O1O2O3 data	92
Figure 7.27	p-values of the band search results for J0824+0028 in O1O2O3 data	93
Figure 7.28	Upper limit sigmoid fit for J0824+0028 in O1O2O3 data	93
Figure 7.29	Upper limit sigmoid fit with restricted prior on $\cos \iota$ for J0824+0028 in O1O2O3 data	94
Figure 7.30	Distribution of $2\mathcal{F}$ in a 2Hz region around the signal frequency of J0509+0856 in O1O2 data	95
Figure 7.31	Upper limit sigmoid fit for J0509+0856 for O1O2 data	96
Figure 7.32	O1O2 data h_0 upper limits in 10 mHz frequency subband searched, based on the most significant result in that 10 mHz subband.	96
Figure 7.33	Distribution of $2\mathcal{F}$ in a 2Hz region around the signal frequency of J0509+0856 in O3 data	97
Figure 7.34	p-values of the band search results for J0509+0856 in O3 data	97
Figure 7.35	Upper limit sigmoid fit for J0509+0856 for O3 data	98

Figure 7.36	Distribution of $2\mathcal{F}$ in a 2 Hz region around the signal frequency of J0509+0856 in O1O2O3 data	98
Figure 7.37	p-values of the band search results for J0509+0856 in O1O2O3 data	99
Figure 7.38	Upper limit sigmoid fit for J0509+0856 in O1O2O3 data	99
Figure 7.39	Distribution of $2\mathcal{F}$ in a 2Hz region around the signal frequency of J0732+2314 in O1O2 data	100
Figure 7.40	Upper limit sigmoid fit for J0732+2314 for O1O2 data	101
Figure 7.41	Upper limit sigmoid fit with restricted prior on $\cos \iota$ for J0732+2314 in O1O2 data	101
Figure 7.42	O1O2 data h_0 upper limits in 10 mHz frequency sub-band searched, based on the most significant result in that 10 mHz sub-band.	102
Figure 7.43	Distribution of $2\mathcal{F}$ in a 2Hz region around the signal frequency of J0732+2314 in O3a data	102
Figure 7.44	p-values of the band search results for J0732+2314 in O3 data.	103
Figure 7.45	Upper limit sigmoid fit for J0732+2314 for O3 data	103
Figure 7.46	Upper limit sigmoid fit with restricted prior on $\cos \iota$ for J0732+2314 for O3a data	104
Figure 7.47	Distribution of $2\mathcal{F}$ in a 2 Hz region around the signal frequency of J0732+2314 in O1O2O3 data.	104
Figure 7.48	p-values of the band search results for J0732+2314 in O1O2O3 data	105
Figure 7.49	Upper limit sigmoid fit for J0732+2314 in O1O2O3 data	105
Figure 7.50	Upper limit sigmoid fit with restricted prior on $\cos \iota$ for J0732+2314 in O1O2O3 data	106
Figure 7.51	Noise ASD in the Hanford (H1) and Livingston (L1) detectors during O1, O2 runs. These plots show in one glimpse the noise levels in the different data-sets.	107
Figure 7.52	Noise ASD in the continuous gravitational wave signal frequency of J0709+0458 at each timestamp during the O1 and O2 observation runs in the Hanford (H1) and Livingston (L1) detectors.	108
Figure 7.53	Distribution of noise ASD in the continuous gravitational wave signal frequency of J0709+0458 during the O1 and O2 observation runs in the Hanford (H1) and Livingston (L1) detectors, as a function of time.	109
Figure 7.54	Distribution of noise ASD in the continuous gravitational wave signal frequency of J0709+0458 during the O1 and O2 observation runs in the Hanford (H1) and Livingston (L1) detectors, after noise removal, as a function of time.	109

- Figure 7.55 Distribution of $2\mathcal{F}$ in a 0.2Hz region around the signal frequency of J0709+0458 in O1O2 data 110
- Figure 7.56 Upper limit sigmoid fit for J0709+0458 for O1O2 data 110
- Figure 7.57 Upper limit sigmoid fit for J0709+0458 for O1O2 data – using restricted priors on $\cos \iota$. 111
- Figure 7.58 O1O2 data h_0 upper limits in 10 mHz frequency subband searched, based on the most significant result in that 10 mHz subband. 111
- Figure 7.59 Distribution of $2\mathcal{F}$ in a 0.2Hz region around the signal frequency of J0709+0458 in O3 data 112
- Figure 7.60 p-values of the band search results for J0709+0458 in O3 data. 112
- Figure 7.61 Upper limit sigmoid fit for J0709+0458 in O3a data – on the left using non-restricted priors on $\cos \iota$, on the right using restricted priors on $\cos \iota$. 113
- Figure 7.62 Distribution of $2\mathcal{F}$ in a 0.23 Hz region around the signal frequency of J0709+0458 in O1O2O3 data. 113
- Figure 7.63 p-values of the band search results for J0709+0458 in O1O2O3 114
- Figure 7.64 Upper limit sigmoid fit for J0709+0458 in O1O2O3 data – on the left using non-restricted priors on $\cos \iota$, on the right using restricted priors on $\cos \iota$. 114
- Figure 7.65 Distribution of $2\mathcal{F}$ in a 0.13Hz region around the signal frequency of J1411+2551 in O1O2 data 115
- Figure 7.66 Upper limit sigmoid fit for J1411+2551 for O1O2 data – on the left using non-restricted priors on $\cos \iota$, on the right using restricted priors on $\cos \iota$. 115
- Figure 7.67 O1O2 data h_0 upper limits in 10 mHz frequency sub-bands searched, based on the most significant result in that 10 mHz sub-band. 116
- Figure 7.68 Distribution of $2\mathcal{F}$ in a 0.13 Hz region around the signal frequency of J1411+2551 in O3a data. 116
- Figure 7.69 p-values of the band search results for J1411+2551 in O3 data. 117
- Figure 7.70 Upper limit sigmoid fit for J1411+2551 for O3a data – on the left using non-restricted priors on $\cos \iota$, on the right using restricted priors on $\cos \iota$. 117
- Figure 7.71 Distribution of $2\mathcal{F}$ in a 0.1 Hz region around the signal frequency of J1411+2551 in O1O2O3 data. 118
- Figure 7.72 p-values of the band search results for J1411+2551 in O1O2O3 data. 118
- Figure 7.73 Upper limit sigmoid fit for J1411+2551 for O1O2O3a data – on the left using non-restricted priors on $\cos \iota$, on the right using restricted priors on $\cos \iota$. 119

Figure 7.74	Distribution of $2\mathcal{F}$ in a 0.1Hz region around the signal frequency of J2204+2700 in O1O2 data 120
Figure 7.75	Upper limit sigmoid fit for J2204+2700 for O1O2 data 120
Figure 7.76	O1O2 data h_0 upper limits in 10 mHz frequency subband searched, based on the most significant result in that 10 mHz subband. 121
Figure 7.77	Distribution of $2\mathcal{F}$ in a 0.1Hz region around the signal frequency of J2204+2700 in O3 data 121
Figure 7.78	p-values of the band search results for J2204+2700 in O3 data. 122
Figure 7.79	Upper limit sigmoid fit for J2204+2700 for O3 data 122
Figure 7.80	Distribution of $2\mathcal{F}$ in a 0.09 Hz region around the signal frequency of J2204+2700 in O1O2O3 data. 123
Figure 7.81	p-values of the band search results for J2204+2700 in O1O2O3 data. 123
Figure 7.82	Upper limit sigmoid fit for J2204+2700 in O1O2O3 data. 124
Figure 7.83	O1O2 (1st row), O3 (2nd row) and O1O2O3 (3rd row) results. The blue circles show the p-values of the targeted searches. The red circles in the left-side plots show the p-value of the most significant result in each 10 mHz sub-band of the band searches. Figure from (Ashok et al., 2021). 125
Figure 7.84	O1O2, O3 and O1O2O3 band-search results. For each 10 mHz frequency band searched, we show the cumulative distribution of the Gaussian p-value of the most significant result. If the data were Gaussian noise, the distribution would follow the dashed black line. Figure from (Ashok et al., 2021). 126
Figure 7.85	Distribution of $2\mathcal{F}$ in a 0.1mHz region around the expected signal frequency for J1526-2744 . The $2\mathcal{F}$ from the targeted search is in red. The theoretically expected distribution of $2\mathcal{F}$ in Gaussian Data is plotted in green. The bottom panel shows the y-axis in a log scale. 128
Figure 7.86	Distribution of $2\mathcal{F}$ in a 3.2Hz region around the expected signal frequency for J1526-2744 . The bottom panel shows the y-axis in a log scale. 128
Figure 7.87	Distribution of band search results in real data and Gaussian noise. 129
Figure 7.88	p-values of the band search results. 129
Figure 7.89	Cumulative distribution of p-values of band search results. The expectation in Gaussian noise is plotted as red-dashed line. 130

- Figure 7.90 Distribution of the band-search results in real data plotted as red stars compared with results in band search in 20 realisations of Gaussian noise. The results from different Gaussian noise realisations are in different colours. 130
- Figure 7.91 The mean and range of the distribution of loudest $2\mathcal{F}$ in a large number of realisations of Gaussian noise compared with the actual search results. The bottom plot has a log scale on y-axis. 131
- Figure 7.92 Upper limit sigmoid fit for J1526-2744 . 131
- Figure 7.93 Bayesian posterior distributions of signal parameter for J1526-2744 . 133
- Figure 7.94 Distribution of $2\mathcal{F}$ in a 0.07 Hz region around the signal frequency of J1139-6247 in O1O2O3a data 134
- Figure 7.95 Distribution of loudest $2\mathcal{F}$ in 10mHz sub-bands in real O1O2O3a data and simulated Gaussian noise for J1139-6247. With a signal frequency of 16.6Hz, the frequency bandwidth probed is 0.07Hz. Hence there are only 7 points in this histogram. 135
- Figure 7.96 Upper limit sigmoid fit for J1139-6247 for O1O2O3a data 135
- Figure 7.97 Distribution of $2\mathcal{F}$ in a 0.09Hz region around the signal frequency of J0744-2525 in O1O2O3 data 136
- Figure 7.98 Distribution of loudest $2\mathcal{F}$ in 10mHz sub-bands in real O1O2O3 data and simulated Gaussian noise for J0744-2525 136
- Figure 7.99 Upper limit sigmoid fit for J0744-2525 for O1O2O3 data 137
- Figure 7.100 Distribution of $2\mathcal{F}$ in a 2.7Hz region around the signal frequency of J0418+6635 in O1O2O3 data 138
- Figure 7.101 Distribution of loudest $2\mathcal{F}$ in 10mHz sub-bands in real O1O2O3 data and simulated Gaussian noise for J0418+6635 138
- Figure 7.102 Upper limit sigmoid fit for J0418+6635 for O1O2O3 data 139
- Figure 7.103 Distribution of $2\mathcal{F}$ in a 2.5Hz region around the signal frequency of J1335-5656 in O1O2O3 data 139
- Figure 7.104 Distribution of loudest $2\mathcal{F}$ in 10mHz sub-bands in real O1O2O3 data and simulated Gaussian noise for J1335-5656 140
- Figure 7.105 Upper limit sigmoid fit for J1335-5656 for O1O2O3 data 140
- Figure 7.106 Distribution of $2\mathcal{F}$ in a 2.2Hz region around the signal frequency of J2034+3632 in O1O2O3 data 141
- Figure 7.107 Distribution of loudest $2\mathcal{F}$ in 10mHz sub-bands in real O1O2O3 data and simulated Gaussian noise for J2034+3632 141
- Figure 7.108 Upper limit sigmoid fit for J2034+3632 for O1O2O3 data 142
- Figure 7.109 Distribution of $2\mathcal{F}$ in a 2.3Hz region around the signal frequency of J1649-3012 in O1O2O3a data 143

Figure 7.110	Distribution of loudest $2\mathcal{F}$ in 10mHz sub-bands in real O1O2O3a data and simulated Gaussian noise for J1649-3012	143
Figure 7.111	Upper limit sigmoid fit for J1649-3012 for O1O2O3a data	144
Figure 8.1	Comparison of continuous gravitational wave upper limits from frequentist and Bayesian pipelines for J1526-2744 which has been searched using both methods. The posterior distribution of h_0 is consistent with the noise-only hypothesis in both cases of the prior distribution function.	147
Figure 8.2	Comparison of the spin-down upper limit, measured upper limit and sensitivity of the data for all the pulsars in this thesis. In choosing to plot these quantities, we adhere to the convention of a typical known pulsar search paper (for example, Figure (2) in Abbott et al. (2022)). For ease of representation, the pulsar names are cut short. The spin-down upper limits are the grey triangles, the measured upper limits from our analysis of the Advanced LIGO data are the blue stars, and these reflect the sensitivity of the searches at that frequency using the data timespans available at the time of the search for the respective pulsar, shown in red circles.	149

LIST OF TABLES

Table 5.1	Signal frequency and bandwidth probed for pulsars. Note that for the first pulsar PSR J1653-0158, the search probed a bandwidth with $\delta f = 10^{-3}$ around the target frequency. $\delta f = 2 \times 10^{-3}$ was adopted afterwards.	55
Table 5.2	Parameters of simulated signals in upper limit Monte Carlos.	59
Table 8.1	95% ellipticity constraints on the pulsars.	150

INTRODUCTION

If I have seen further, it is by standing on the shoulders of giants.

– Isaac Newton, Letter to Robert Hooke (1675).

A child throwing a ball up knows that it will inevitably come down into her hands. Our tryst with gravity starts early in life. Soon it becomes just one of those ubiquitous, unremarkable features of living on Earth. But if you stop and think about it for a moment: gravity is that law that ensures that we stay rooted onto Earth and at the same time that nothing escapes a black-hole. It defines how planets move around the Sun, and how the Sun moves in the galaxy. It is one of the four fundamental forces in nature.

Sir Isaac Newton in [Newton \(1687\)](#) described gravity as a force of attraction that exists between any two objects that have mass. For several hundred years after, the theory reigned, explaining practical phenomena observable to humans. Even today, Newton's theory remains successful in sending rockets to outer space. But it had shortcomings that were known to Newton himself, namely that the theory entails action taking place over any distance at infinite speed.

Albert Einstein's radically new take on gravity, describing it as geometry of space time arrived, originally, in [Einstein \(1915\)](#) and in a consolidation of his work of November 1915 in [Einstein \(1916\)](#). Over the next couple of years, Einstein's general theory of relativity was proved correct by a number of observations - the very first one being Arthur Eddington's 1919 observation of the solar eclipse ([Dyson, Eddington, and Davidson, 1920](#)), which confirmed that the angle at which light bent due to the mass of the Sun matched predictions of the theory.

Einstein's theory of gravity predicted the existence of gravitational waves ([Einstein, 1918](#)), an idea that he himself found hard to believe. In the Chapel Hill conference of 1957 (two years after the death of Einstein), both Felix Pirani and Richard Feynman presented the argument that gravitational waves carry energy ([Pirani, Felix, 2011](#); [Rickles, Dean and DeWitt, Cécile M., 2011](#); [Saulson, 2011](#)), and thus are indeed physical. A first indirect, observational confirmation of the existence of gravitational waves came from measuring the loss of orbital energy of the binary pulsar system PSR 1913+16 in [Taylor et al. \(1979\)](#).

Interest in measuring gravitational waves on Earth began in the 1960s with Joseph Weber, who attended the Chapel Hill conference and later devised a bar detector. The principle behind the bar detector was that a passing gravitational wave would set the detector vibrating at its resonant frequency. Soon after, in the 1970s, interferometric detectors began to be developed. See [Papa](#) for an overview of the efforts towards detecting gravitational waves and also for a general history of the field.

On 14th September 2015, a gravitational wave was received and recorded for the first time on Earth. It was emitted by two black holes spiralling around each other, eventually merging. This first detection opened a whole new window to probe some of the most exotic objects in this Universe. We got a new tool to do astronomy with; a new messenger joined the league of electromagnetic waves and neutrinos from the far ends of our Universe.

Fast forward to seven years later. Today, nearly ninety compact binary coalescences have been observed using the ground-based gravitational wave detectors (Abbott et al., 2021; Nitz et al.; Venumadhav et al., 2020; Olsen et al., 2022). Gravitational wave astronomy is a reality today. But gravitational waves from compact binary coalescences remain the only type of gravitational waves that have been observed so far. A number of other kinds of gravitational waves still evade detection. This thesis concerns the search for one such type of gravitational waves - those that are persistent and nearly-monochromatic, the ‘continuous gravitational waves’.

Continuous gravitational waves are expected from rotating neutron stars with a non-axisymmetric distribution of mass. We will see in Chapter 3 why that is. Our galaxy is believed to host a population of a billion neutron stars (Sartore et al., 2010; Reed et al., 2021). So there is no dearth of sources for continuous gravitational waves.

There are three main strategies for searching for these signals - blind searches for signals coming from any source in the sky, directed searches, in which a source is expected at a certain sky location, and searches targeted at specific sources. Targeted searches are possible because some of the neutron stars in our galaxy are observable as pulsars. A pulsar emits a beam of electromagnetic radiation, and in its rotation, as this beam sweeps past our line of sight, we see a pulse of light. These pulses are observed by telescopes operating in a range of the electromagnetic spectrum in which the pulsar emits. The pulses can be timed precisely. These timing solutions then provide us with a wealth of information about the neutron star, including how fast it spins, how quickly it loses its rotational kinetic energy, how fast it is moving in the sky and, of course, its location in the sky. This information is priceless for a search for continuous gravitational wave signals from it, effectively helping to predict the signal that the source would emit.

The crux of this thesis is the targeted search for continuous gravitational waves from newly discovered pulsars. But it tries to tell the story from the beginning. Chapter 2 shows how Einstein’s theory of gravity predicts the generation and propagation of gravitational waves. This chapter also touches upon the various types of gravitational wave signals and their respective astrophysical sources before moving to a brief description of the ground-based interferometric detectors for these signals, which are nothing short of a feat of human endeavour right from its conception to the technology involved. Chapter 3 zooms into the topic of continuous gravitational waves, starting with the mathematical description of gravitational waves from rigid rotating objects. It then touches upon the sources and describes in detail the search strategies opted for

such signals. Chapter 4 focuses on pulsars, which are key ingredients to this thesis. It focuses on those details of pulsar astronomy and pulsar physics that are relevant to the continuous gravitational wave emission from pulsars. Chapter 5 and Chapter 6 are methods chapters, elaborating on a frequentist and a Bayesian method, respectively, that we adopted to analyse and infer from the detector data. The former chapter describes a single-template search and a band-search using the multi-detector \mathcal{F} -statistics (Cutler and Schutz, 2005) and the assessment of the significance of search results. As mentioned before, we do not detect a continuous gravitational wave signal. Chapter 5 concludes with a description of the calculation of frequentist upper limits on the gravitational wave amplitude based on the null results. The latter chapter on methods, Chapter 6 describes a new Bayesian formalism. It starts with a derivation of the underlying likelihood function, describes the software implementation of the method and presents results from tests of the method. Chapter 7 presents the results from the known pulsar searches carried out by me during this Ph.D work. Each targeted pulsar is treated as a specific source, and results from its single-template and band search and the upper-limit calculation procedure are presented. For one of the pulsars, results from the search using the method in chapter 6 are presented. Chapter 8 summarises the work. It discusses the continuous gravitational wave search results and their implications, especially on the constraints on the ellipticities of the targeted pulsars. It closes by pondering on the scope of targeted continuous wave searches and, more generally, on the power of multi-messenger astronomy.

GRAVITATIONAL WAVES

It is as if a wall which separated us from Truth has collapsed.

– Herman Weyl on *General Theory of Relativity*,
Preface to First Edition (1918), Space, Time, Matter (1952)

Gravitational waves are ripples in space-time that travel outwards from their sources at the speed of light. In this chapter, we will look at gravitational waves in detail. I will assume that the reader is familiar with the Special Theory of Relativity and start at Einstein's Field equations and go on to establish that, according to the General Theory of Relativity, gravitational waves must exist. I will only go into those details of the General Theory of Relativity that are relevant to the task at hand. Then I ask, what can source gravitational waves? And finally, I dwell on how we can detect them. Today, gravitational waves have been proven to exist through observation, and I will conclude with a quick look at the current status of gravitational wave astronomy.

Maggiore (2007) and Schutz (1985) contain details of the arguments presented in Section 2.1, 2.2 and 2.3.

2.1 EINSTEIN'S THEORY OF GRAVITATION

Einstein combined the three-dimensional space (described by the co-ordinates $\vec{x} = x, y, z$) and time into one entity, spacetime. Spacetime is thus the four-dimensional co-ordinate system given by

$$x^\mu = (ct, \vec{x}) \quad (2.1)$$

where c is the speed of light.

In (Einstein, 1916), Einstein suggested that what is experienced as gravitation is the curving of spacetime in the presence of mass. This idea is mathematically written as

$$R_{\mu\nu} - \frac{1}{2}R g_{\mu\nu} = \frac{8\pi G}{c^4} T_{\mu\nu}, \quad (2.2)$$

where the Greek indices μ and $\nu = 0, 1, 2, 3$. The left-hand side of equation 2.2 is called Einstein's tensor, and there are several mathematical objects in it that needs to be unpacked to see that it expresses the curvature of spacetime. Let us start at the coordinates in spacetime given in 2.1. The line element in flat spacetime is given by

$$ds^2 = -c^2 dt^2 + dx^2 + dy^2 + dz^2 \quad (2.3)$$

$$\begin{aligned}
&= \begin{bmatrix} -1 & 0 & 0 & 0 \\ 0 & 1 & 0 & 0 \\ 0 & 0 & 1 & 0 \\ 0 & 0 & 0 & 1 \end{bmatrix} \begin{bmatrix} c^2 dt^2 \\ dx^2 \\ dy^2 \\ dz^2 \end{bmatrix} \\
&= \eta_{\mu\nu} dx^\mu dx^\nu
\end{aligned}$$

where $\eta_{\mu\nu}$ is the metric in the flat spacetime, given the special name, Minkowski metric. For a general, curved spacetime, the line element is given by

$$ds^2 = g_{\mu\nu} dx^\mu dx^\nu \quad (2.4)$$

where the metric in spacetime, $g_{\mu\nu}$, encodes the curvature of the spacetime.

The Christoffel connections are constructed from the metric as

$$\Gamma_{\mu\nu}^\lambda = \frac{1}{2} g^{\lambda\sigma} (\partial_\mu g_{\nu\sigma} + \partial_\nu g_{\sigma\mu} - \partial_\sigma g_{\mu\nu}), \quad (2.5)$$

where

$$\partial_\mu \equiv \frac{\partial}{\partial x^\mu}. \quad (2.6)$$

The Riemann tensor contains everything we want to know about the curvature of spacetime and is obtained from the Christoffel connections as

$$R_{\sigma\mu\nu}^\rho = \partial_\mu \Gamma_{\nu\sigma}^\rho - \partial_\nu \Gamma_{\mu\sigma}^\rho + \Gamma_{\mu\lambda}^\rho \Gamma_{\nu\sigma}^\lambda - \Gamma_{\nu\lambda}^\rho \Gamma_{\mu\sigma}^\lambda. \quad (2.7)$$

The Ricci tensor is a contraction of the Riemann tensor,

$$R_{\mu\nu} = R_{\mu\lambda\nu}^\lambda, \quad (2.8)$$

and the trace of the Ricci tensor is the Ricci scalar given by

$$R = g^{\mu\nu} R_{\mu\nu}. \quad (2.9)$$

On the right-hand side of 2.2, $T_{\mu\nu}$ is the stress-energy tensor of an object in spacetime. It contains physical insights into the energetics of the system. The component most relevant to us is T_{00} which is the rest-frame energy-density of the source, ρ .

This story of the interplay between matter and spacetime was summarised by John Wheeler in the catchy one-liner ‘Matter tells spacetime how to curve, spacetime tells matter how to move’ (Misner et al., 1973).

2.1.1 Linearised weak field equations

Let us assume a coordinate frame in which we can write

$$g_{\mu\nu} = \eta_{\mu\nu} + h_{\mu\nu}, \quad (2.10)$$

where $\eta_{\mu\nu}$ is the Minkowski metric with the signature $(-,+,+,+)$ and $|h_{\mu\nu}| \ll 1$. Far away from the source that curves spacetime, the metric can be approximated as a perturbation on flat spacetime as above. We will use the metric in equation 2.10 and expand equation 2.2 to first order in $h_{\mu\nu}$ and omit $\mathcal{O}(h^2)$ terms which will be negligibly small. First of all, the Christoffel connection considering only the linear quantities, is

$$\Gamma_{\mu\nu}^{\lambda} = \frac{1}{2}\eta^{\lambda\sigma} (\partial_{\mu}h_{\nu\sigma} + \partial_{\nu}h_{\sigma\mu} - \partial_{\sigma}h_{\mu\nu}). \quad (2.11)$$

The Riemann tensor is then given by,

$$R_{\sigma\mu\nu}^{\rho} = \partial_{\mu}\Gamma_{\nu\sigma}^{\rho} - \partial_{\nu}\Gamma_{\mu\sigma}^{\rho}. \quad (2.12)$$

The Riemann and Ricci tensors and the Ricci scalar in linearised gravity are explicitly worked out in the Appendix in Section A.1. Plugging in Ricci tensor and Ricci scalar as written in equations A.7 and A.10 into Einstein's equations (2.2) gives

$$\frac{1}{2} \left[\partial_{\sigma}\partial_{\mu}h_{\nu}^{\sigma} - \square h_{\mu\nu} - \partial_{\nu}\partial_{\mu}h + \partial_{\nu}\partial^{\sigma}h_{\mu\sigma} - \eta_{\mu\nu}\partial_{\sigma}\partial^{\lambda}h_{\lambda}^{\sigma} + \eta_{\mu\nu}\square h \right] = \frac{8\pi G}{c^4} T_{\mu\nu}, \quad (2.13)$$

where, $\square = -(\frac{1}{c^2})\partial_t^2 + \nabla^2$ as mentioned in Appendix A.

Einstein's equation is, in the most general sense, a set of 16 equations. The symmetry of the metric tensor reduces the number of degrees of freedom to 10. The equation can be further simplified (the number of degrees of freedom further reduced) if we choose the appropriate coordinate system or *gauge*. Why are we allowed to 'choose' an appropriate coordinate system? Equation 2.10 does not result in a unique $h_{\mu\nu}$ – if one coordinate system exists where the metric can be written as 2.10, then there are many such coordinate systems. The physical predictions made from all coordinate systems will be the same, but the mathematical work in a poorly chosen coordinate system might make it harder to arrive at the predictions or, in the worst cases, prevent us from seeing the physics clearly. So it is time to choose a coordinate system, first, in which 2.10 holds.

Also, we change the notation of the metric perturbation by expressing it in terms of trace-reversed tensor given by,

$$\bar{h}_{\mu\nu} = h_{\mu\nu} - \frac{1}{2}\eta_{\mu\nu}h, \quad (2.14)$$

where

$$h = \text{trace}(h_{\mu\nu}) = g^{\mu\nu}h_{\mu\nu} = \eta^{\mu\nu}h_{\mu\nu} \quad (2.15)$$

in the linear order. This is done because the field equations simplify (as we will shortly see) when the metric perturbations are expressed in the trace-reversed form. $\bar{h}_{\mu\nu}$ is called *trace-reversed* because

$$\bar{\bar{h}} = -h \quad (2.16)$$

as shown in section A.2 of appendix A. The Einstein equation in terms of $\bar{h}_{\mu\nu}$ is worked out in section A.3 of appendix A. The final expression is in equation A.24, re-written here –

$$\partial_\sigma \partial_\mu \bar{h}_\nu^\sigma - \square \bar{h}_{\mu\nu} + \partial_\nu \partial^\sigma \bar{h}_{\mu\sigma} - \eta_{\mu\nu} \partial_\sigma \partial^\lambda \bar{h}_\lambda^\sigma = \frac{16\pi G}{c^4} T_{\mu\nu}. \quad (2.17)$$

Even after fixing the coordinate system to be one in which 2.10 holds, there is a residual symmetry under which $h_{\mu\nu}$ will not change. Consider two coordinate systems, $x^{\mu'}$ and x^μ which differ from each other by a very small amount ξ^μ so that

$$x^{\mu'} = x^\mu + \xi^\mu. \quad (2.18)$$

The metric then transforms ¹ into

$$h'_{\mu\nu} = h_{\mu\nu} - \partial_\mu \xi_\nu - \partial_\nu \xi_\mu, \quad (2.19)$$

and the trace-reversed metric transforms to

$$\bar{h}'_{\mu\nu} = \bar{h}_{\mu\nu} - \partial_\mu \xi_\nu - \partial_\nu \xi_\mu + \eta_{\mu\nu} \partial^\sigma \xi_\sigma. \quad (2.20)$$

Using the freedom of 2.18, we can apply a gauge transformation that satisfies the Lorentz (also called Hilbert or De Donder) gauge condition

$$\partial^\mu \bar{h}_{\mu\nu} = 0. \quad (2.21)$$

As long as the infinitesimal coordinate transformation satisfies

$$\square \xi_\mu = \partial^\nu \bar{h}_{\mu\nu}, \quad (2.22)$$

the metric perturbation $\bar{h}_{\mu\nu}$ can be put into a Lorentz gauge. Under the Lorentz gauge with 2.21 being true, 2.17 simplifies to

$$\square \bar{h}_{\mu\nu} = \frac{-16\pi G}{c^4} T_{\mu\nu}. \quad (2.23)$$

Equation 2.23 shows that in linearised weak fields, under the Lorentz gauge, the Einstein tensor reduces to the wave operator acting on the trace reversed metric perturbation. In vacuum, this reduces to

$$\square \bar{h}_{\mu\nu} = 0, \quad (2.24)$$

the solution to which is the wave,

$$\bar{h}_{\mu\nu} = \text{Re} \left(A_{\mu\nu} e^{ik^\lambda x_\lambda} \right) = \text{Re} \left(A_{\mu\nu} e^{ik^i x_i} e^{-i\omega t} \right), \quad (2.25)$$

¹ Under a coordinate transformation, a metric transforms according to the rule,
 $g_{\mu\nu}(x) \rightarrow g'_{\mu\nu}(x') = \frac{\partial x^\rho}{\partial x'^\mu} \frac{\partial x^\sigma}{\partial x'^\nu} g_{\rho\sigma}(x)$

where k^μ is the wave vector with $k^0 = \omega$, the frequency of the wave, and k^i are the spatial components. The solution 2.25 must satisfy the condition in 2.21. This gives,

$$A_{\mu\nu}k^\mu = 0, \quad (2.26)$$

meaning that the $A_{\mu\nu}$ must be orthogonal to \vec{k} , the direction of propagation, implying that gravitational waves are transverse waves.

We began with the 10 degrees of freedom of Einstein's equation. Under the Lorentz gauge in 2.21, which is a set of 4 equations, the degrees of freedom of $\bar{h}_{\mu\nu}$ reduced to 6. Further, the conditions to be satisfied by ζ^μ , given in the 4 equations of 2.22, reduced the degrees of freedom of $\bar{h}_{\mu\nu}$ to 2. Thus, there are two degrees of freedom for $\bar{h}_{\mu\nu}$, which are called the polarisations of the gravitational wave. Staying in the Lorentz gauge, we can do coordinate transformations – a coordinate transformation of the form $x^\mu \rightarrow x^\mu + \zeta^\mu$ provided that

$$\square\zeta_\mu = 0 \quad (2.27)$$

is still allowed in the Lorentz gauge without breaking the condition of 2.21. One such transformation called the transverse-traceless gauge further helps to bring out the actual physical content of the theory. Under this gauge,

$$h^{00} = 0; h^{0i} = 0; h_i^i = 0; \partial^i h_{ij} = 0. \quad (2.28)$$

The solution for 2.24 in the transverse-traceless gauge is, for a plane wave travelling along the z-axis, given by

$$\bar{h}_{ij}(t, z) = \begin{bmatrix} 0 & 0 & 0 & 0 \\ 0 & h_+ & h_\times & 0 \\ 0 & h_\times & -h_+ & 0 \\ 0 & 0 & 0 & 0 \end{bmatrix} \cos[\omega(t - z/c)] \quad (2.29)$$

where h_+ and h_\times are the two remaining degrees of freedom, called the 'plus' and 'cross' polarisations of the gravitational wave. Figure 2.1 helps visualise what these two different polarisations do to a ring of particles in the $x - y$ plane, lying in their path. The effect of h_+ is to stretch space in one direction and compress it in the direction perpendicular to the first. This can be seen in panel (b) as the distortion of the proper distance between the particles. The effect of h_\times is to distort space in a similar manner as h_+ but rotated at an angle of 45° relative to it. We will look at the interaction of gravitational waves with test particles in detail in section 2.3.

2.2 SOURCES OF GRAVITATIONAL WAVES

We have seen that gravitational waves are a prediction of Einstein's theory of gravity. The next question is, what sources these gravitational waves? This is described by the quadrupole formula. First, we look at the quadrupole formula. Then, a discussion of the astrophysical sources of detectable gravitational waves follows.

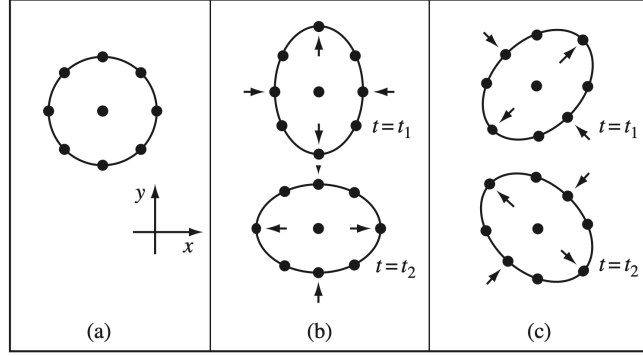


Figure 2.1: Effect of the two polarisations of gravitational waves travelling along the z axis on a ring of test particles lying perpendicular to their path. (a) the ring of particles before the wave reaches them (b) effect produced by the h_+ polarisation (c) effect of the h_\times polarisation. Figure from Schutz (1985)

2.2.1 Quadrupole formula

The wave equation in the presence of a source, equation 2.23, is an inhomogeneous partial differential equation which can be solved using Green's function so that

$$\bar{h}_{\mu\nu}(r, t) = \frac{1}{4\pi} \frac{16\pi G}{c^2} \int \frac{1}{|r - r'|} T_{\mu\nu}(r', t - \frac{|r - r'|}{c}) d^3 x', \quad (2.30)$$

where $t - \frac{|r - r'|}{c}$ is the retarded time, time at which the wave should have left the source located at r' if it has to reach a distance r at time t . When $r \gg r'$,

$$\bar{h}_{\mu\nu}(r, t) = \frac{4G}{c^2} \frac{1}{r} \int T_{\mu\nu}(r', t - \frac{r}{c}) d^3 x'. \quad (2.31)$$

The stress-energy tensor obeys the conservation law,

$$\partial_\nu T^{\mu\nu} = 0. \quad (2.32)$$

For spatial co-ordinates, $\mu = k$, and time co-ordinate denoted by 0, this becomes

$$\frac{1}{c^2} \frac{\partial T^{k0}}{\partial t} = - \frac{\partial T^{kl}}{\partial x^l}. \quad (2.33)$$

When $\mu = 0$, equation 2.32 becomes,

$$\partial_\nu T^{0\nu} = 0 \quad (2.34)$$

implying,

$$\frac{1}{c^2} \frac{\partial T^{00}}{\partial t} = - \frac{\partial T^{0l}}{\partial x^l}. \quad (2.35)$$

Differentiating 2.35 once again with respect to time, and using equation 2.33,

$$\frac{1}{c^2} \frac{\partial^2 T^{00}}{\partial t^2} = \frac{\partial^2 T^{kl}}{\partial x^k \partial x^l}. \quad (2.36)$$

Multiplying both sides by $x^m x^n$ and integrating over spatial volume,

$$\frac{1}{c^2} \int \frac{\partial^2 T^{00}}{\partial t^2} x^m x^n d^3x = \int \frac{\partial^2 T^{kl}}{\partial x^k \partial x^l} x^m x^n d^3x. \quad (2.37)$$

The term on the right-hand side is integrated by parts, and 2.37 becomes,

$$\frac{1}{c^2} \frac{\partial^2}{\partial t^2} \int T^{00} x^m x^n d^3x = 2 \int T^{mn} d^3x. \quad (2.38)$$

In the spatial part of equation 2.31, using 2.38,

$$\bar{h}^{mn}(r, t) = \frac{2G}{c^4 r} \frac{\partial^2}{\partial t^2} \int T^{00} x^m x^n d^3x. \quad (2.39)$$

The integral

$$Q^{mn}(r, t) = \int T^{00} x^m x^n d^3x \quad (2.40)$$

is the quadrupole moment of the source. An object's gravitational monopole is just the total amount of its mass. Its gravitational dipole is a measure of how much that mass is distributed away from the centre in a particular direction. The quadrupole represents how stretched-out along some axis the mass is. A sphere has zero quadrupole. A rod has a finite quadrupole.

Thus, we have the quadrupole formalism, which tells that a time-varying quadrupole moment generates gravitational waves -

$$\bar{h}^{mn}(r, t) = \frac{2G}{c^4 r} \ddot{Q}^{mn}(r, t). \quad (2.41)$$

2.2.2 Astrophysical sources of gravitational waves

There are four broad classes of astrophysical sources that are expected to emit gravitational waves that could be measured on Earth.

1. Coalescence

Binary systems with compact objects such as black holes or neutron stars lose energy over time and inspiral towards each other, eventually merging, and forming, in most cases, a stable black hole. The three stages, inspiral, merger and ringdown, result in a transient gravitational wave signal whose frequency and amplitude increase to a peak during merger and die exponentially post-merger. Since two compact objects are involved in the process, a large amount of energy is emitted as gravitational waves, and as we shall see shortly, such signals have been routinely detected in ground-based detectors already.

2. Continuous gravitational waves

Isolated neutron stars with a non-axisymmetric distribution of mass can generate continuous gravitational waves, which are simple quasi-monochromatic signals. This thesis focuses on continuous gravitational waves, and so they will be described in detail in Chapter 3.

3. Stochastic gravitational wave background

A gravitational wave background formed from the superposition of signals of cosmological as well as astrophysical origin is expected to be present in the universe. This background is not a deterministic signal and cannot be modelled but, instead, is of a stochastic nature. A large number of random processes in the early stages of the universe, approximately 10^{-36} to 10^{-32} seconds after the Big Bang, and perturbations to the metric of the universe could have, for instance, produced this gravitational wave background. The stochastic gravitational wave background is analogous to the Cosmic Microwave Background and could carry information about the early universe. Gravitational waves from astrophysical processes like supernovae, magnetars or the inspiral and merger of compact objects over the history of the universe could also produce such a background. Searches for such a background are underway but yielded no detection (Abbott et al., 2022).

4. Bursts

Bursts of gravitational waves are expected to be emitted in high-energy astrophysical phenomena such as a supernova explosion or a gamma-ray burst. But the sources are not confined to known high-energy events. With the possibility of gravitational wave transients from hitherto unknown types of astrophysical events, burst gravitational waves are those with the least a priori information on the source. In other words, bursts are surprise events from the universe and are largely unmodelled.

2.3 MEASUREMENT OF GRAVITATIONAL WAVES

We next look at techniques to measure gravitational waves. The question of how a gravitational wave affects particles in its path is relevant now.

2.3.1 Interaction of gravitational waves with test particles

The trajectory $X^\mu(\tau)$ of a test particle obeys the geodesic equation

$$\frac{d^2 X^\mu}{d\tau^2} + \Gamma_{\rho\sigma}^\mu \frac{dX^\rho}{d\tau} \frac{dX^\sigma}{d\tau} = 0, \quad (2.42)$$

where τ is the proper time as measured by an observer travelling along the geodesic. Consider two freely falling particles, one following geodesic A and another following geodesic B. The second time derivative of the displacement between the two particles is given by the geodesic deviation equation.

In the transverse traceless gauge, consider the two particles lying at rest at $\tau = 0$. The geodesic equation at $\tau = 0$ is

$$\frac{d^2 X^i}{d\tau^2} = -\Gamma_{\rho\sigma}^i \frac{dX^\rho}{d\tau} \frac{dX^\sigma}{d\tau} = -\Gamma_{00}^i \frac{dX^0}{d\tau} \frac{dX^0}{d\tau}. \quad (2.43)$$

Now,

$$\Gamma_{00}^i = \frac{1}{2} \eta^{ij} (\partial_0 h_{0j} + \partial_0 h_{j0} + \partial_j h_{00}) = 0 \quad (2.44)$$

from the conditions in equation 2.28. This means

$$\frac{d^2 X^i}{d\tau^2} = 0, \quad (2.45)$$

which means that the particles remain at rest forever, even if the wave passes. But note that, 'at rest' only means that the coordinate positions of the particles remain constant. Essentially what happens is that, by choosing to be in the transverse-traceless gauge, we ended up in a gauge in which the coordinate system remains attached to the individual particles and moves with the waves. We have to instead look at the proper distance between the two particles.

Consider that one particle lies at rest at the origin and the other at $x = L, y = z = 0$ at $\tau = 0$ as shown in figure 2.2.

Let the gravitational wave travel along the z -axis. The proper distance S between the two particles in the presence of the gravitational wave is,

$$S = \int_0^L |ds^2|^{\frac{1}{2}}. \quad (2.46)$$

Using equations 2.4 and 2.10,

$$\begin{aligned} S &= \int_0^L [dx dx (\eta_{xx} + h_{xx})]^{\frac{1}{2}} \\ &= \int_0^L dx [1 + h_{xx}^{TT}(\tau, z = 0)]^{\frac{1}{2}} \\ &\simeq \int_0^L dx \left[1 + \frac{1}{2} h_{xx}^{TT}(\tau, z = 0) \right] \\ &S = L \left[1 + \frac{1}{2} h_{xx}^{TT} \right]. \end{aligned} \quad (2.47)$$

If the change in proper distance is $S - L$ is denoted by ΔL , then equation 2.47 tells us that,

$$\frac{\Delta L}{L} \simeq \frac{1}{2} h_{xx}^{TT} \simeq \frac{1}{2} h_+^{TT} \cos \omega t \quad (2.48)$$

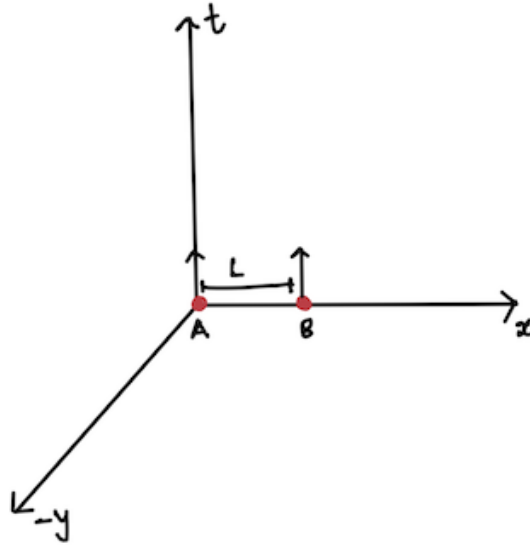


Figure 2.2: Two test particles lying at rest at $\tau = 0$ in the x - y plane with the time axis along the vertical.

using equation 2.29. Thus the presence of the gravitational wave comes out as its effect on the proper distance between two particles. One can see that h_+^{TT} acts as a fractional length change – a strain. For this reason, the magnitude h of the wave is called a ‘wave strain’.

2.3.2 Gravitational wave detectors - The Advanced LIGO

Equation 2.48 already lays down quite a few conditions to be satisfied by a gravitational wave detector. The change in distance as a result of the gravitational wave is directly proportional to the initial distance between two particles. So a gravitational wave detector should have a huge scale and involve large distances between the test particles. The effect of the gravitational wave is directly proportional to h_{ij}^{TT} . So the experiment should be able to measure relative length changes of the order of one part in 10^{21} , in order to detect the loudest black hole coalescences. The Laser Interferometer Gravitational-wave Observatory (LIGO) (Abbott et al., 2009) is the ground-based detector that has successfully collected gravitational wave data since 2002. This thesis deals closely with analysing the data from LIGO detectors. So we will focus on its working and experimental setup.

Figure 2.4 shows a schematic diagram of the LIGO detectors. Let us describe the working principle of these detectors in a simplistic manner. At their heart, the LIGO detectors are L-shaped Michelson interferometers. A beam of Nd-YAG laser light is split into two arms perpendicular to each other. On each arm are two test masses at a distance of $L = 4$ km from each other. The test masses are four suspended mirrors

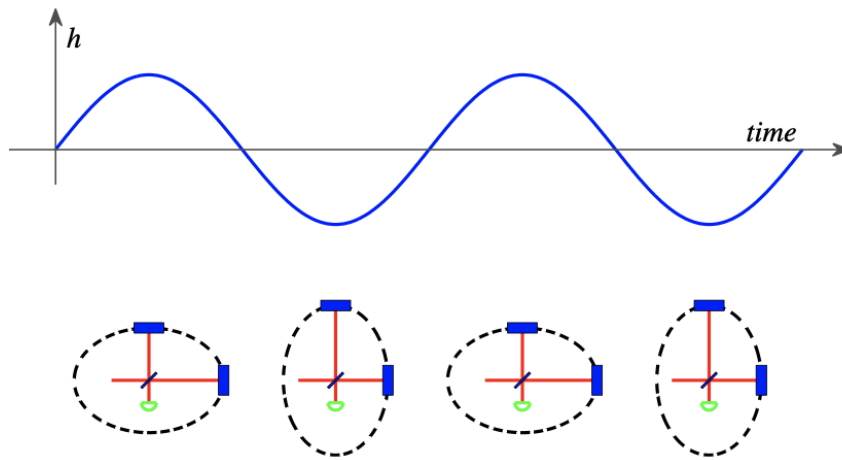


Figure 2.3: The effect of the plus polarisation of gravitational waves in changing the arm lengths of the detector shown in red. The signal evolution over time is shown in the top figure. Figure credit: [Abbott et al. \(2009\)](#)

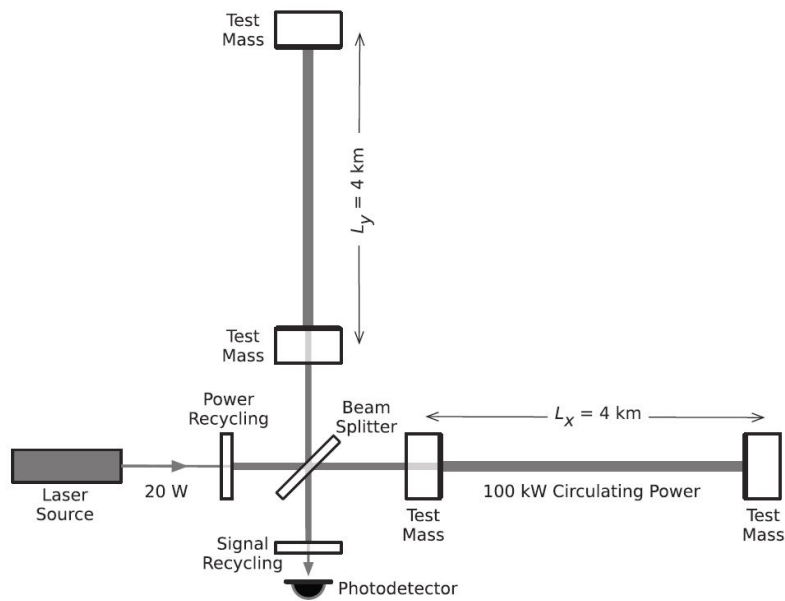


Figure 2.4: Schematic diagram of LIGO interferometer. Figure credit: [Abbott et al. \(2016\)](#)

that form Fabry-Perot arm cavities. A Fabry-Perot cavity is different from a Michelson interferometer because of the additional mirror in each arm near the beam splitter, causing the laser light in each arm to bounce between the two mirrors a number of times before merging with the beam from the other arm. Thus, the optical path of the light is folded a large number of times, effectively increasing the arm-length of the cavity.

In the absence of a gravitational wave, the two arm lengths are equal. The beams return from each arm and undergo destructive interference with each other at the beam splitter, and no light reaches the photodetector (note once again that this is only a simplistic description of the principle). But in the presence of a gravitational wave, the arm lengths stretch and compress as happens to a ring of particles shown in Figure 2.3. Thus, the beams produce interference on returning from the arms, which is detected in the photodetector. Following equation 2.48, the relationship between the change in arm length and the gravitational wave strain h is

$$\Delta L = \frac{1}{2}h, \quad (2.49)$$

where

$$\Delta L = \Delta L_x - \Delta L_y. \quad (2.50)$$

With an arm length of $L = 4$ km, to measure the effect of a gravitational wave with a (somewhat high) amplitude of $h_0 \sim 10^{-21}$, the detector should be able to measure a ΔL ,

$$\Delta L \sim \frac{1}{2} \times 10^{-21} \times 4 \times 10^3 = 2 \times 10^{-18}, \quad (2.51)$$

which is a thousand times smaller than the size of a nucleus. What does it mean to ‘measure a length change that is smaller than the size of a nucleus’? First of all, given that the mirror surface is made of atoms, and it is impossible to have an infinitely smooth surface, how are we even sure that the length L is a well-defined quantity, let alone make a measurement at a level 10^8 times smaller than individual atoms? The answer is that the laser beam has a transverse size of a few centimetres, so what is being measured is the position of the surface of the mirror averaged over a macroscopic area rather than the position of individual atoms on the surface. The individual atomic fluctuations are cancelled out in this area. This is a fundamental factor in how an interferometer could at all detect such small length changes induced by a gravitational wave. Secondly, the quantity causing the final measurement is the phase shift in the laser beams that traverse back from the two arms. Without going into a derivation (see, for example, Maggiore (2007) for details), the phase shift in a Michelson interferometer is given by $\Delta\phi_{\text{Michelson}} = (\frac{4\pi}{\lambda_L})h_0L$ where λ_L is the wavelength of the laser light. Using a laser of $\lambda_L = 1\mu\text{m}$, the phase shift caused by a $h_0 = 10^{-21}$ is $\sim 5 \times 10^{-11}$ rad. Now, inside a Fabry-Perot cavity, the light storage time is larger. Consequently, there is a gain in the phase shift $\Delta\phi_{\text{Mich}}$ by a factor of $\frac{2\mathcal{F}}{\pi}$ where \mathcal{F} is the Finesse of the cavity (see Maggiore

(2007) for a discussion). In Advanced LIGO detectors, the Fabry-Perot cavity has an $\mathcal{F} \approx 200$. This means that the phase shift we aim to measure is $\Delta\phi_{\text{Fabry-Perot}} \sim 10^{-8}$ rad.

2.3.2.1 Noise sources

The detectors are sensitive to the strain in space-time caused by a gravitational wave of astrophysical origin as well as to noise sources of non-astrophysical origin which cause differential arm length changes. The noise sources reduce the sensitivity of the detectors. In attempting to measure an effect as weak as that produced by a gravitational wave signal, it becomes necessary to understand the noise sources in the detector. The dominant noise source is different at different frequency ranges of the detector, and the most important classes of noise are depicted in the noise budget of Advanced LIGO shown in Figure 2.5. We will look at the major noise sources in this figure.

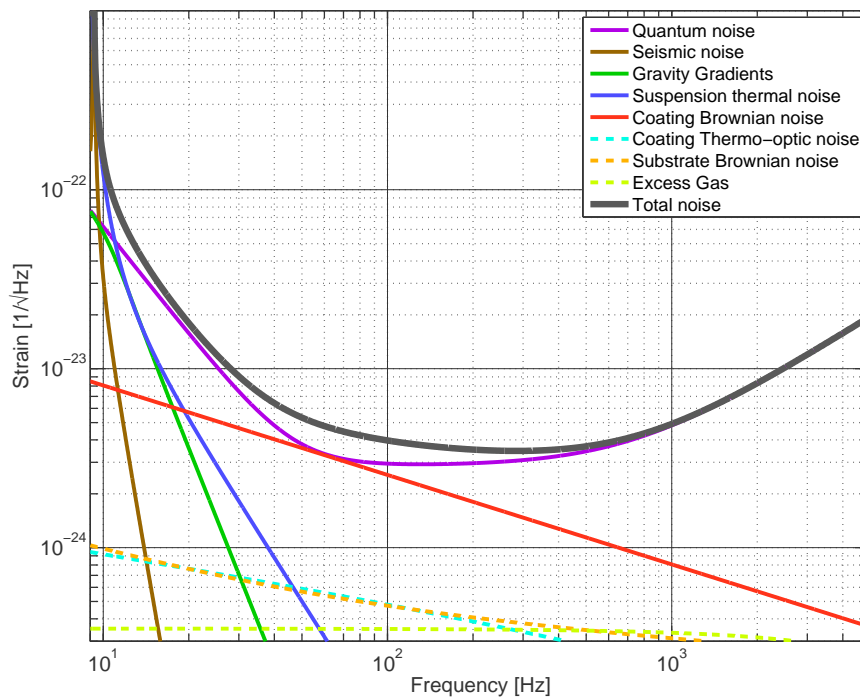


Figure 2.5: Noise budget of Advanced-LIGO detector. Figure credit: [Aasi et al. \(2015\)](#)

The low frequency is dominated by seismic noise that shakes the mirrors. These originate from environmental vibrations, the seismic activity of the earth, weather, and human activity in the vicinity of the detectors. To isolate the test masses mirrors from seismic noise, they are suspended as pendulums. Such suspensions further lead to disturbances at certain frequencies due to the resonance vibrations of the silicon strings that hold the mirrors, called violin modes. In the LIGO detectors, the violin modes are at

$\approx 500\text{Hz}$ and at harmonics of that frequency. Figure 2.6 shows the Amplitude Spectral Density (ASD) in the frequencies near 500 Hz in O1 data. ASD will be described in chapter 5. Violin modes play an important role in this thesis. One of the sources focused on in this thesis had signal frequencies which lie in the second harmonic of the violin mode in the Hanford (H1) and Livingston (L1) LIGO detectors. We will see in section 7.2.1 how a search in highly contaminated data can be carried out.

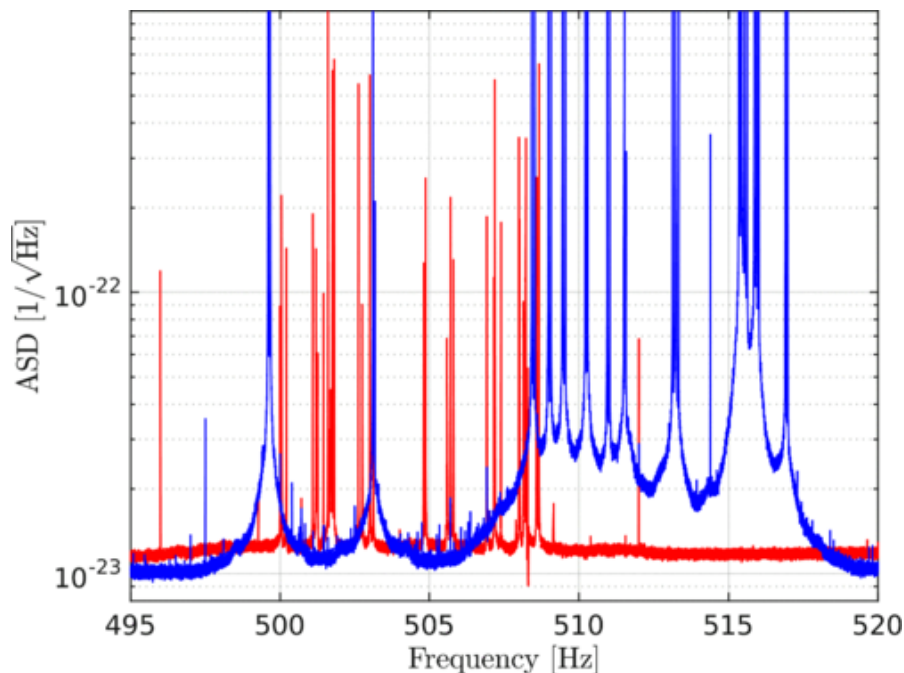


Figure 2.6: First harmonic violin mode region in H1 (red) and L1 (blue) during O1. The y-axis is the average Amplitude Spectral Density during O1. Figure credit: [Covas et al. \(2018\)](#)

The gravity gradient noise (also called Newtonian noise) arises due to fluctuations of local gravity fields around the test masses – caused by, for example, vibrations of the buildings, walls of the vacuum chambers (inside which the optical components are housed), and the density of the Earth itself, which lead to changes in the gravitational force acting on the test mass mirrors.

At intermediate frequency ranges, the dominant noise source is thermal noise, which induces vibrations in the mirrors and in the suspensions. Several sources of thermal noise have been identified – thermal vibrations of the suspension fibres, optical coatings on the mirrors, and in the interiors of the test masses, to name a few examples. Thermal noise is considered one of the biggest problems for the sensitivity improvement of gravitational wave detectors.

The high-frequency range of the detectors is limited by shot noise, which is due to the quantum nature of light in the laser beam. Shot noise is caused by the random fluctuations in the photon count in the beam. The higher the laser power, the lower the

shot noise. But increasing the laser power to reduce the shot noise introduces another source of quantum noise called the radiation pressure noise. Radiation pressure noise arises because the impinging of a large number of photons on the mirrors causes mirror displacement.

2.4 CURRENT STATUS OF GRAVITATIONAL WAVE ASTRONOMY

The LIGO detectors saw first light in August 2002. After thirteen years of improvements in sensitivity and collecting data in the Science runs, they caught their first gravitational wave signal on 14th September 2015, merely two days after the beginning of the first observation run.

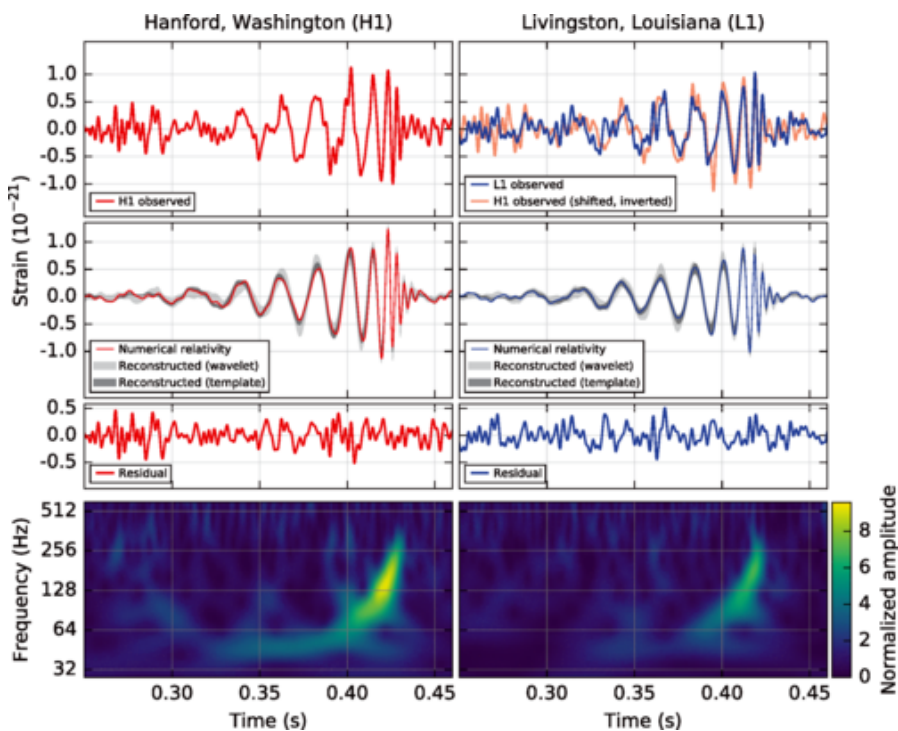


Figure 2.7: The first ever detection of gravitational waves GW₁₅₀₉₁₄. Figure credit: [Abbott et al. \(2016\)](#)

Figure 2.7 summarises the signal and the source of this first detection – GW₁₅₀₉₁₄. Two black holes of masses $29 M_{\odot}$ and $36 M_{\odot}$, 400 Mpc away, spiralled around each other and merged, releasing energy worth $3M_{\odot}c^2$ in gravitational waves. This detection was not only the first direct observation of a merging binary black hole system but also the first proof of the existence of stellar-mass black holes. The bottom panels show the spectrogram of the strain data, showing the ‘chirp’ signal in which frequency and amplitude increase over time, as expected for such a system.

As of the day of writing, the LIGO detectors have completed 3 observation runs - O1, O2, O3, between September 2015 and March 2020. Figure 2.8 shows the masses of the sources and the remnants of all compact binary coalescences detected by the gravitational wave detectors in these three observation runs. These detections of com-

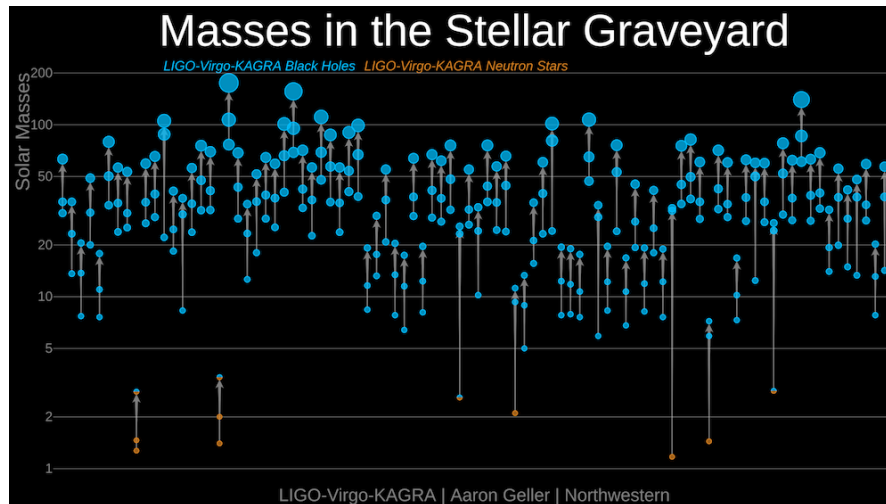


Figure 2.8: Masses of observed black holes and neutron stars so far. Figure credit: LIGO-Virgo/Aaron Geller/Northwestern

compact binary coalescences are aiding astrophysics – to infer the population of black holes in the universe and trace their formation channels and evolution (Abbott et al., 2021; Mandel, 2017), to constrain properties of neutron stars (Abbott et al., 2018), and in cosmology (Abbott et al., 2021) to mention a few examples. The first detection of a binary neutron star merger in gravitational waves and in electromagnetic waves (Abbott et al., 2017) kickstarted ‘multi-messenger astronomy’. It also contributed to the understanding of r-process nucleosynthesis, which produces heavy elements in the universe (Kasen et al., 2017). Continuous, stochastic and burst gravitational wave searches in the detector data are underway.

The Virgo detector in Italy joined the observation run O2. The Kagra detector in Japan joined the observation run in O3. An interferometric detector is being set up in India. The existing ground-based interferometric detector network is not only being expanded but also improved. LIGO A+ aims to double the sensitivity of Advanced LIGO via improvements in tackling coating thermal noise and quantum noise (Zucker, 2016). Beyond advanced detectors, the Einstein Telescope is a proposed underground gravitational wave observatory with a triangular interferometer of 10 km arm length with 20 times better sensitivity than existing detectors. The Cosmic Explorer is a proposed L-shaped overground detector of 40 km arm-length. Both these detectors will be sensitive to larger distances in the universe, up to redshift $z = 30$. A detailed

description of future science with current and upcoming gravitational wave detectors is in (Kalogera et al., 2021).

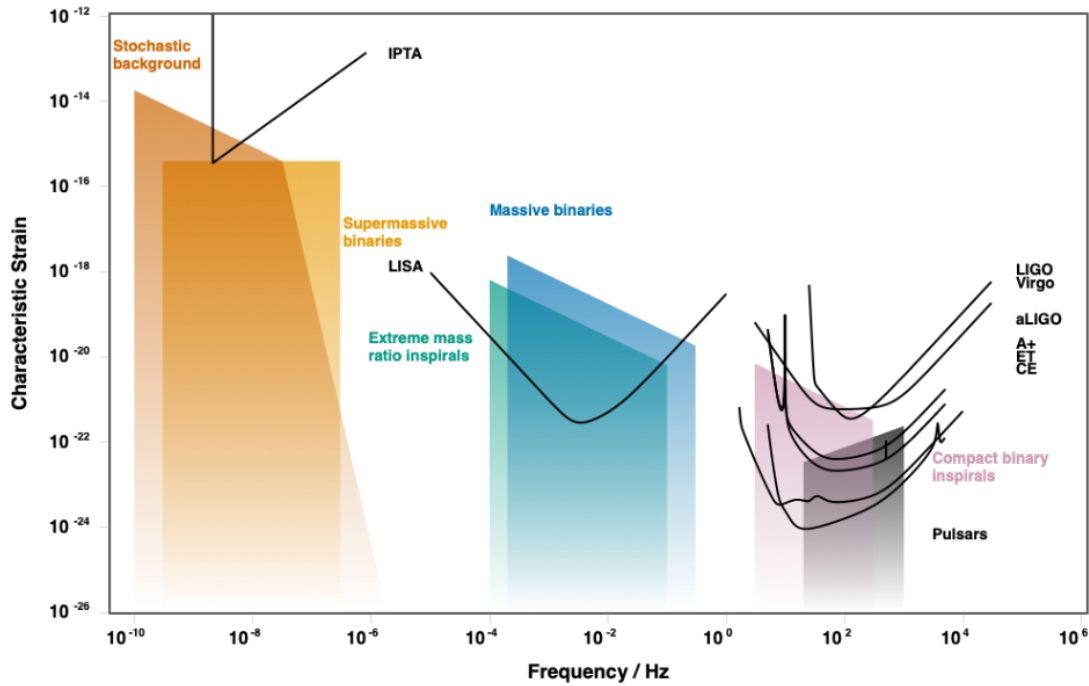


Figure 2.9: Sources, sensitive frequencies and strains for current and future detectors. Figure credit: gwplotter.com, Moore et al. (2015). Note that a more realistic sensitivity curve for Pulsar Timing Arrays can be found, for example, in Hazboun et al. (2019).

A space-based detector Laser Interferometer Space Antenna (LISA) is being built by the European Space Agency (ESA) and the National Aeronautics and Space Administration (NASA). LISA will observe massive ($> 10^4 M_{\odot}$) black holes, and extreme mass ratio inspirals, trace the history of the galaxy formation and structure, explore the stellar-mass compact objects in the galactic nuclei, search for unforeseen sources of gravitational waves and aims to come up with a coherent picture of the universe by combining all the findings (Danzmann et al.).

Pulsar Timing Arrays (PTAs) try to measure gravitational waves by detecting their effect on the arrival times of pulses from pulsars. Pulsars (especially millisecond pulsars, which we will discuss in more detail in chapter 4) have high stability in their rotational period. In the absence of gravitational waves, the arrival times of pulses from these pulsars should have equal intervals after accounting for Earth and binary orbital motions. In the presence of gravitational waves, one would measure timing residuals when comparing observed time or arrivals of pulses with those predicted by a model. The effect of a gravitational wave can be seen as a correlated signature in the residuals in the arrival times from pairs of pulsars. Depending on the angular

separation between the pulsars in each pair, the correlation in timing residuals due to the presence of a gravitational wave follows a specific relationship called the Hellings-Downs curve (Hellings and Downs, 1983). PTAs aim to detect stochastic gravitational backgrounds of astrophysical and cosmological origin in the nanoHz frequency range. Currently, gravitational wave astronomy using PTAs is entering an interesting time, anticipating a detection, with the data from PTAs indicating evidence of a stochastic process (Arzoumanian et al., 2020; Goncharov et al., 2022; Chen et al., 2021).

A comprehensive picture of current and some of the future detectors, the sources and the characteristic strain of gravitational wave signals they aim to detect are in figure 2.9.

CONTINUOUS GRAVITATIONAL WAVES

Of all the communities available to us, there is not one I would want to devote myself to, except for the society of true searchers, which has very few living members at any time.

– Albert Einstein, Letter to Max Born (1971)

Continuous gravitational waves are nearly-monochromatic gravitational waves expected to be emitted by rotating neutron stars with a non-axisymmetric distribution of mass.

These signals are always present in the data collected by gravitational wave detectors. At the time of writing, continuous gravitational wave signals have not been detected. The primary reason is that these signals are several orders of magnitude weaker than gravitational waves emitted during the merger of compact objects like black holes and neutron stars. For a typical source rotating at 100 Hz at a distance of 100 pc and having an ellipticity of 10^{-6} , the continuous gravitational wave signals have a strain value of $\approx 10^{-25}$. On the other hand, thanks to the persistent presence of the signal in the data, the signal power can be accumulated coherently over time to increase the signal-to-noise ratio following the relation (Cutler and Schutz, 2005)

$$SNR \propto h_0 \sqrt{\frac{T_{data}}{S_h}} \quad (3.1)$$

where h_0 is the strength of the signal, T_{data} , the amount of data used in the search and S_h is the noise level in the data, quantified in terms of the power spectral density (which will be described in chapter 5).

This thesis concerns the searches for continuous gravitational wave signals. Hence this chapter is dedicated to this type of gravitational wave. We start, in Section 3.1, with the theory of gravitational waves emitted by rotating rigid objects to get an idea of what feature causes the emission and to arrive at the mathematical expressions describing the signal. In Section 3.2, we will discuss the potential astrophysical sources of this signal. Moving on, in Section 3.3, we will describe the continuous gravitational wave signal model we expect in the detector data. Then in Section 3.4, we look at the three broad search strategies adopted to search for these signals.

3.1 GRAVITATIONAL WAVES FROM ROTATING OBJECTS LIKE NEUTRON STARS

We saw in chapter 2 that a perfectly symmetric mass distribution cannot produce gravitational waves. For rotating neutron stars, the simplest way to generate gravitational

waves is to have a non-axisymmetric mass distribution. Let us return to the quadrupole formula to generate gravitational waves, this time from a rotating rigid body. We start at the inertia tensor of the rigid body, in the most general form,

$$I^{ij} = \int d^3x \rho(\vec{x})(r^2\delta^{ij} - x^i x^j), \quad (3.2)$$

where ρ is the mass density and δ^{ij} is the Kronecker delta function. Since I_{ij} is real and symmetric, there exists a coordinate frame in which I_{ij} is diagonal. This frame, called the body frame, has coordinates x'_i . In the body frame, the axes are called the principal moments of inertia of the body and are given by,

$$I_1 = \int d^3x' \rho(\vec{x}')(x_2'^2 + x_3'^2), \quad (3.3)$$

$$I_2 = \int d^3x' \rho(\vec{x}')(x_1'^2 + x_3'^2), \quad (3.4)$$

$$I_3 = \int d^3x' \rho(\vec{x}')(x_1'^2 + x_2'^2). \quad (3.5)$$

We also introduce a fixed reference frame with coordinates (x_1, x_2, x_3) with $x_3 = x'_3$. The neutron star with a rotation frequency ω_{rot} is depicted as a triaxial ellipsoid in figure 3.1. If the body is rotating about one of its principal axes, x'_3 , the two frames are

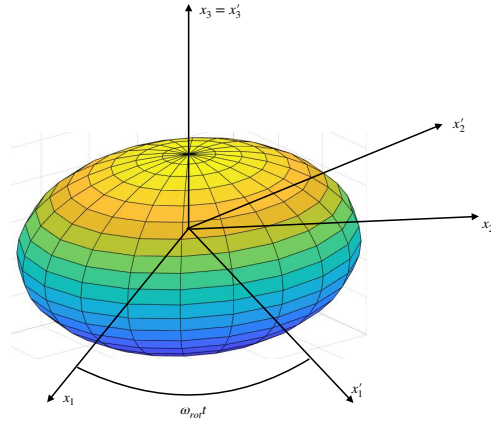


Figure 3.1: The principal axes (x'_1, x'_2, x'_3) rotate with the rigid body and the fixed frame is (x_1, x_2, x_3) .

related to each other through a time-dependent rotation matrix \mathcal{R}_{ij} given by

$$\mathcal{R}_{ij} = \begin{bmatrix} \cos \omega_{rot} t & \sin \omega_{rot} t & 0 \\ -\sin \omega_{rot} t & \cos \omega_{rot} t & 0 \\ 0 & 0 & 1 \end{bmatrix} \quad (3.6)$$

as

$$x'_i = \mathcal{R}_{ij} x_j. \quad (3.7)$$

Then the inertia tensor in the body frame $I'_{ij} = \text{diag}(I_1, I_2, I_3)$ is

$$I'_{ij} = (\mathcal{R} I \mathcal{R}^T)_{ij}. \quad (3.8)$$

Therefore we can calculate the inertia tensor in the fixed frame by

$$I = \mathcal{R}^T I' \mathcal{R}. \quad (3.9)$$

This yields

$$I_{11} = 1 + \frac{I_1 - I_2}{2} \cos 2\omega_{rot} t, \quad (3.10)$$

$$I_{12} = \frac{I_1 - I_2}{2} \sin 2\omega_{rot} t, \quad (3.11)$$

$$I_{22} = 1 - \frac{I_1 - I_2}{2} \cos 2\omega_{rot} t, \quad (3.12)$$

$$I_{33} = I_3, \quad (3.13)$$

and $I_{13} = I_{23} = 0$. We saw in equation 2.39 that a time-varying quadrupole moment leads to the generation of gravitational waves. From equation 2.40, quadrupole moment, is

$$Q^{ij} = \int \rho(\vec{x}) x^i x^j d^3x, \quad (3.14)$$

because T^{00} is the density of the source. Comparing expressions 3.14 and 3.2, we see that Q^{ij} differs from I^{ij} by an overall minus sign. That is,

$$Q_{ij} = -I_{ij} + \text{constant}, \quad (3.15)$$

where I_{ij} are given above. This gives us

$$Q_{11} = -\frac{I_1 - I_2}{2} \cos 2\omega_{rot} t + \text{constant}, \quad (3.16)$$

$$Q_{12} = -\frac{I_1 - I_2}{2} \sin 2\omega_{rot} t + \text{constant}, \quad (3.17)$$

$$Q_{22} = +\frac{I_1 - I_2}{2} \cos 2\omega_{rot} t + \text{constant} \quad (3.18)$$

and $Q_{13} = Q_{23} = Q_{33} = \text{constant}$. We can already see that it is $I_1 - I_2$, the asymmetry of the object, that causes a non-zero quadrupole.

Next, we compute the second-order time derivative of Q_{ij} and plug them into equation 2.39. If the observer is at distance r , and denoting $I_1 \equiv I_{xx}$, $I_2 \equiv I_{yy}$ and $I_3 \equiv I_{zz}$, we have

$$h_+(t) = \frac{1}{r} \frac{4G\omega_{rot}^2}{c^4} \frac{I_{xx} - I_{yy}}{I_{zz}} I_{zz} \cos(2\omega_{rot}t) \quad (3.19)$$

and

$$h_\times(t) = \frac{1}{r} \frac{4G\omega_{rot}^2}{c^4} \frac{I_{xx} - I_{yy}}{I_{zz}} I_{zz} \sin(2\omega_{rot}t) \quad (3.20)$$

which are the amplitudes of the two polarisations of the gravitational wave emitted. Recall that equation 2.39 is the expression for the gravitational wave along the z (i.e., the x_3) axis. If one wants the emission along a direction in the line of sight of the observer, one can first compute the angular distribution of the quadrupolar radiation (Maggiore, 2007), and plug in the second-derivatives of Q_{ij} in to get,

$$h_+(t) = \frac{1}{r} \frac{4G\omega_{rot}^2}{c^4} \frac{I_{xx} - I_{yy}}{I_{zz}} I_{zz} \frac{1 + \cos^2 \iota}{2} \cos(2\omega_{rot}t) \quad (3.21)$$

and

$$h_\times(t) = \frac{1}{r} \frac{4G\omega_{rot}^2}{c^4} \frac{I_{xx} - I_{yy}}{I_{zz}} I_{zz} \cos \iota \sin(2\omega_{rot}t) \quad (3.22)$$

where ι is the angle between the line-of-sight from the observer to the source and the neutron star's spin axis. Thus, a non-axisymmetric object with a time-varying quadrupole moment owing to its rotation will continuously emit gravitational waves of the form in equations 3.21 and 3.22. Notice that the frequency of the gravitational wave is twice the rotational frequency of the star,

$$f_{gw} = \frac{\omega_{rot}}{\pi} = 2 \times f_{rot}. \quad (3.23)$$

We introduce the ellipticity ϵ given as

$$\epsilon = \left| \frac{I_{xx} - I_{yy}}{I_{zz}} \right|, \quad (3.24)$$

which is a very important quantity that decides the strength of the continuous gravitational wave emitted. We can write Equations 3.21 and 3.22 as

$$h_+(t) = h_0 \frac{1 + \cos^2 \iota}{2} \cos(2\omega_{rot}t) \quad (3.25)$$

and

$$h_\times(t) = h_0 \cos \iota \sin(2\omega_{rot}t), \quad (3.26)$$

where

$$h_0 = \frac{4\pi^2 G}{c^4} \frac{I_{zz} \epsilon f_{gw}^2}{r} \quad (3.27)$$

is the intrinsic gravitational wave amplitude of a star at a distance r , and spinning about a symmetry axis z .

Assuming that the neutron star has the typical mass of $1.4M_\odot$ and a radius of 10 km, I_{zz} has a canonical value of 10^{38} kgm².

3.2 ASTROPHYSICAL SOURCES OF CONTINUOUS GRAVITATIONAL WAVES

The simplest scenario in which a continuous gravitational wave is emitted is when a neutron star has a deformation leading to a non-axisymmetric distribution of mass (ϵ), which results in a non-zero quadrupole moment. The rotation of the star leads to a changing quadrupole moment. Then gravitational waves of the form in equation 3.25 and 3.26 are continuously emitted.

The neutron star loses energy over time for various reasons, leading to an \dot{f}_{rot} . A theoretical estimate on the maximum possible strength of the continuous gravitational wave signal detectable at a distance r from a neutron star can be calculated by assuming that all of the rotational kinetic energy lost by the neutron star is converted into gravitational waves. This is called the spin down upper limit h_{sd}^0 and can be calculated knowing the distance to the source by

$$h_0^{sd} = \left(\frac{5}{2} \frac{GI_{zz} |\dot{f}_{rot}|}{c^3 r^2 f_{rot}} \right)^{1/2}. \quad (3.28)$$

In Section 4.4, we will arrive at this expression from energy considerations for a rotating pulsar.

A neutron star precesses when it is not spinning about one of its symmetry axes. For such a star, continuous gravitational wave emission is expected near two distinct frequencies $f_{gw} = f_{rot} + f_{prec}$ and $f_{gw} = 2(f_{rot} + f_{prec})$ where f_{prec} is the frequency of precession (Zimmermann and Szedenits, 1979).

Another scenario for continuous gravitational wave emission is through the current quadrupoles instead of the mass quadrupoles of neutron stars. The r-mode is a toroidal mode of fluid oscillations in the interior of the star. The r-modes are unstable to gravitational wave emission (Andersson et al., 1999). Young pulsars, shortly after their birth, are spinning very rapidly and are expected to have r-mode emission. The frequency of continuous gravitational wave from r-mode emission is expected to be around $\frac{4}{3}f_{rot}$. Studies on glitching pulsars (Andersson et al., 1999) also indicate the possibility of r-mode gravitational wave emission in the inter-glitch timespan.

Some exotic sources for continuous gravitational wave emission include boson clouds around a black hole (Arvanitaki et al., 2017). Quantum fluctuations near rotating black holes can lead to the formation of a cloud of ultralight bosonic particles like axions

around the black hole. These clouds grow in number due to superradiance, a process in which the particles scatter off and extract angular momentum from the rotating black hole. The superradiance process stops when the black hole's angular momentum falls below a threshold. The axion particles being anti-particles of themselves, begin to annihilate, emitting gravitational waves continuously, leading to a depletion of the cloud. The emitted gravitational waves are at a frequency parameterised by the mass of the particle (Arvanitaki and Dubovsky, 2011).

3.3 SIGNAL MODEL

A continuous gravitational wave signal is a nearly-monochromatic signal at twice the spin frequency of the pulsar. Two reasons cause a frequency evolution, one the inherent

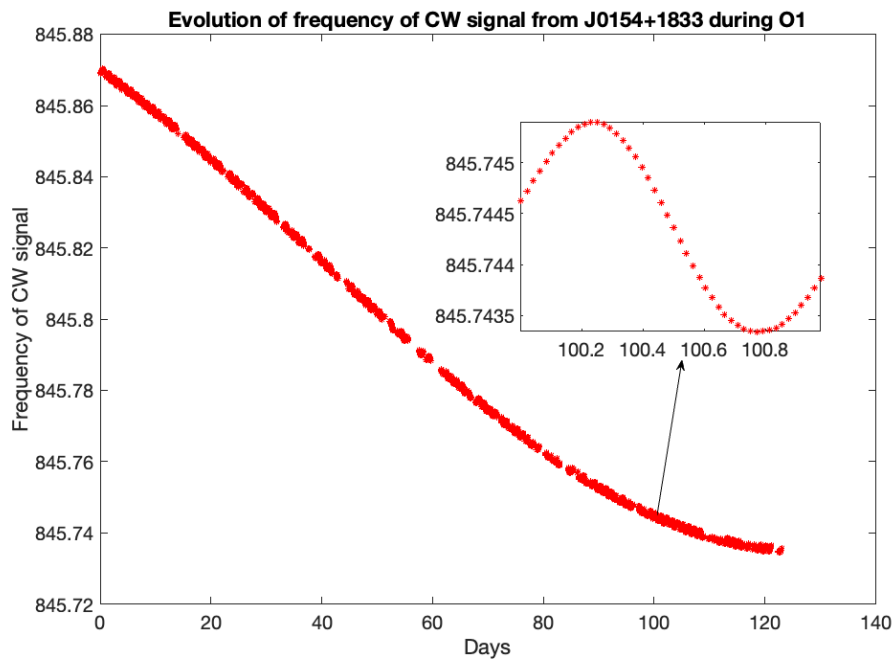


Figure 3.2: Doppler modulation due to Earth's motion during O1 on the frequency of continuous wave signal from PSR J0154+1833. The gaps in the curve correspond to gaps in the time when data was collected.

spinning down of the source, resulting in a \dot{f}_{gw} . The other reason is that Earth-based gravitational wave detectors move with the Earth's orbital motion around the sun and its intrinsic spin. This causes a Doppler modulation of the signal, as shown, for example, in Figure 3.2 for an isolated pulsar, PSR J0154+1833, with $f_{gw} \approx 800\text{Hz}$. The frequency modulation during 120 days reflects the Earth's motion around the sun. The frequency modulation of the signal during one day, as shown in the inset, reflects the Earth's daily

rotation. For a source in a binary orbit with a companion star, the binary orbital motion also contributes to the signal's Doppler modulation.

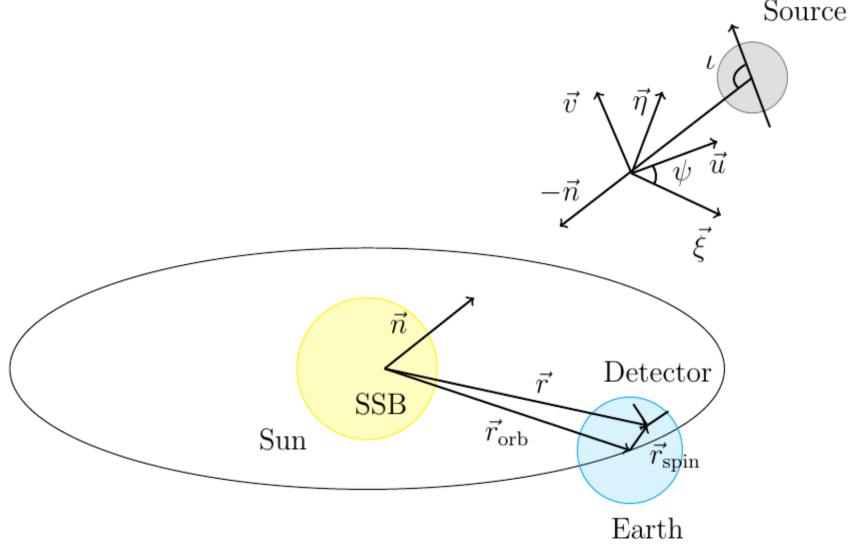


Figure 3.3: Geometry of continuous wave signal reception and analysis, showing the source, detector on Earth and SSB. The various frames of reference needed in the description are also shown. Figure Credit: [Miroslav Shaltev \(2013\)](#)

An amplitude modulation is caused due to the fact that the detector is not equally sensitive in all directions. A full description of the continuous gravitational wave signal can be found in Section II of [Jaranowski et al. \(1998\)](#). Here, we will revisit the geometry of the system, best expressed with the help of Figure 3.3, and the fundamental equations describing the signal as received by the ground-based gravitational wave detectors.

Figure 3.3 illustrates first the reference system fixed at the Solar System Barycenter (SSB). The direction of wave propagation is $-\hat{n}$. Additionally, we have a wave frame, $\{\hat{u}, \hat{v}, -\hat{n}\}$ where \hat{u} and \hat{v} lie in a plane transversal to the wave. $\{\hat{\xi}, \hat{\eta}, -\hat{n}\}$ form a polarisation-independent frame in the wave plane. The polarization angle ψ relates these two frames in the wave plane by

$$\sin \psi = \hat{u} \cdot \hat{\eta} \quad (3.29)$$

The inclination angle, $0 \leq \iota \leq \pi$, is the angle between the total angular momentum of the star and the line of sight, \hat{n} . It is worth noting that the sources we are interested in are far away so that \hat{n} from the SSB to the source is in the same direction as the line of sight from the detectors on earth to the source. The source is at a sky-position expressed in right ascension, α and declination, δ . The signal from this source in the strain data from a gravitational wave detector has the form ([Jaranowski et al., 1998](#))

$$h(t) = F_+(\alpha, \delta, \psi; t)h_+(t) + F_\times(\alpha, \delta, \psi; t)h_\times(t), \quad (3.30)$$

where $F_+(\alpha, \delta, \psi; t)$ and $F_\times(\alpha, \delta, \psi; t)$ are the detector antenna pattern functions to the $+$ and \times polarisations of the gravitational wave. These depend on the relative orientation between the detector and the source, hence on time t , and on ψ , the polarisation angle as well as the sky-position of the source.

The waveforms $h_+(t)$ and $h_\times(t)$ in Equations 3.25 and 3.26 are usually written more compactly as

$$\begin{aligned} h_+(t) &= A_+ \cos \Phi(t) \\ h_\times(t) &= A_\times \sin \Phi(t), \end{aligned} \quad (3.31)$$

with

$$\begin{aligned} A_+ &= \frac{1}{2} h_0 (1 + \cos^2 \iota) \\ A_\times &= h_0 \cos \iota. \end{aligned} \quad (3.32)$$

$\Phi(t)$ of Eq. 3.31 is the phase of the gravitational wave signal at time t . If τ_{SSB} is the arrival time of the wave with phase $\Phi(t)$ at the solar system barycenter, then $\Phi(t) = \Phi(\tau_{\text{SSB}}(t))$. The gravitational wave phase as function of τ_{SSB} is assumed to be

$$\Phi(\tau_{\text{SSB}}) = \Phi_0 + 2\pi [f(\tau_{\text{SSB}} - \tau_{0\text{SSB}}) + \frac{1}{2} \dot{f}(\tau_{\text{SSB}} - \tau_{0\text{SSB}})^2]. \quad (3.33)$$

$\tau_{0\text{SSB}}$ is the reference time with respect to which the spin parameters are defined. The choice of reference time $\tau_{0\text{SSB}}$ in our searches are discussed in 5.1.1. We will see the signal model in detail in 5.1.2 and 5.1.3.

3.4 SEARCH STRATEGIES

There are broadly three strategies to search for continuous gravitational wave signals based on how much is known about the source and, consequently, the size of the parameter space and the computational cost. This thesis focuses on targeted searches for continuous gravitational wave signals emitted from known pulsars.

3.4.1 Targeted searches

Almost 3300 pulsars are known today in the ATNF catalogue (Manchester et al., 2005). Pulsars are a crucial ingredient to this thesis and will be discussed in Chapter 4. When a pulsar has a rotational frequency such that its f_{gw} lies in the sensitivity band of the Advanced LIGO detectors, it becomes a potential target for continuous gravitational wave searches, as, for example, done in the most recent observation run O3 in Abbott et al. (2022) and Abbott et al. (2022). In this thesis, we searched for continuous gravitational wave emission from newly discovered millisecond pulsars. Seven new

pulsars were targeted in all of the observation runs so far in [Ashok et al. \(2021\)](#). The discovery of and search for continuous gravitational wave signals from a high energy black widow pulsar is reported in [Nieder et al. \(2020\)](#). A newly discovered binary pulsar was targeted in [Clark et al. \(2023\)](#). The results from the search for continuous gravitational wave signals from a set of 6 gamma-ray pulsars discovered in the Fermi-LAT data using preliminary timing solutions are also presented in this thesis. When final parameters for these pulsars are available, the search for continuous wave signals will be repeated and published in a peer-reviewed journal.

We assume that the phase of the gravitational wave is locked with the rotational phase of the pulsar. Then the continuous gravitational wave shape is completely known, and we can build a single template for the signal. We then coherently combine all the data from the Advanced LIGO detectors and carry out a search for the template. Also, less the number of templates probed in a search, the weaker the signal detectable with the method. This single-template search thus has the maximum sensitivity that can be achieved in a continuous gravitational wave search.

As mentioned before, we have not yet detected a continuous gravitational wave signal. So we set upper limits on the strength of the gravitational wave signal from the targeted pulsar. Our upper limits are informative if they are smaller than the spin-down upper limit of the pulsar, given in Equation 3.28. In such a case, our upper limits on h_0 can set an upper limit on the fraction of the rotational kinetic energy of the source converted into gravitational waves. For the Crab pulsar, which is valuable for such searches because of its high spin-down luminosity, the most recent continuous gravitational wave upper limits in [Abbott et al. \(2022\)](#) mean that $< 0.009\%$ of rotational energy lost is converted into gravitational waves.

Figure 3.4 shows the latest upper limits on continuous wave searches from 236 known pulsars, compared against the sensitivity of the two detectors during observation run in pink, from the LIGO-Virgo-Kagra collaboration. Pulsars for which h_0^{95} , the 95% confidence upper limits, beat the spin-down limits are within shaded circles.

The upper limits on the strength of the gravitational waves can be translated into upper limits on the ellipticity of the source by equation 3.27, thus constraining an important property of the pulsar, namely its deformation.

Most pulsars targeted so far have spin-down upper limits smaller than the 95% confidence upper limits on h_0 . And for the pulsars whose spin down upper limits have been beaten, the constraints on ellipticity values are too large that they are less likely to be physically sustained by the crust of the neutron star. [Morales and Horowitz \(2022\)](#), [Gittins et al. \(2020\)](#) and [Ushomirsky et al. \(2000\)](#) for example discuss the maximum possible ellipticities sustainable by neutron star crusts without breaking. Even so, looking forward, targeted searches are a good idea. New pulsars are being discovered by electromagnetic surveys at a faster rate than ever before, thanks to new and improved telescopes. There might be a neutron star that is close enough and deformed enough to be emitting continuous gravitational waves with a strength detectable with the

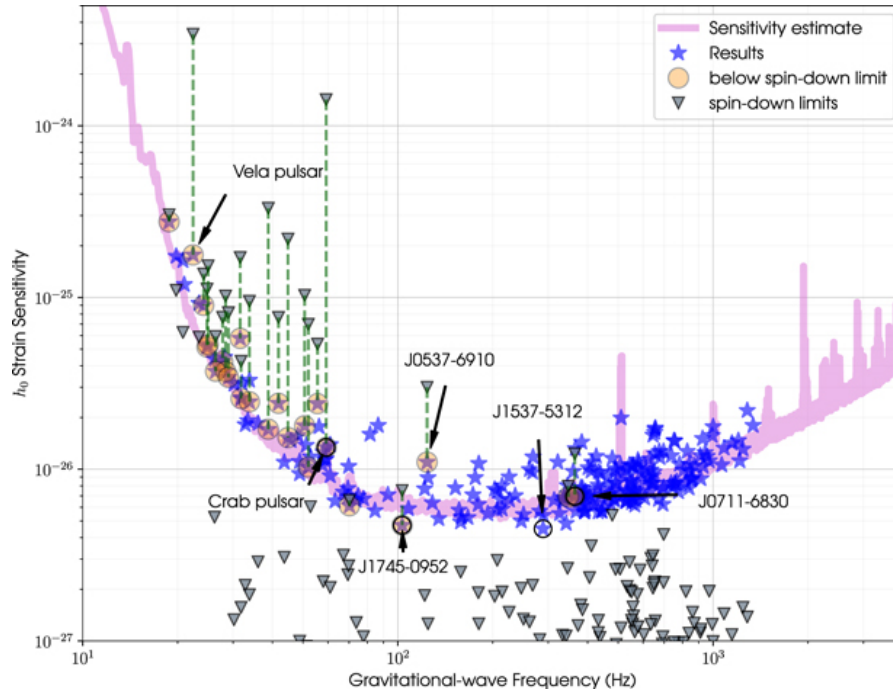


Figure 3.4: Upper limits on h_0 for ≈ 200 pulsars using O3 data. The stars show 95% confident upper limits on the amplitudes of h_0 . Figure Credit - [Abbott et al. \(2022\)](#)

sensitivity allowed by a targeted search. The higher the frequency of the pulsar, the stronger the gravitational wave it emits because $h_0 \propto f_{gw}^2$, and with 40,000 millisecond pulsars expected in our galaxy ([Lorimer, 2008](#)), as we move forward in time it can only be that more promising pulsars are discovered. For the already known pulsars, more observation time provides more precise pulsar parameters helping to sharpen the waveform template. Also, being computationally the least expensive and, at the same time most sensitive type of search, targeted searches are attractive. Added on, the sensitivity of gravitational wave data is increasing with the amount of data used, bridging the gap between spin down upper limit and achievable 95% upper limit on h_0 from pulsars, especially in the high sensitivity region of the detectors near 200Hz.

3.4.2 Directed searches

In a directed search, the sky position of a potential source is known, but its spin parameters are unknown. So broad ranges must be searched in the spin parameter spaces, making the search computationally expensive. Promising sky locations are those of supernova remnants where a neutron star is expected to be present ([Ming et al., 2019](#); [Papa et al., 2020](#)) and neutron stars in Low Mass X-Ray Binaries such as Scorpius X-1 ([Zhang et al., 2021](#); [Abbott et al., 2022](#)). Young objects are favoured for

such searches because they are expected to be more energetic and have larger energy potentially converted into gravitational waves. Optimisation techniques are employed in setting up parameter space range and resolutions in directed searches to gain maximum sensitivity, given the limited computational power (Ming et al., 2018). At AEI, the first stage of such searches is carried out with the computational power harnessed through Einstein@Home, which is a citizen volunteer computing system. Then the results are followed up in a hierarchical procedure with several stages. Figure 3.5 shows Ming et al. (2022)'s upper limits on continuous wave emission from the supernova remnant G347.3 in the most sensitive search carried out to date for the source. So far, no pulsations from the neutron star in this supernova remnant have been observed. A detected continuous gravitational wave emission would provide the first gravitational wave pulsar timing solution.

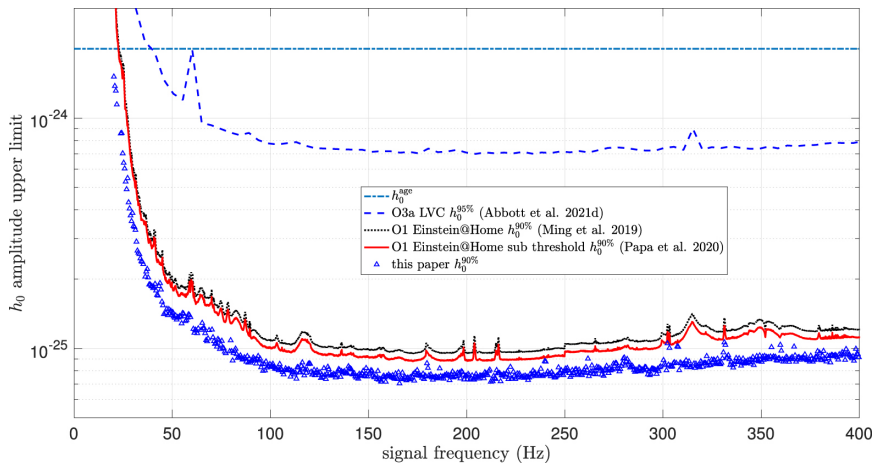


Figure 3.5: 90% confidence upper limits on h_0 for continuous waves from the neutron star in the supernova remnant G347.3 for signal frequencies between 20-400Hz in O2 data. Figure from Ming et al. (2022)

Another type of directed search aims at sky locations which are expected to host a large number of neutron stars, for example, the centre of the galaxy most recently in Abbott et al. (2022) or the globular cluster, Terzan 5 Dergachev et al. (2019).

3.4.3 All-sky searches

All-sky searches such as Steltner et al. (2023), Abbott et al. (2022) assume no particular source and search for signals from everywhere in the sky. Probing $\approx 10^{18}$ templates, all-sky searches are computationally the most expensive type of continuous gravitational wave search. So they are carried out using a semi-coherent approach: the data is divided

into time segments on which coherent searches are carried out. The results from each segment are then combined. In [Steltner et al. \(2023\)](#), the first stage of the search runs on Einstein@Home for several months. The results from the Einstein@Home search then undergo a hierarchical follow-up in which, at each stage, the span of the time segments is progressively increased. At each consecutive stage, more noise is rejected while a true astrophysical signal gains significance. So far, no candidate has survived all stages of the hierarchical follow-up. So, based on the null results, frequency-dependent upper limits have been set on h_0 , which say that, in each frequency bin, there is no source anywhere in the sky that emits a continuous gravitational wave signal stronger than the h_0 upper limit. Figure 3.6 shows the h_0 upper limits from all-sky search in O3 data. Assumed distances to sources parameterise the ellipticity upper limits following these h_0 upper limits.

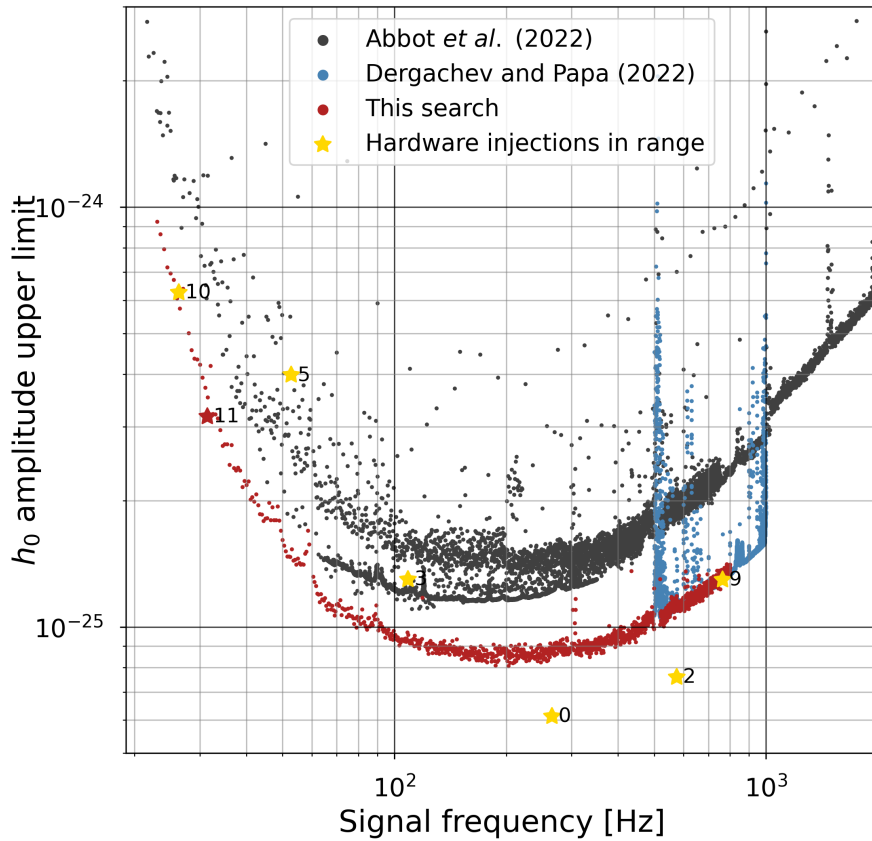


Figure 3.6: 90% confidence upper limits on h_0 for continuous waves all sky search in public O3 data. Figure from [Steltner et al. \(2023\)](#). The different searches in this plot probe slightly different parameter spaces.

PULSARS

From one particular piece of the sky an unclassifiable signal sometimes recurred, and my brain started to say: "You've seen something like this before, haven't you? You've seen something like this before from this bit of the sky, haven't you?"

*– Professor Dame Jocelyn Bell Burnell,
Journeys of Discovery, University of Cambridge*

In this chapter, we take a look at topics in pulsar astronomy that are relevant to the searches for continuous gravitational waves they emit. One can find further details in [Lorimer and Kramer \(2004\)](#).

Pulsars are neutron stars from which pulses of electromagnetic energy have been observed on Earth. Neutron stars are highly magnetised, harbouring magnetic fields with strengths of the order of 10^7 to 10^{15} G. With the rotation of the neutron star, charged particles in its magnetosphere are accelerated in this magnetic field, leading to the emission of electromagnetic radiation. During its rotation, as the magnetic axis of the neutron star crosses our line of sight, we see this electromagnetic radiation as a pulse. Thus, in very simplistic terms, one pulse is observed per rotation of the star. This model makes the pulsar analogous to a lighthouse, as shown in [Figure 4.1](#). Observations of these pulses and the timing of their arrival give us valuable information about the pulsar.



Figure 4.1: The rotating neutron star is modelled as a lighthouse to explain pulsed emission. The bottom panel shows the evolution of the pulse as the beam of radiation rotates with the neutron star. Credit: Animation designed by Michael Kramer

4.1 KNOWN PULSARS

The first pulsar was discovered in 1967 by Jocelyn Bell Burnell ([Hewish et al., 1968](#)). Today ≈ 3300 pulsars are known, with rotational frequency-spin-down distribution as shown in [4.2](#).

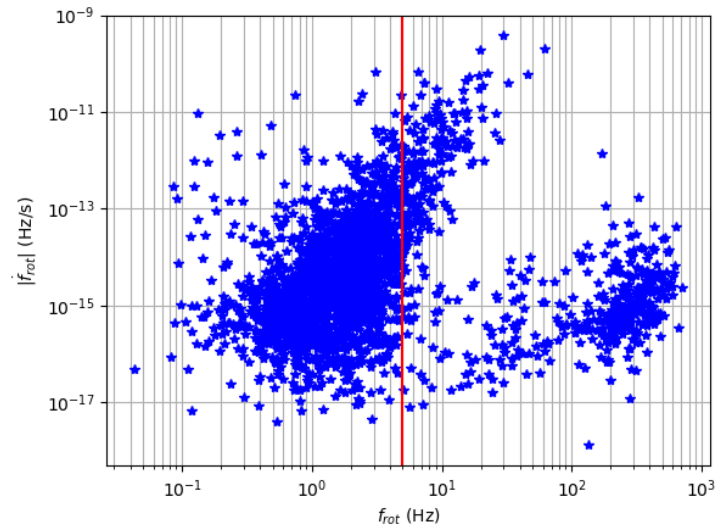


Figure 4.2: Population of known pulsars (3308) as of 20th August 2023 in the ATNF Catalog. The pulsars to the right of the red line lie in the sensitive frequency range of Advanced LIGO detectors. Credit: [Manchester et al. \(2005\)](#)

The Parkes radio telescope, Arecibo telescope, the Green Bank Telescope, and GMRT have, over the years, contributed most to the discovery of new pulsars. Seven of the pulsars targeted in this thesis were discovered and timed by the Arecibo telescope and reported in [Martinez et al. \(2019, 2017\)](#). The Arecibo telescope was decommissioned after the platform hosting the data collecting instrument crashed into the dish of the antenna at the end of 2020, devastating it as shown in figure 4.3. As older telescopes close their eyes to the radio sky, the future is still in the safe hands of new, advanced observatories. MeerKAT observatory, based in South Africa, has several ongoing surveys aiming to detect pulsars in various environments. [Clark et al. \(2023\)](#) reports the discovery of nine new millisecond pulsars, one of which was targeted in this thesis for continuous gravitational wave emission because of the availability of precise timing solutions.

Notable for pulsar discoveries in other wavelengths, the Large Area Telescope (LAT) on board the Fermi Gamma-ray Space Telescope was launched in 2008 and today has contributed more than 278 new pulsars (FLP). 145 of these were discovered in following up unidentified LAT sources with observations in other wavelengths. Two of the pulsars in this thesis were discovered and timed using the Fermi-LAT data. The pulsar in [Nieder et al., 2020](#) was radio-quiet and was detected in Fermi-LAT data with the help of parameter space constraints from optical and X-ray observations. The pulsar in [Clark et al., 2023](#) was discovered and timed thanks to a joint effort of MeerKAT and Fermi-LAT.



Figure 4.3: The Arecibo telescope has now been decommissioned following irreparable damage to the antenna. Credit: Nature, News dated 2 December 2020

Current and future telescopes like the Square Kilometer Array, with the ability to see much deeper into the galaxy, promise the discovery of new pulsars (Smits et al., 2009). Among these discoveries, hopefully, lies one or many neutron stars with a high deformity and the right rotational frequency making its gravitational wave emission observable in Advanced LIGO data with the sensitivity afforded by a targeted search.

4.2 TYPES OF PULSARS IN THIS THESIS

All the pulsars targeted in this thesis are millisecond pulsars (MSPs). Pulsars that spin faster than the fastest-spinning pulsar in a double-neutron star system, PSR J1946+2052, are generally classified as MSPs (Martinez et al., 2019). This means that pulsars with rotational frequency $> 60\text{Hz}$ are MSPs. Note, however, that other definitions exist in the community as to the exact spin frequency threshold above which a pulsar can be classified as an MSP. In figure 4.2, MSPs occupy the lower-right corner, with the shortest known periods. They spin down more gradually as well. MSPs are theorised to be 'recycled'. Recycled pulsars have a history of binary interaction (Srinivasan, 2010). The neutron star in the binary system is born first and, over time, loses its rotational energy to a variety of radiation, including gravitational and electromagnetic ones and slows down. Having expended its rotational energy over time, the neutron star's spin period is now long, lasting a couple of seconds. The slow-rotating magnetic field will continue to accelerate the charged particles, but the pulsar emits only low-energy radiation that is absorbed in the interstellar medium and is not detectable – the pulsar is said to have 'died'. In a later stage, when the companion star reaches the end of

its main sequence lifetime, the neutron star's gravitational field attracts matter from it, resulting in a process called accretion. The mass and angular momentum transfer during accretion from the companion star spins up the neutron star to short periods, burying its magnetic field in the process.

This binary interaction, if sustained, in principle, can cause non-axisymmetric distortions to the star (Abbott et al., 2020). Recycled pulsars are old neutron stars, $\gtrsim 10^8$ years in age, and this could be a caveat in that they have enough time to anneal their distortions. But they spin rapidly. Since the continuous gravitational wave signal amplitude is proportional to the square of twice the spin frequency, small ellipticities could lead to detectable emission.

Ashok et al. (2021) targeted seven newly discovered (at that point in time) recycled pulsars. Six are millisecond pulsars, and one is a mildly recycled pulsar with a rotational frequency of $\approx 29\text{Hz}$. Six pulsars are currently in binary systems, and one is an isolated pulsar. The origin of isolated recycled pulsars is unclear (Lorimer and Kramer, 2004). But theoretically, they could have either evaporated their companions (Fruchter et al., 1989) or lost the companion in an exchange interaction in a globular cluster (Verbunt and Freire, 2014). In a post-recycling phase, the pulsar might have run away in a supernova explosion that disrupted the binary (Tauris and Takens, 1998).

The pulsar targeted in (Clark et al., 2023), PSR J1526-2744, is a millisecond pulsar with a 402 Hz spin frequency. It is in a binary orbital system with a period of ≈ 5 hours, and its companion has a minimum mass $\approx 0.08M_{\odot}$. Optical observations suggest that the companion is a lightweight white dwarf.

The pulsar in (Nieder et al., 2020), J1653-0158 is a 'black-widow' pulsar. Optical modelling predicts that it is heavy with mass $\gtrsim 2M_{\odot}$. It spins at a high frequency of 508 Hz. It is in a compact binary orbit of period ≈ 75 minutes. Its companion has a low mass of $0.01M_{\odot}$ and is being evaporated because of the energetic pulsar wind.

4.3 PULSAR TIMING

Pulsars are very stable clocks. And their rotation periods can be measured to a precision of one part in 10^{13} or better as was measured for example, in Davis et al. (1985). Figure 4.4 shows the schematic of measuring the time-of-arrival (TOA) of pulses using the example of a radio telescope.

Pulses from the star travel through the interstellar medium. The interstellar medium is made of ionised plasma. As the pulse travels through this medium, different frequencies in electromagnetic radiation will experience different indices of refraction. The result is that the pulses undergo dispersion – the pulses observed at different frequencies arrive at different times after their travel through the interstellar medium. This can be seen, for example, in figure 4.5. Once received at the telescope, the pulses are first de-dispersed.

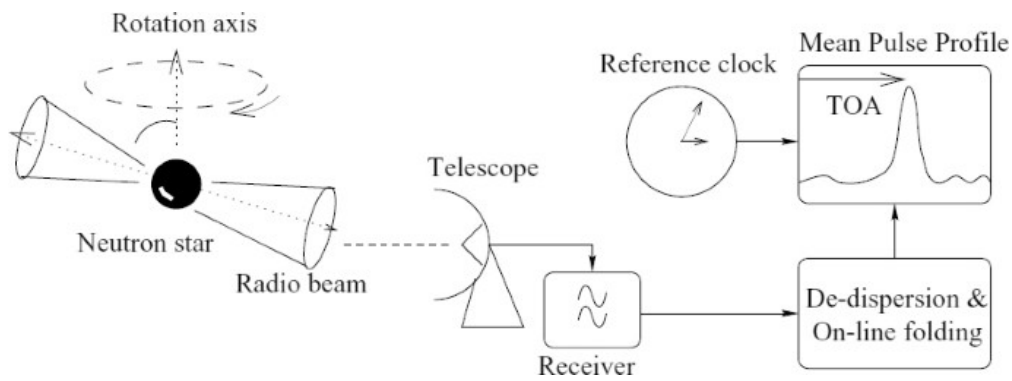


Figure 4.4: Main stages in a pulsar timing observation. Credit: Lorimer (2008)

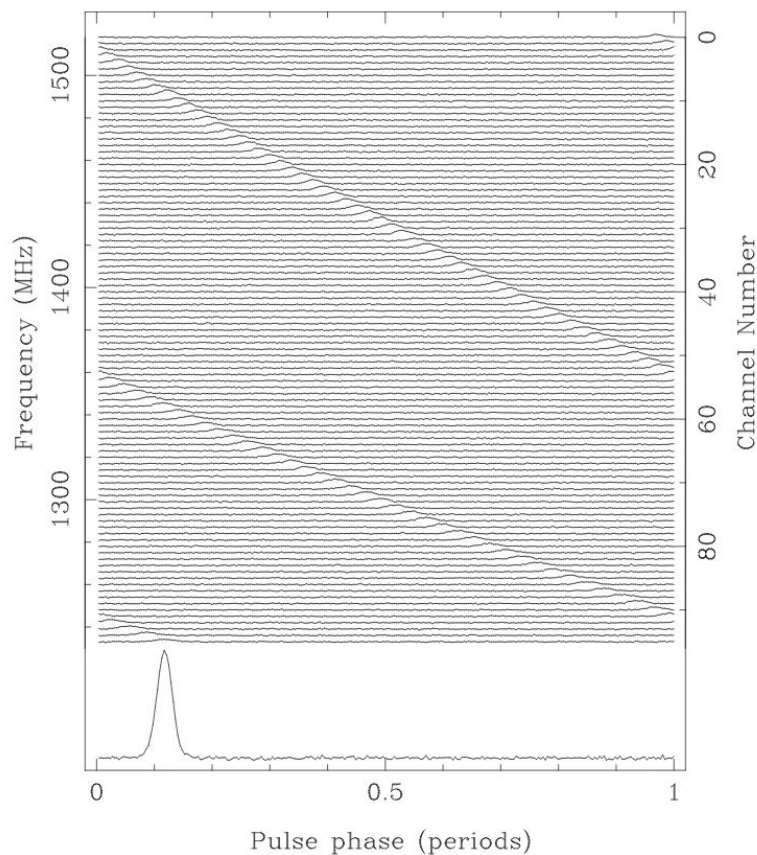


Figure 4.5: Pulse dispersion in the Parkes observation of pulsar B1356-60. Credit: Lorimer (2008)

The observations of TOA suffer modulations due to the relative motions between the Earth and the source. During Earth's annual orbit around the sun, at the time when the Earth is closest to the pulsar, the pulses arrive at the telescope early, and when the Earth is farthest from the pulsar, the pulses arrive after a delay. Thus, even if the pulsar

is emitting the pulses at equal time intervals throughout the year, there is an annual modulation of the signal purely due to the Earth's orbital motion around the sun. To circumvent this, the TOAs observed on Earth are transformed into a reference frame attached to the solar system barycentre (SSB). A planetary ephemeris, which provides the position of the planet at different times, is used for this transformation. With the accumulation of a number of TOAs, a Taylor expansion around the rotational frequency f_{rot} usually suffices to fit the TOA data and predict the arrival of future pulses. Thus, the pulse phase Φ of the pulsar is modelled by

$$\Phi(\tau) = \Phi_0 + 2\pi f_{rot}(\tau - \tau_0) + \pi \dot{f}_{rot}(\tau - \tau_0)^2 \quad (4.1)$$

where τ is the barycentric time, Φ_0 is the pulse phase at a reference time τ_0 .

The time series data collected by the telescope usually contains weak pulsating signals from the pulsar. Many pulses are added (folded) so that a signal is discernible above the noise. This process is possible because we know that the pulses arrive at a regular period. A pulse profile shows the emission from the neutron star averaged over many pulses as a function of its rotational phase. Each pulsar has a unique pulse profile. Figure 4.6 shows the pulse profiles of the nine pulsars, including PSR J1526-2744, which was targeted for continuous gravitational wave emission, discovered in Clark et al. (2023) as examples. Pulses from two rotations of each pulsar are shown.

A pulsar timing solution provides the sky position and the spin parameters of the pulsar. For a pulsar in a binary system, orbital parameters are also provided. Figure 4.7 shows an example timing solution, that of PSR J1526-2744, based on which a continuous gravitational wave search was set up (Clark et al., 2023). This timing solution is a TEMPO2-style file, which means that the file can be read by the TEMPO2 pulsar timing software (Hobbs, 2012). Note that TEMPO2 is only one example of several different pulsar timing software available. The first two columns are the pulsar parameter labels, and their observed values, the third column is a flag which shows if the parameter has been fit (1) or held constant (0), and the last column provides the 1σ , i.e. 68% uncertainty in the observed values. Sky positions are expressed in terms of Right Ascension, RAJ and Declination, DECJ. $F0$ is the rotational frequency in Hz, $F1$ is the spin-down in Hz/s. PEPOCH is the reference time in Modified Julian Day (MJD) at which these values were measured. ELL1 (Lange et al., 2001) is the binary orbital model that was used to infer the orbital parameters. Figure 4.8 shows a simple geometry for the binary orbit of the pulsar. The orbit of the pulsar is, in the most general scenario, an eccentric orbit of eccentricity e . The orbital period of the pulsar is given in the timing solution as PB in days. The projected semi-major axis of the orbit is the projection of the semi-major axis (a) onto the line of sight. In the figure, therefore, it is equal to $a \sin i$, where i is the inclination angle between the plane of the orbit and the plane of the sky. The timing solution writes the projected semi-major as A1 in light-seconds. For this pulsar, there was no measurement of the eccentricity of the orbit. The binary model ELL1 is used for systems with low eccentricity, $\approx 1 \times 10^{-5}$. When measurable,

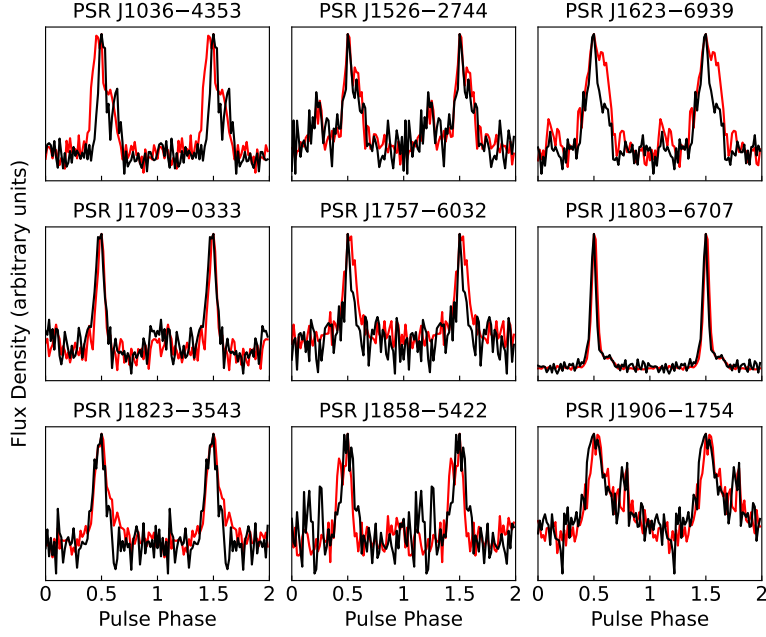


Figure 4.6: Pulse profile for nine pulsars discovered by [Clark et al. \(2023\)](#). The black and red curves show the pulse profiles observed in two wavelengths, the L-band (856-1712MHz) and Ultra High Frequency (544-1088MHz) band of the MeerKAT telescope.

eccentricity (e) and argument of periapsis (ω , which is the angle between ascending node and periapsis) are provided in terms of EPS1 and EPS2 defined by this model as

$$\text{EPS1} = e \sin \omega, \quad \text{EPS2} = e \cos \omega \quad (4.2)$$

For nearly circular orbits, periapsis and apoapsis are not defined. TASC is the time of ascending node, in MJD.

The binary orbital model DD ([Damour and Deruelle, 1986](#)) is used when eccentricity is high enough to be observable. With this model, eccentricity (E) and argument of periapsis (OM) are provided in the timing solution. In an eccentric orbit, periapsis is a well-defined point, and the time of periapsis of the pulsar is provided as $T0$ in MJD.

PSRJ	J1526-2744		
RAJ	15:26:45.103143174773805	1	1.22447858372069e-07
DECJ	-27:44:05.912804593135093	1	3.85234765940031e-07
F0	401.744602097496	1	2.62370693438065e-10
F1	-5.70865795989642e-16	1	1.22993413764598e-18
PEPOCH	59355.468037		
BINARY	ELL1		
PB	0.202810828455367	1	6.84806307298376e-10
A1	0.224097093580642	1	3.0326078024144e-05
TASC	59303.2059777742	1	9.58144227167222e-06
START	54681.0		
FINISH	59476.0		
CLK	TT(TAI)		
UNITS	TDB		
EPHEM	DE405		
EPHVER	5		
TZRSITE	@		
TZRFREQ	0		
TZRMJD	59355.468037		
CORRECT_TROPOSPHERE	N		

Figure 4.7: Gamma-ray timing solution for PSR J1526-2744 provided by Clark et al. (2023).

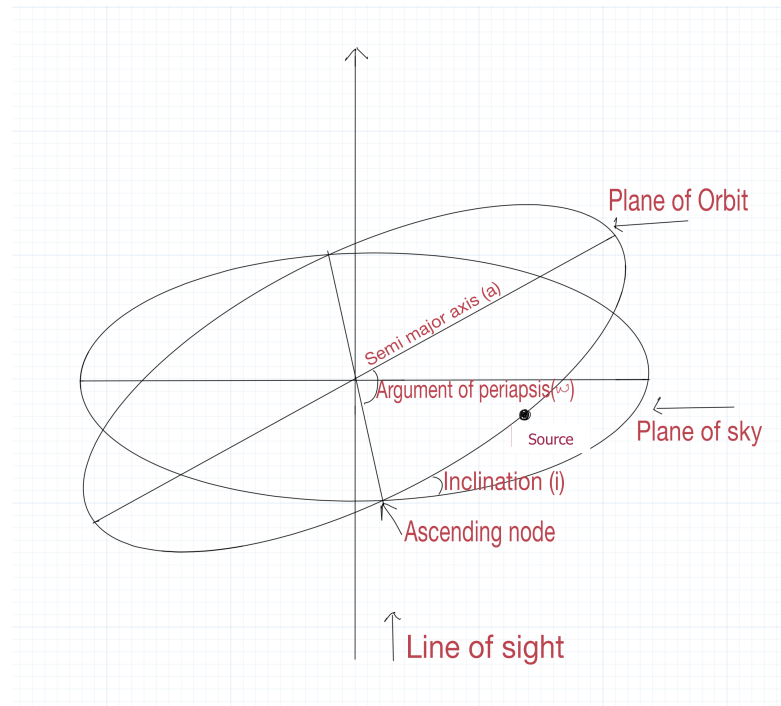


Figure 4.8: Geometry of an eccentric orbit of a Pulsar.

4.4 PULSAR PHYSICS RELEVANT TO GRAVITATIONAL WAVE SEARCHES

 4.4.1 *Spin evolution*

The spin-down upper limit on the continuous wave emission from a pulsar mentioned in Chapter 3 is calculated from the rate of loss of rotational kinetic energy of the pulsar (Lorimer and Kramer, 2004). This is given by

$$\dot{E}_{rot} \equiv -\frac{dE_{rot}}{dt} = -\frac{d(I\Omega^2/2)}{dt} = -I\Omega\dot{\Omega} = -4\pi^2 I f_{rot} \dot{f}_{rot} \quad (4.3)$$

where $\Omega = 2\pi f_{rot}$ is the rotational angular frequency and I is the moment of inertia of the pulsar. Assuming that all this lost rotational energy is converted into gravitational waves, we can equate it to the gravitational wave luminosity (Schutz, 1985) given by

$$L_{GW} = \frac{1}{10} \frac{G}{c^5} (4\pi f_{rot})^6 I^2 \epsilon^2 \quad (4.4)$$

for a pulsar with ellipticity ϵ . Equating 4.3 and 4.4 yields the ellipticity value that would support gravitational wave emission at the observed spin down rate –

$$\epsilon_{sd} = \sqrt{\frac{5c^5}{2(4\pi)^4 GI} \frac{|\dot{f}_{rot}|}{f_{rot}}} \quad (4.5)$$

Substituting this ϵ_{sd} into the equation for intrinsic amplitude of continuous gravitational wave in equation 3.27 gives

$$h_0^{sd} = \frac{1}{r} \sqrt{\frac{5GI}{2c^3} \frac{|\dot{f}_{rot}|}{f_{rot}}}. \quad (4.6)$$

The assumption that all energy lost has gone in gravitational waves may sound unreasonable in light of the fact that other carriers of energy, like pulsar wind and magnetic dipole radiation, exist. This is why the h_0^{sd} is considered an upper limit on the gravitational wave amplitude.

 4.4.2 *Proper motion*

Due to the relative motion of the Sun and the pulsar through space, the pulsar will be observed to move in the sky in a constant direction. The velocity of the pulsar with respect to the Sun can be decomposed into a radial component directed along the line of sight and a transverse component that is perpendicular to the line of sight. The transverse component causes a proper motion. The proper motion μ has two components. One along declination, $\mu_\delta \equiv \dot{\delta}$ and one along the right ascension, $\mu_\alpha \equiv \dot{\alpha} \cos \delta$. The total proper motion μ_T is

$$\mu_t = \sqrt{\mu_\alpha^2 + \mu_\delta^2}. \quad (4.7)$$

Knowing the distance d to the pulsar, we can find the transverse velocity by

$$v_t = \mu_t d. \quad (4.8)$$

Proper motion leads to an increase in the distance from the pulsar to the SSB. The

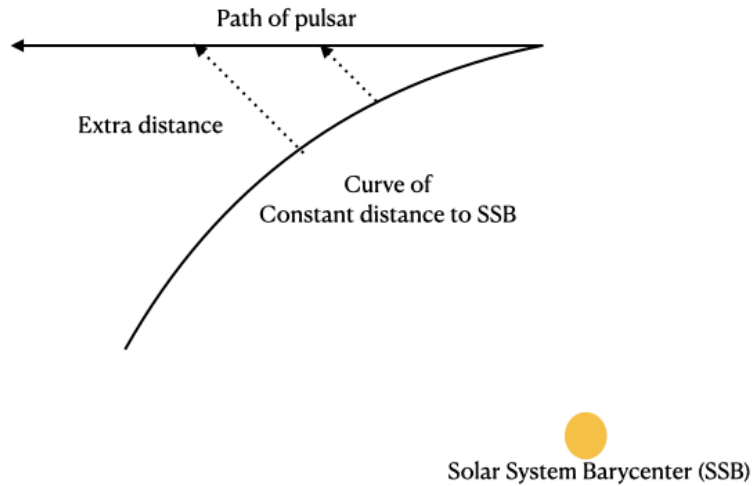


Figure 4.9: The transverse motion of the pulsar adds an extra distance to the curve of constant distance to the SSB. The pulse of light from it has to travel an ever-increasing distance causing the observed spin period to be different from the intrinsic spin period.

pulses are coming from an ever-increasing distance, as shown in figure 4.9, and at each time t suffer a delay given by

$$t_{delay}(t) = \frac{v_t^2 t^2}{2dc} \quad (4.9)$$

leading to a change \dot{P} in the observed period, P given by

$$\frac{\dot{P}}{P} = \frac{1}{c} \frac{v_t^2}{d}. \quad (4.10)$$

This effect was first pointed out by [Shklovskii \(1970\)](#), and is now known as the Shklovskii effect. Thus, for pulsars with measurements of proper motion, there is a Shklovskii correction to the spin-down, and the apparent spin-down can be distinguished from its intrinsic spindown. This distinction must be considered when calculating the spin-down upper limits on the continuous gravitational wave emission from the pulsar. One should use the intrinsic spin-down for such a calculation. But in the actual search for the continuous gravitational wave signal from the source, one should use the observed

spin-down value because any effect on the electromagnetic signal from the pulsar will also be found in its gravitational wave.

4.5 PULSARS AND GRAVITATIONAL WAVES

Pulsars have played and continue to play a vital role in gravitational wave astronomy. The first observational evidence for the existence of gravitational waves came from the shrinking of the orbit of the Hulse-Taylor binary pulsar system PSR B1913+16 (Hulse and Taylor, 1975). The observed decrease in the orbital period was consistent with the expected energy emitted in gravitational waves. In Pulsar Timing Arrays, pulsars come together to form a unique type of gravitational wave detector in which a passing gravitational wave induces correlations between pulse arrival times for pairs of pulsars, which depend on their angular separations.

The observability of pulsars in electromagnetic and potentially in gravitational waves is an example showcasing the potential of multi-messenger astronomy, where different physics help each other and eventually lead to new scientific discoveries. Targeted searches for continuous gravitational wave signals exploit such alliance. Take the story of pulsar J1526-2744 (Clark et al., 2023). A gamma ray source was identified in Fermi-LAT data. In a dedicated follow-up, this source location was observed using the MeerKAT radio telescope, confirming its nature as a pulsar. MeerKAT also helped further pinpoint its location and constrain some of the orbital parameters. With this information, a focussed search in Fermi-LAT data found and timed pulsations from the source. This timing solution was then used to inform the search for continuous gravitational waves from the pulsar in Advanced LIGO data. Such information exchanges between multiple wavelengths of the electromagnetic spectrum culminating in a precise timing solution which could then aid the search for a whole new messenger, showcases the true essence of targeted continuous wave searches.

METHOD I - TEMPLATED SEARCHES USING THE MULTI-DETECTOR \mathcal{F} -STATISTIC

One's instinct is at first to try and get rid of a discrepancy, but I believe that experience shows such an endeavour to be a mistake. What one ought to do is to magnify a small discrepancy with a view to finding out the explanation.

– Sir John William Strutt (Lord Rayleigh),
Proceedings of the Royal Institution (1895), 14, 525

We want to target continuous gravitational waves emitted by a pulsar. Unlike all-sky and directed searches, the wealth of information about the source available from pulsar timing solutions provides a single waveform template for the gravitational wave signal from the pulsar. We search for the presence of this waveform in the Advanced LIGO data. We also search for templates with (f_{gw}, \dot{f}_{gw}) in narrow bands of the waveform parameters, centred at the values derived from the timing solutions, to allow for possible differences between twice the spin frequency and the gravitational wave signal frequency. Both single-template and narrow-band searches can be carried out in a fully coherent manner. Currently, targeted searches are the only type of continuous gravitational wave searches where it is computationally affordable to do a fully-coherent search in the detector data. Also, the fewer the templates probed, the higher the sensitivity of the search and the weaker the detectable signal. The number of templates probed in a band search is many orders of magnitude smaller than those probed in large-scale surveys. For example, the all-sky search in [Steltner et al. \(2023\)](#) probed 10^{19} templates; this is $\approx 10^{10}$ times more templates than the largest band search (for PSR J0154+1833 as seen in table 5.1) in this thesis.

This chapter describes one method to search for continuous gravitational wave emission from a known pulsar. In section 5.1, we will look at the parameters that define the single template. Once we have a template for the signal, we ask – is this signal present in the noise-dominated data (described in section 5.2) from Advanced LIGO detectors? A detection statistic quantifies the answer to this search problem. We should also quantify the significance of this answer. These steps constitute the single-template search described in section 5.3. In a detection problem, assuming a strict signal model and looking for nothing else is dangerous. Especially given that there is a lot of uncertainty surrounding neutron star physics. So, we also search for signals with parameters in a range of values around those provided by the timing solution. Section 5.4 describes this search. In the event of non-detection of a signal, we set upper limits on the gravitational wave amplitude from the pulsar. Section 5.5 describes this procedure. As we will see, these steps constitute a frequentist approach

to signal detection followed by a frequentist approach to constrain the strength of such emission.

5.1 SEARCH PARAMETERS

This section describes how the continuous gravitational wave search parameters are set up from the pulsar parameters available from the timing solution.

Assuming a quasi-monochromatic gravitational wave signal with slowly varying intrinsic frequency, the signal phase $\Phi(\tau)$ can be Taylor-expanded as

$$\Phi(\tau) = \Phi|_{\tau_{ref}} + 2\pi \sum_{k=0}^s \frac{f^{(k)}(\tau_{ref})}{(k+1)!} (\tau - \tau_{ref})^{k+1} \quad (5.1)$$

where $2\pi f(\tau) \equiv d\Phi(\tau)/d\tau$ is the intrinsic signal frequency and the $s+1$ spin parameters are

$$f^{(k)}(\tau_{ref}) \equiv \left. \frac{d^k f(\tau)}{d\tau^k} \right|_{\tau_{ref}} \quad (5.2)$$

and τ_{ref} is the reference time.

5.1.1 Reference time

Every continuous gravitational wave search has a reference time, τ_{ref} , and all time elapsed is counted with respect to this time. The spin parameters $f^{(k)}$ of the signal waveform at τ_{ref} are fixed, and the waveform at each point in time is determined by these. Further, we search for signals originating from the pulsar's location in the sky at time τ_{ref} . In our searches, we define the reference time to be the time epoch with respect to which the pulsar timing solution is reported, henceforth t_{epoch} . That is,

$$\tau_{ref} = t_{epoch}. \quad (5.3)$$

5.1.2 Doppler parameters

In section 3.3, we saw that the continuous gravitational wave signal is Doppler-modulated by the relative motion of the detector with respect to the source. Let us elaborate on this. Consider the general case of a pulsar in a binary orbit, with orbital parameters b . Let \hat{n} be the unit vector pointing in the direction of the source, as in the geometry of the system depicted in figure 3.3. If a wave-front that leaves the source at time $\tau(t)$ arrives at the detector at time t , the relation between these two times is

$$\tau(t; b, n) = t + \frac{\vec{r}(t) \cdot \hat{n}}{c} - \frac{d}{c} + \Delta_{bin}(t; b), \quad (5.4)$$

where $r(t)$ is the vector from the Solar-System Barycenter (SSB) to the detector (see figure 3.3), and $\frac{r(t) \cdot n}{c}$ is called the Roemer delay, $\Delta_{bin}(t; b)$ is the time delay between the pulsar and the Binary-System Barycenter (BSB) and vanishes for an isolated source, d is the distance between the SSB and the BSB. Inserting this timing relation in equation 5.1, we find that the phase evolution in the detector frame, $\phi(t)$ has the general form

$$\phi(t; \lambda) = \phi(\tau(t; \lambda)), \quad (5.5)$$

where $\lambda \equiv \{f^{(k)}, \hat{n}, b\}$, defines the set of Doppler parameters.

Let us look at how to set up the Doppler parameters of the gravitational wave signal template. We assume a triaxial ellipsoid neutron star emitting gravitational waves at twice the spin frequency of the star, as shown in equation 3.23. So the spin parameters of the continuous gravitational wave signal are,

$$f_{gw} = 2f_{rot} \quad (5.6)$$

$$\dot{f}_{gw} = 2\dot{f}_{rot} \quad (5.7)$$

Spin frequency and its first derivative are the spin parameters that are observable in most cases. But for some pulsars, higher-order derivatives of frequency are needed to describe the pulse timing. In such cases, we can generalise,

$$f_{gw}^k = 2 \times f_{rot}^k \quad (5.8)$$

We saw in section 4.4.2 that if the pulsar is moving with respect to Solar System Barycenter (SSB), the transverse component of this velocity causes the apparent spin period (\dot{P}) to be larger than the intrinsic spin period (\dot{P}_{int}). For some pulsars we targeted, there are observations of such proper motion across the sky. Since these pulsars have been observed in radio/gamma-ray during a timespan that overlaps with the gravitational wave observations, the apparent spin-down of these pulsars in both electromagnetic and gravitational wave data will be the same. So we use the observed spin-down value in Equation (5.7) for the search even if the pulsar has a measured proper motion.

The sky location of the source is expressed in terms of right ascension (α) and declination (δ) of the pulsar at t_{epoch} as observed by the telescope. Then $n = (\cos \delta \cos \alpha, \cos \delta \sin \alpha, \sin \delta)$. If the pulsar is in a binary orbit with another object, then its orbital parameters - orbital period, time of ascending node, projected semi-major axis, the eccentricity of the orbit and argument of periapsis – comprise b in defining the template. In section 4.3, we saw that the timing solutions provide these parameters.

5.1.3 Amplitude parameters

The amplitude h_0 , initial phase ϕ_0 , polarisation angle ψ and the cosine of the angle between our line-of-sight to the pulsar and its spin axis, $\cos \iota$, together form the

Amplitude parameters of the signal. These are usually unknown properties of the source, which are maximised over in the \mathcal{F} -statistic.

For recycled pulsars, which are very old pulsars ($\gtrsim 10^8$ year), such as many in this thesis, the orbital inclination angle is aligned with the angle ι . This is useful when there are observed values for the orbital inclination angle, providing information on $\cos \iota$. In section 5.5 we will see how we use this constraint on $\cos \iota$ to set more informative upper limits on the signal strength.

5.2 DATA

This section describes the Advanced LIGO data in which the search is carried out. The time-domain strain data $x(t)$ from detector X of the two Advanced LIGO detectors is converted into the frequency domain via Short-baseline Fourier Transforms (SFTs).

$$\tilde{x}_X(f) = \int_0^{T_{\text{SFT}}} x_X(t) e^{-i2\pi ft} dt. \quad (5.9)$$

The frequency resolution of the SFT is $\delta f = 1/T_{\text{SFT}}$ and the timebase T_{SFT} is chosen in such a way that even with the Doppler modulation during this time the signal power is maintained in one frequency bin. The SFTs used in the searches for isolated pulsars have a timebase of 1800s, while those used for binary pulsars have a timebase of 60s.

At the time of writing, the first three observation runs, O₁, O₂ and O₃, of Advanced LIGO detectors are concluded, and the data from these runs are publicly available. In principle, we would use data from all the observing runs of the Advanced LIGO detectors because the signal is expected to be present in the data all the time. If the timing solution of the pulsar overlaps with the timespan of the Advanced LIGO observations, then we can coherently combine the data without worrying about changes in the spin frequency of the pulsar. If a pulsar is known to have glitched during the Advanced LIGO observation, we can no longer coherently combine all the data. We need to split the observation time into pre-glitch and post-glitch times and search in them with different signal templates. None of the pulsars encountered in this thesis is known to have glitched within the Advanced LIGO observations. But for a subset of pulsars, the timing solutions are not based on observations that completely bracket the Advanced LIGO runs. These are recycled pulsars, objects that are considered stable and non-glitching. Yet, purely based on the timing solutions, glitches cannot be ruled out. So we performed three different searches – (i) in the coherent combination of O₁ and O₂ data (ii) in the O₃ data, (iii) in the coherent combination of all the observation runs, O₁O₂O₃.

The searches in this thesis were carried out at different points in time during 2018-2022. Each search was done in the data from the Advanced LIGO observation runs that were publicly available at that point in time. The data used for each pulsar will be explicitly mentioned in the section dedicated to the pulsar in chapter 7, which presents the results.

We are searching for a signal that is buried in detector noise. Noise in the detector data has to be understood and removed as much as possible to allow for a sensitive search. First, loud detector glitches in Advanced LIGO detectors are removed in a process called gating (Steltner et al., 2022). Data is ‘cleaned’ to remove known lines. Lines and combs are noise artefacts whose origins could be instrumental, environmental or unknown. They are usually monochromatic, with combs repeating in multiples of a starting frequency and lasting for long timespans in the data and hence are particularly problematic for continuous gravitational wave searches because they mimic a continuous gravitational wave signal by virtue of their monochromatic, persistent nature. If a line coincides with the expected frequency of a continuous gravitational wave signal from a pulsar, it becomes impossible to search for this signal in the data.

Advanced LIGO data with sensitive frequency range 20-2000 Hz, is first narrow-banded to reduce the amount of data in the next steps to just the frequency range that is relevant for the signal from the pulsar.

The noise power spectral densities (PSD) in this frequency range gives a first sense of how disturbed the data is. The per-detector PSD is practically estimated by

$$S_X(f') \equiv \frac{2}{T_{SFT}} |\tilde{x}_X(f')|^2 \quad (5.10)$$

and averaged over the number of SFTs from that detector. The Amplitude Spectral Density (ASD) is the square root of the PSD. The per-detector ASD shows features present in the frequency range around the signal frequency and helps decide which data needs detailed noise analysis.

An advantage of knowing the signal evolution beforehand is that we know, at every specific time of the data, precisely which frequency bins will be used in the computation of the detection statistic. This allows for a meticulous choice of data to be used in the search. If the noise in a detector at the continuous gravitational wave signal frequency at a specific time is high, we exclude the SFT data from that time from the search. Such a thorough data choice procedure was necessary (see section 7.2.1) for the search of PSR J1653-0158 whose continuous gravitational wave signal frequency lay in the second harmonic of the violin mode near the H1 and L1 detectors.

The search weighs the data according to the noise in it, so highly noisy data will be down weighed in calculating the detection statistic. This process is most often sufficient to ensure that noise does not contribute towards the search results. But when a pulsar is near known instrumental artefacts like the 60 Hz power line (see section 7.7), additional noise removal steps prior to the search are carried out. Also, when a pulsar with high promise owing to its closeness to Earth, high spin frequency and the possibility to set an h_0 upper limit that beats the spin-down upper limit presents itself in noisy data, it makes more sense to carry out careful data choices.

5.3 SINGLE TEMPLATE SEARCH

Before doing a single template search, the first question that arises is the possibility of such a search. The data from radio/gamma-ray observations of a pulsar spans several years. The resulting timing solutions report the pulsar parameters at a reference time t_{epoch} . t_{epoch} for many pulsars in this thesis lay before the start time of the gravitational wave data. An uncertainty in $f^{(k)}$ at t_{epoch} results in a range of possible values for $f^{(k-1)}$ at later times. For pulsars in this work, $\dot{f} = 0$. So, we focus on the evolution of f -range due to the uncertainty in observed \dot{f} . If $\delta\dot{f}$ is the uncertainty in \dot{f} and Δt is the time elapsed between the mid-point of LIGO observations and t_{epoch} , then, we check if the range in f is resolvable by the search, i.e, if

$$\delta\dot{f}\Delta t < df, \quad (5.11)$$

where df is the frequency resolution of the search. For the pulsars in this thesis, the uncertainties in observed rotational \dot{f} are between 10^{-18} and 10^{-20} Hz/s. And, the maximum time elapsed between t_{epoch} and LIGO-O1 start time is 684 days. With $\Delta t = 684$ days and $\delta\dot{f} = 10^{-18}$, the maximum values of both quantities, the maximum range in f is $< 7 \times 10^{-11}$ Hz. The frequency resolution of the longest search is $\approx 10^{-9}$ Hz (as we will see in section 5.4.2). So we can do single-template searches for continuous gravitational wave from these pulsars.

We use the matched-filter detection statistic - \mathcal{F} -statistic ($2\mathcal{F}$, Cutler and Schutz (2005)) as our detection statistic. \mathcal{F} -statistic is essentially the log of the maximum likelihood ratio between two hypotheses. One hypothesis is that the data contains a continuous wave signal parameterised by Doppler parameters, λ . The second hypothesis is that the data contains Gaussian noise. Details on the expressions for this detection statistic can be found in chapter 6 in which the likelihood odds-ratio for these two hypotheses is written down.

In Gaussian noise, the \mathcal{F} -statistic has a χ^2 distribution with a zero non-centrality parameter and 4 degrees of freedom. This helps us quantify the significance of the $2\mathcal{F}$ with respect to Gaussian noise. But in practice, the distribution of $2\mathcal{F}$ in Gaussian noise is not a perfect χ^2 distribution. So we calculate the significance of $2\mathcal{F}$ from a search in terms of frequentist p-values based on search results in a parameter space which does not contain the signal. The p-value associated with the realisation $2\mathcal{F}'$ is defined as

$$p(2\mathcal{F}') = \int_{2\mathcal{F}'}^{\infty} p_0(2\mathcal{F}) d2\mathcal{F} \quad (5.12)$$

where p_0 is the distribution of $2\mathcal{F}$ when there is no signal, and we evaluate it on real data in frequencies close to the target frequency. Such off-source data leads to a realistic p-value for the search result as opposed to the perfect Gaussian noise expectations. Results from an off-source search in real data can be used as a representative of the null hypothesis (which here is the hypothesis that the on-source searched data contains no

signal) as long as the noise in the off-source frequencies is similar to the noise present in the on-source search. Thus the off-source search must not be carried out in a parameter space region which has noise artefacts that are not present in the targeted search. For a single-template search, it is possible to use the real data in a frequency bandwidth that is large enough to build a reference distribution but is not so large that the nature of noise varies from that which contributes to the actual search result. This is worth mentioning because, in the next section, which discusses a band search, we will see that to assign p-values to band search results, a reference distribution cannot be built from search results in real data.

In chapter 7, where the results will be presented, three p-values will be reported in figures that show the significance of targeted search results, like for example, 7.9. These are denoted with 'p_v' (where v stands for value) and are p-values based on (i) theoretical distribution of $2\mathcal{F}$ (ii) $2\mathcal{F}$ distribution from search in Gaussian noise (iii) $2\mathcal{F}$ distribution from search in real data.

5.4 BAND SEARCH

The single template search assumes that the gravitational wave frequency is locked with the observed spin frequency. But this is a strong assumption, and there could be mechanisms that produce a small difference between the gravitational wave frequency and twice the spin frequency. It could be that the component of the star dominating the gravitational wave emission (which, for instance, may be an asymmetry in the core of the star) and the component emitting the electromagnetic radiation spin differently. There could be a small difference between the spin axis and the symmetry axis of the star leading to free precession. Acknowledging the current limitations in the understanding of gravitational wave emission mechanisms and the geometry of electromagnetic emission, we perform a search in a band of (f_{gw}, \dot{f}_{gw}) parameter space.

5.4.1 Bandwidth

We consider that the signal frequency can vary in the interval

$$f_{gw} \in [(2f_{rot} - \delta), (2f_{rot} + \delta)] \quad (5.13)$$

where δ parameterises a possible discrepancy between the true gravitational wave parameters and those derived from electromagnetic observations. Such a relationship holds if the component of the star emitting gravitational waves rotates separately from the component emitting electromagnetic waves, and the two components are linked by a torque which tries to enforce corotation between them on a timescale $\tau_{coupling}$. Then,

$$\delta \sim \frac{\tau_{coupling}}{\tau_{spin-down}}, \quad (5.14)$$

where,

$$\tau_{\text{spin-down}} \sim \frac{f_{\text{rot}}}{\dot{f}_{\text{rot}}}, \quad (5.15)$$

is the characteristic spin-down time of the pulsar, which is an indicator of the approximate age of the pulsar.

In the scenario that the gravitational wave is produced by the free precession of a nearly biaxial star (Jones and Andersson, 2002),

$$\delta \sim \mathcal{O} \left[\frac{I_{zz} - I_{xx}}{I_{xx}} \right], \quad (5.16)$$

where I_{zz} is the moment of inertia of the star along the principal axis aligned with the rotation axis, and I_{xx} is with respect to the principal axis in the equatorial plane of the star.

Early narrowband searches like Abbott et al. (2008) used a $\delta \sim \mathcal{O}(10^{-4})$. The reasoning was based on the characteristic age and glitch recovery periods of the Crab pulsar. A corotation between the two components is expected to occur during the glitch recovery period. This value of δ also accounts for the scenario of free precession in the following way in that $\delta \sim 10^{-4}$ is on the high end of deformations sustainable by a neutron star.

More recently, Abbott et al. (2022) chose a larger bandwidth with $\delta = 2 \times 10^{-3}$, owing to less computational limitation. Our search bandwidths are consistent with this and amount to a total of

$$\Delta f_{gw}^k = 4 \times 10^{-3} \times 2f_{rot}^k, \quad (5.17)$$

for the gravitational wave signal spin parameters around the central value $2f_{rot}^k$. Although the first estimate of δ was based on the Crab pulsar, our pulsars are much older than Crab. For our pulsars, a δ spanning $\mathcal{O}(10^{-3})$ covers more spin parameter range than recommended by equation 5.14. Hence, there is no risk of losing signal that isn't coupled with the electromagnetic emission.

Thus we want to probe a frequency range (Δf_{gw}) of 0.4% of f_{gw} and likewise for spin-down. For spin-down, this range is smaller than the search resolution for the majority of the pulsars in this thesis, so we search one \dot{f}_{gw} template on each side of the targeted \dot{f}_{gw} . Table 5.1 shows the frequency bandwidths around the targeted frequency probed for different pulsars.

5.4.2 Search resolution

Our template parameter space is discrete. As a result, it could be that none of the templates exactly matches the true signal. This results in a mismatch, μ , (Owen, 1996) between a true signal and the template. It is impossible to entirely avoid a mismatch between the true signal and the template because we cannot have an infinite number of

Pulsar	f_{gw} (Hz)	Δf_{gw} (Hz)	\dot{f}_{gw} (Hz/s)	$\Delta \dot{f}_{gw}$ (Hz/s)
J1653-0158	1016.5	2.0	-1.3×10^{-15}	3.8×10^{-17}
J0154+1833	845.8	3.38	-1.1×10^{-15}	3.8×10^{-17}
J0509+0856	493.1	1.97	-5.6×10^{-16}	3.8×10^{-17}
J0709+0458	58.1	0.23	-6.6×10^{-16}	3.8×10^{-17}
J0732+2314	489.0	1.96	-7.5×10^{-16}	3.8×10^{-17}
J0824+0028	202.8	0.81	-3×10^{-15}	3.8×10^{-17}
J1411+2551	32.0	0.13	-6.8×10^{-17}	3.8×10^{-17}
J2204+2700	23.6	0.09	-5.6×10^{-17}	3.8×10^{-17}
J1526-2744	803.5	3.2	-1.2×10^{-15}	1.9×10^{-17}
J0418+6635	687.2	2.7	-3.2×10^{-15}	1.8×10^{-17}
J0744-2525	21.7	0.09	-2.2×10^{-13}	9×10^{-16}
J1139-6247	16.6	0.07	-5.6×10^{-13}	2.2×10^{-15}
J1335-5656	617.7	2.5	-2.3×10^{-15}	1.8×10^{-17}
J1649-3012	584.0	2.3	-2.3×10^{-15}	1.8×10^{-17}
J2034+3632	547.9	2.2	-2.7×10^{-16}	1.8×10^{-17}

Table 5.1: Signal frequency and bandwidth probed for pulsars. Note that for the first pulsar PSR J1653-0158, the search probed a bandwidth with $\delta f = 10^{-3}$ around the target frequency. $\delta f = 2 \times 10^{-3}$ was adopted afterwards.

templates. The mismatch produces a reduction in the signal-to-noise ratio with respect to what would have resulted from a perfectly matched search. If we indicate with $2\mathcal{F}_{pm}$ the detection statistic in the case of a perfect match between the signal and template and $2\mathcal{F}_m$ the detection statistic in the presence of a mismatch between the signal and the template, we measure the mismatch with

$$\mu = \frac{2\mathcal{F}_{pm} - 2\mathcal{F}_m}{2\mathcal{F}_{pm}} \quad (5.18)$$

in the absence of Gaussian noise.

The search resolution is decided based on the mismatch that we can afford in the search. Since a targeted search is not computationally intensive, we can demand a mismatch as small as 1% for the search, as compared to the $\approx 50\%$ mean mismatch in an all-sky search which is at the opposite end of computational expense. Once we decide on the mismatch value, we compute the resolutions for (f_{gw}, \dot{f}_{gw}) . For $\mu \lesssim 1\%$ it was found (Owen, 1996; Dhurandhar and Sathyaprakash, 1994) that

$$\mu(\vec{\lambda}_s, \vec{\lambda}_t) = g_{ij} \Delta \lambda^i \Delta \lambda^j, \quad (5.19)$$

where λ^i indicate the signal parameters (and in our case, $\vec{\lambda} = (f_{gw}, \dot{f}_{gw})$) and $\Delta \vec{\lambda}$ is the distance between the signal and template parameters : $\Delta \vec{\lambda} = \vec{\lambda}_t - \vec{\lambda}_s$. g_{ij} is the metric in the parameter space, defined in (Owen, 1996). As has always been observed in the comparison of metric mismatch with the true mismatch, the metric mismatch is an overestimation of the mismatch. This effect has recently been illustrated and explained by Allen (2019). So we do not directly use equation 5.19 to calculate the resolutions because the resolutions predicted by the metric will be finer than necessary for the desired mismatch. We do Monte Carlo studies starting with the grid resolutions recommended by the metric and progressively decrease the resolution to arrive at the grid resolutions that practically provide us with our desired mismatch. Since our band searches are not computationally challenging, we can aim for a dense grid with a very small mismatch of the order of $\approx 1\%$ mismatch. For a search in the timespan of O1O2 coherent combination, this means a search grid with resolutions

$$df_{gw} = 2.55 \times 10^{-9} \text{ Hz}, \quad d\dot{f}_{gw} = 1.9 \times 10^{-17} \text{ Hz/s}. \quad (5.20)$$

For an O1O2O3 search, which has a longer timespan, this grid results in $\approx 7\%$ mismatch. To obtain 1% mismatch in O1O2O3 search, we use a grid

$$df_{gw} = 1.09 \times 10^{-9} \text{ Hz}, \quad d\dot{f}_{gw} = 9.23 \times 10^{-18} \text{ Hz/s}. \quad (5.21)$$

That is, to achieve a mismatch μ , with a longer observation time, we need a finer grid than would be necessary with a shorter observation time.

5.4.3 Search

The full frequency bandwidth is split into smaller sub-bands of 10 mHz. The highest (or loudest) detection statistic, $2\mathcal{F}_l$, in each sub-band is regarded as the result from that sub-band. And the collection of these $2\mathcal{F}_l$ from all sub-bands is referred to as the ‘band search results’. Thus, there are

$$N^\alpha = \frac{\Delta f_{gw}}{10\text{mHz}} \quad (5.22)$$

results from a band search for a pulsar α .

The significance of these results are expressed in terms of p-values based on a reference distribution of the loudest $2\mathcal{F}$ from band searches in Gaussian noise. To get the reference distribution, we carry out searches in 10 mHz bands ≈ 7000 times, each time in a different realisation of Gaussian times. In practice, this is achieved by producing a number of Gaussian noise realisations for a pulsar and repeating the band search procedure exactly as was done in real data for that pulsar and combining the loudest $2\mathcal{F}$ from all the fake Gaussian noise realisations for all the pulsars to arrive at the reference distribution, $p_0(2\mathcal{F}_l)$. Then the p-value of a band-search result is calculated according to equation 5.12 with this $p_0(2\mathcal{F}_l)$ as the reference distribution of search results. We do not use real data to build the reference distribution in this case because, with thousands of independent realisations of 10 mHz bandwidth, we would be considering target frequencies several Hz away from the original pulsar frequency where the noise is not necessarily representative of the noise contributing to the original results. The Gaussian noise p-value is conservative in that we would not accidentally discard a potential signal because it will overestimate the significance of a result compared to the p-value evaluated based on real data. A reference distribution based on search results in real data, $p_{real}(2\mathcal{F}_l)$, is more likely to have an abundance of higher $2\mathcal{F}_l$ than a reference distribution based on search results in Gaussian noise. With $p_{real}(2\mathcal{F}_l)$ instead of $p_0(2\mathcal{F}_l)$, equation 5.12 would lead to a higher p-value implying lower significance for any $2\mathcal{F}_l$.

In works like [Ashok et al. \(2021\)](#) where a number of pulsars are targeted simultaneously, after analysing the band search results from individual pulsars and concluding that they are consistent with the noise-only hypothesis, we have the chance to confirm that the statistical combination of the band search results from all pulsars is consistent with the noise-only hypothesis. Additionally, we can compare the most significant result for each pulsar, the largest amongst the $2\mathcal{F}_l$ to make sure we understand the reason for the relative significance of results with respect to one another. This cannot be done directly because N^α is different for different pulsars, and so the loudest among the loudest 10mHz $2\mathcal{F}_l$ for each pulsar does not come from the same distribution. Simply due to the trials factor, the larger the frequency bandwidth searched, the lower the expected lowest p-value for that pulsar. To allow a direct comparison of these, we first estimate the trials factor to be the number of independent 10 mHz sub-bands N^α and

then introduce the following measure of significance for the most significant result for pulsar α

$$s^\alpha = N^\alpha \min_{i \in [1, N^\alpha]} \{p_i^\alpha\}, \quad (5.23)$$

where p_i^α is the p-value associated with the i^{th} sub-band for pulsar α . $s^\alpha < 1$ implies that we would have to repeat the band search for pulsar α in random noise $\frac{1}{s^\alpha}$ times before we can expect a result as significant as the observed one. In this case, s^α behaves as a p-value. When $s^\alpha > 1$ it means that in a band search in random noise we expect that in s^α sub-band the loudest result will be at least as significant as the observed result. For detection we need that $s^\alpha \lll 1$.

Section 7.10 presents the combined analysis for 7 recycled pulsars using the method described above.

5.5 UPPER LIMITS

In the event of a non-detection, we set frequentist upper limits on the intrinsic gravitational wave amplitude h_0 at the detector. As we saw before, a non-significant detection statistic is the indicator of the non-detection of the signal. We ask - what signal strength from the pulsar would have resulted in a detection statistic that is greater than what was obtained in the search? We use a series of Monte Carlos, where we simulate signals at a fixed amplitude in real data and measure the detection efficiency of our search. The detection efficiency is the fraction of simulated signals recovered with a detection statistic larger than the targeted search result. The simulated signals from a pulsar have the Doppler parameters of the pulsar and amplitude parameters randomly drawn from a uniform distribution as in Table 5.2. The frequencies of the fake signals are drawn from a small range around the signal frequency to allow for different realisations of noise to be used in each injection search. But this range must not be too large lest the noise characteristics vary from what contributes to the actual search. As mentioned before, when there is a measurement of the orbital inclination angle, we use it to constrain the $\cos \iota$ of the signal.

The detection criterion is that the obtained value of the detection statistic is equal to or greater than the one found in the real search. The higher the measured detection statistic, the higher the gravitational wave amplitude needed for the simulated signal to be detected. We repeat this for various values of h_0 . For each value of h_0 , the fraction of detected signals is calculated to get the confidence $C(h_0)$ for detecting a signal with h_0 ,

$$C(h_0) = \frac{N_{\text{detected}}(h_0)}{N_{\text{total}}(h_0)}. \quad (5.24)$$

We fit this $(h_0, C(h_0))$ with a sigmoid of the form

$$C(h_0) = \frac{1}{1 + \exp\left(\frac{a-h_0}{b}\right)} \quad (5.25)$$

Parameter	Range
f_{gw}	0.1 mHz around signal f
\dot{f}_{gw}	3.8×10^{-17} Hz/s around signal \dot{f}
ψ	uniformly distributed with $ \psi \leq \pi/4$
Φ_0	uniformly distributed in $[0, 2\pi]$
$\cos i$ unrestricted case	uniformly distributed in $[-1, 1]$
$\cos i$ restricted case	fixed at the value of the orbital inclination when available
Orbital Parameters	same as expected signal

Table 5.2: Parameters of simulated signals in upper limit Monte Carlos.

and from it we read off the h_0 amplitude that corresponds to 95% confidence as our upper limit value, h_0^{95} .

For the band search, we repeat the procedure above in each of the 10mHz sub-bands and base the detection criterion on the $2\mathcal{F}_l$ in that sub-band. This produces frequency-dependent upper limits $h_0^{95}(f)$ in each sub-band, one per 10mHz band.

5.6 ENDING NOTE

This chapter described a templated search whose results are evaluated based on frequentist p-values. The upper limits on h_0 are set via a frequentist injection-recovery method. So overall, this method follows the frequentist approach to analysing the data for the presence of continuous gravitational wave signals from a known pulsar. In the next chapter, we will describe a method based on Bayesian inference to tackle this search problem.

METHOD II - A NEW BAYESIAN METHOD FOR TARGETED SEARCHES FOR CONTINUOUS GRAVITATIONAL WAVES

But the real reason is because it is such good fun.

– Albert Michelson,
on why he wanted to do his last experiment on the velocity of light,
(Gale, 1931)

There are two broad philosophies of statistical inference from data. The frequentist philosophy which was discussed in chapter 5 is based on the idea that the more times an observation occurs in the data, the more the assigned confidence to the inference. The second approach, called Bayesian inference, starts with an existing understanding of the system and uses observed data to update it. A Bayesian pipeline for targeted searches of continuous waves from known pulsars had been developed and used by the LVK collaboration (Pitkin et al., 2017). In this chapter, we present a new pipeline to do these searches. At its core, this method is based on the calculation of \mathcal{F} -statistic (Cutler and Schutz, 2005), stopping one step before it culminates as a detection statistic on maximisation over the four amplitude parameters.

Section 6.1 describes the method starting at the basics of Bayesian inference and goes through the details of signal detection in data to arrive at the likelihood function. This section is the framework for the \mathcal{F} -statistic as well, as was mentioned in the previous chapter. Section 6.2 shows some tests carried out to validate the method and the software that executes it. Section 6.3 closes this methods chapter by discussing the practicalities of a targeted continuous wave signal using the new pipeline and re-stating its relevance.

This chapter is a scientific paper under preparation and will be published as Ashok et. al., 2023. The paper will also include details/developments in the method that we worked on after this thesis was written.

6.1 METHOD

6.1.1 Bayesian Inference

We want to search for a continuous gravitational wave signal with parameters θ in gravitational wave detector data, \mathbf{D} . That is, we want to test the hypothesis that \mathbf{D} contains the signal described by parameters θ against the hypothesis that \mathbf{D} is purely noise. If $P(\theta)$ is our prior knowledge about the probability distribution of θ , then \mathbf{D}

contains observations using which we can update this prior knowledge. The inference consists in deriving the posterior probability distribution for the parameters θ , given data \mathbf{D} . This posterior is calculated according to the Bayes theorem

$$P(\theta|\mathbf{D}) = P(\theta) \frac{P(\mathbf{D}|\theta)}{P(\mathbf{D})}. \quad (6.1)$$

where $P(\mathbf{D}|\theta)$ is the likelihood of observing the data with signal described by θ and $P(\mathbf{D})$ is the probability of observing data \mathbf{D} taking into account all possible hypotheses.

6.1.2 Likelihood function

We search for continuous gravitational wave from a known pulsar. This means the Doppler parameters of the signal are known, and the amplitude parameters are unknown. Our aim is to find the probability distribution of the amplitude parameters, $\{h_0, \cos \iota, \psi, \phi_0\}$ of the continuous gravitational wave from a pulsar, given the observed data. The first step is to find the likelihood function $P(\mathbf{D}|\theta)$.

In equations 3.30, 3.31, 3.32 we saw the expressions for the continuous gravitational waveform. Here we go into the details of detecting this waveform in the data. The following is also the background for the \mathcal{F} -statistic as was mentioned in section 5.3.

In the strain data from a gravitational wave detector, the signal has the form

$$h(t) = F_+(\alpha, \delta, \psi; t)h_+(t) + F_\times(\alpha, \delta, \psi; t)h_\times(t). \quad (6.2)$$

The "+" and "×" indicate the two gravitational wave polarisations. $F_+(\alpha, \delta, \psi; t)$ and $F_\times(\alpha, \delta, \psi; t)$ are the detector sensitivity pattern functions, which depend on the relative orientation between the detector and the source, and hence on time t , on the position (α, δ) of the source, and on ψ , the polarisation angle. The waveforms $h_+(t)$ and $h_\times(t)$ are

$$\begin{aligned} h_+(t) &= A_+ \cos \phi(t) \\ h_\times(t) &= A_\times \sin \phi(t), \end{aligned} \quad (6.3)$$

with

$$\begin{aligned} A_+ &= \frac{1}{2}h_0(1 + \cos^2 \iota), \\ A_\times &= h_0 \cos \iota. \end{aligned} \quad (6.4)$$

The angle between the total angular momentum of the star and the line of sight is $0 \leq \iota \leq \pi$ and $h_0 \geq 0$ is the intrinsic gravitational wave amplitude. $\phi(t)$ of Eq. 6.3 is the phase of the gravitational wave signal at time t . $\phi(t)$ depends upon the frequency of the signal, f_{gw} , the sky-position of the source and the binary orbital parameters if the source is part of a binary system, collectively called the phase-evolution parameters

$\vec{\lambda}$. As shown in [Jaranowski et al. \(1998\)](#) the dependence of the signal on the intrinsic parameters $\{h_0, \cos \iota, \psi, \phi_0\}$ can be re-parametrised into a set of four amplitude coordinates \mathcal{A}^μ as

$$\begin{aligned}\mathcal{A}^1 &= A_+ \cos \phi_0 \cos 2\psi - A_\times \sin \phi_0 \sin 2\psi, \\ \mathcal{A}^2 &= A_+ \cos \phi_0 \sin 2\psi + A_\times \sin \phi_0 \cos 2\psi, \\ \mathcal{A}^3 &= -A_+ \sin \phi_0 \cos 2\psi - A_\times \cos \phi_0 \sin 2\psi, \\ \mathcal{A}^4 &= -A_+ \sin \phi_0 \sin 2\psi + A_\times \cos \phi_0 \cos 2\psi,\end{aligned}\tag{6.5}$$

and the signal in detector X can be written as

$$h^X(t; \mathcal{A}, \lambda) = \sum_{\mu=1}^4 \mathcal{A}^\mu h_\mu^X(t; \lambda)\tag{6.6}$$

where $h_\mu^X(t; \lambda)$ only depend on the signal phase parameters and \mathcal{A}^μ on the amplitude parameters. Furthermore:

$$\begin{aligned}h_1^X(t) &\equiv a^X(t) \cos \phi^X(t), \\ h_2^X(t) &\equiv b^X(t) \cos \phi^X(t), \\ h_3^X(t) &\equiv a^X(t) \sin \phi^X(t), \\ h_4^X(t) &\equiv b^X(t) \sin \phi^X(t),\end{aligned}\tag{6.7}$$

in terms of the antenna-pattern functions $a^X(t)$ and $b^X(t)$ and they can also be expressed as complex basis functions

$$\begin{aligned}h_a^X(t) &\equiv h_1^X - ih_3^X = a^X(t) e^{-i\phi^X(t)}, \\ h_b^X(t) &\equiv h_2^X - ih_4^X = b^X(t) e^{-i\phi^X(t)}.\end{aligned}\tag{6.8}$$

The detection of the signal (6.6) in data $x(t)$ boils down to calculating the ratio of the likelihood of the signal hypothesis to the likelihood of the noise hypothesis. The signal hypothesis that the data contains the signal and Gaussian noise $n(t)$ is expressed as

$$x(t) = n(t) + h(t; \mathcal{A}, \lambda),\tag{6.9}$$

and has likelihood $P(x|\mathcal{A}, \lambda)$. The noise hypothesis says that the data contains only Gaussian noise $n(t)$ and has likelihood $P(x|0)$. The likelihood ratio

$$\mathcal{L}(x; \mathcal{A}, \lambda) \equiv \frac{P(x|\mathcal{A}, \lambda)}{P(x|0)}\tag{6.10}$$

is found as ([Jaranowski et al., 1998](#))

$$\begin{aligned}\log \mathcal{L}(x; \mathcal{A}, \lambda) &= (x|h) - \frac{1}{2} (h|h) \\ &= \mathcal{A}^\mu x_\mu - \frac{1}{2} \mathcal{A}^\mu \mathcal{M}_{\mu\nu} \mathcal{A}^\nu\end{aligned}\tag{6.11}$$

where the scalar product (Cutler and Schutz, 2005) is

$$(x|y) \equiv 2 \sum_X^{N_{\text{Det}}} S_X^{-1} \int_0^T x^X(t) y^X(t) dt \quad (6.12)$$

and

$$\begin{aligned} x_\mu(\lambda) &\equiv (x|h_\mu) \\ \mathcal{M}_{\mu\nu}(\lambda) &\equiv (h_\mu|h_\nu). \end{aligned} \quad (6.13)$$

S_X is the noise floor in detector X . We define the overall noise floor \mathcal{S} such that

$$\mathcal{S}^{-1} \equiv \frac{1}{N_{\text{Det}}} \sum_X S_X^{-1}. \quad (6.14)$$

(6.11) is our likelihood function in the conceptually most basic form. Let's dwell on how it is practically computed.

The time series from detector X is converted into Short-Fourier-Transforms (SFTs) of length T_{SFT} . Let α denote an SFT. We assume that the noise is stationary over the T_{SFT} and is given as $S_{X\alpha}(f)$. Now, we can compute all quantities per SFT. The scalar product, in equation (6.12) becomes,

$$(x|y) \approx 2 \sum_{X=1}^{N_{\text{Det}}} \sum_{\alpha=1}^{N_{\text{SFT}}^X} S_{X\alpha}^{-1}(f) \int_0^{T_{\text{SFT}}} x_{X\alpha}(t) y_{X\alpha}(t) dt, \quad (6.15)$$

where $x_{X\alpha}(t) \equiv x_X(t_{X\alpha} + t)$ if $t_{X\alpha}$ is the start-time of the SFT $X\alpha$, and N_{SFT}^X is the number of SFTs from detector X . Henceforth we will use the notation,

$$\sum_{X\alpha} \equiv \sum_{X=1}^{N_{\text{Det}}} \sum_{\alpha=1}^{N_{\text{SFT}}^X}. \quad (6.16)$$

We normalise the $S_{X\alpha}^{-1}(f)$ in the scalar product in terms of *noise weights*, $w_{X\alpha}$ according to,

$$w_{X\alpha}(f) \equiv \frac{S_{X\alpha}^{-1}(f)}{\mathcal{S}^{-1}}. \quad (6.17)$$

Then, the scalar product becomes,

$$(x|y) \approx 2\mathcal{S}^{-1} \sum_{X\alpha} w_{X\alpha} \int_0^{T_{\text{SFT}}} x_{X\alpha}(t) y_{X\alpha}(t) dt, \quad (6.18)$$

so that we are left with a noise-weighted sum over SFTs.

Lastly, delving one step deep into the implementation of these computations in the search codes, it is a matter of numerical convenience if we further normalise the Fourier transformed data, $\tilde{x}_{X\alpha}(f)$ as

$$\tilde{y}_{X\alpha}(f) \equiv \frac{\tilde{x}_{X\alpha}(f)}{\sqrt{\frac{1}{2} T_{\text{SFT}} S_{X\alpha}(f)}}, \quad (6.19)$$

so that $\tilde{y}_{X\alpha}(f) \sim \mathcal{O}(1)$.

Now, let's take the two terms on the right-hand side of (6.11) separately and see how they are computed.

The first term on the right-hand side of (6.11) is $\mathcal{A}^\mu x_\mu$. Here, $\mathcal{A}^\mu = \mathcal{A}^1 \mathcal{A}^2 \mathcal{A}^3 \mathcal{A}^4$ as written in equation (6.5). Let's focus on x_μ . x_μ , as given in equation (6.13), can be written as

$$\begin{aligned} x_a &= (x|h_a) \equiv x_1 - ix_3 \\ x_b &= (x|h_b) \equiv x_2 - ix_4 \end{aligned} \quad (6.20)$$

in terms of the complex basis of equation (6.8). From equation 6.19,

$$\tilde{x}_{X\alpha}(f) \equiv \tilde{y}_{X\alpha}(f) \sqrt{\frac{1}{2} T_{\text{SFT}} S_{X\alpha}(f)} \quad (6.21)$$

and using the definition of noise weights in equation 6.17, $\tilde{x}_{X\alpha}(f)$ is

$$\tilde{x}_{X\alpha}(f) \equiv \tilde{y}_{X\alpha}(f) \sqrt{\frac{\frac{1}{2} T_{\text{SFT}}}{w_{X\alpha} \mathcal{S}^{-1}}}. \quad (6.22)$$

Then, in terms of $y_{X\alpha}(t)$ and $\{h_a, h_b\}$ from expression (6.8), equation (6.20)

$$\begin{aligned} x_a &= \sqrt{2\mathcal{S}^{-1} T_{\text{SFT}}} \sum_{X\alpha} \sqrt{w_{X\alpha}} \int_0^{T_{\text{SFT}}} y_{X\alpha}(t) a_{X\alpha}(t) e^{-i\phi_{X\alpha}(t)} dt, \\ x_b &= \sqrt{2\mathcal{S}^{-1} T_{\text{SFT}}} \sum_{X\alpha} \sqrt{w_{X\alpha}} \int_0^{T_{\text{SFT}}} y_{X\alpha}(t) b_{X\alpha}(t) e^{-i\phi_{X\alpha}(t)} dt \end{aligned} \quad (6.23)$$

using the expression of scalar product in equation (6.18). Here, the noise weights $\sqrt{w_{X\alpha}}$ can be completely absorbed into $\{a_{X\alpha}(t), b_{X\alpha}(t)\}$ to define the noise-weighted antenna-pattern functions,

$$\begin{aligned} \check{a}_{X\alpha}(t) &= \sqrt{w_{X\alpha}} a_{X\alpha}(t), \\ \check{b}_{X\alpha}(t) &= \sqrt{w_{X\alpha}} b_{X\alpha}(t). \end{aligned} \quad (6.24)$$

With,

$$\check{\gamma} \equiv \mathcal{S}^{-1} T_{\text{SFT}} \quad (6.25)$$

and

$$F_a^{X\alpha} \equiv \int_0^{T_{\text{SFT}}} y_{X\alpha}(t) \check{a}_{X\alpha}(t) e^{-i\phi_{X\alpha}(t)} dt, \quad (6.26)$$

$$F_b^{X\alpha} \equiv \int_0^{T_{\text{SFT}}} y_{X\alpha}(t) \check{b}_{X\alpha}(t) e^{-i\phi_{X\alpha}(t)} dt \quad (6.27)$$

from equation (6.23),

$$\begin{aligned} x_a^{X\alpha} &= \sqrt{2\check{\gamma}} F_a^{X\alpha} \\ x_b^{X\alpha} &= \sqrt{2\check{\gamma}} F_b^{X\alpha}. \end{aligned} \quad (6.28)$$

$F_{\{a,b\}}$ over all SFTs from all detectors is computed as

$$F_{\{a,b\}} \equiv \sum_{X\alpha} F_{\{a,b\}}^{X\alpha}. \quad (6.29)$$

Using equation (6.20) and equation (6.28),

$$\begin{aligned} F_a &= \frac{1}{\sqrt{2\tilde{\gamma}}}(x_1 - ix_3) \\ F_b &= \frac{1}{\sqrt{2\tilde{\gamma}}}(x_2 - ix_4) \end{aligned} \quad (6.30)$$

So, x_μ are

$$\begin{aligned} x_1 &\equiv \sqrt{2\tilde{\gamma}} F_a^{\Re} \\ x_2 &\equiv \sqrt{2\tilde{\gamma}} F_b^{\Re} \\ x_3 &\equiv -\sqrt{2\tilde{\gamma}} F_a^{\Im} \\ x_4 &\equiv -\sqrt{2\tilde{\gamma}} F_b^{\Im}. \end{aligned} \quad (6.31)$$

where \Re denotes the real part of the complex $F_{\{a,b\}}$ and \Im denotes the imaginary part. Thus, the first term on the right-hand side of (6.11),

$$\mathcal{A}^\mu x_\mu = \sqrt{2\tilde{\gamma}}[\mathcal{A}^1 F_a^{\Re} + \mathcal{A}^2 F_b^{\Re} - \mathcal{A}^3 F_a^{\Im} - \mathcal{A}^4 F_b^{\Im}] \quad (6.32)$$

Let's focus on the second term in (6.11), $-\frac{1}{2}\mathcal{A}^\mu \mathcal{M}_{\mu\nu} \mathcal{A}^\nu$. As expressed in equation (6.13),

$$\mathcal{M}_{\mu\nu} \equiv (h_\mu | h_\nu). \quad (6.33)$$

h_a and h_b contain antenna pattern functions $\{a(t), b(t)\}$ and oscillatory functions of signal phase, $\{\sin \phi(t), \cos \phi(t)\}$. The antenna patterns are slowly varying with Earth's daily rotation, and the phase functions oscillate at short timescales $\frac{1}{f} \ll T_{\text{SFT}}$. Using these properties and the definition of scalar product, $\mathcal{M}_{\mu\nu}$ is approximated as

$$\mathcal{M}_{\mu\nu} = \gamma \begin{pmatrix} A & C & 0 & 0 \\ C & B & 0 & 0 \\ 0 & 0 & A & C \\ 0 & 0 & C & B \end{pmatrix} \quad (6.34)$$

where,

$$\begin{aligned} A &\equiv \langle |a|^2 \rangle \\ B &\equiv \langle |b|^2 \rangle \\ C &\equiv \Re \langle a^* b \rangle. \end{aligned} \quad (6.35)$$

In the practical implementation, in terms of the noise-weighted antenna pattern functions of equation (6.24), we have

$$\begin{aligned}\check{A} &\equiv \sum_{X\alpha} \langle \check{a}_{X\alpha}^2 \rangle \\ \check{B} &\equiv \sum_{X\alpha} \langle \check{b}_{X\alpha}^2 \rangle \\ \check{C} &\equiv \sum_{X\alpha} \Re \langle \check{a}_{X\alpha}^* \check{b}_{X\alpha} \rangle\end{aligned}\tag{6.36}$$

giving

$$\mathcal{M}_{\mu\nu} = \check{\gamma} \begin{pmatrix} \check{A} & \check{C} & 0 & 0 \\ \check{C} & \check{B} & 0 & 0 \\ 0 & 0 & \check{A} & \check{C} \\ 0 & 0 & \check{C} & \check{B} \end{pmatrix}\tag{6.37}$$

Adding equation (6.32) and $-\frac{1}{2}\mathcal{A}^\mu \mathcal{M}_{\mu\nu} \mathcal{A}^\nu$ with $\mathcal{M}_{\mu\nu}$ as written in equation (6.37), the full-likelihood function, (6.11), is implemented in the form

$$\begin{aligned}\log \mathcal{L} &= \sqrt{2\check{\gamma}}[\mathcal{A}^1 F_a^{\Re} + \mathcal{A}^2 F_b^{\Re} - \mathcal{A}^3 F_a^{\Im} - \mathcal{A}^4 F_b^{\Im}] - \\ &\check{\gamma} \left[\check{A} [(\mathcal{A}^1)^2 + (\mathcal{A}^3)^2] + \check{B} [(\mathcal{A}^2)^2 + (\mathcal{A}^4)^2] \right. \\ &\quad \left. + 2\check{C} [\mathcal{A}^1 \mathcal{A}^2 + \mathcal{A}^3 \mathcal{A}^4] \right].\end{aligned}\tag{6.38}$$

In equation (6.1), we now have, $P(\mathbf{D}|\theta)$.

Additionally, note that, to arrive to the \mathcal{F} statistic, we analytically maximise the likelihood-ratio in equation 6.11 with respect to the four amplitudes A_μ by

$$\mathcal{F}(x; \lambda) \equiv \max_{\mathcal{A}} \log \mathcal{L}(x; \mathcal{A}, \lambda) = \frac{1}{2} x_\mu \mathcal{M}^{\mu\nu} x_\nu,\tag{6.39}$$

where $\mathcal{M}^{\mu\nu} \equiv \{\mathcal{M}^{-1}\}^{\mu\nu}$, i.e. $\mathcal{M}_{\mu\sigma} \mathcal{M}^{\sigma\nu} = \delta_\mu^\nu$.

6.1.3 Priors

We look at the component $P(\theta)$ in equation 6.1. Our prior knowledge of amplitude parameters is non-informative in the general case. For $\cos \iota$, the prior probability density is in general uniform over $[-1, 1]$, the full range of values that the quantity can have. Similarly for ϕ_0 , the prior is uniform over $[0, 2\pi]$, and for ψ , uniform over $[-\pi/4, \pi/4]$. The question of h_0 prior is less straightforward. One thing we know is that the spindown upper limit (h_0^{sd}) of the pulsar, the strength of the continuous gravitational wave signal if all the rotational kinetic energy lost by the pulsar was converted into gravitational waves, should be included in the prior range. Defining the h_0 prior range as $[h_{\text{low}}, h_{\text{high}}]$,

we have $h_{\text{low}} < h_0^{\text{sd}}$. (Dupuis and Woan, 2005) spends some thought on the question of h_0 priors. They ponder if a prior for h_0 that falls sharply at strain levels above h_0^{sd} is a good choice. They concluded that at that stage of gravitational wave astronomy (as of 2005, when no signal was yet detected), it is better to interpret observational data independent of spin-down arguments. This line of thought is still valid in the era when continuous gravitational waves have not yet been detected. This calls for a uniform prior in the range $[h_{\text{low}}, h_{\text{high}}]$, one that does not fall above h_0^{sd} . A uniform prior favours larger values of h_0 (the prior probability for 0.1 to 1 is 10 times less than for 1 to 10) and can lead to conservative upper limits on the signal strengths.

We used a $h_{\text{high}} = 10^{-24}$ in the first (and only so far) application of this pipeline for a known-pulsar search, whose results are presented in section 7.11.1. This h_{high} is several orders of magnitude larger than the h_0^{sd} of the pulsar and is justified based on the frequentist upper limit for the pulsar at 1.25×10^{-26} .

(Isi et al., 2017) found that a log-uniform h_0 prior is a better choice when we are ignorant of the scale of the signal amplitude in the absence of a strong signal. In the scenario of a strong signal, the prior distribution on h_0 should not matter since the likelihood function will be strongly peaked and will dominate the posterior. In the absence of such a strong signal, the choice of priors will matter. In our pipeline, we do two sets of inference, one with a uniform prior in the range $[h_{\text{low}}, 10^{-24}]$ (the value of h_{high} is not fixed rigorously and can be chosen on a per-pulsar basis), and one with a log-uniform prior in this range. Furthermore, we will always do the Bayesian search in combination with the frequentist method of chapter 5, which makes no assumptions on the h_0 values of the signal. Ultimately, the inference from the two methods should agree with each other. This reduces the possibility of making a wrong inference of the data compared to when the inference is made using a single method. Sometimes observations of pulsars are able to constrain the inclination angle of the pulsar. For example, for some binary millisecond pulsars, their inclination angle is aligned with the orbital inclination angle. This helps to constrain the priors used for $\cos \iota$.

6.1.4 Software Implementation

The aim of the Bayesian inference described so far is to derive posterior probability distribution for the amplitude parameters of a continuous gravitational wave from a known pulsar. In practice, this is achieved by a combination of software like LALSuite (LIGO Scientific Collaboration, 2018), pyCW (pyC), BILBY (Ashton et al., 2019) and samplers.

The computation of log-likelihood in (6.38) is done in an XLAL function. An XLAL function is a module in LALSuite, which is a collection of C-codes to carry out the analysis of gravitational wave data.

pyCW, a new python-based interface to the XLAL C-codes, sets up the data, the parameter space for the signal to be searched. The pyCW-XLAL interface is provided

by SWIGLAL (Wette, 2020). SWIGLAL provides python understandable wrappers around the C functions and objects in LALSuite using SWIG (Beazley, 1996). The XLAL likelihood function is called using the SWIG wrapper.

The next step is the computation of equation (6.38) at samples in the prior parameter space. We use BILBY to do this. BILBY is a recent python-based Bayesian Inference library for Gravitational-wave Astronomy. BILBY's class `core.samplers` links the likelihood function that needs to be computed at points in the parameter space, with the preferred variant of a sampler. A sampler is a software tool that moves through the parameter space to evaluate a function at different points. A number of algorithms exist to achieve this sampling, differing mainly in the scheme using which the sampler decides, after each evaluation, the consecutive point in the parameter space at which it will evaluate the function.

6.1.5 Inferences

In the presence of a signal, the posterior distribution of signal parameters will peak near the true signal parameters. In the absence of a detectable signal, the posterior distribution of h_0 will peak at the lower end of the prior range, indicating that the data is consistent with just noise. In such a scenario of non-detection we set upper limits to the h_0 by integrating the posterior h_0 curve upto the value of h_0 such that 95% of the curve lies to the left of the h_0 . This is the h_0^{95} , the upper limit on the strength of the signal that we can quote with 95% credibility.

6.2 TESTS

6.2.1 Recovery of fake signals

The first test demonstrates that the method recovers fake continuous gravitational wave signals with posterior distributions of parameters consistent with their known true values. We test first in the absence of noise to avoid any extra effects that the presence of noise would cause. We simulate data spanning 1 day containing a fake continuous gravitational wave signal from an isolated source. A typical targeted continuous wave search will analyse years of gravitational wave data, but for the purpose of testing software, data spanning a day is sufficient and has the benefit that the codes converge fast. The fake signal has strength h_0 of $\approx 3 \times 10^{-24}$ and an assumed noise floor of $1 \times 10^{-24} \sqrt{Hz}$, to scale the results. The Doppler parameters of the search (the prior range in these parameters) are fixed as they would be in a targeted search. The priors on the angular amplitude parameters are as mentioned in the previous section. For h_0 the prior range is uniform in $[1 \times 10^{-25}, \approx 6 \times 10^{-24}]$. The nested sampler DYNESTY (Speagle, 2020), with controls `nlive` = 500 and `dlogz` = 0.1 is used. Figure 6.1 shows the posterior distributions of the amplitude parameters recovered by our pipeline; the true

amplitude parameters of the injected signal have been recovered with high posterior probability density.

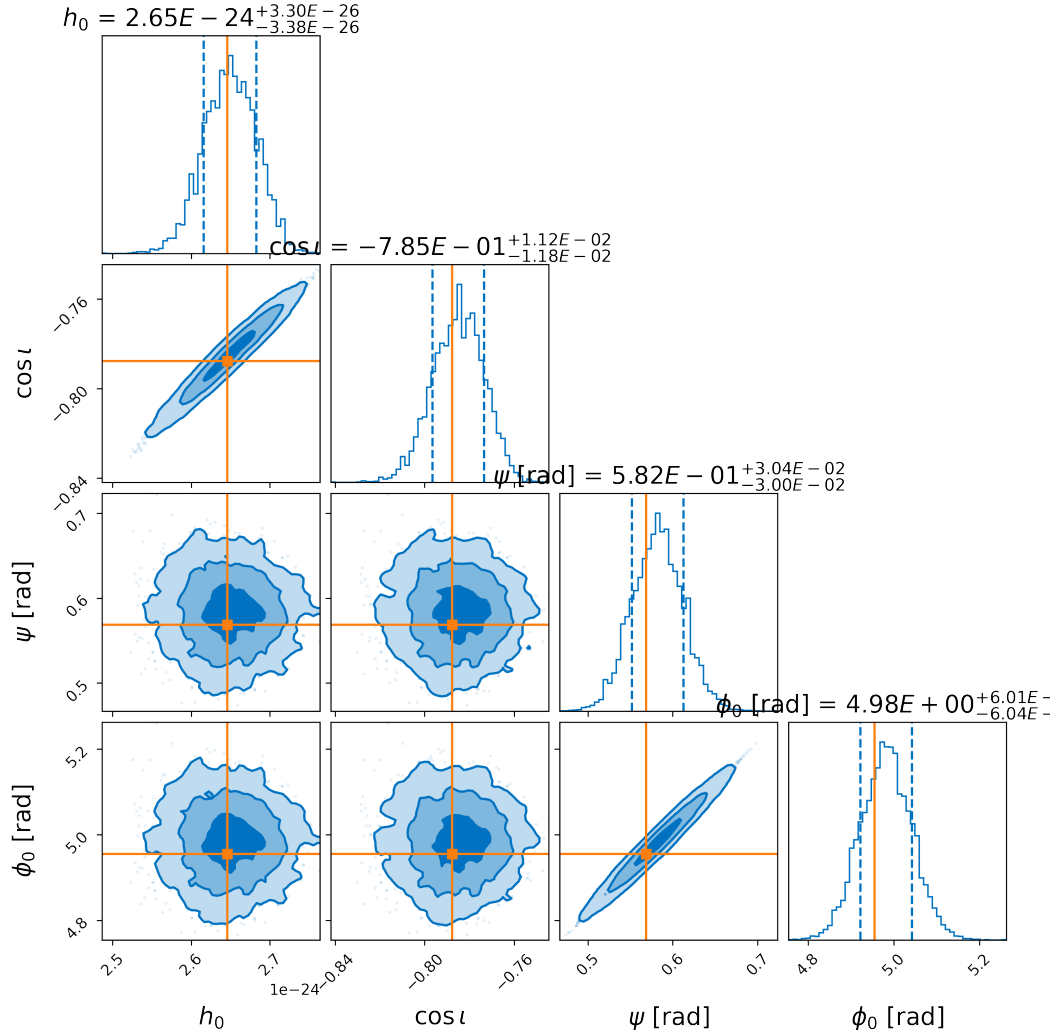


Figure 6.1: Recovery of a high SNR fake signal using the pipeline.

6.2.2 PP Plots

Another question to ask is if the credible intervals in the posterior distribution behave like the frequentist confidence intervals. To do this, we set up a fake signal-recovery Monte Carlo with a large number of injections whose amplitude parameters are drawn randomly from their prior interval, as would be done in an actual search. We set h_0 to be drawn from a log-uniform distribution in the prior $[10^{-29}, 10^{-27}]$. This lands us in the

signal strength regime that is realistically expected in a continuous wave search. We use real data from O1, O2 and O3 from detectors H1 and L1 in the test. We search for each of these injected signals using our method. Ideally, $x\%$ of the total number of injections should be recovered in a credible interval $C.I = x$. Figure 6.2 shows that this is indeed the case for the four amplitude parameters. The shaded regions show the 1-, 2-, and 3- σ confidence intervals in decreasing opacity. A Kolmogorov-Smirnov (KS) p-value is calculated for every parameter individually. A KS p-value quantifies the probability that the observed samples are drawn from a reference probability distribution. In this case, the samples are the fraction of events as a function of C.I, and the reference distribution is a uniform distribution in $[0, 1]$. A combined p-value for all the parameter, representing the probability that the ensemble of individual-parameter p-values is drawn from a uniform distribution, is also computed.

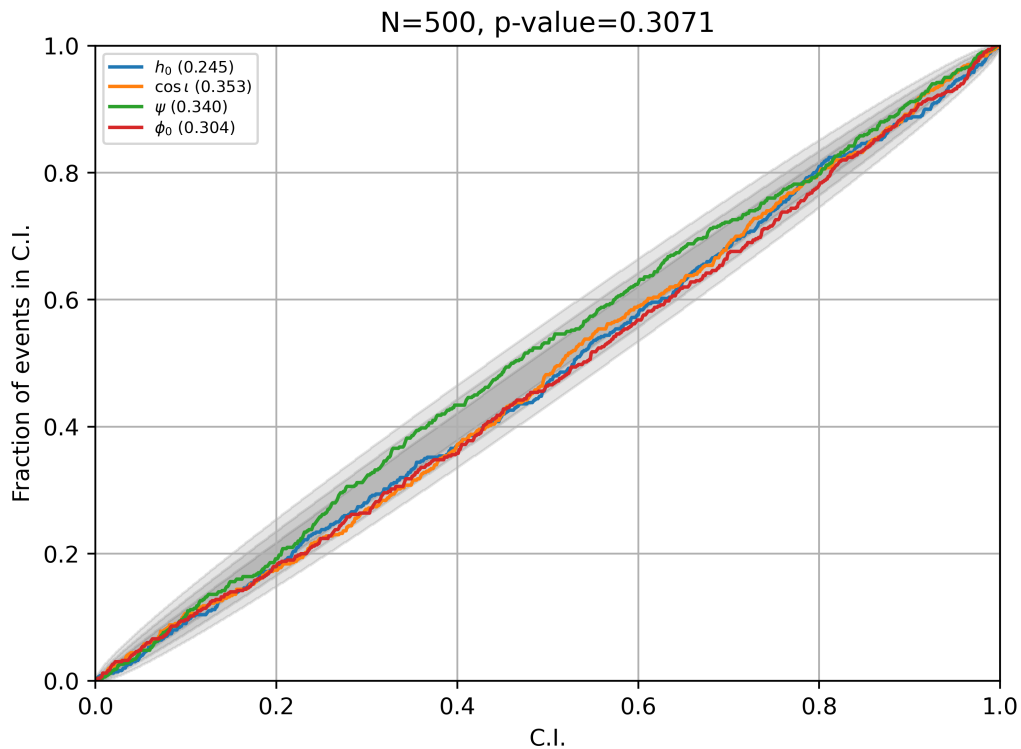


Figure 6.2: PP plot for weak signal regime with h_0 priors in $[10^{-29}, 10^{-27}]$

6.3 DISCUSSION

This chapter presented a new Bayesian method for searches for continuous gravitational waves from known pulsars. The method combines well-established machinery like

the \mathcal{F} -statistic, LALSuite, Bilby, and sampling techniques to search for continuous gravitational waves from known pulsars. Tests based on the recovery of simulated signals have shown the pipeline to work.

In a real known pulsar search, we also include Doppler parameters in the search with the prior ranges for these parameters defined by the uncertainties in their observed values in the pulsar timing solution. As mentioned in the discussion on priors, we do two searches using different distributions of the h_0 prior range. We used the pipeline for the first time in the search for continuous gravitational waves from PSR J1526-2744. The results from this search were consistent with the noise-only hypothesis and are presented in section 7.11.1.

New pulsars are being discovered at a rate faster than ever before. Thanks to the ability to achieve maximum possible sensitivity by a coherent combination of Advanced LIGO data, targeted searches such as Ashok et al. (2021) probe astrophysically interesting regimes of ellipticity for neutron stars, setting ellipticity constraints at the level of the minimum expected neutron star ellipticities proposed by Woan et al. (2018). Targeted searches thus form a very important class of continuous gravitational wave searches. Yet, there is only one method that tackles this problem from a Bayesian point of view. This method (Pitkin et al., 2017), variously called the *Time Domain Method*, or the *Heterodyne method*, has been successfully used for targeted searches since Abbott et al. (2004). Pitkin et al. (2017)'s *lalpulsar_knope* and its modern implementation CWInPy operate in the time-domain exploiting the knowledge of the signal model to reduce the amount of the data to be analysed via heterodyning, low-pass filtering and down-sampling. Our method works in the frequency domain. It requires data from only a limited bandwidth of frequency based on the evolution of the signal frequency and the uncertainties in the observed Doppler parameters. More tests comparing the two pipelines in terms of performance are underway and form a part of the work in progress in this project. In any case, the motivation is not to have a better pipeline than the existing one but to have a distinct one when it is possible to design one using a combination of existing, well-tested software. In the era where gravitational wave astronomy is a reality, and the detection of continuous gravitational waves is much anticipated, it makes sense to have multiple pipelines attacking the search problem. A claim of detection can either be confirmed with better confidence or refuted with the help of multiple, well-tested search methods. In the event of non-detection, it is always a good idea to look at the data in different ways, and multiple methods let us do that.

RESULTS

In some strange way, any new fact or insight that I may have found has not seemed to me as a “discovery” of mine, but rather something that had always been there and that I had chanced to pick up.

– Subrahmanyan Chandrasekhar,
Truth and Beauty: Aesthetics and Motivations in Science
Preface, ix.

7.1 INTRODUCTION

The methods described in chapter 5 and 6 were used in the search for continuous gravitational wave signals from several newly discovered pulsars. This chapter presents the results from these searches. Some of these pulsars were first targeted for continuous wave emission in this work.

PSR J1653-0158 is a binary gamma-ray millisecond pulsar discovered in the Fermi-LAT data. Its discovery and our continuous gravitational wave search are reported in [Nieder et al. \(2020\)](#). At the time of the search, data from the O1 and O2 observation runs of the Advanced LIGO detectors were publicly available. The gravitational wave target frequency at ≈ 1016.4 Hz lies in a disturbed region of the data, close to the second harmonic of the mirror suspension violin modes. For the \mathcal{F} -statistic search, we exclude data taken during times when the relevant frequency regions are excessively noisy; for instance, we do not use data from the Livingston detector (L1) in the first observation run. In the end, this yields 50.6% of the Hanford detector (H1) data and 20.4% of the L1 data. The search results and analysis are presented in Section 7.2.

Next, we targeted seven recycled pulsars discovered and timed in the radio wavelength with the Arecibo telescope as part of the AO327 survey, reported in [Martinez et al. \(2019\)](#) and [Martinez et al. \(2017\)](#). Recycled pulsars have a history of binary interaction, and are believed to be spun up to high frequencies due to the accretion of mass and angular momentum from a companion star. This increases the probability that they have a high non-axisymmetry in their mass distribution. Their high rotational frequency from the recycling is an added benefit, because the continuous gravitational wave signal amplitude is proportional to the square of the frequency. Thus, recycled pulsars are particularly interesting targets for continuous gravitational wave searches. Our targets in this section are all in binary systems, except one. At the time of the search, data from Advanced LIGO O1,O2 and first six months of O3 (called O3a) were

publicly available. Figure 7.1 shows that the ARECIBO data from which the timing solutions are derived do not entirely overlap the LIGO observation timespan for all pulsars. Even though recycled pulsars are old and stable, based on the timing solutions alone, we cannot exclude the possibility of pulsar glitches or other irregularities. So we perform three different searches by

- 1) coherently combining data from O₁ and O₂
- 2) in only O_{3a}
- 3) coherently combining data from O₁, O₂ and O_{3a}.

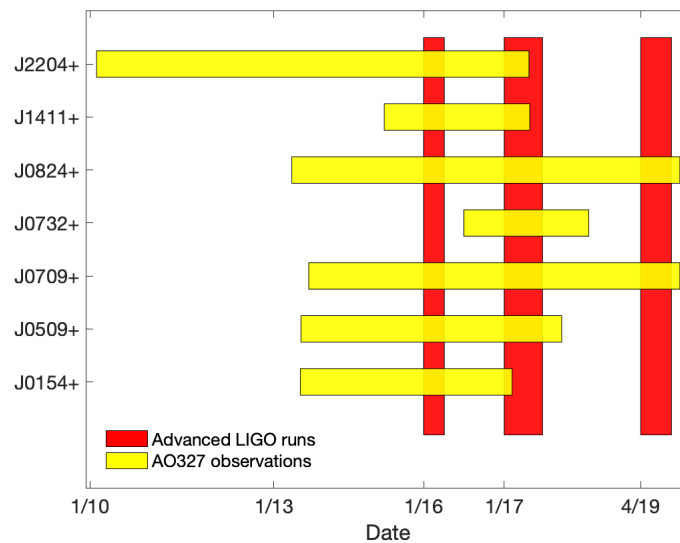


Figure 7.1: Time intervals of radio observation and gravitational wave observation for the pulsars in Section 7.3 to 7.9

The results for these pulsars have been published in [Ashok et al. \(2021\)](#) and are presented here in Sections 7.3 to 7.9. The search results and upper limits in each data set are presented as sub-sections.

J1526-2744 is a binary pulsar discovered by the Transients and Pulsars with MeerKAT (TRAPUM) collaboration in a MeerKAT follow-up of unidentified gamma-ray sources in Fermi-LAT data. The timing solution was derived from 13-years of Fermi-LAT data, covering the Advanced LIGO observation runs. Based on this we carried out searches for continuous gravitational wave signals. The discovery of the pulsar and our search are reported in [Clark et al. \(2023\)](#). We use Advanced LIGO data from the O₁-O₂-O₃ runs, i.e all of the gravitational wave data available at the time of the search. The continuous gravitational wave signal frequency for the pulsar, near 803.5 Hz, is a non-contaminated frequency range, and data from all times were included in the search. The results and detailed analysis are presented in Section 7.11. For this pulsar, we carried out our first

Bayesian search using the pipeline described in chapter 6. The results from this analysis are also presented.

The continuous gravitational wave search for a set of pulsars newly discovered in the Fermi-LAT data but yet unpublished are presented in Sections 7.14 to 7.12. These searches were carried out using preliminary timing solutions provided by Colin Clark et.al. So these results are regarded as preliminary.

7.2 PSR J1653-0158

7.2.1 Data Choices

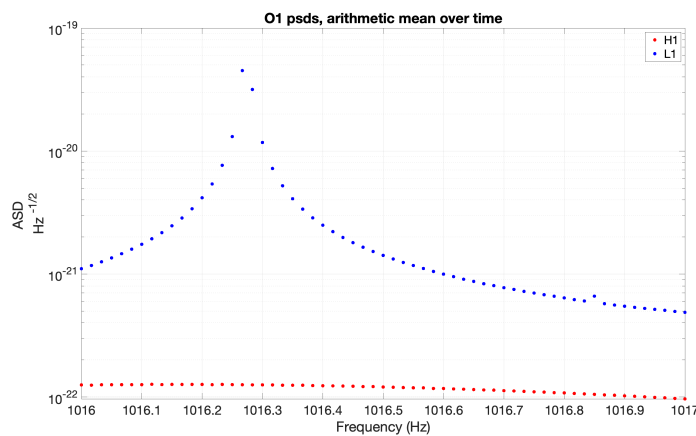


Figure 7.2: Time averaged ASD of the detectors in 1Hz around 1016.4 Hz, the signal frequency of J1653-0158 in O1 data.

PSR J1653-0158 has a continuous gravitational wave signal frequency of 1016.4Hz, which is highly contaminated due to the resonance in the silicon wires that hang the test mass in both the Advanced LIGO detectors. Data from this frequency range is usually discarded in scientific analysis. But here, we are presented with a source with its signal frequency in this range! And so, we roll up our sleeves and try to hand-pick data which can be used in this search. As a first step, figures 7.2 and 7.3 show the disturbances as peaks in the Amplitude Spectral Density (ASD) of the detectors near the signal frequency in O1 and O2 data, respectively. In O1 data, the H1 detector is much quieter than the L1 detector at the signal frequency, and hence we chose only data from the H1 detector for the next step. In O2, we use data from both detectors in the next step of noise analysis.

Next, we ask – is the noise present at all times during the observation or are there times when the detector is quiet in the frequency range? This can be answered by

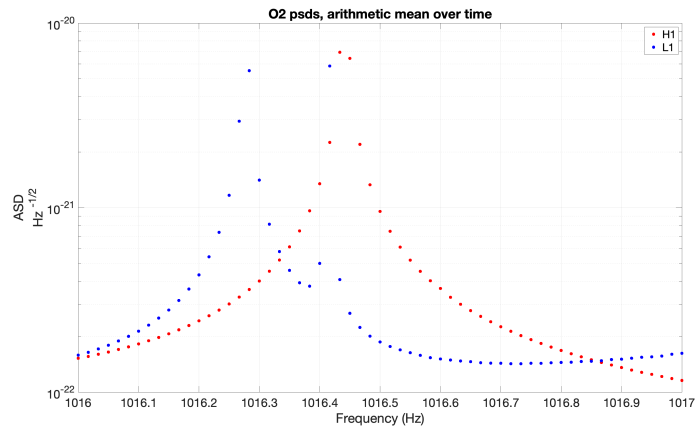


Figure 7.3: Time averaged ASD of the detectors in 1Hz around 1016.4 Hz, the signal frequency of J1653-0158 in O2 data.

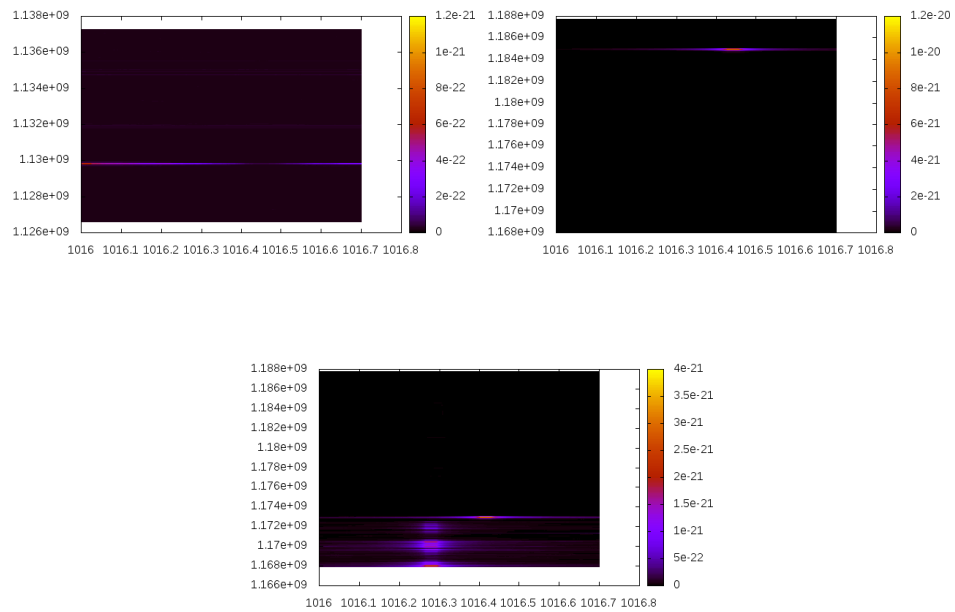


Figure 7.4: Time-frequency maps (time along x-axis and frequency along y-axis) of the noise near the signal frequency of J1653 in (i) H1 during O1 in top left, (ii) H1 during O2 in the top right and (iii) L1 during O2 in the bottom panel. The disturbances are not present in the same frequency bins at all times.

the heatmaps in figure 7.4. They indicate that the violin mode powers are not always present in the same frequencies at all times.

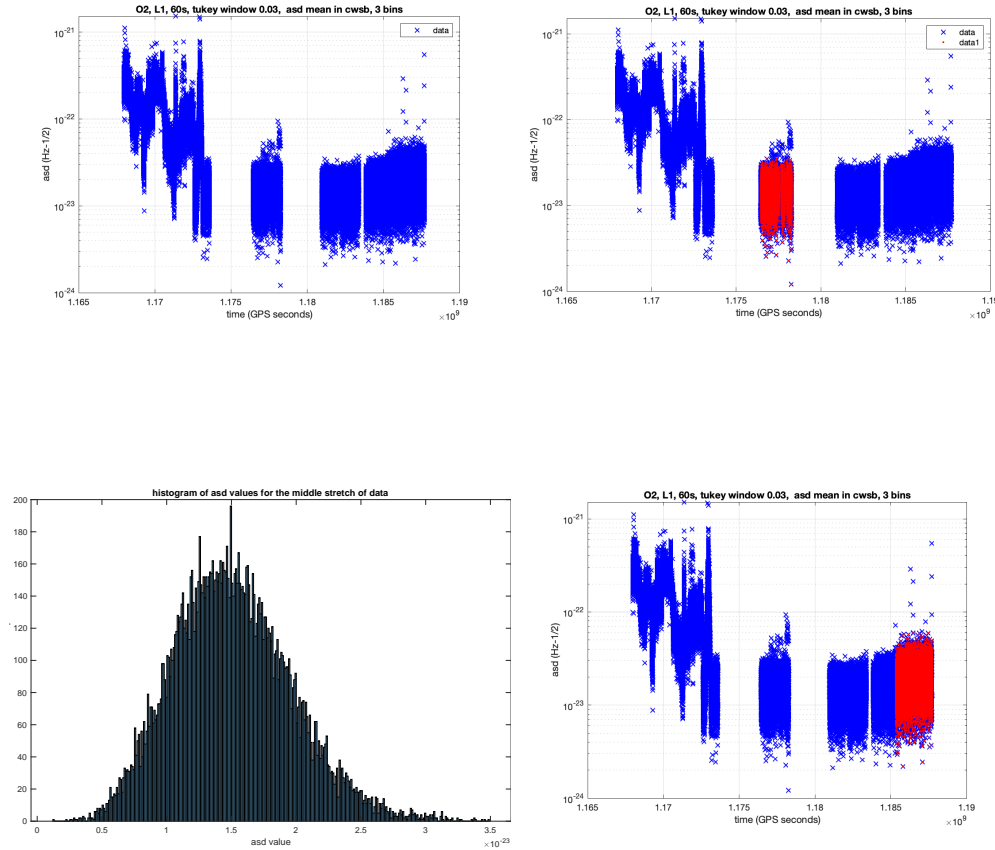


Figure 7.5: Noise in the signal frequency of J1653 in L1 detector during O2. (i) ASD in the signal frequency bin during the times of the observation (ii) middle stretch of O2 highlighted in red (iii) distribution of noise power in the middle stretch after removing fluctuations (iv) final stretch of O2 data (without fluctuations) on which running mean is computed.

Now we are hopeful and wonder if there are times when the noise due to violin mode is not egregiously high in the frequency bin that the signal from our pulsar would occupy at that given time. We can check this with the knowledge of the signal waveform we are looking for. We can calculate the evolution of the signal frequency at each time. So in the next stage, we calculate the detector noise in each data set in the signal frequency bin at each time. We carried out this stage in the following general steps:

1. we determine the expected frequency of the signal during the observation with a resolution of 60s

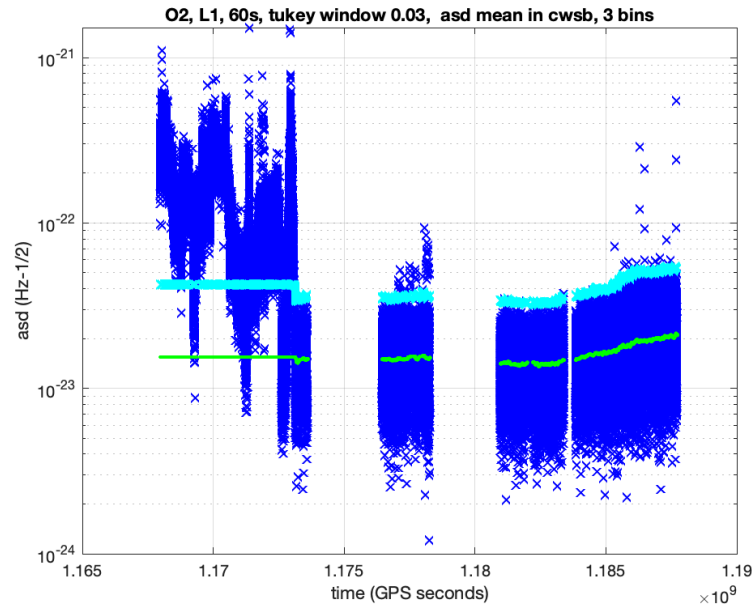


Figure 7.6: Data choices for L1 data in O2 run for the search for J1653. The running mean is in green, and the threshold is in cyan.

2. we calculate the mean ASD of power in three frequency bins centred at the frequency bin of signal at that time
3. we determine a threshold on the ASD value
 - a) we compute the running mean of this quantity over a window of 1000 timestamps, taking care not to include timestamps when there are obvious high disturbances in the computation. In these extreme cases, the running mean from the end of the preceding non-disturbed time is simply extrapolated to the disturbed times.
 - b) compute the running standard deviation

$$\text{threshold} = \text{mean} + 4.5 \times \text{standard deviation}. \quad (7.1)$$

4. we discard data at which the noise goes above this threshold ASD value

As an example demonstrating the details of this analysis, consider the data from L1 detector in O2. The mean of ASD in three frequency bins centred at the frequency bin of signal at each timestamp in O2 data is given in the first panel of figure 7.5. For the analysis, the O2 data can be split into three parts divided by the gaps in the data. Let's call these the initial timespan, the middle timespan and the end timespan.

During the initial times of the observation, a large disturbance is seen. The running mean was not computed for these initial times. Rather, the value was set to be equal to that at the first timestamp of the stretch following the disturbance, at=1173119631 GPS sec.

In the remaining two stretches, the running mean was calculated by excluding the occasional high fluctuations in ASD. For times when there are fluctuations, the ASD value is first forced to be the mean value of the bulk of the distribution. Then, the running mean is calculated. This way, the threshold of allowable noise is based on the characteristics of the bulk of the data. Eventually, the fluctuations will be discarded on account of being above the threshold.

For the middle stretch, as highlighted in the second panel of 7.5, the fluctuations are suppressed by forcing the ASD value to be the mean for the undisturbed data. One can visually see that the fluctuations in ASD are greater than $3.5 \times 10^{-23} \text{Hz}^{-1/2}$. So for any timestamp when the ASD is greater than $3.5 \times 10^{-23} \text{Hz}^{-1/2}$, the ASD value is set to $1.5 \times 10^{-23} \text{Hz}^{-1/2}$, also learnt from the plot. After this step, the distribution of ASD in this stretch is seen in the third panel of figure 7.5.

For the end stretch, there are two parts – one 1180975619 GPS sec to 1185306020 GPS sec where the running statistics are computed. Then the second part, highlighted in red in the panel (iv) of 7.5, where fluctuations are suppressed. For any timestamp with ASD greater than $6e-23$, the value was set as the running mean value for the last timestamp of the previous stretch. This is done because this stretch of data has a varying noise floor, unlike the middle stretch. So it is not possible to arrive at a mean value of the bulk.

The running standard deviation was also computed following the same treatment as for the running mean, described above. The threshold was calculated according to equation 7.1 for the timespan of O2 data as shown in cyan in 7.6. The example of O2-L1 data was chosen to demonstrate our analysis of noise in the data because it was the worst of the different data sets for J1653. The data for the other detector and the other observation runs were chosen following a similar but not exact line of argument. Note that this is not a recipe for data choice. Every set of data is different, especially in the presence of noise artefacts. It needs to be looked at critically, and a different approach to data choice might be necessary based on what the noise presents to us.

7.2.2 The search

The single template search yields a $2\mathcal{F}$ value of 5.7, corresponding to a p-value of 27% , consistent with a null result calculated according to the method described in section 5.3. We search in a ~ 2 Hz band around twice the rotation frequency, a factor of 10^{-3} of the gravitational wave frequency, as in Abbott et al. (2019). The spin-down range is $2\dot{f} \in (-1.260, -1.2216) \times 10^{-15} \text{Hz/s}$. In this two dimensional parameter space we use 2.4×10^9 templates with an average mismatch of 1%. We examine the results

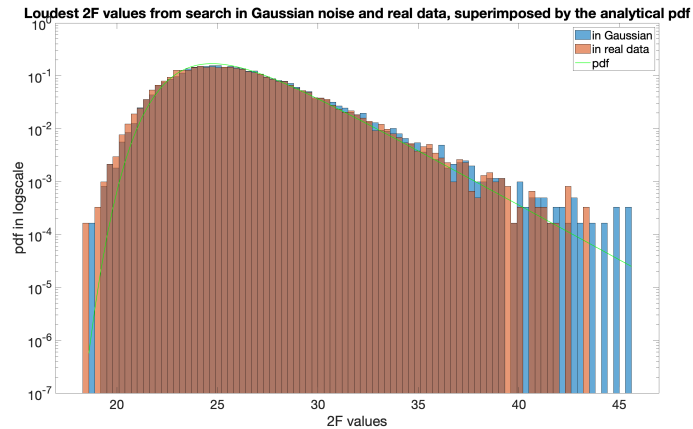


Figure 7.7: Band search results for J1653-0158. Normalised Histogram of the loudest $2\mathcal{F}$ in 0.1mHz slice, obtained from a search in real data and search in Gaussian noise, in semi-log scale.

in 0.1mHz wide bands, by comparing them against results from searching in pure Gaussian noise. Knowing how the search results should look like in pure noise, we can infer the significance of the search results from real data.

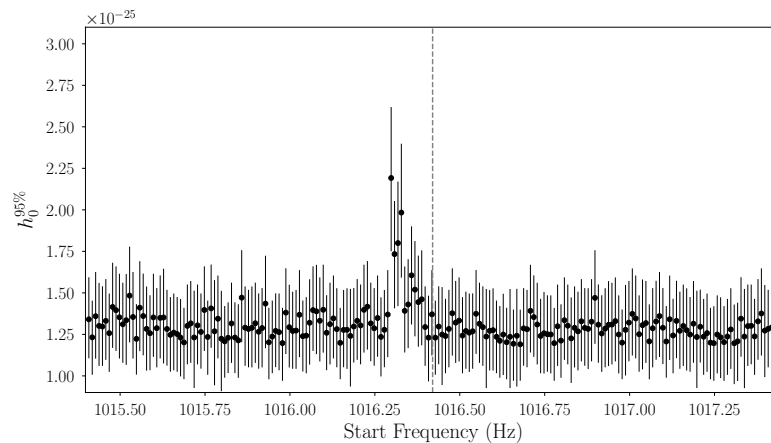


Figure 7.8: 95% confidence upper limits on the gravitational wave amplitude in a 2 Hz band around twice the rotation frequency of PSR J1653-0158. The x-axis shows the start frequency of the sub-bands and the bars indicate a conservative estimate of the uncertainty on the upper limit values. The “spike” does not indicate a detection: it is due to disturbance in L1 around ≈ 1016.32 Hz.

The 2Hz bandwidth was split into sub-bands of 0.1mHz bandwidth. The search was carried out in the resulting 20,000 sub-bands. A probability distribution of the loudest $2\mathcal{F}$ in the 20,000 sub-bands is computed. The distribution of top $2\mathcal{F}$ values in both

real data and Gaussian data show very similar behaviour (Figure 7.7), indicating that the search results are consistent with those expected from Gaussian noise. We then superimpose the analytical form of the probability density function for the highest $2\mathcal{F}$ values, given by

$$p^{loudest}(2\mathcal{F}|n^{eff}) = n^{eff} F_{\chi^2}^{(n^{eff}-1)} p_{\chi^2}. \quad (7.2)$$

where p_{χ^2} denotes the probability density of a central χ^2 distribution with 4 degrees of freedom. This is the distribution of $2\mathcal{F}$ in the absence of any signal and assuming Gaussian Noise. F_{χ^2} is its cumulative distribution given by

$$F_{\chi^2} = \int_0^{2\mathcal{F}} p_{\chi^2}(2\mathcal{F}) d(2\mathcal{F}) \quad (7.3)$$

and n^{eff} is the effective number of templates. n^{eff} is usually lesser than the actual number of templates because all templates are not independent. This basically stems from the fact that the templates are very close to each other. To find n^{eff} , we curve fit the expected distribution over the actual distribution of top $2\mathcal{F}$ values with the analytical form of the probability density function given above. This fitted curve gives us an effective number of templates. We see in figure 7.7 that the normalised probability density function for this effective number of templates superimposes well with the $2\mathcal{F}$ obtained. This shows that there is nothing out of ordinary about the results, and they are consistent with the results expected from Gaussian noise. Figure 7.7 has the y-axis in a logarithmic scale, in order to see clearly, what happens near the tail of the distribution.

In the description above of analysis of band search results, we used sub-bands of bandwidth 0.1mHz. Note that in the final published results, we adopted sub-bands of bandwidth 10mHz and carried out a similar procedure using the loudest candidates from 10mHz bands. This choice was adopted because in the next step, the upper limits in the band are set based on the loudest candidates in sub-bands. With the former choice, we end up with 20,000 sub-bands and the upper limit Monte Carlos become computationally expensive. So we use the larger 10mHz bands for the upper limits.

The 95% confidence upper limit on the intrinsic gravitational wave amplitude, $h_0^{95\%}$, is 4.4×10^{-26} , with an uncertainty $\lesssim 20\%$ including calibration uncertainties. These $h_0^{95\%}$ are comparable to the upper limits on other known pulsars at similar frequencies from Abbott et al. (2019). We also set upper limits in each sub-band. The values are plotted in Figure 7.8. The mean value is 1.3×10^{-25} and it is higher than the targeted search upper limit, as expected due to the larger volume of searched wave shapes.

7.3 PSR J0154+1833

PSR J0154+1833 is an isolated millisecond pulsar with a gravitational wave frequency of 845 Hz making it the fastest pulsar in the ARECIBO set. At 860 pc Martinez et al.

(2019), it is also the closest among all the pulsars in this thesis. Its high frequency, combined with its small distance, made it the pulsar for which the most constraining ellipticity was found among the pulsars in this thesis. We will discuss this further in the Conclusions.

7.3.1 Search In O1O2

The targeted search returned a $2\mathcal{F}=0.65$ and has a p-value of 0.9 calculated with respect to off-source data as shown in top panel of figure 7.9. In such figures, the distribution of $2\mathcal{F}$ from the band search as well as the p-value of the targeted search, are shown. The results from searching in real data (red distribution) are compared against results from searching in pure Gaussian noise (blue distribution). The green curve is the equivalent expected distribution of $2\mathcal{F}$ in Gaussian noise. We had seen in chapter 5 that $2\mathcal{F}$ showed deviations from the χ^2 distribution with 4 degrees of freedom and non-centrality parameter of 0. So we find the best-fitting non-centrality parameter (called *nc* in the plots) to the distribution of $2\mathcal{F}$ in Gaussian noise and calculate the p-values of the targeted search with respect to this pseudo-theoretical distribution of $2\mathcal{F}$ as well. The p-values are denoted by 'p_v' in these plots.

A search region of 3.4Hz around the targeted template frequency was probed and the the distribution of $2\mathcal{F}$ in this range is in Figure 7.9. We find that the distribution of $2\mathcal{F}$ in real data is consistent with that from Gaussian noise.

The 95% upper limit based on a null detection in the targeted search is $2.7\text{e-}26$. This h_0^{95} is a factor of 30 larger than the spin-down upper limit. The h_0 vs detection efficiency and the sigmoid fit is shown in figure 7.10. The upper limits in 10mhz sub-bands are in Figure 7.11.

7.3.2 Search In only O3a

In O3a data, the targeted search returned a $2\mathcal{F}=4.9$ and has a p-value of 0.3 calculated with respect to off-source data. Figure 7.12 shows the distribution of $2\mathcal{F}$ in this off-source band search and the p-value of the targeted search result.

A band search in 3.4 Hz around the targeted template frequency in O3a yielded results that are consistent with expectations from Gaussian noise as seen in figure 7.12. The p-values of the loudest result in each sub-band is shown in figure 7.13.

The 95% upper limit based on a null detection in the targeted search is $1.9\text{e-}26$. This h_0^{95} is a factor of 21.2 larger than the spin-down upper limit. The h_0 vs detection efficiency and the sigmoid fit is shown in figure 7.14. The upper limits in 10mhz sub-bands are in Figure 7.11.

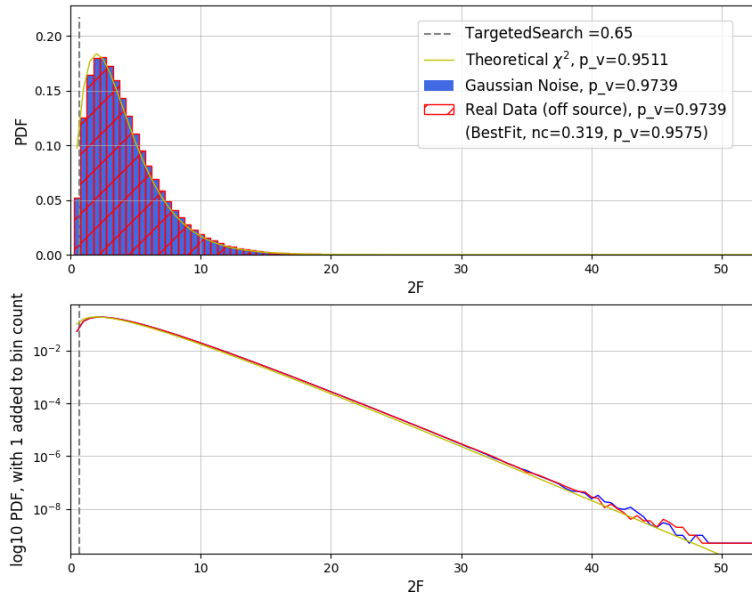


Figure 7.9: Distribution of $2\mathcal{F}$ in a 3.4 Hz region around the signal frequency of J0154+1833 in O1O2 data. The dashed-grey line shows the $2\mathcal{F}$ value returned in the targeted search. The p-values of this $2\mathcal{F}$ result calculated with respect to different distributions are denoted by 'p_v' in these plots. The different distributions are (i) a central χ^2 distribution of 4 degrees of freedom which is the theoretical distribution of $2\mathcal{F}$ in Gaussian noise, plotted in green (ii) search results from simulated Gaussian noise as a blue histogram (iii) search results from off-source real data as a red histogram (iv) the best fitting χ^2 distribution for the results from Gaussian noise, 'nc' stands for the non-centrality parameter.

7.3.3 Search In O1O2O3a

In all O1O2O3a, the targeted search returned a $2\mathcal{F}=4.0$ and has a p-value of 0.41 calculated with respect to off-source data as shown in figure 7.15.

A search region of 3.4Hz around the targeted template frequency was probed. Figure 7.15 shows the distribution of $2\mathcal{F}$ in this range compared with search results from Gaussian noise.

The distribution of this loudest $2\mathcal{F}$ from search in real data is found to be consistent with expectations in Gaussian noise in figure 7.15. The significance of the band search results in real data is expressed in terms of their p-values with respect to a reference distribution of such results in Gaussian noise. The p-values of the loudest result in each sub-band is shown in figure 7.16.

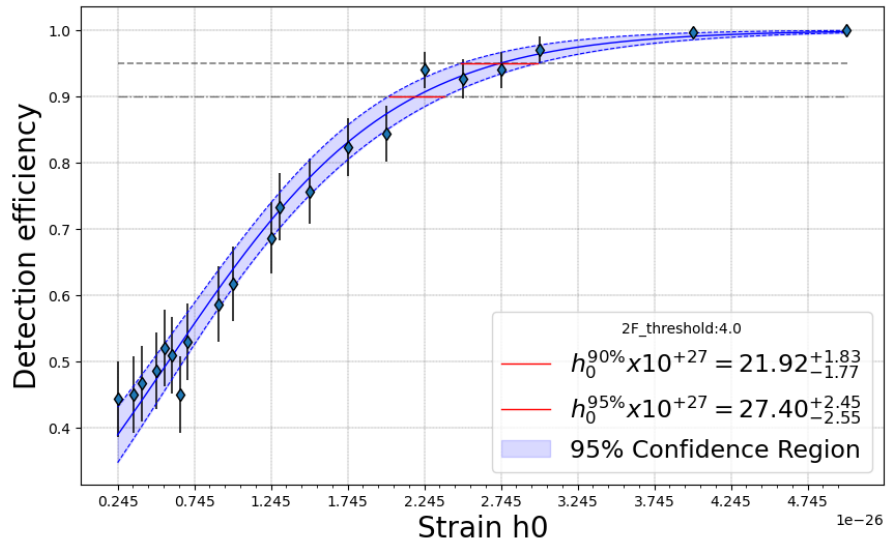


Figure 7.10: Upper limit sigmoid fit for J0154+1833 in O1O2 data. The grey dashed line stands for the 95% upper limit. The dash-dotted line shows the 90% upper limit.

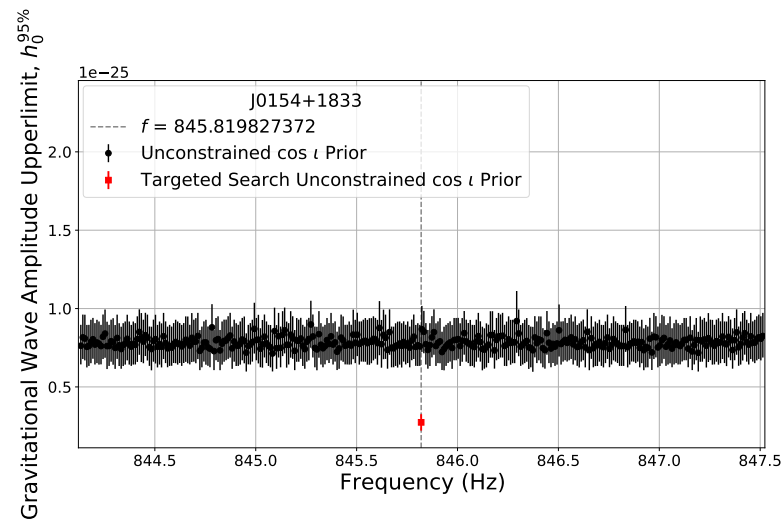


Figure 7.11: O1O2 data h_0 upper limits in 10 mHz frequency subband searched, based on the most significant result in that 10 mHz subband.

The 95% upper limit based on a null detection in the targeted search is 1.5×10^{-26} . This 95% UL is a factor of 17 larger than the spin-down upper limit. The h_0 vs detection efficiency and the sigmoid fit is shown in figure 7.17.

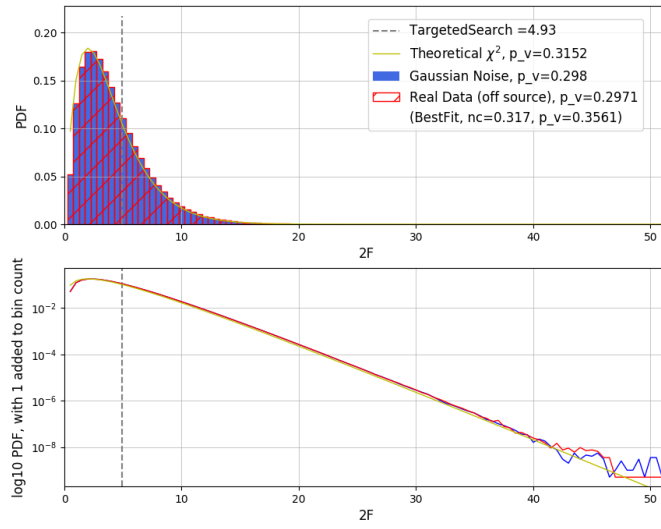


Figure 7.12: Distribution of $2\mathcal{F}$ in a 3.4Hz region around the signal frequency of J0154+1833 in O₃ data

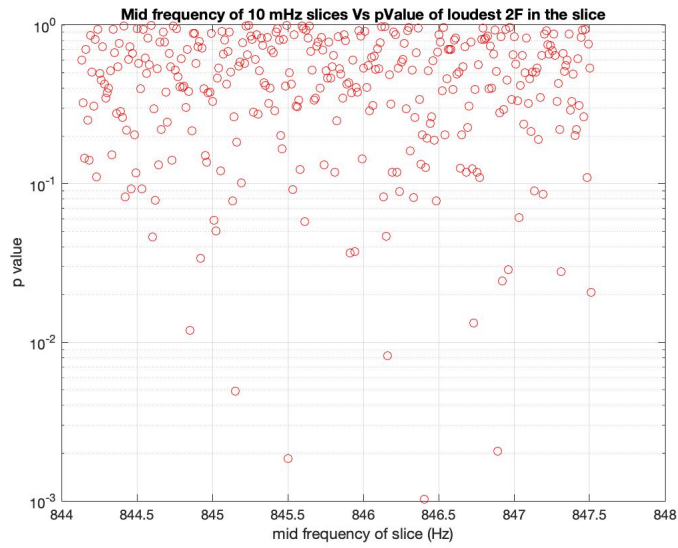


Figure 7.13: p-values of the band search results for J0154+1833 in O₃ data

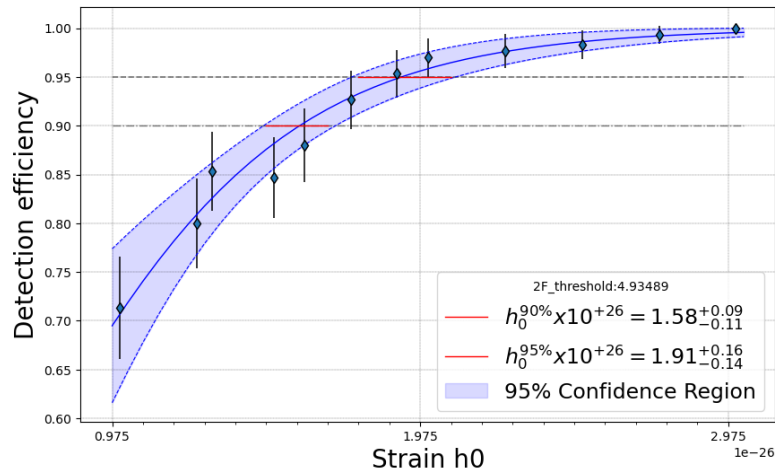


Figure 7.14: Upper limit sigmoid fit for J0154+1833 for O3 data

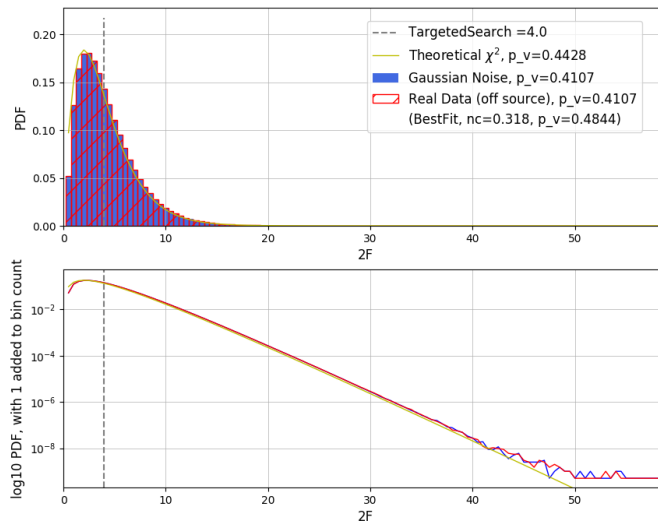


Figure 7.15: Distribution of $2\mathcal{F}$ in a 3.4Hz region around the signal frequency of J0154+1833 in O1O2O3 data

7.4 PSR J0824+0028

PSR J0824+0028 was targeted using parameters derived from a timing solution valid over all of the Advanced LIGO observation as seen in Figure 7.1. With a gravitational wave frequency of 203Hz, this pulsar lies in the most sensitive frequency region of Advanced LIGO detectors. Such pulsars are valuable candidates for continuous

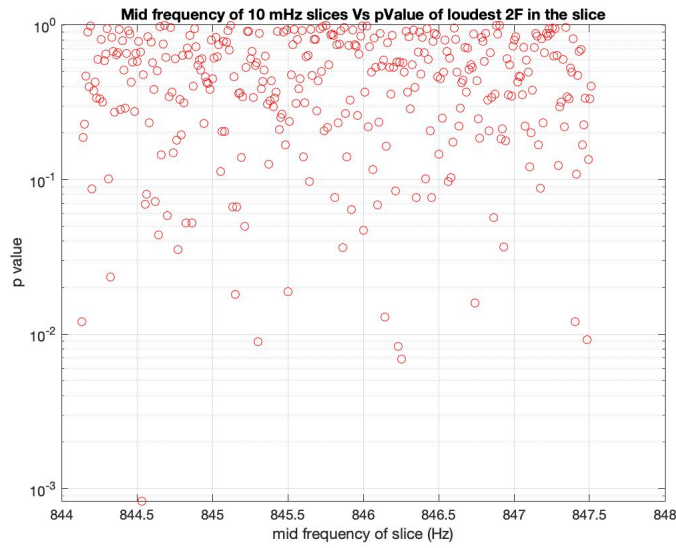


Figure 7.16: p-values of the band search results for J0154+1833 in O1O2O3 data

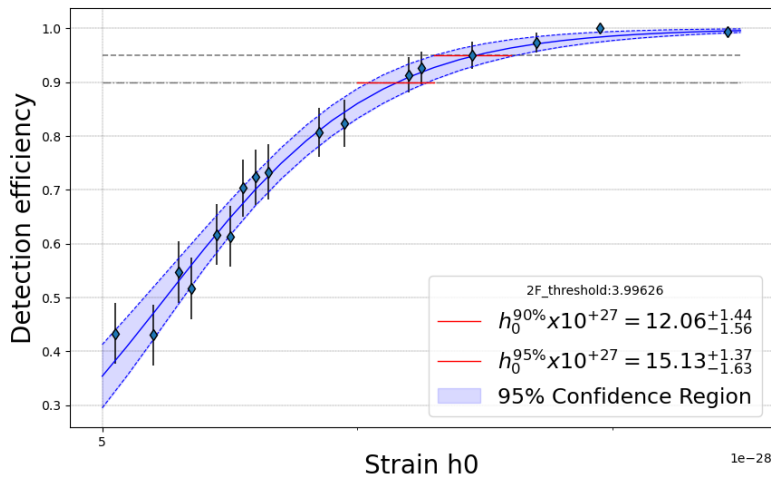


Figure 7.17: Upper limit sigmoid fit for J0154+1833 in O1O2O3 data

gravitational wave searches. Thanks to the sensitivity of data at this frequency, PSR J0824+0028 is the pulsar for which we came closest to the spin-down upper limit, with a h_0^{95} factor of 5.8 above the h_0^{sd} . It is a binary pulsar with an eccentricity of orbit that was found to be non-negligible in terms of mismatch induced in the signal recovery, and hence was part of the searched parameter space. . Measurements of orbital inclination angle were available for this pulsar. So upper limits based on a restricted range in allowed $\cos i$ are also calculated for this pulsar.

7.4.1 Search In O1O2

The targeted search returned a $2\mathcal{F}=2.4$ and has a p-value of 0.4 calculated with respect to off-source data as shown in figure 7.18.

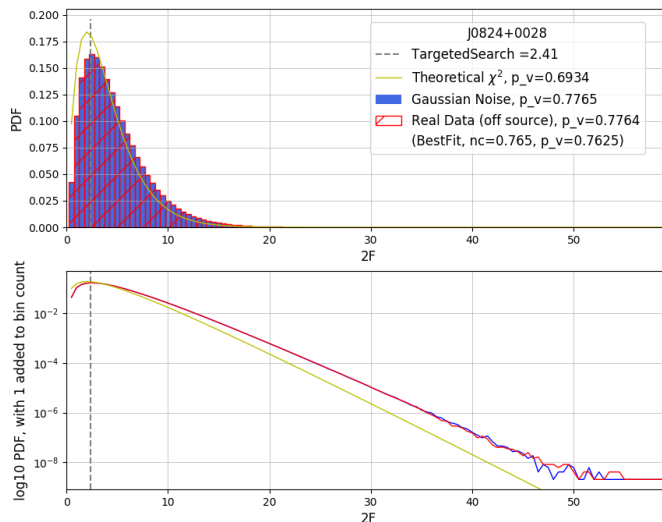


Figure 7.18: Distribution of $2\mathcal{F}$ in a 0.8Hz region around the signal frequency of J0824+0028 in O1O2 data

A search region of 0.8 Hz around the targeted template frequency was probed. Figure 7.18 shows the distribution of $2\mathcal{F}$ in this range compared with search results from Gaussian noise.

The 95% upper limit based on a null detection in the targeted search is $1.4\text{e-}26$. This h_0^{95} is a factor of 7 larger than the spin-down upper limit. The h_0 vs detection efficiency and the sigmoid fit is shown in figure 7.19.

Using a restricted prior on $\cos \iota$ we set an h_0^{95} of $1.8\text{e-}26$. This h_0^{95} is a factor of 8.8 larger than the spin-down upper limit. The h_0 vs detection efficiency and the sigmoid fit in the restricted $\cos \iota$ case is shown in figure 7.20.

Figure 7.21 shows the upper limits in 10mHz sub-bands. The upper limits with constrained priors on $\cos \iota$ are also in the figure. The upper limit values are indicative of the significance of the loudest $2\mathcal{F}$ in the 10mHz sub-bands – higher the upper limit in a sub-band, higher was the $2\mathcal{F}$ in that band.

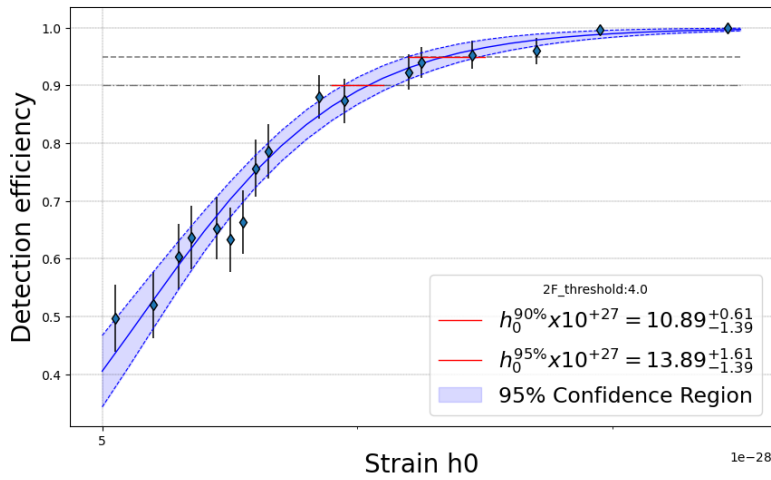
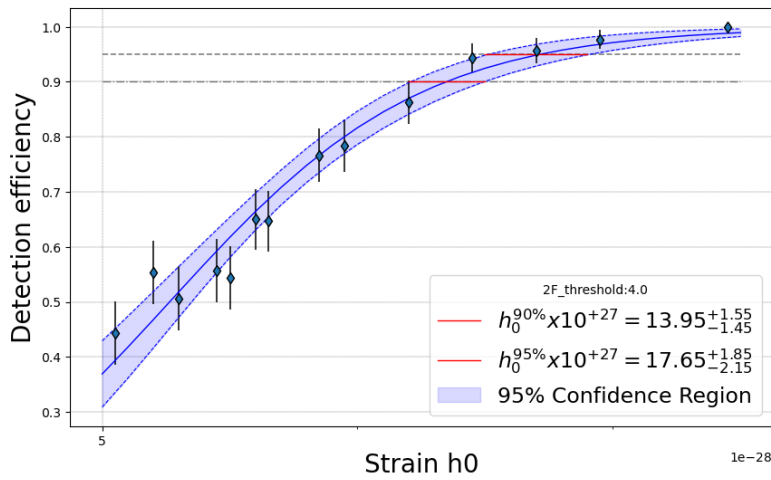


Figure 7.19: Upper limit sigmoid fit for Jo824+0028 for O1O2 data

Figure 7.20: Upper limit sigmoid fit with restricted prior on $\cos i$ for Jo824+0028 in O1O2 data

7.4.2 Search In only O3a

The targeted search returned a $2\mathcal{F}=1.0$ and has a p-value of 0.7 calculated with respect to off-source data. Figure 7.22 shows the distribution of $2\mathcal{F}$ in this off-source band search and the p-value of the targeted search result. A band search in 0.8 Hz around the targeted template frequency in O3a yielded results that are consistent with expectations from Gaussian noise as seen in figure 7.22. The p-values of the loudest result in each sub-band is shown in figure 7.23.

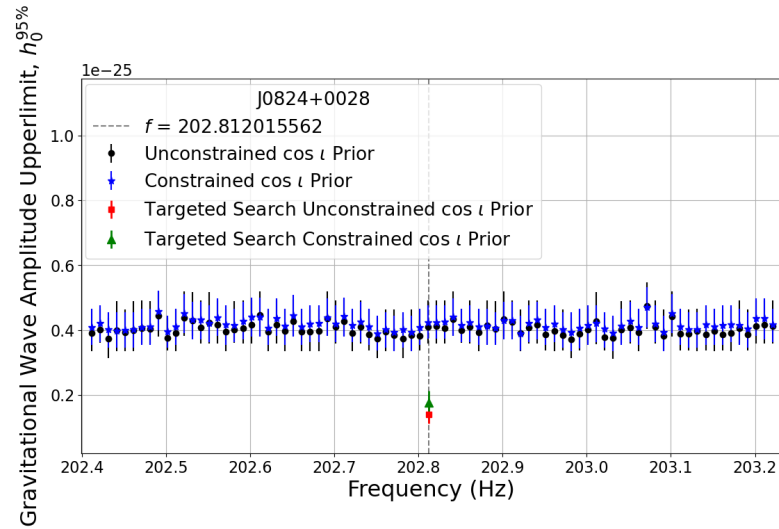


Figure 7.21: O1O2 data h_0 upper limits in 10 mHz frequency subband searched, based on the most significant result in that 10 mHz subband.

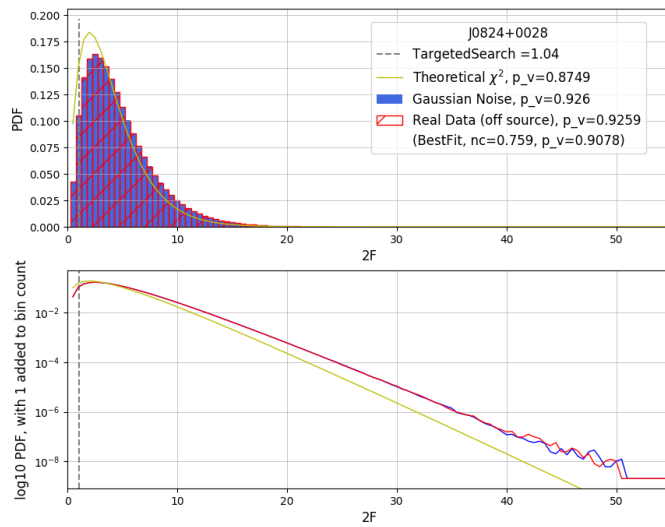


Figure 7.22: Distribution of $2\mathcal{F}$ in a 0.8Hz region around the signal frequency of J0824+0028 in O3 data

The 95% upper limit based on a null detection in the targeted search is $9.9e-27$. This h_0^{95} is a factor of 5.0 larger than the spin-down upper limit. The h_0 vs detection efficiency and the sigmoid fit is shown in figure 7.24.

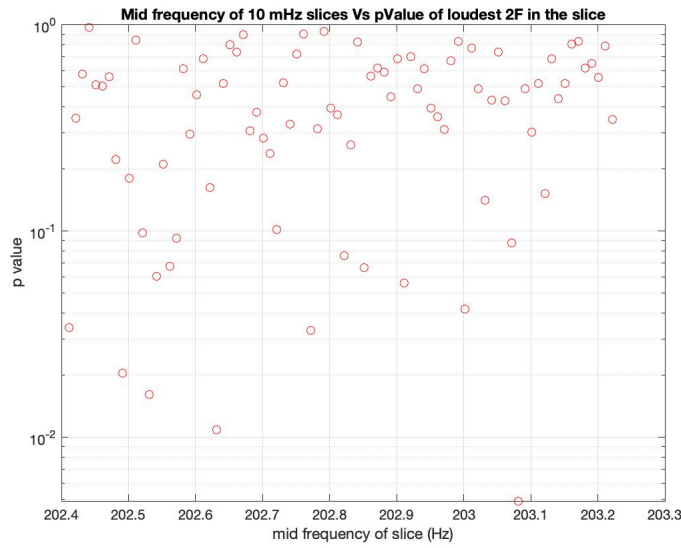


Figure 7.23: p-values of the band search results for J0824+0028 in O₃ data

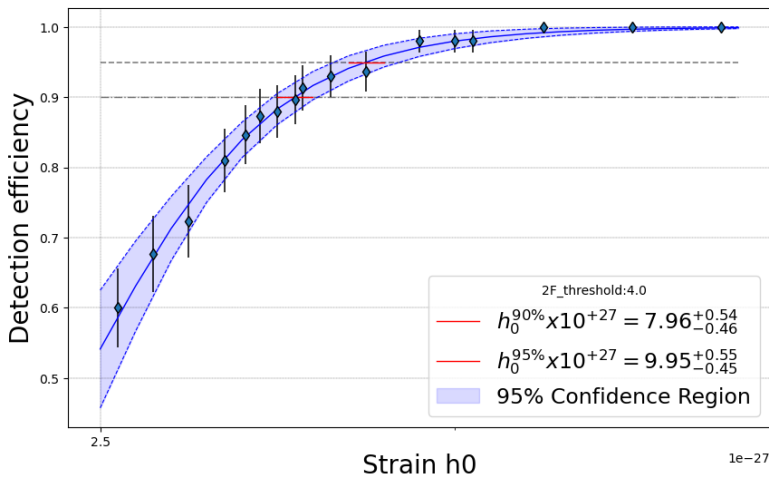


Figure 7.24: Upper limit sigmoid fit for J0824+0028 for O₃ data

Using a restricted prior on $\cos \iota$ we set an h_0^{95} of 1.2×10^{-26} . This h_0^{95} is a factor of 6.0 larger than the spin-down upper limit. The h_0 vs detection efficiency and the sigmoid fit is shown in figure 7.25.

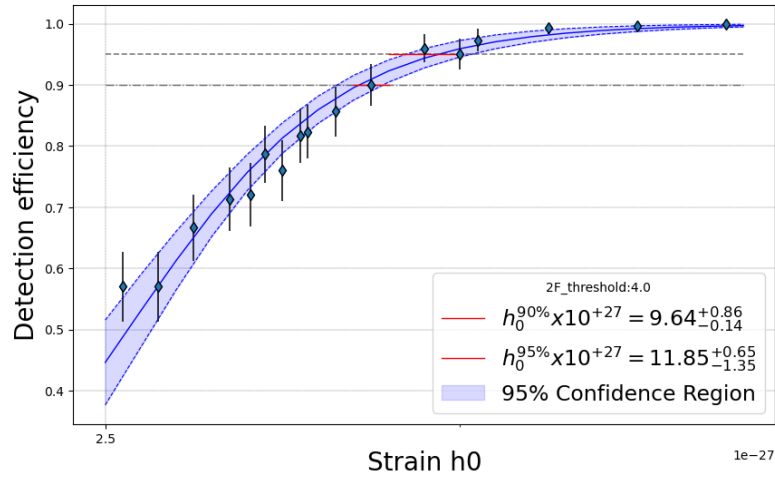


Figure 7.25: Upper limit sigmoid fit with restricted prior on $\cos \iota$ for J0824+0028 for O3 data

7.4.3 Search In O1O2O3a

The targeted search returned a $2\mathcal{F}=0.64$ and has a p-value of 0.9 calculated with respect to off-source data as shown in figure 7.26. A search region of 0.8Hz around the

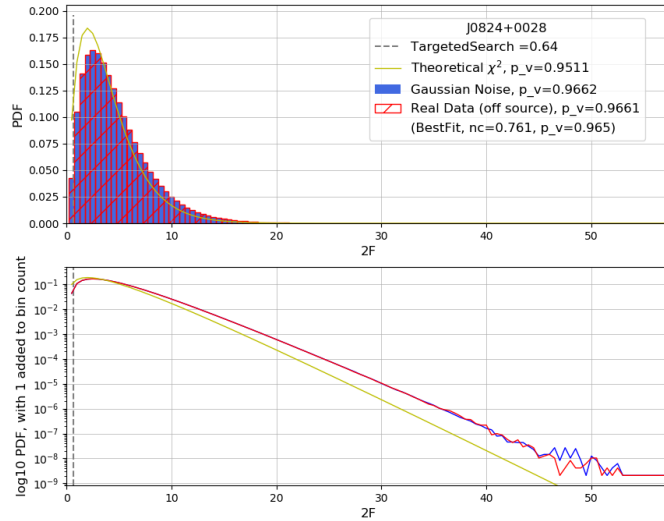


Figure 7.26: Distribution of $2\mathcal{F}$ in a 0.8 Hz region around the signal frequency of J0824+0028 in O1O2O3 data

targeted template frequency was probed. The results are consistent with expectations

from Gaussian noise as seen in figure 7.26. The p-values of the loudest result in each sub-band is shown in figure 7.27.

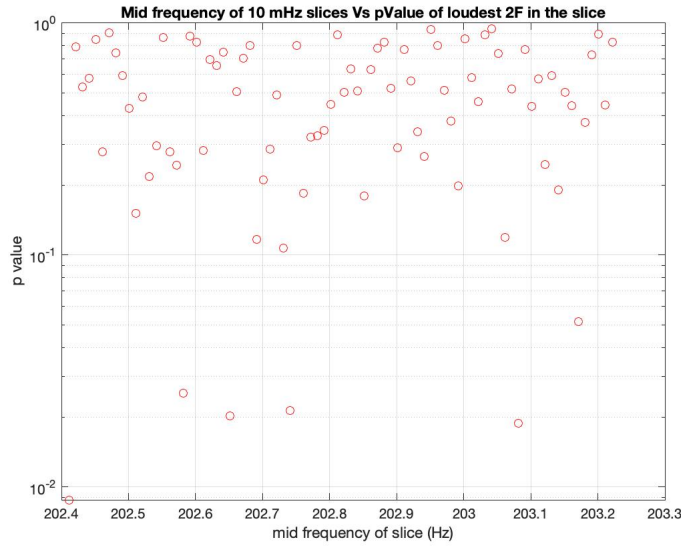


Figure 7.27: p-values of the band search results for J0824+0028 in O1O2O3 data

The 95% upper limit based on a null detection in the targeted search is $7.6e-27$. This 95% UL is only a factor of 3.8 larger than the spin-down upper limit. This is the closest we have come to the spin-down upper limit for this set of pulsars. The h_0 vs detection efficiency and the sigmoid fit is shown in figure 7.28.

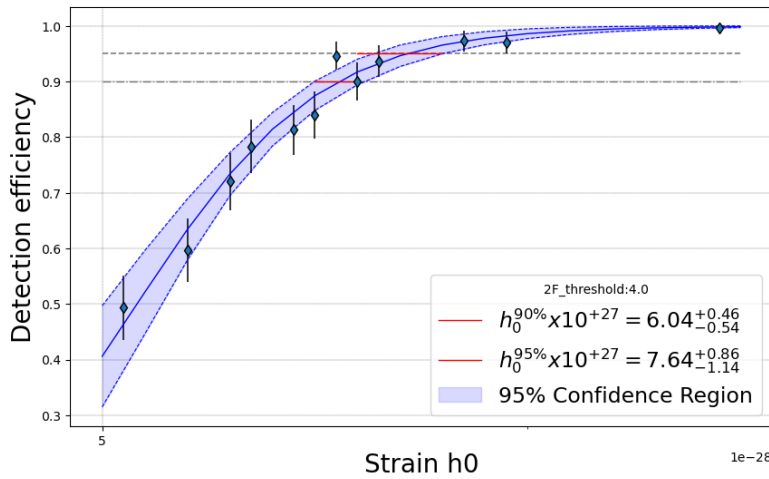


Figure 7.28: Upper limit sigmoid fit for J0824+0028 in O1O2O3 data

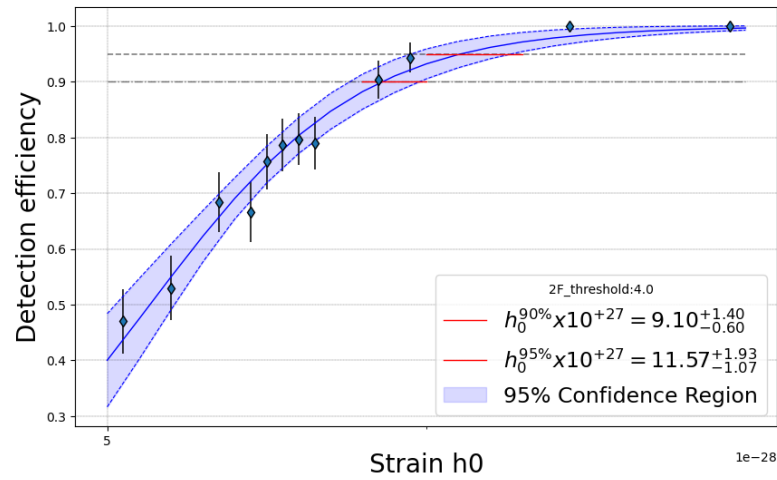


Figure 7.29: Upper limit sigmoid fit with restricted prior on $\cos \iota$ for J0824+0028 in O1O2O3 data

Using a restricted prior on $\cos \iota$ we set an h_0^{95} of 1.2×10^{-26} . This h_0^{95} is a factor of 5.8 larger than the spin-down upper limit. The h_0 vs detection efficiency and the sigmoid fit is shown in figure 7.29.

7.5 PSR J0509+0856

PSR J0509+0856 with a gravitational wave frequency of 493 Hz is one of the two pulsars in this frequency range. It is at a distance of 1.45 kpc. It is a binary pulsar but there was no measurement of orbital inclination angle. The ellipticity constraint on this pulsar using O1O2O3 data is one of the most stringent to date.

7.5.1 Search In O1O2

The targeted search returned a $2\mathcal{F}=2.7$ and has a p-value of 0.6 calculated with respect to off-source data as shown in figure 7.30. A search region of 0.8Hz around the targeted

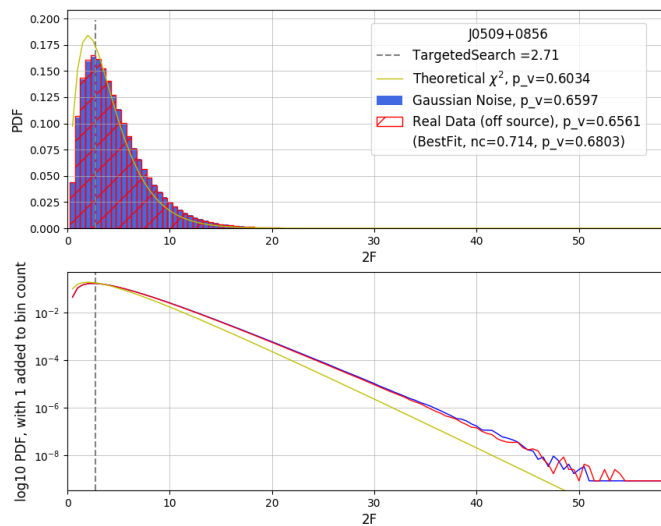


Figure 7.30: Distribution of $2\mathcal{F}$ in a 2Hz region around the signal frequency of J0509+0856 in O1O2 data

template frequency was probed. The results are consistent with expectations from Gaussian noise as seen in figure 7.30.

The 95% upper limit based on a null detection in the targeted search is $1.9e-26$. This h_0^{95} is a factor of 36 larger than the spin-down upper limit. The h_0 vs detection efficiency and the sigmoid fit is shown in figure 7.31. The band search upper limits in 7.32 are indicative of how significant the results in each sub-band is. The higher the upper-limit, lower the p-value of the loudest $2\mathcal{F}$.

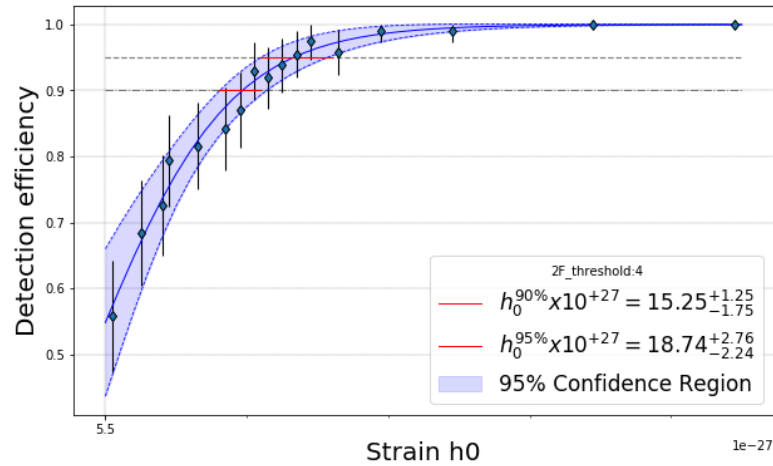


Figure 7.31: Upper limit sigmoid fit for J0509+0856 for O1O2 data

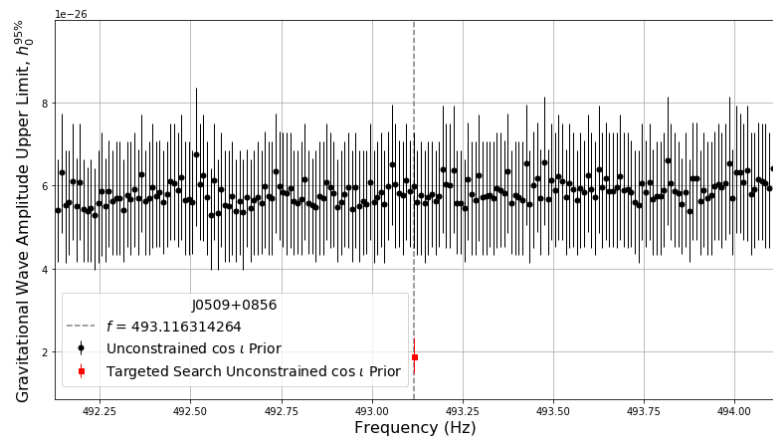


Figure 7.32: O1O2 data h_0 upper limits in 10 mHz frequency subband searched, based on the most significant result in that 10 mHz subband.

7.5.2 Search In only O3a

The targeted search returned a $2\mathcal{F}=1.6$ and has a p-value of 0.8 calculated with respect to off-source data. Figure 7.33 shows the distribution of $2\mathcal{F}$ in this off-source band search and the p-value of the targeted search result. A band search in 2 Hz around the targeted template frequency in O3a yielded results that are consistent with expectations from Gaussian noise as seen in figure 7.33. The p-values of the loudest result in each sub-band is shown in figure 7.34. The 95% upper limit based on a null detection in the targeted search is 1.2×10^{-26} . This h_0^{95} is a factor of 23.7 larger than the spin-down upper limit. The h_0 vs detection efficiency and the sigmoid fit is shown in figure 7.35.

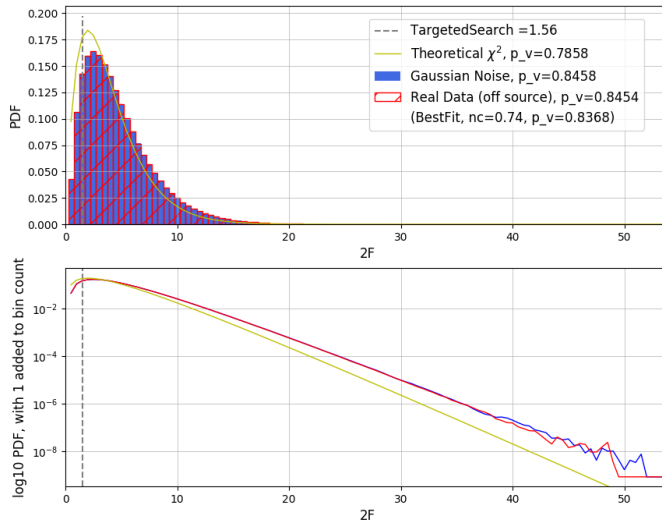


Figure 7.33: Distribution of $2\mathcal{F}$ in a 2Hz region around the signal frequency of J0509+0856 in O₃ data

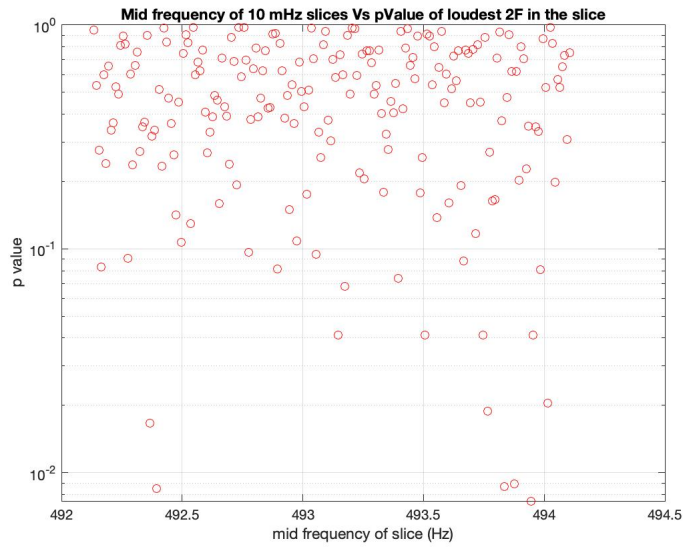


Figure 7.34: p-values of the band search results for J0509+0856 in O₃ data

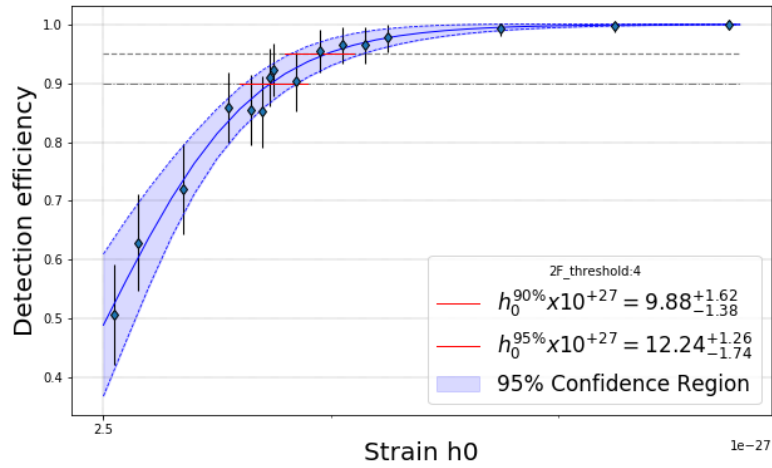


Figure 7.35: Upper limit sigmoid fit for J0509+0856 for O3 data

7.5.3 Search In O1O2O3a

The targeted search returned a $2\mathcal{F}=2.0$ and has a p-value of 0.8 calculated with respect to off-source data as shown in figure 7.36.

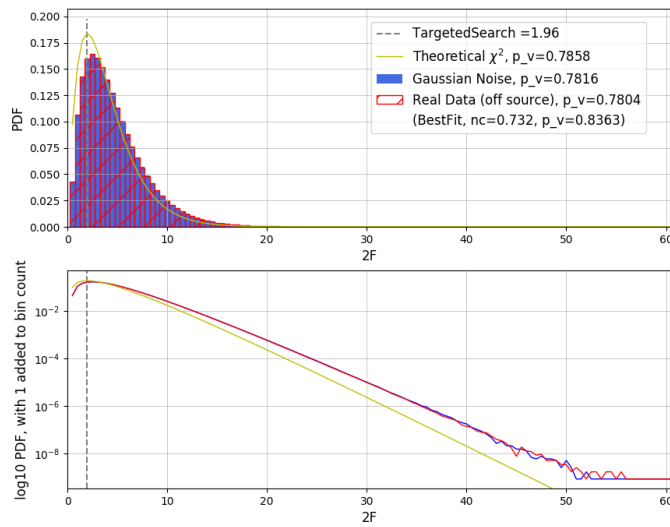


Figure 7.36: Distribution of $2\mathcal{F}$ in a 2 Hz region around the signal frequency of J0509+0856 in O1O2O3a data

A search region of 2Hz around the targeted template frequency was probed. The results are consistent with expectations from Gaussian noise as seen in figure 7.36. The p-values of the loudest result in each sub-band is shown in figure 7.37.



Figure 7.37: p-values of the band search results for J0509+0856 in O1O2O3 data

The 95% upper limit based on a null detection in the targeted search is $1e-26$. This 95% UL is a factor of 20 larger than the spin-down upper limit. The h_0 vs detection efficiency and the sigmoid fit is shown in figure 7.38.

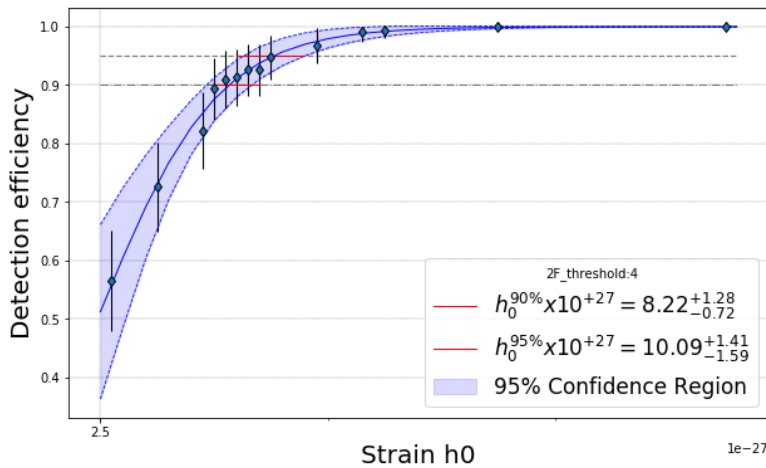


Figure 7.38: Upper limit sigmoid fit for J0509+0856 in O1O2O3 data

7.6 PSR J0732+2314

PSR J0732+2314 is yet another pulsar near $\approx 490\text{Hz}$ and is at a distance of 1.66kpc. Being in a frequency close to PSR J0509+0856 (Section 7.5) and having a similar distance, the upper limits on the continuous gravitational wave emission for these two pulsars are nearly equal in all data sets. The difference is that an orbital inclination angle measurement is available for J0732, so there are two sets of upper limits for this pulsar. This pulsar is a part of the NANOGrav Pulsar Timing Array.

7.6.1 Search In O1O2

The targeted search returned a $2\mathcal{F}=0.9$ and has a p-value of 0.9 calculated with respect to off-source data as shown in figure 7.39.

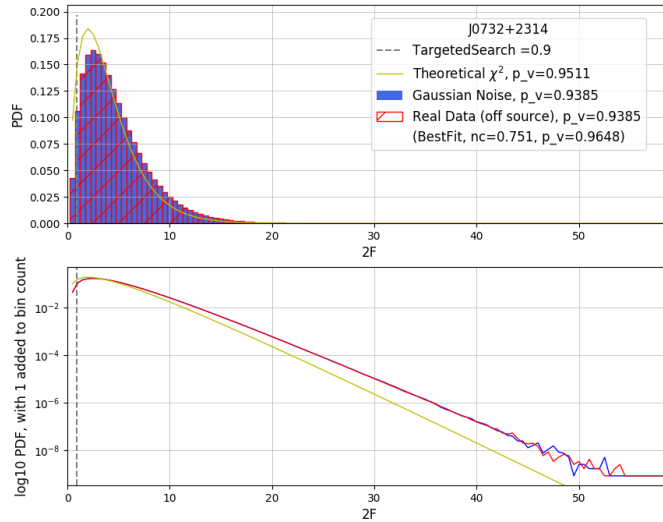


Figure 7.39: Distribution of $2\mathcal{F}$ in a 2Hz region around the signal frequency of J0732+2314 in O1O2 data

A band search in 2 Hz around the signal frequency yielded results consistent with Gaussian noise. The significance of loudest results in 10 mHz sub-bands can be inferred from the band-search upper limits in figure 7.42.

The 95% upper limit based on a null detection in the targeted search is $1.9\text{e-}26$. This h_0^{95} is a factor of 32 larger than the spin-down upper limit. The h_0 vs detection efficiency and the sigmoid fit is shown in figure 7.40.

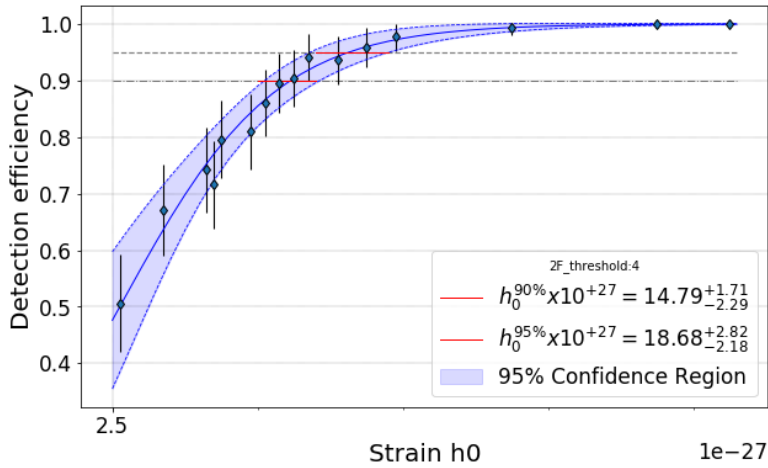
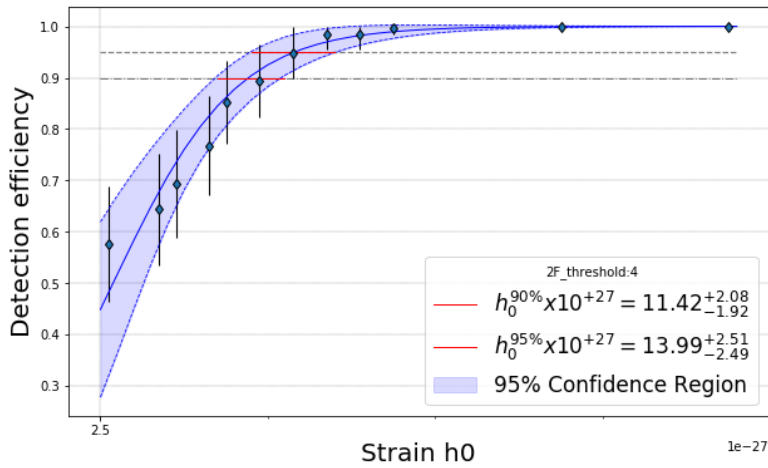


Figure 7.40: Upper limit sigmoid fit for J0732+2314 for O1O2 data

Figure 7.41: Upper limit sigmoid fit with restricted prior on $\cos i$ for J0732+2314 in O1O2 data

Using a restricted prior on $\cos i$ we set an h_0^{95} of 1.4×10^{-26} . This h_0^{95} is a factor of 24.0 larger than the spin-down upper limit. The h_0 vs detection efficiency and the sigmoid fit, in this case, are shown in figure 7.41.

7.6.2 Search In only O3a

The targeted search returned a $2\mathcal{F} = 0.59$ and has a p-value of 0.9 calculated with respect to off-source data. Figure 7.43 shows the distribution of $2\mathcal{F}$ in this off-source band search and the p-value of the targeted search result.

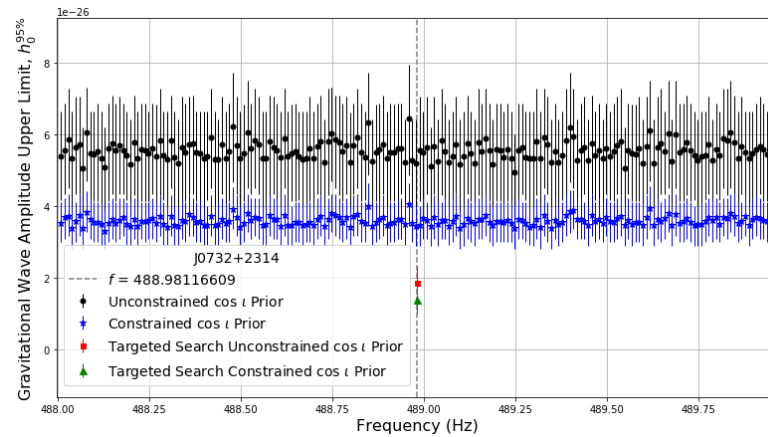


Figure 7.42: O1O2 data h_0 upper limits in 10 mHz frequency sub-band searched, based on the most significant result in that 10 mHz sub-band.

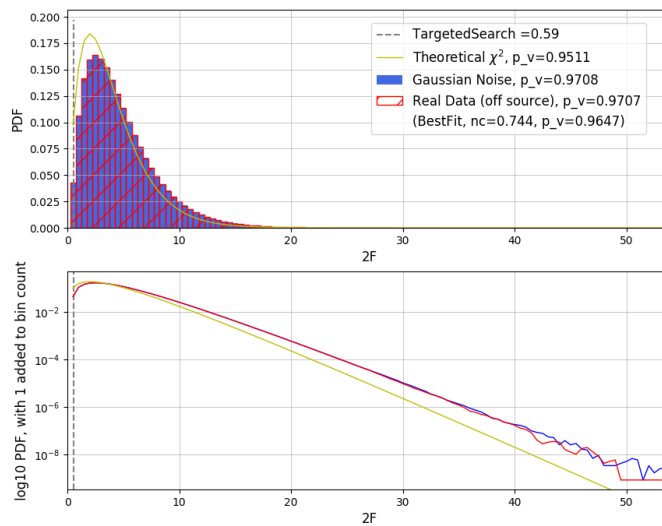


Figure 7.43: Distribution of $2\mathcal{F}$ in a 2Hz region around the signal frequency of J0732+2314 in O3a data

A band search in 2 Hz around the targeted template frequency in O3a yielded results that are consistent with expectations from Gaussian noise as seen in figure 7.43. The p-values of the loudest result in each sub-band is shown in figure 7.44.

The 95% upper limit based on a null detection in the targeted search is 1.2×10^{-26} . This h_0^{95} is a factor of 20.6 larger than the spin-down upper limit. The h_0 vs detection efficiency and the sigmoid fit is shown in figure 7.45.

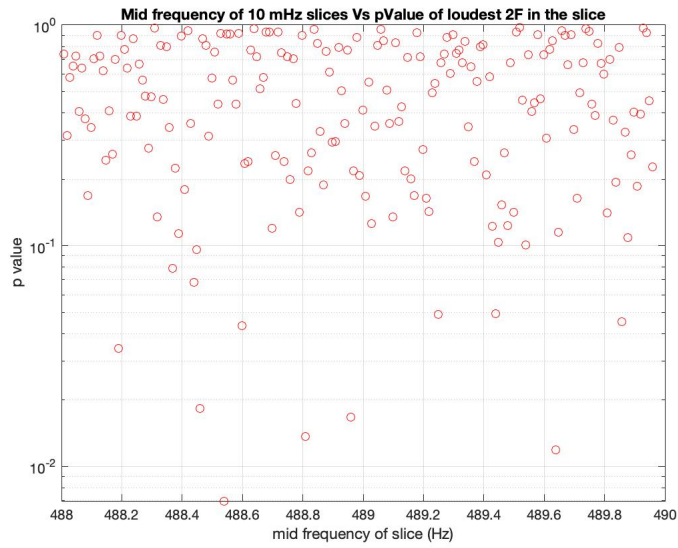


Figure 7.44: p-values of the band search results for J0732+2314 in O₃ data.

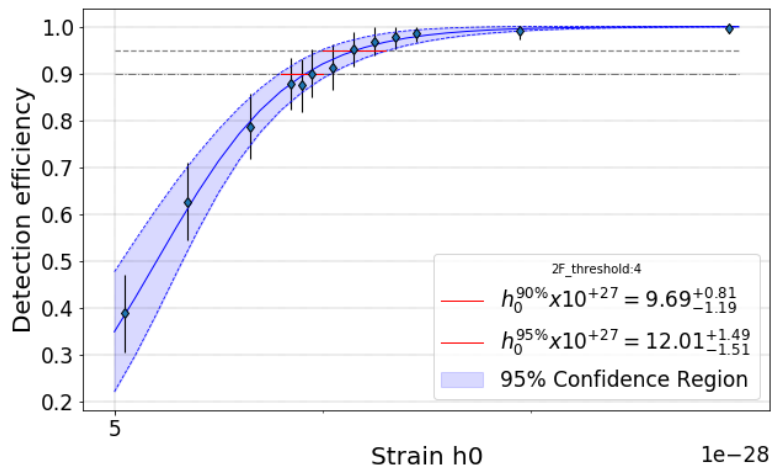


Figure 7.45: Upper limit sigmoid fit for J0732+2314 for O₃ data

Using a restricted prior on $\cos \iota$ we set an h_0^{95} of $1e-26$. This h_0^{95} is a factor of 17.1 larger than the spin-down upper limit. The h_0 vs detection efficiency and the sigmoid fit is shown in figure 7.46.

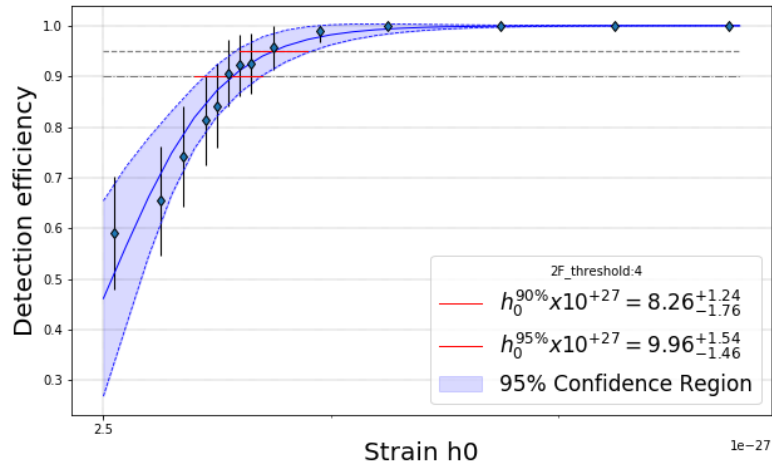


Figure 7.46: Upper limit sigmoid fit with restricted prior on $\cos \iota$ for J0732+2314 for O3a data

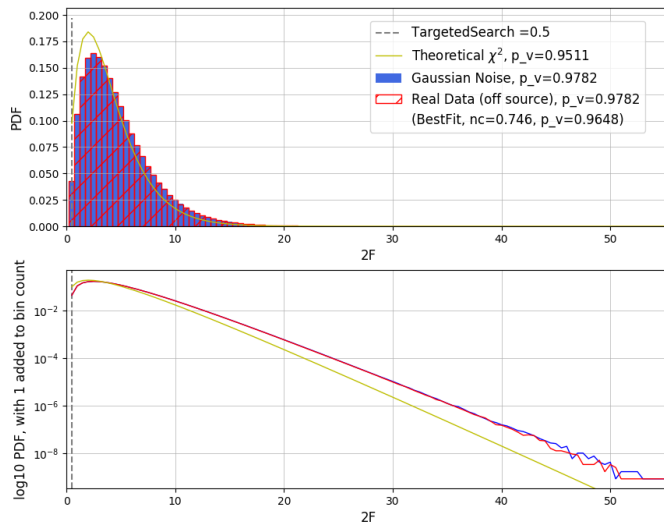


Figure 7.47: Distribution of $2\mathcal{F}$ in a 2 Hz region around the signal frequency of J0732+2314 in O1O2O3 data.

7.6.3 Search In O1O2O3a

The targeted search returned a $2\mathcal{F}=0.5$ and has a p-value of 0.9 calculated with respect to off-source data as shown in figure 7.47.

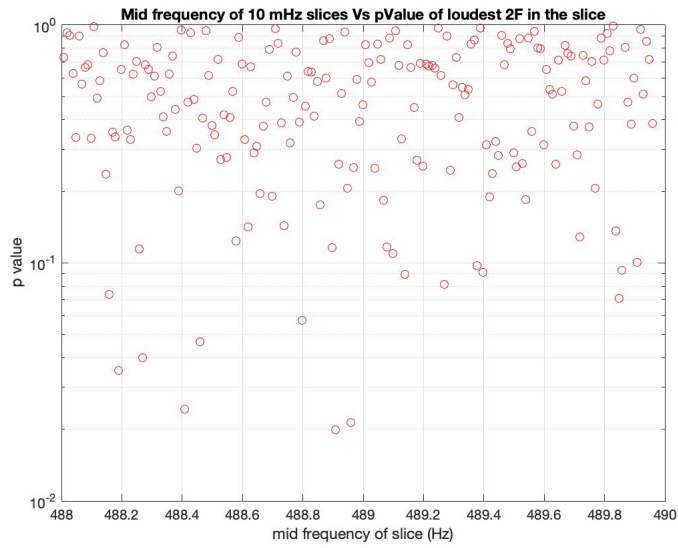


Figure 7.48: p-values of the band search results for J0732+2314 in O1O2O3 data

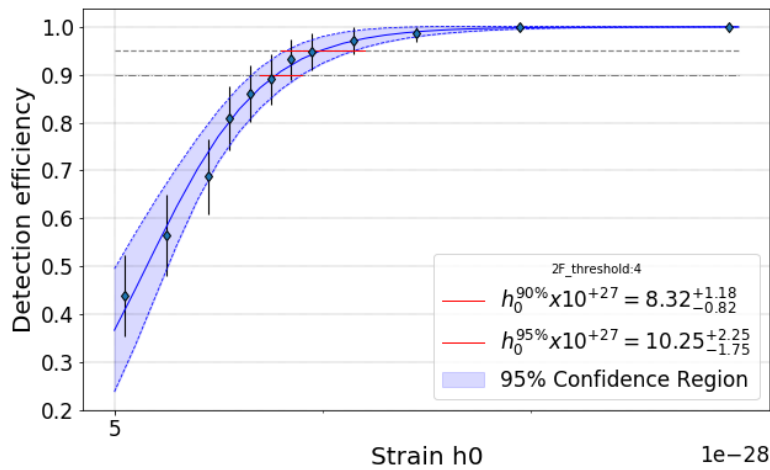


Figure 7.49: Upper limit sigmoid fit for J0732+2314 in O1O2O3 data

A search region of 2Hz around the targeted template frequency was probed. The results are consistent with expectations from Gaussian noise as seen in figure 7.47. The p-values of the loudest result in each sub-band is shown in figure 7.48.

The 95% upper limit based on a null detection in the targeted search is $1e-26$. This 95% UL is a factor of 18 larger than the spin-down upper limit. The h_0 vs detection efficiency and the sigmoid fit is shown in figure 7.49.

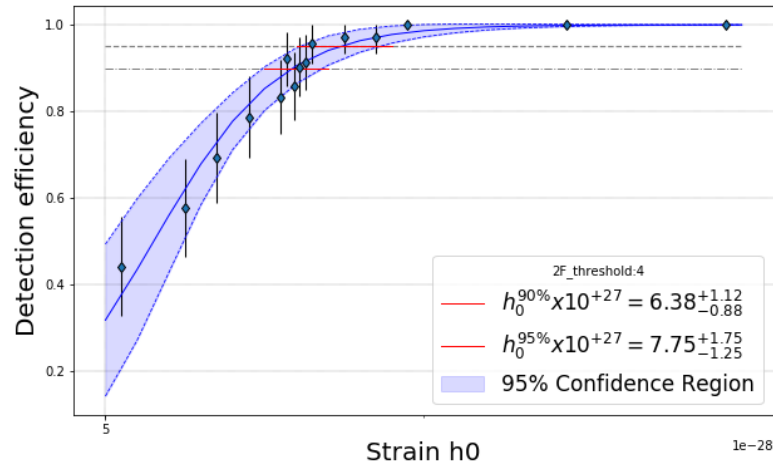


Figure 7.50: Upper limit sigmoid fit with restricted prior on $\cos \iota$ for J0732+2314 in O1O2O3 data

Using a restricted prior on $\cos \iota$ we set an h_0^{95} of 7.8×10^{-27} . This h_0^{95} is a factor of 13.3 larger than the spin-down upper limit. The h_0 vs detection efficiency and the sigmoid fit for this case are shown in figure 7.50.

7.7 PSR J0709+0458

PSR J0709+0458 is a mildly recycled pulsar with a larger spin period than the rest of the pulsars in the set. Its gravitational wave frequency is thus low, and at 58Hz it lies near the 60Hz contamination in Advanced LIGO detectors due to the frequency of the alternating current in the USA. The noise Amplitude Spectral Density (ASD) plots for the two detectors in O1 and O2, in 7.51 show the range of these disturbances. The noise ASD is the square root of the noise PSD described in chapter 5. The O3a data had just been publicly released, and we did not wait for the preparation of 60s SFTs with line cleaning. So the non-cleaned O3a data was directly used.

For O1 and O2, we looked at the noise ASD at the signal frequency as a function of time. Figure 7.52 shows the mean ASD in the signal frequency bin ± 1 frequency bin at each timestamp, and excess noise in the H1 detector in some timestamps of O1 run is seen.

This is also seen as the tail in the curve for H1 in O1 in Figure 7.53 which shows on the left the distribution of this mean ASD and on the right the cumulative distribution of the mean ASD. After removing the times when there is excessive noise in the H1 detector, data with distribution of ASD in the continuous gravitational wave signal frequency of PSR J0709+0458 as shown in figure 7.54 was used in the search.

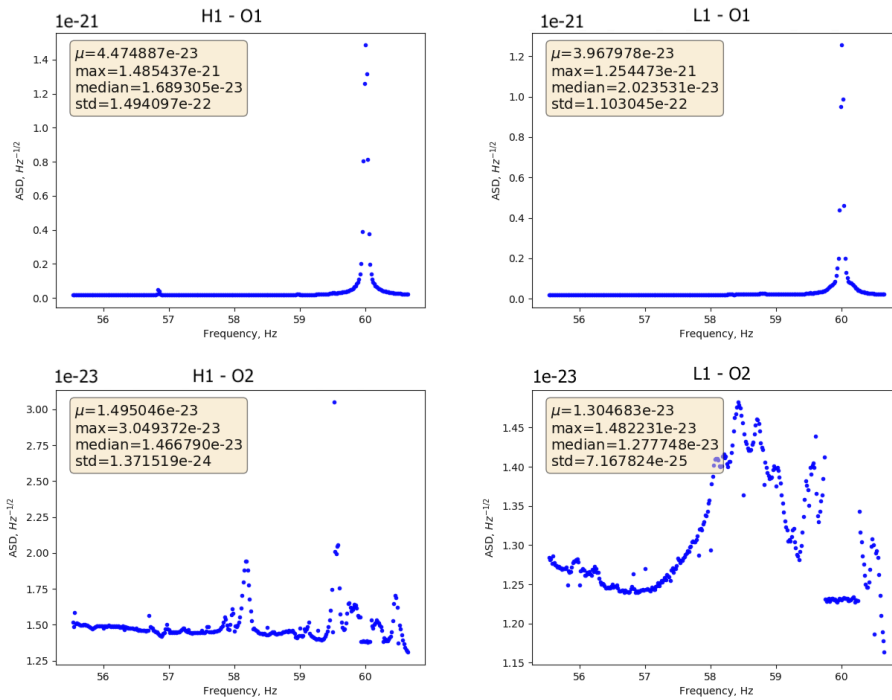


Figure 7.51: Noise ASD in the Hanford (H1) and Livingston (L1) detectors during O1, O2 runs. These plots show in one glimpse the noise levels in the different data-sets.

7.7.1 Search In O1O2

The targeted search returned a $2\mathcal{F}=6.1$ and has a p-value of 0.5 calculated with respect to off-source data as shown in figure 7.55.

A band search in 0.2Hz around the signal frequency gave results which were consistent with those from Gaussian noise. The 95% upper limit based on a null detection in the targeted search is 3.3×10^{-26} . This h_0^{95} is a factor of 22 larger than the spin-down upper limit. The h_0 vs detection efficiency and the sigmoid fit is shown in figure 7.56.

Using a restricted prior on $\cos \iota$ we set an h_0^{95} of 3.9×10^{-26} . This h_0^{95} is a factor of 26.5 larger than the spin-down upper limit. The h_0 vs detection efficiency and the sigmoid fit is shown in figure 7.57. The band search upper limits in figure 7.58

7.7.2 Search In only O3a

The targeted search returned a $2\mathcal{F}=6.4$ and has a p-value of 0.2 calculated with respect to off-source data. Figure 7.59 shows the distribution of $2\mathcal{F}$ in this off-source band

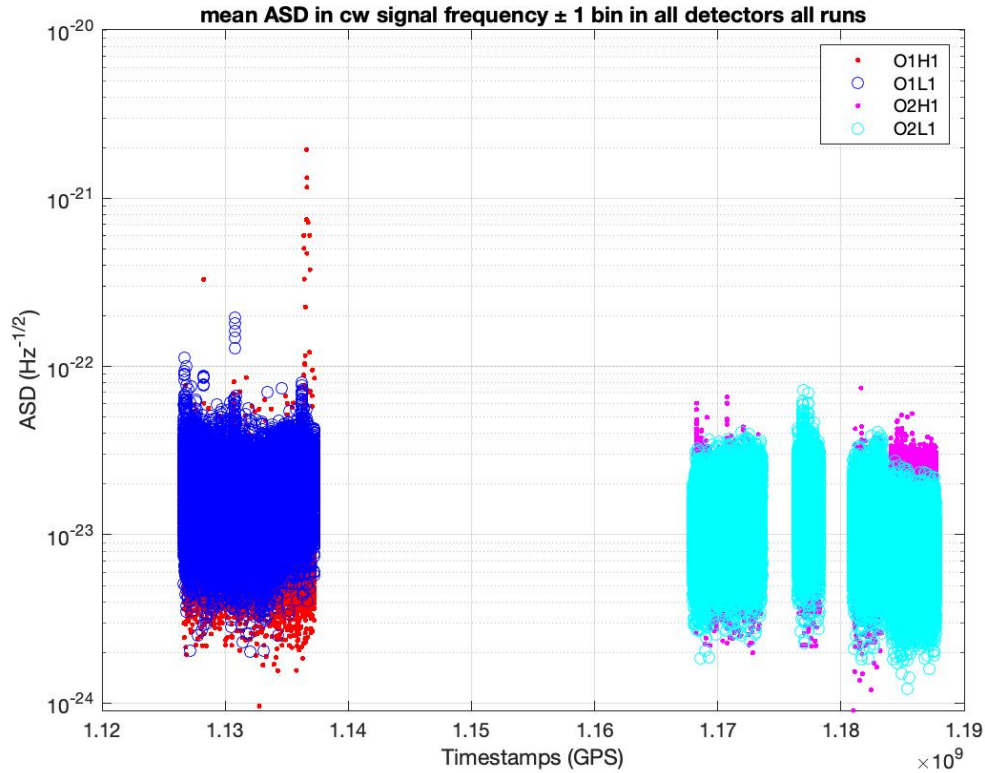


Figure 7.52: Noise ASD in the continuous gravitational wave signal frequency of J0709+0458 at each timestamp during the O1 and O2 observation runs in the Hanford (H1) and Livingston (L1) detectors.

search and the p-value of the targeted search result. A band search in 0.2 Hz around the targeted template frequency in O3a yielded results that are consistent with expectations from Gaussian noise as seen in figure 7.59. The p-values of the loudest result in each sub-band is shown in figure 7.60. The 95% upper limit based on a null detection in the targeted search is $2.2e-26$. This h_0^{95} is a factor of 14.6 larger than the spin-down upper limit. The h_0 vs detection efficiency and the sigmoid fit is shown in the left plot of figure 7.61. Using a restricted prior on $\cos \iota$ we set an h_0^{95} of $2.4e-26$. This h_0^{95} is a factor of 16.1 larger than the spin-down upper limit. The h_0 vs detection efficiency and the sigmoid fit is shown in the right plot of figure 7.61.

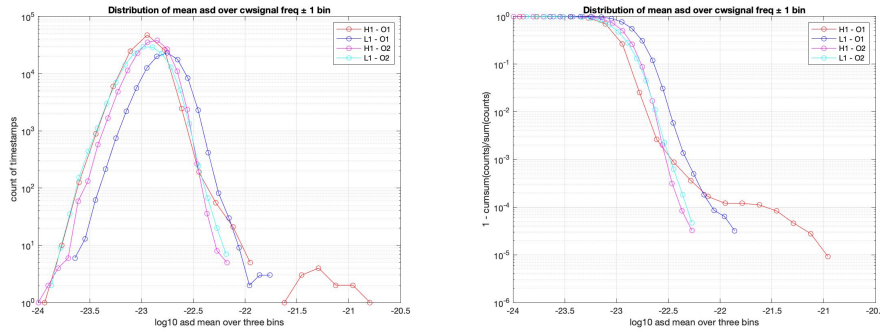


Figure 7.53: Distribution of noise ASD in the continuous gravitational wave signal frequency of J0709+0458 during the O1 and O2 observation runs in the Hanford (H1) and Livingston (L1) detectors, as a function of time.

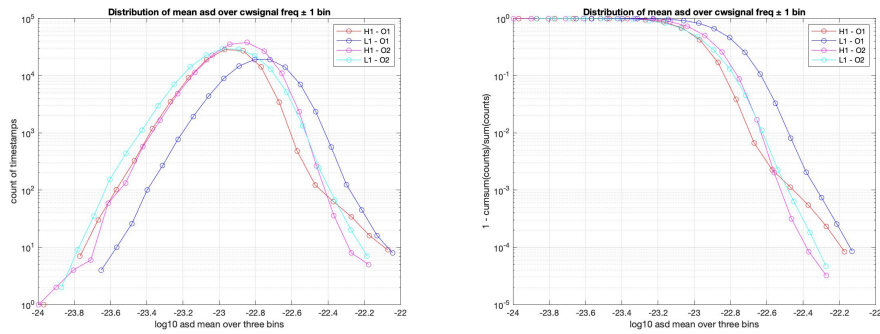


Figure 7.54: Distribution of noise ASD in the continuous gravitational wave signal frequency of J0709+0458 during the O1 and O2 observation runs in the Hanford (H1) and Livingston (L1) detectors, after noise removal, as a function of time.

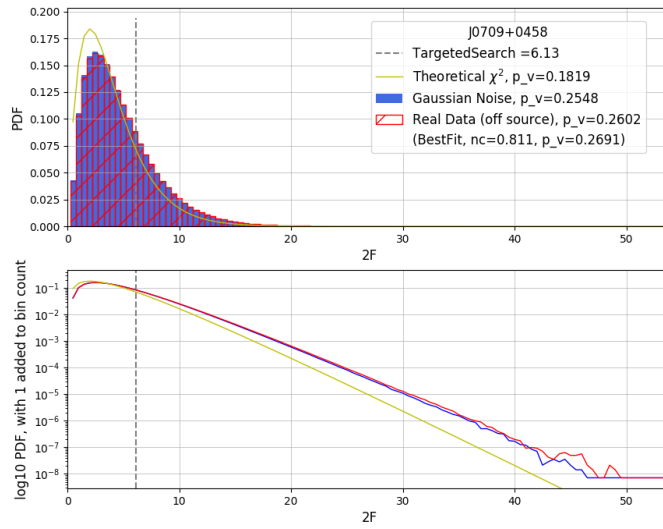


Figure 7.55: Distribution of $2\mathcal{F}$ in a 0.2Hz region around the signal frequency of J0709+0458 in O1O2 data

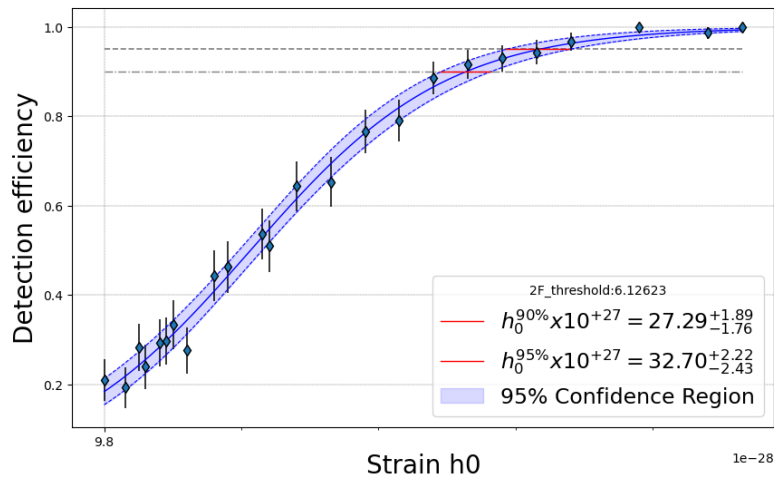


Figure 7.56: Upper limit sigmoid fit for J0709+0458 for O1O2 data

7.7.3 Search In O1O2O3a

The targeted search returned a $2\mathcal{F}=1.6$ and has a p-value of 0.8 calculated with respect to off-source data as shown in figure 7.62.

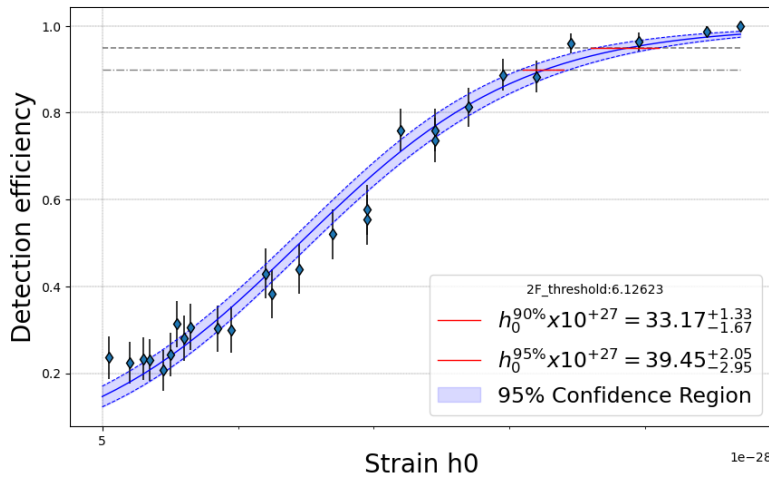


Figure 7.57: Upper limit sigmoid fit for J0709+0458 for O1O2 data – using restricted priors on $\cos \iota$.

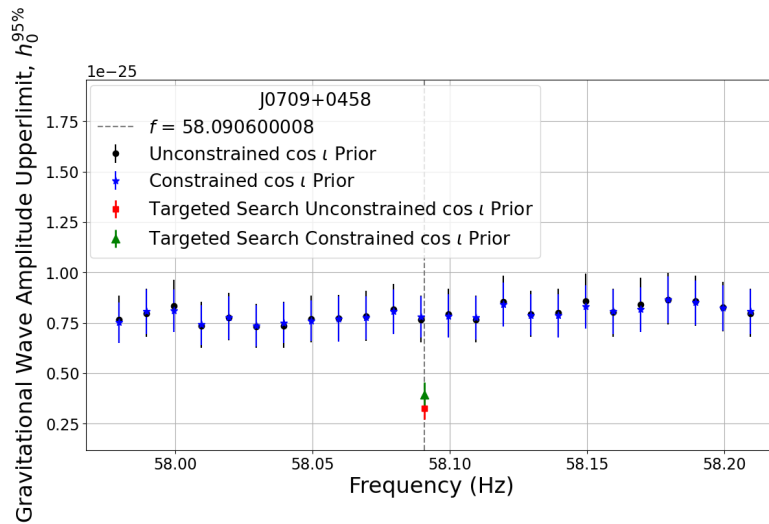


Figure 7.58: O1O2 data h_0 upper limits in 10 mHz frequency subband searched, based on the most significant result in that 10 mHz subband.

A search region of 0.2Hz around the targeted template frequency was probed. The results are consistent with expectations from Gaussian noise as seen in figure 7.62. The p-values of the loudest result in each sub-band is shown in figure 7.63.

The 95% upper limit based on a null detection in the targeted search is $1.5e-26$. This 95% UL is a factor of 10 larger than the spin-down upper limit. The h_0 vs detection efficiency and the sigmoid fit is shown in the left plot of figure 7.64. Using a restricted prior on $\cos \iota$ we set an h_0^{95} of $1.9e-26$. This h_0^{95} is a factor of 12.7 larger than the spin-

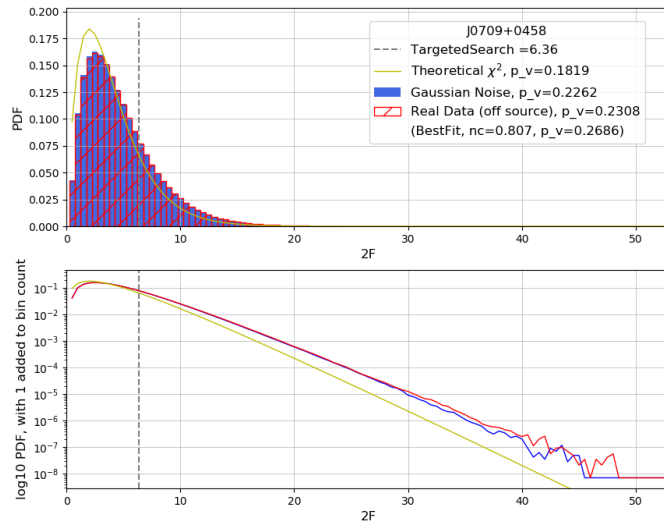


Figure 7.59: Distribution of $2\mathcal{F}$ in a 0.2Hz region around the signal frequency of J0709+0458 in O_3 data

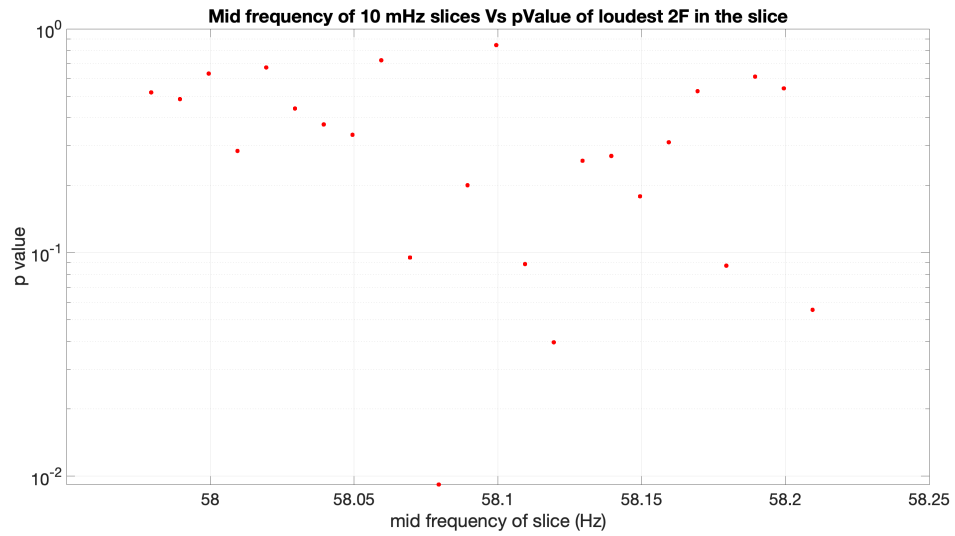


Figure 7.60: p-values of the band search results for J0709+0458 in O_3 data.

down upper limit. The h_0 vs detection efficiency and the sigmoid fit is shown in the right plot of figure 7.64.

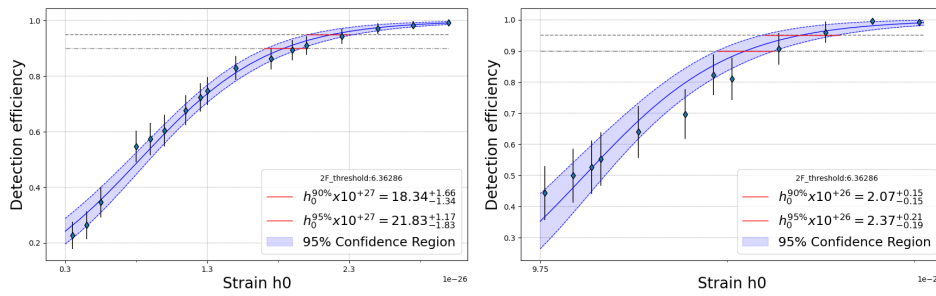


Figure 7.61: Upper limit sigmoid fit for J0709+0458 in O3a data – on the left using non-restricted priors on $\cos i$, on the right using restricted priors on $\cos i$.

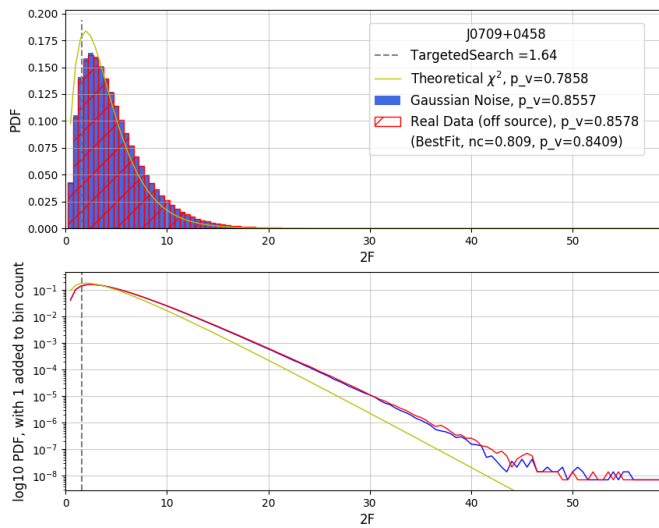


Figure 7.62: Distribution of $2\mathcal{F}$ in a 0.23 Hz region around the signal frequency of J0709+0458 in O1O2O3 data.

7.8 PSR J1411+2551

PSR J1411+2551 is in a binary orbit with another neutron star, forming the lightest known to date double neutron star system. Pulsations from the companion neutron star have not been detected yet. It has been mildly recycled by accretion of matter from the progenitor of the companion star and has a gravitational wave frequency of 32 Hz.

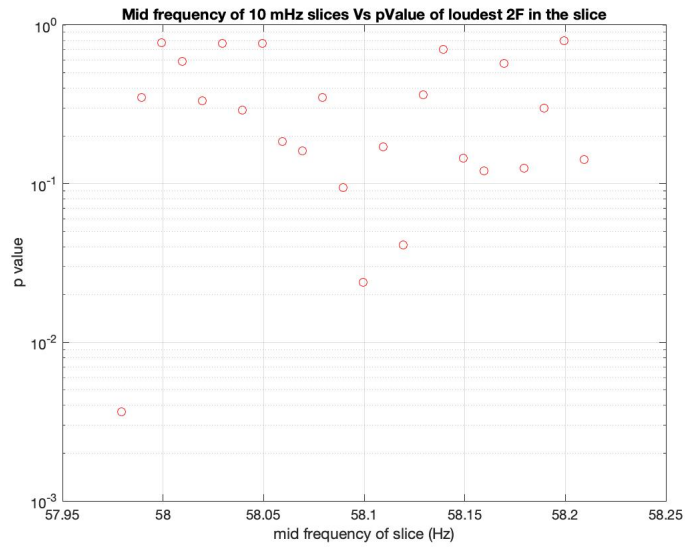


Figure 7.63: p-values of the band search results for J0709+0458 in O1O2O3

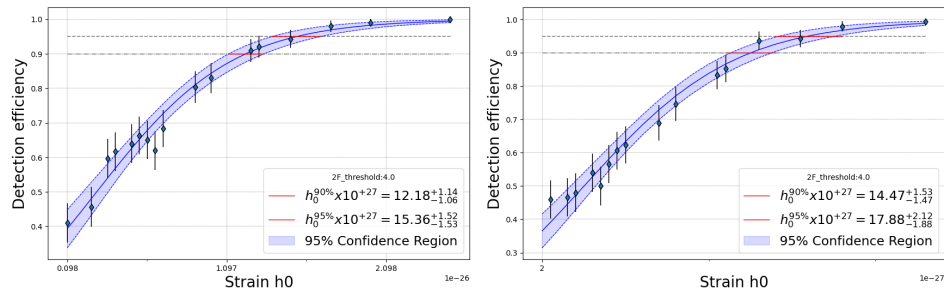


Figure 7.64: Upper limit sigmoid fit for J0709+0458 in O1O2O3 data – on the left using non-restricted priors on $\cos i$, on the right using restricted priors on $\cos i$.

7.8.1 Search In O1O2

The targeted search returned a $2\mathcal{F}=1.8$ and has a p-value of 0.8 calculated with respect to off-source data as shown in figure 7.65. A band of 0.13 Hz around the signal frequency was probed for gravitational wave emission slightly offset from the twice the spin frequency, but no significant results were found.

The 95% upper limit based on a null detection in the targeted search is $5.2e-26$. This h_0^{95} is a factor of 48 larger than the spin-down upper limit. The h_0 vs detection efficiency and the sigmoid fit is shown in figure 7.66. Using a restricted prior on $\cos i$ we set an h_0^{95} of $3.6e-26$. This h_0^{95} is a factor of 32.9 larger than the spin-down upper limit as shown on the right plot in figure 7.66.

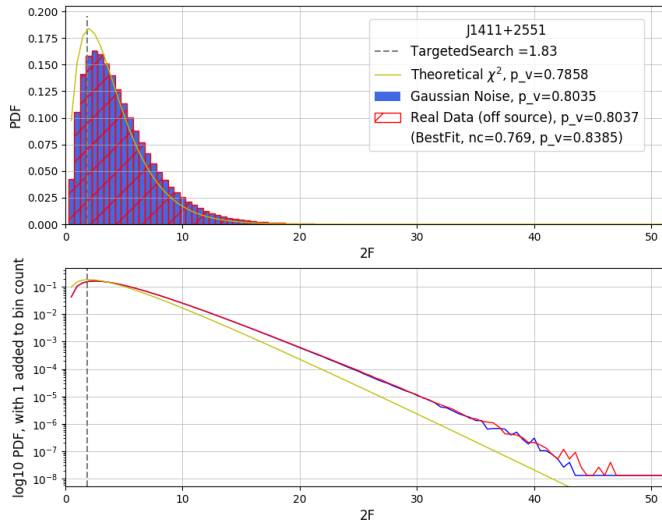


Figure 7.65: Distribution of $2\mathcal{F}$ in a 0.13Hz region around the signal frequency of J1411+2551 in O1O2 data

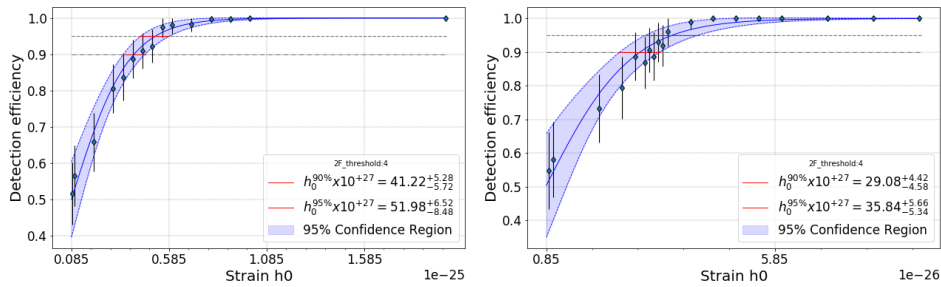


Figure 7.66: Upper limit sigmoid fit for J1411+2551 for O1O2 data – on the left using non-restricted priors on $\cos \iota$, on the right using restricted priors on $\cos \iota$.

The band search upper limits are presented in figure 7.67, with both unrestricted and restricted priors on $\cos \iota$.

7.8.2 Search In only O3a

The targeted search returned a $2\mathcal{F}=3.6$ and has a p-value of 0.5 calculated with respect to off-source data. Figure 7.68 shows the distribution of $2\mathcal{F}$ in this off-source band search and the p-value of the targeted search result.

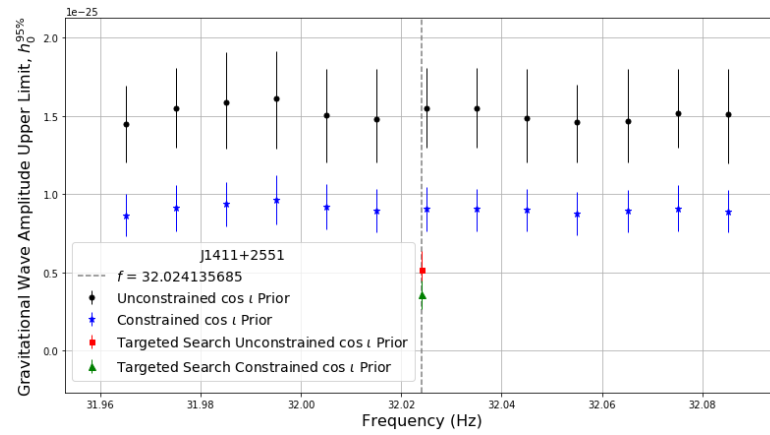


Figure 7.67: O1O2 data h_0 upper limits in 10 mHz frequency sub-bands searched, based on the most significant result in that 10 mHz sub-band.

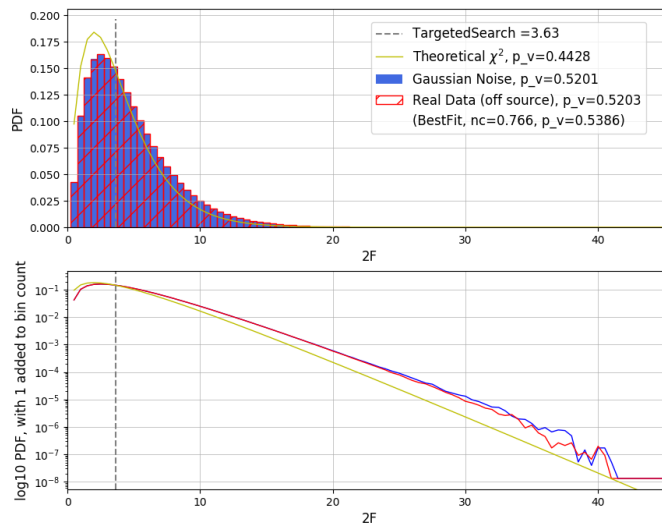


Figure 7.68: Distribution of $2\mathcal{F}$ in a 0.13 Hz region around the signal frequency of J1411+2551 in O3a data.

A band search in 0.13 Hz around the targeted template frequency in O3a yielded results that are consistent with expectations from Gaussian noise as seen in figure 7.68. The p-values of the loudest result in each sub-band is shown in figure 7.69.

The 95% upper limit based on a null detection in the targeted search is $3.9\text{e-}26$. This h_0^{95} is a factor of 35.7 larger than the spin-down upper limit. The h_0 vs detection efficiency and the sigmoid fit is shown in figure 7.70. Using a restricted prior on $\cos i$

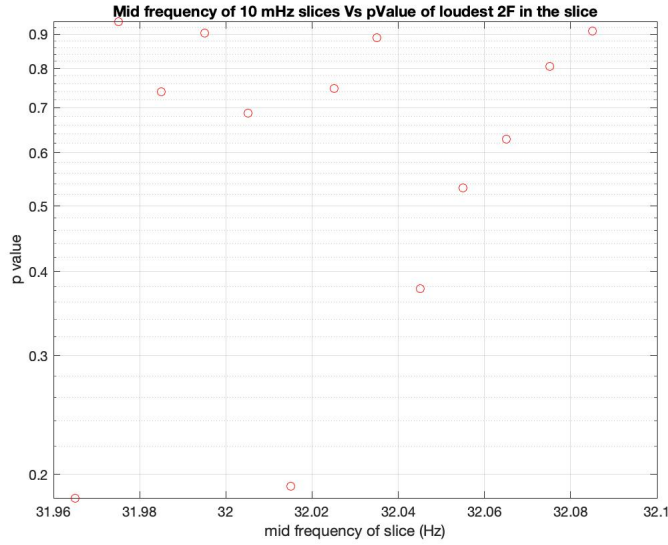


Figure 7.69: p-values of the band search results for J1411+2551 in O3 data.

we set an h_0^{95} of $2.7e-26$. This h_0^{95} is a factor of 25.1 larger than the spin-down upper limit. The h_0 vs detection efficiency and the sigmoid fit are shown in the right panel of figure 7.70.

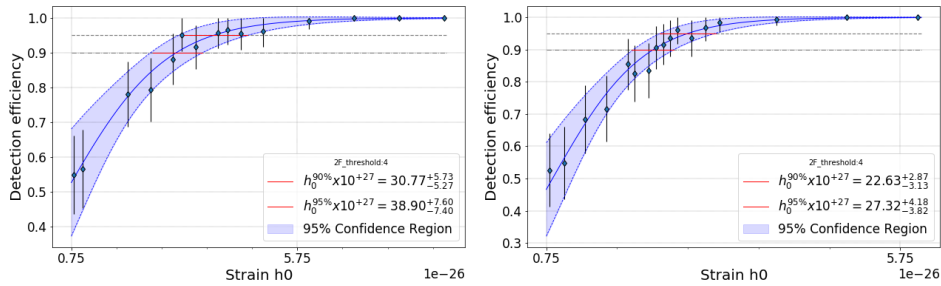


Figure 7.70: Upper limit sigmoid fit for J1411+2551 for O3a data – on the left using non-restricted priors on $\cos i$, on the right using restricted priors on $\cos i$.

7.8.3 Search In O1O2O3a

The targeted search returned a $2\mathcal{F}=4.2$ and has a p-value of 0.4 calculated with respect to off-source data as shown in figure 7.71.

A search region of 0.13Hz around the targeted template frequency was probed. The results are consistent with expectations from Gaussian noise as seen in figure 7.71 and the p-values of loudest results in 10mHz sub-bands are in figure 7.72.

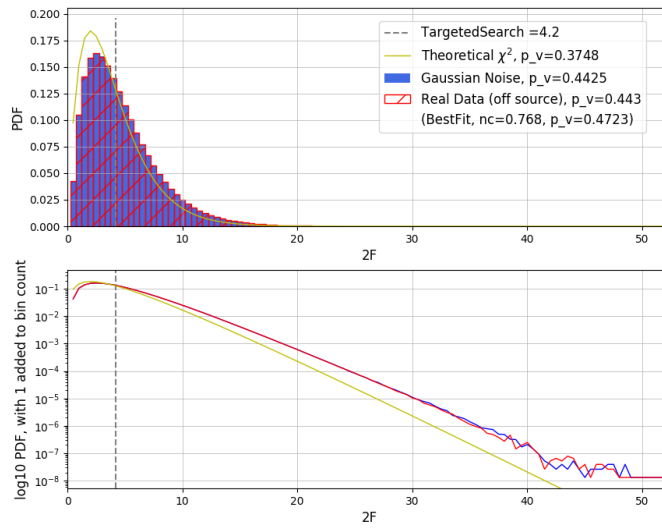


Figure 7.71: Distribution of $2\mathcal{F}$ in a 0.1 Hz region around the signal frequency of J1411+2551 in O1O2O3 data.

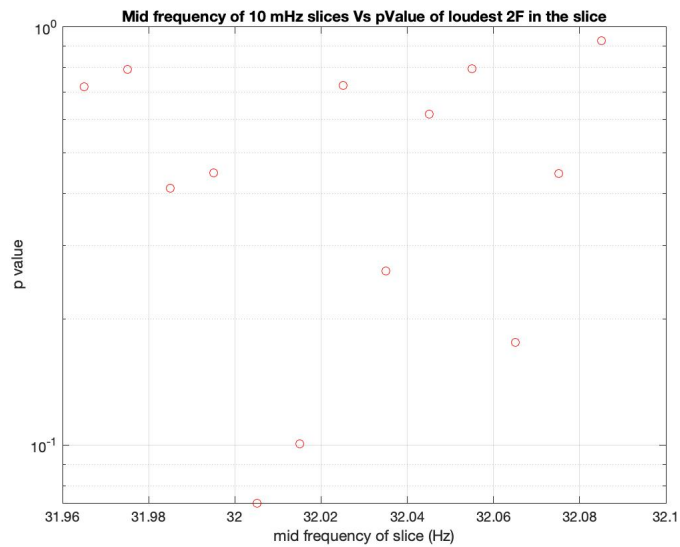


Figure 7.72: p-values of the band search results for J1411+2551 in O1O2O3 data.

The 95% upper limit based on a null detection in the targeted search is $3.1e-26$. This 95% UL is a factor of 28 larger than the spin-down upper limit. The h_0 vs detection efficiency and the sigmoid fit is shown in the left plot of figure 7.73. Using a restricted

prior on $\cos \iota$ we set an h_0^{95} of $2.2e-26$. This h_0^{95} is a factor of 19.9 larger than the spin-down upper limit. The h_0 vs detection efficiency and the sigmoid fit are shown in right plot of figure 7.73.

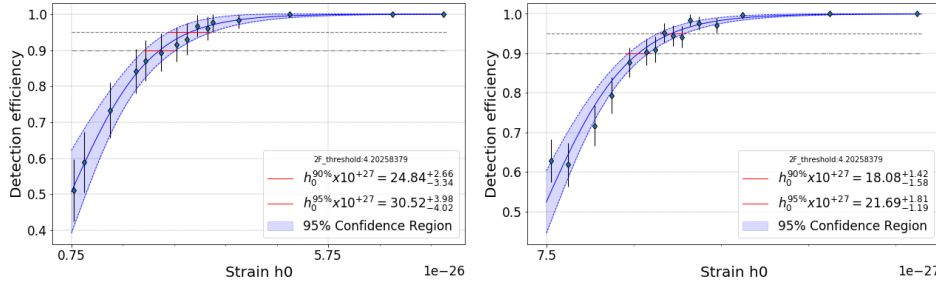


Figure 7.73: Upper limit sigmoid fit for J1411+2551 for O1O2O3a data – on the left using non-restricted priors on $\cos \iota$, on the right using restricted priors on $\cos \iota$.

7.9 PSR J2204+2700

PSR J2204+2700 is the farthest pulsar in the set, at a distance of 2.15kpc. It is also a mildly recycled pulsar giving it a gravitational wave frequency of 23 Hz. Its low signal frequency and large distance put it on the opposite end of PSR J0154, lending it the least constraining h_0^{95} upper limits, two order of magnitude larger than its spin-down upper limit.

7.9.1 Search In O1O2

The targeted search returned a $2\mathcal{F}=0.98$ and has a p-value of 0.9 calculated with respect to off-source data as shown in figure 7.74. A band search of 0.1Hz yielded no significant results. The significance of the loudest results in 10mHz bands can be inferred from the band-search upper limits in figure 7.76.

The 95% upper limit based on a null detection in the targeted search is $1.5e-25$. This h_0^{95} is a factor of 319 larger than the spin-down upper limit. The h_0 vs detection efficiency and the sigmoid fit is shown in figure 7.75.

7.9.2 Search In only O3a

The targeted search returned a $2\mathcal{F}=2.7$ and has a p-value of 0.7 calculated with respect to off-source data. Figure 7.77 shows the distribution of $2\mathcal{F}$ in this off-source band search and the p-value of the targeted search result.

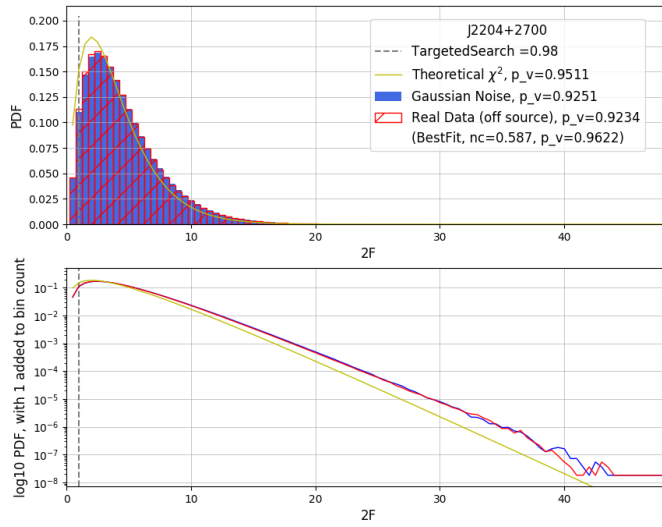


Figure 7.74: Distribution of $2\mathcal{F}$ in a 0.1Hz region around the signal frequency of J2204+2700 in O1O2 data

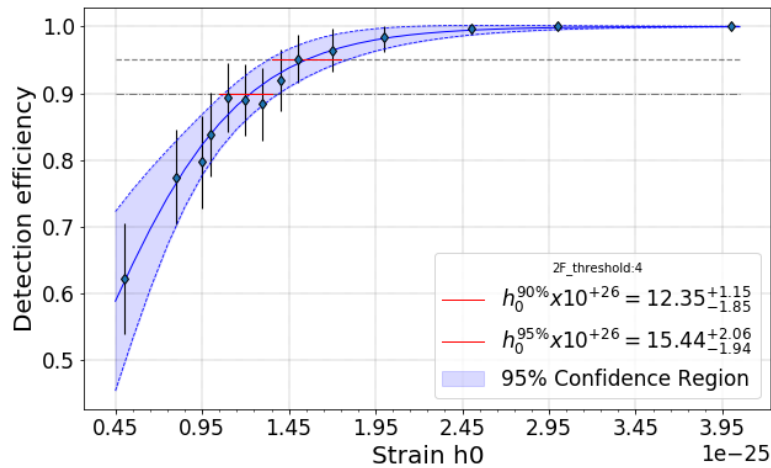


Figure 7.75: Upper limit sigmoid fit for J2204+2700 for O1O2 data

A band search in 0.1 Hz around the targeted template frequency in O3a yielded results that are consistent with expectations from Gaussian noise as seen in figure 7.77. The p-values of the loudest result in each sub-band is shown in figure 7.78.

The 95% upper limit based on a null detection in the targeted search is $9.9e-26$. This h_0^{95} is a factor of 204.0 larger than the spin-down upper limit. The h_0 vs detection efficiency and the sigmoid fit is shown in figure 7.79.

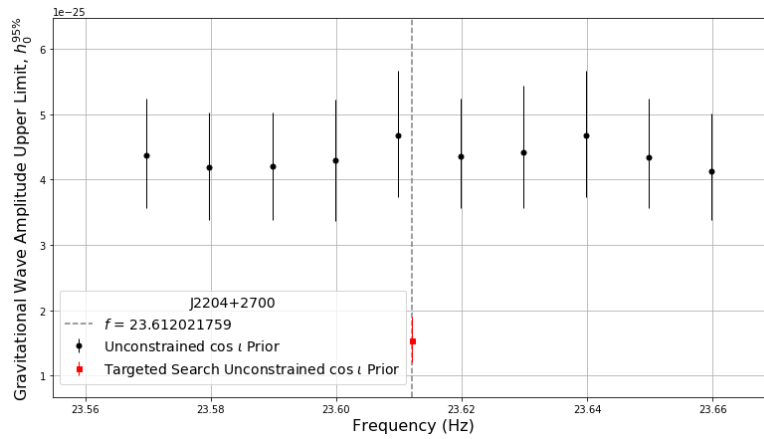


Figure 7.76: O1O2 data h_0 upper limits in 10 mHz frequency subband searched, based on the most significant result in that 10 mHz subband.

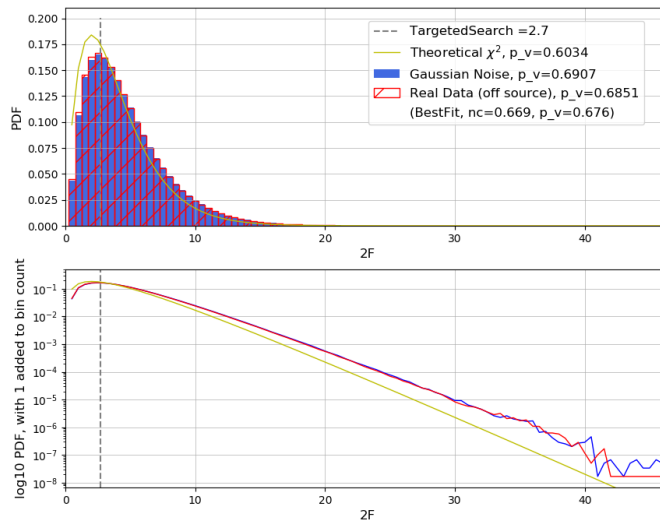


Figure 7.77: Distribution of $2\mathcal{F}$ in a 0.1Hz region around the signal frequency of J2204+2700 in O3 data

7.9.3 Search In O1O2O3a

The targeted search returned a $2\mathcal{F}=1.8$ and has a p-value of 0.8 calculated with respect to off-source data as shown in figure 7.80.

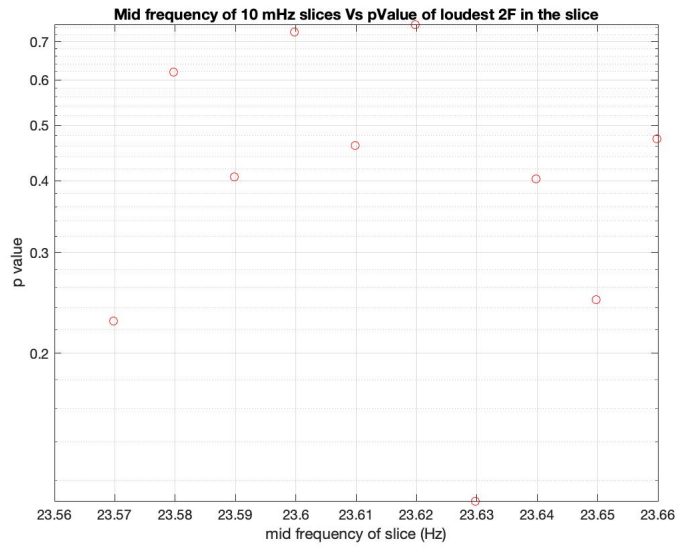


Figure 7.78: p-values of the band search results for J2204+2700 in O₃ data.

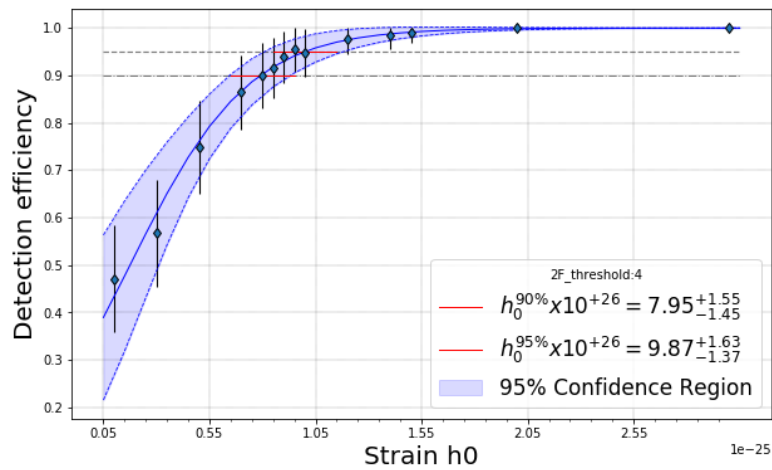


Figure 7.79: Upper limit sigmoid fit for J2204+2700 for O₃ data

A search region of 0.1Hz around the targeted template frequency was probed. The results are consistent with expectations from Gaussian noise as seen in figure 7.80. The p-values of the loudest result in each sub-band is shown in figure 7.72.

The 95% upper limit based on a null detection in the targeted search is $8.1e-26$. This 95% UL is a factor of 166 larger than the spin-down upper limit. The h_0 vs detection efficiency and the sigmoid fit is shown in figure 7.82.

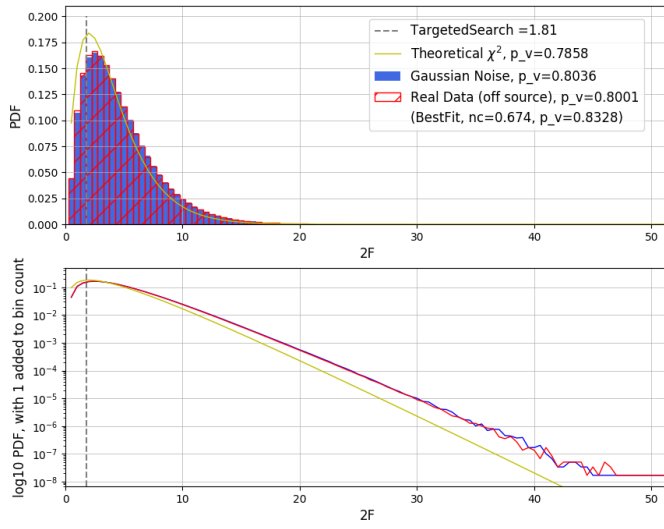


Figure 7.80: Distribution of $2\mathcal{F}$ in a 0.09 Hz region around the signal frequency of J2204+2700 in O1O2O3 data.

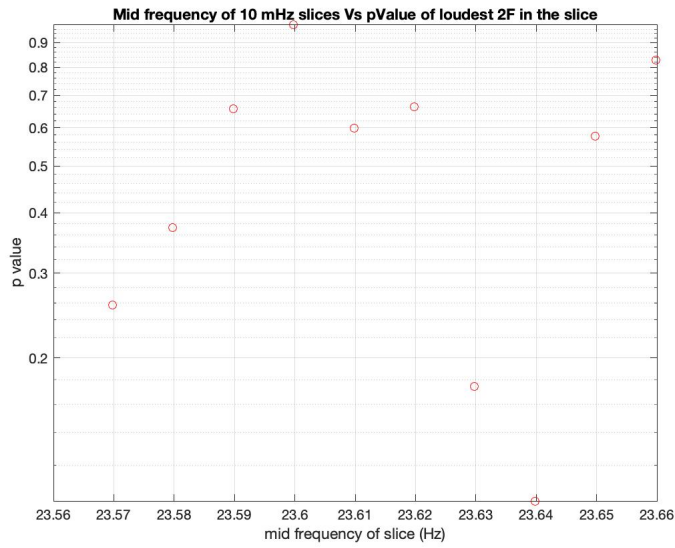


Figure 7.81: p-values of the band search results for J2204+2700 in O1O2O3 data.

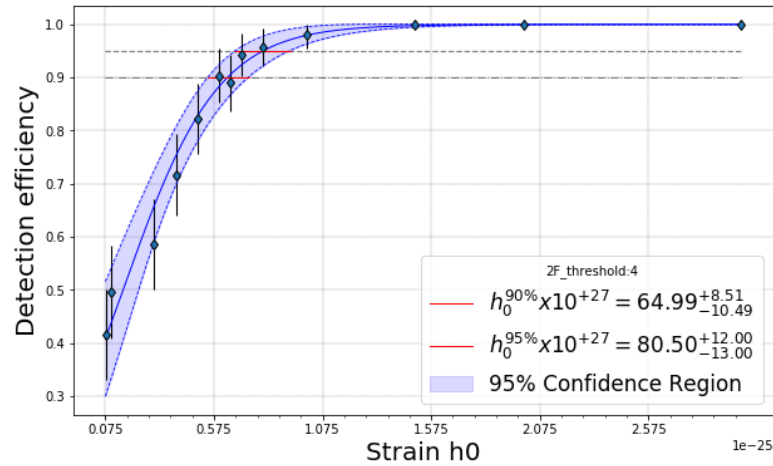


Figure 7.82: Upper limit sigmoid fit for J2204+2700 in O1O2O3 data.

7.10 COMBINED ANALYSIS FOR ARECIBO PULSARS

In this section, we see all the search results in different data sets for pulsars from Section 7.3 to 7.9 in one place. These are in figure 7.83. First, the plots on the left-hand side of 7.83 simply show the p-values of all the search results. The significance of band search results (red) are generally higher than that of the targeted search p-values because they are maxima over 10 mHz, whereas the targeted searches probe only a single waveform. Next, as mentioned in chapter 5, when we want to check if the band search result for any pulsar is significant, we compare the loudest results from their searches. These are the normalised p-values. The red circles in the right-side plots show for each pulsar the lowest p-value amongst the sub-bands rescaled according to equation 5.23, s^α . When $s^\alpha \leq 1$ it can be directly interpreted as p-value. When $s^\alpha > 1$ it represents the number of 10 mHz sub-bands in which we would expect, in a band search of Gaussian noise data like that performed for pulsar α , to measure a result more significant than the most significant found in real data. In either case, the lowest rescaled p-value can be taken as a measure of the significance of the band-search results for each pulsar and compared with that of other pulsars. Then we look at the cumulative distribution of the p-values from all 10 mHz band search results for these pulsars and compare it against the expectation in Gaussian noise in figure 7.84. Had there been a detected signal, it would show up in this plot with very low p-values.

The most significant targeted-search result comes from PSR J0709+0458 from the O3 data search, with a p-value of $\approx 23\%$. The product of the $\approx 55\%$ p-value of the O1O2 result and the O3 result is $\approx 12\%$, however the coherent O1O2O3 data search yields a totally insignificant p-value of $\approx 83\%$. The most significant result from the band searches comes again from PSR J0709+0458 in the O1O2O3 coherent search and is

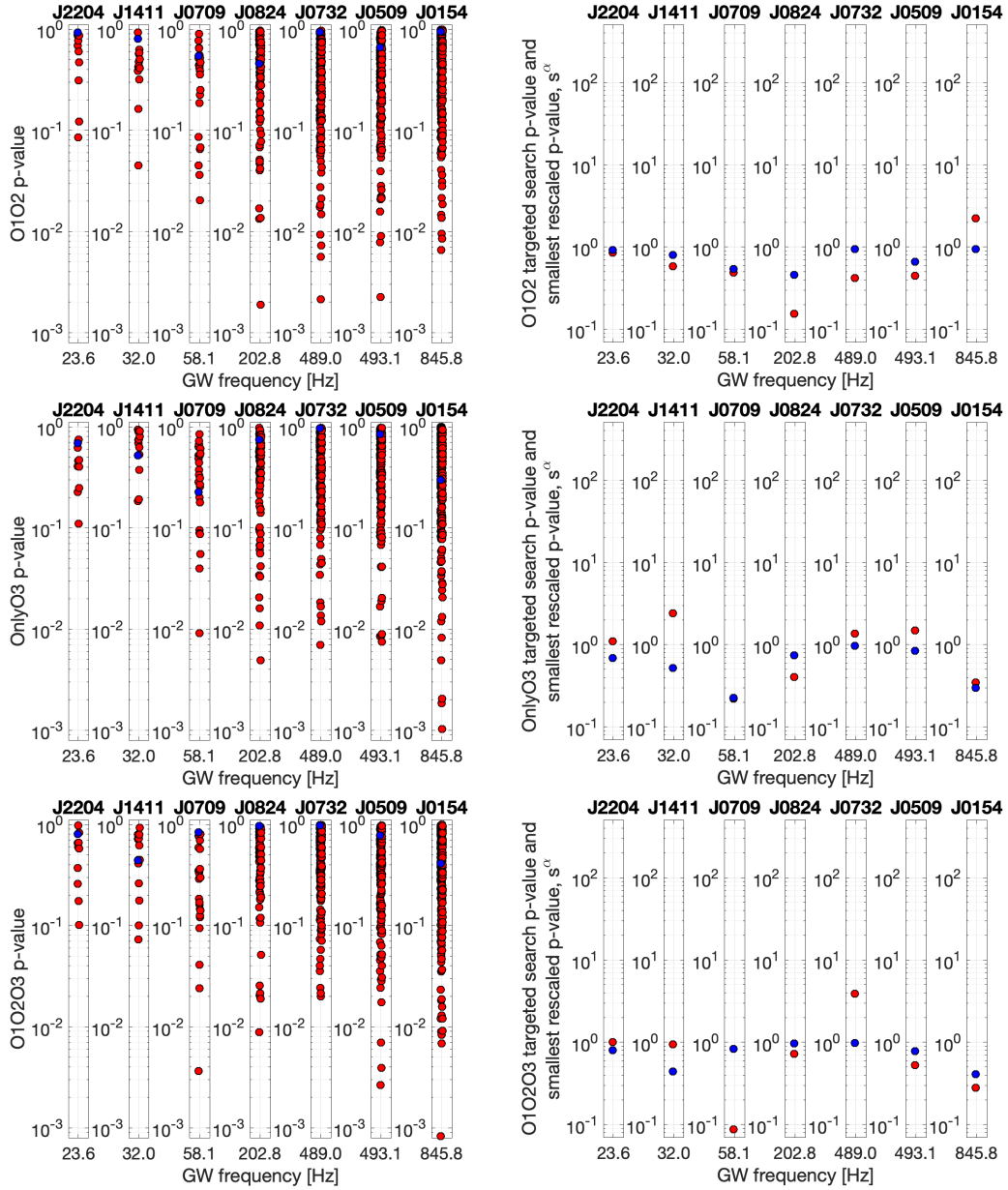


Figure 7.83: O₁O₂ (1st row), O₃ (2nd row) and O₁O₂O₃ (3rd row) results. The blue circles show the p-values of the targeted searches. The red circles in the left-side plots show the p-value of the most significant result in each 10 mHz sub-band of the band searches. Figure from (Ashok et al., 2021).

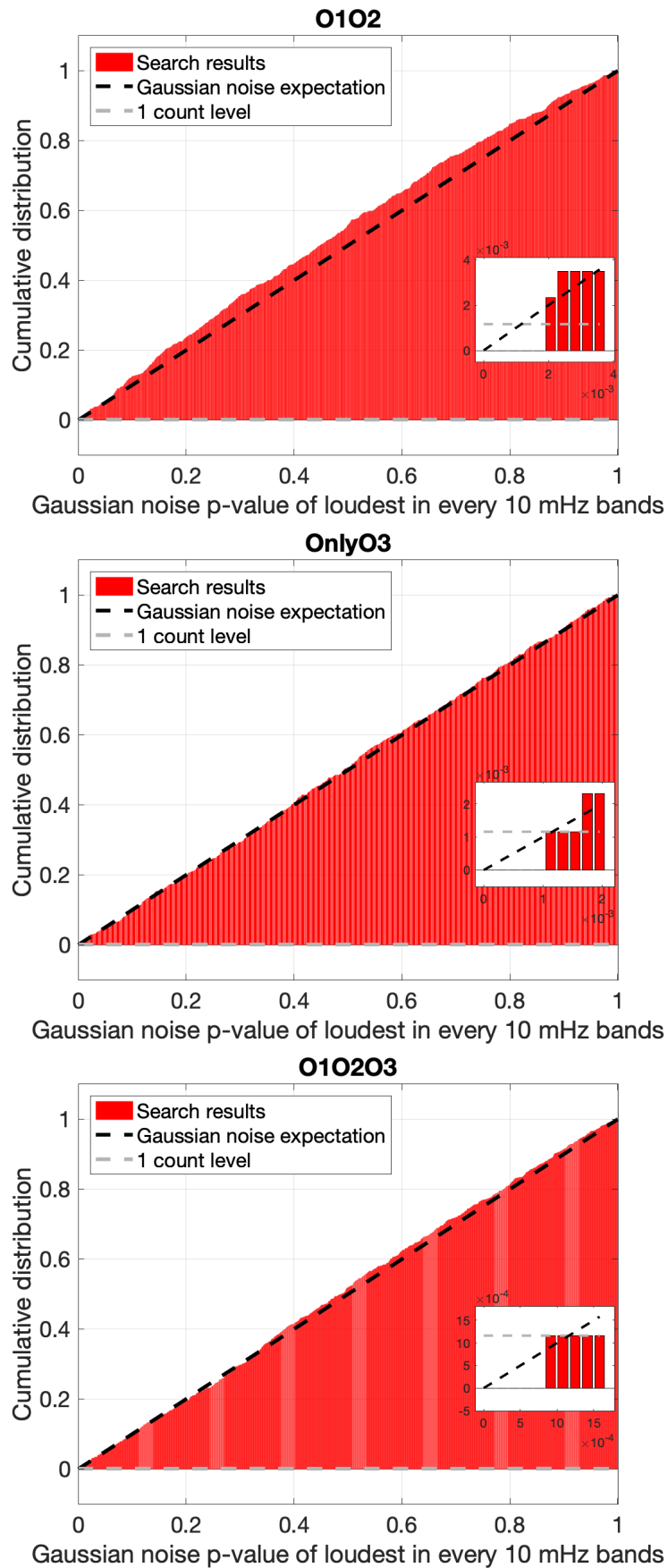


Figure 7.84: O₁O₂, O₃ and O₁O₂O₃ band-search results. For each 10 mHz frequency band searched, we show the cumulative distribution of the Gaussian p-value of the most significant result. If the data were Gaussian noise, the distribution would follow the dashed black line. Figure from (Ashok et al., 2021).

at the level of $\approx 9\%$. However, this significance is not confirmed in the O₃ data where the lowest p-value (s^{J0709}) is 22% and it is at a different sub-band than the one that produced the O₁O₂O₃ most significant result as seen in Figure 7.60. PSR J0709+0458 has a timing solution that is based on observations that completely bracket all the Advanced LIGO data (Figure 7.1) – so there are no observed irregularities in its spin parameters. Note that the target frequency for PSR J0709+0458 is at $\approx 58\text{Hz}$, which is a highly contaminated region. In any case, a detection should have a p-value of the order of 10^{-5} followed by other channels of confirmations independent from the p-value method.

7.11 PSR J1526-2744

J1526-2744 was discovered first as a faint gamma-ray source in Fermi-LAT data. With dedicated observations using MeerKAT telescope, the TRAPUM collaboration confirmed its identity as a binary pulsar and constrained the positions, orbital semi-major axis and time of ascending node of the system (Clark et al., 2023). But the spin-down rate was not measurable. A search for gamma-ray pulsations in Fermi-LAT data incorporating the new parameters constraints resulted in a measurement of spin-down and a precise 13-year timing solution for the pulsar, covering the Advanced LIGO observation runs. Based on this gamma-ray timing solution, we carried out searches for continuous gravitational wave signals.

With a gravitational wave frequency of 803 Hz, PSR J1526-2744 occupies a fairly uncontaminated frequency region in the Advanced LIGO detectors. Data from all of the observation runs till date (O₁,O₂,O₃) were publicly available at the time of the search – so for this pulsar, we carried out the most sensitive search possible.

The targeted search returned a $2\mathcal{F}=5.6$. Figure 7.85 is a first look at the search result set against the distribution of the detection statistics in a 0.1mHz band around the targeted frequency. The $2\mathcal{F}$ value lies in the bulk of the distribution and clearly points to a non-detection of the signal.

Figure 7.89 shows the cumulative distribution of p-value. The absence of a spike of low p-values would indicates that there is no detection.

This result has a p-value of 29%, estimated using off-source data of 3.2Hz bandwidth.

A search region of 3.2Hz around the targeted template frequency was probed. One spin down template on each side of the targeted template spin down was probed. The resolutions in frequency, and spin-down parameter space are:

$$df = 1.09 \times 10^{-9} \text{Hz} \quad (7.4)$$

$$d\dot{f} = 9.23 \times 10^{-18} \text{Hz/s} \quad (7.5)$$

This grid gives a mean mismatch of 1% in an O₁O₂O₃ search. The loudest $2\mathcal{F}$ in 10mHz slices of the full band (3.2Hz) are treated to be the results of the band search.

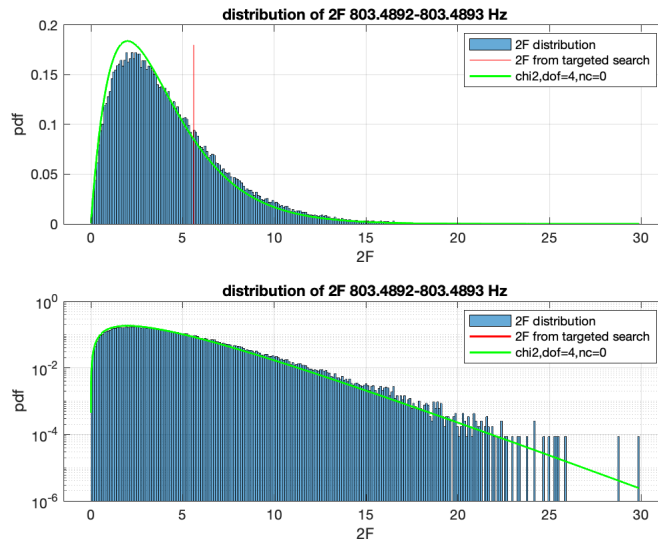


Figure 7.85: Distribution of $2\mathcal{F}$ in a 0.1mHz region around the expected signal frequency for J1526-2744 . The $2\mathcal{F}$ from the targeted search is in red. The theoretically expected distribution of $2\mathcal{F}$ in Gaussian Data is plotted in green. The bottom panel shows the y-axis in a log scale.

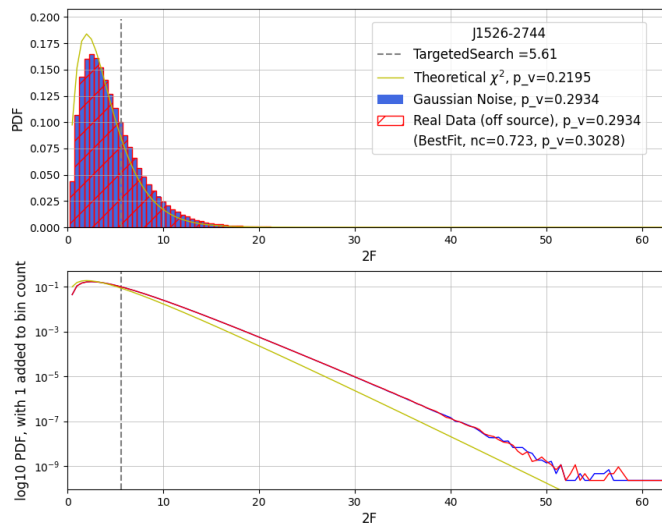


Figure 7.86: Distribution of $2\mathcal{F}$ in a 3.2Hz region around the expected signal frequency for J1526-2744 . The bottom panel shows the y-axis in a log scale.

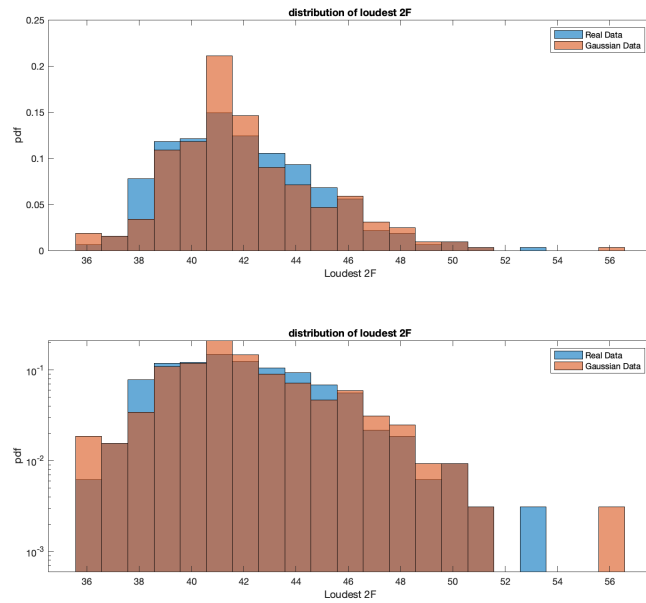


Figure 7.87: Distribution of band search results in real data and Gaussian noise.

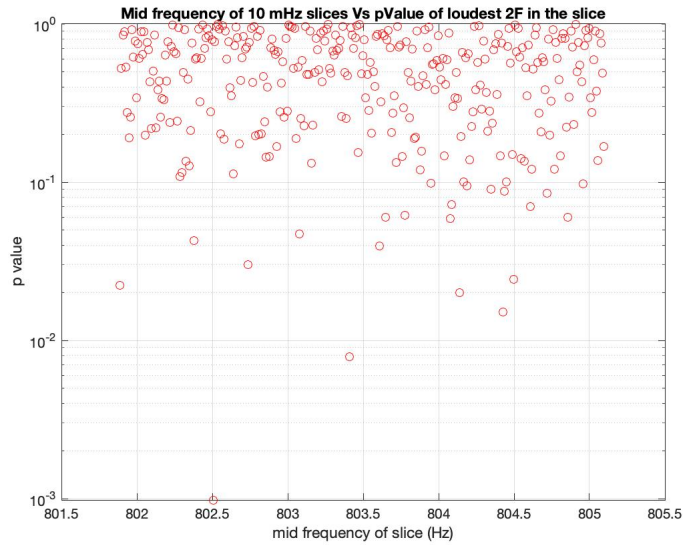


Figure 7.88: p-values of the band search results.

The distribution of this loudest $2\mathcal{F}$ from search in real data is found to be consistent with expectations in Gaussian noise in figure 7.87.

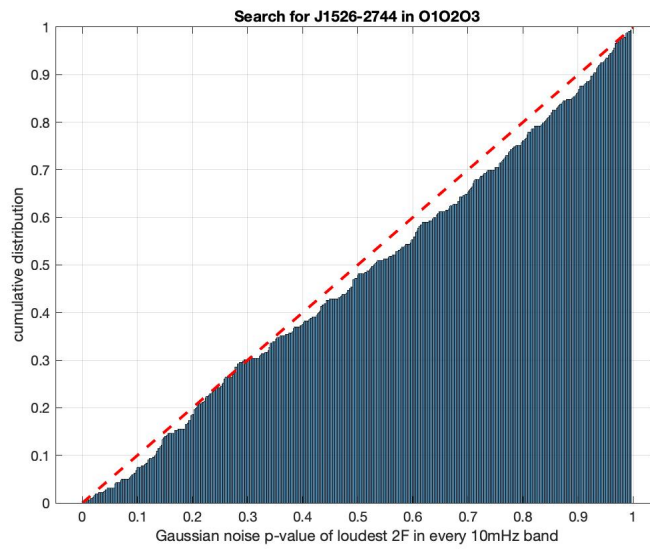


Figure 7.89: Cumulative distribution of p-values of band search results. The expectation in Gaussian noise is plotted as red-dashed line.

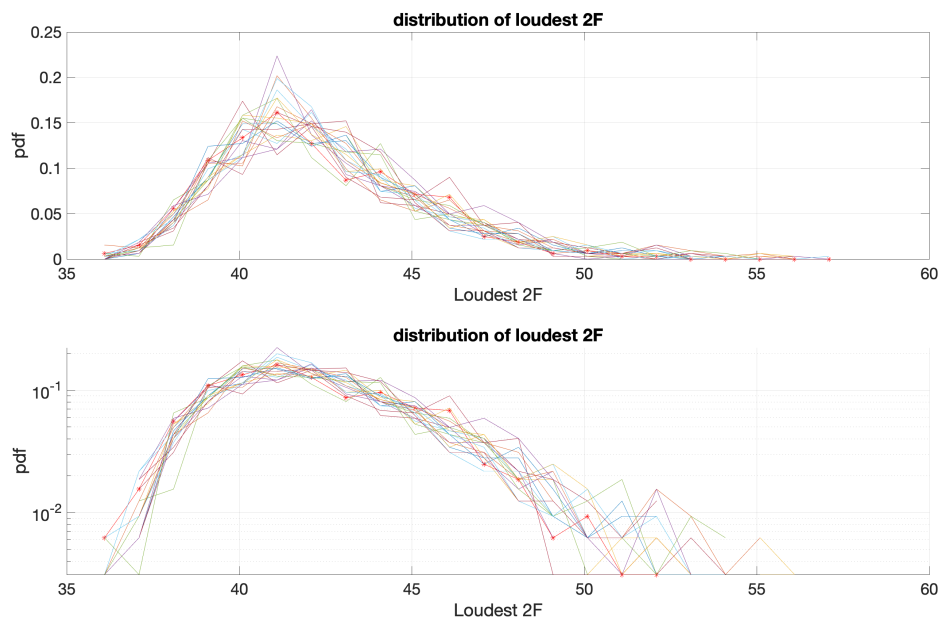


Figure 7.90: Distribution of the band-search results in real data plotted as red stars compared with results in band search in 20 realisations of Gaussian noise. The results from different Gaussian noise realisations are in different colours.

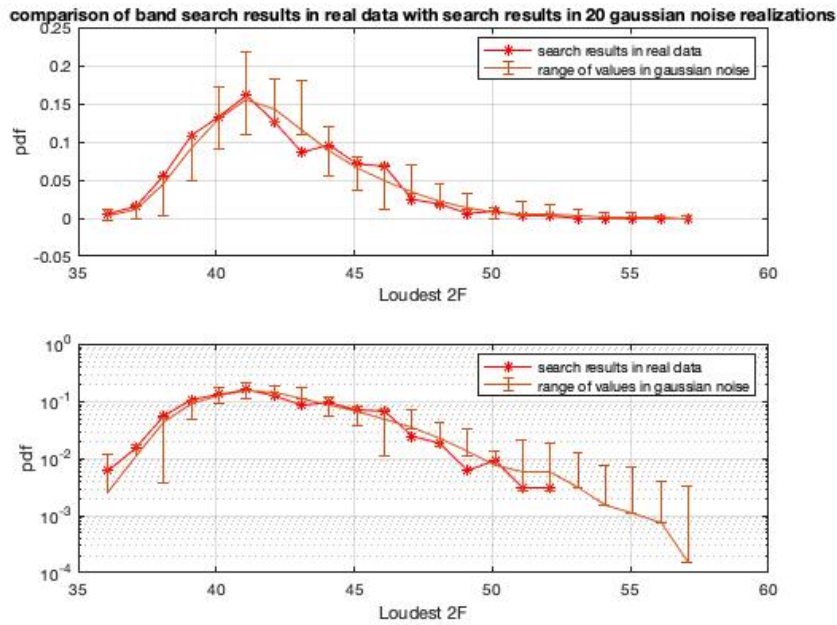


Figure 7.91: The mean and range of the distribution of loudest $2\mathcal{F}$ in a large number of realisations of Gaussian noise compared with the actual search results. The bottom plot has a log scale on y-axis.

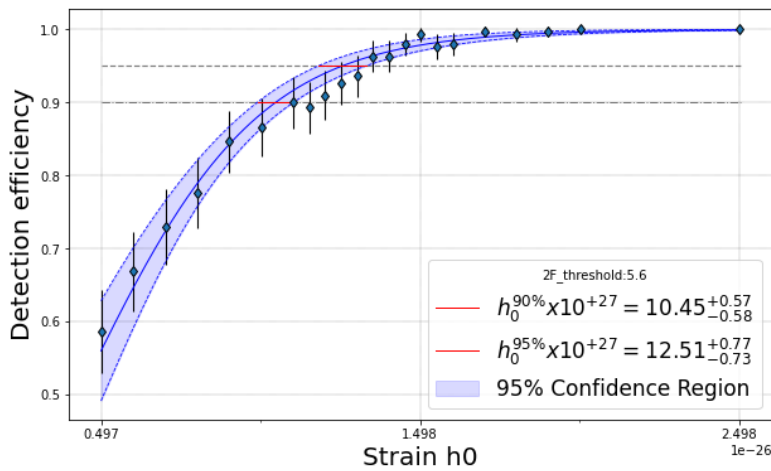


Figure 7.92: Upper limit sigmoid fit for J1526-2744 .

The significance of the band search results in real data is expressed in terms of their p-values with respect to a reference distribution of such results in Gaussian noise, as described in chapter 5. The p-values of the loudest result in each sub-band are shown in figure 7.88.

Taking this check one step further, we ask if we can conclude that the band search results do not deviate from expectations in Gaussian noise. To check this, we compare the loudest $2\mathcal{F}$ s from searching in real data against the loudest $2\mathcal{F}$ s from searching in 20 realisations of Gaussian noise in figure 7.90 and are further convinced that the results from both types of data are indistinguishable. In figure 7.91, the mean value of the distribution of loudest $2\mathcal{F}$ in 20 realisations of Gaussian noise is found to be consistent with the results in real data for the most part and falls within the error bar in other cases. Note, in the bottom plot, the last 5 bins contain no counts in real data.

The 95% upper limit based on a null detection in the targeted search is 1.25×10^{-26} . This 95% UL is a factor of 17 larger than the spin-down upper limit. The h_0 vs detection efficiency and the sigmoid fit are shown in figure 7.92.

7.11.1 Bayesian results

J1526-2744 is the first pulsar for which we carried out an alternative search using the Bayesian method described in chapter 6. We probe the full prior range for $\cos \iota$, ψ and ϕ_0 . For h_0 the prior range is $[1 \times 10^{-28}, 1 \times 10^{-24}]$, probing below the spin down upper limit of the pulsar and several orders of magnitude above it. Figure 7.93 shows the resulting posterior distributions on the signal parameters. The h_0 posterior peaks at the lowest end of the prior range and is consistent with expectations from noise. Since there is no detection of a signal, the posteriors for all the other signal parameters are non-informative.

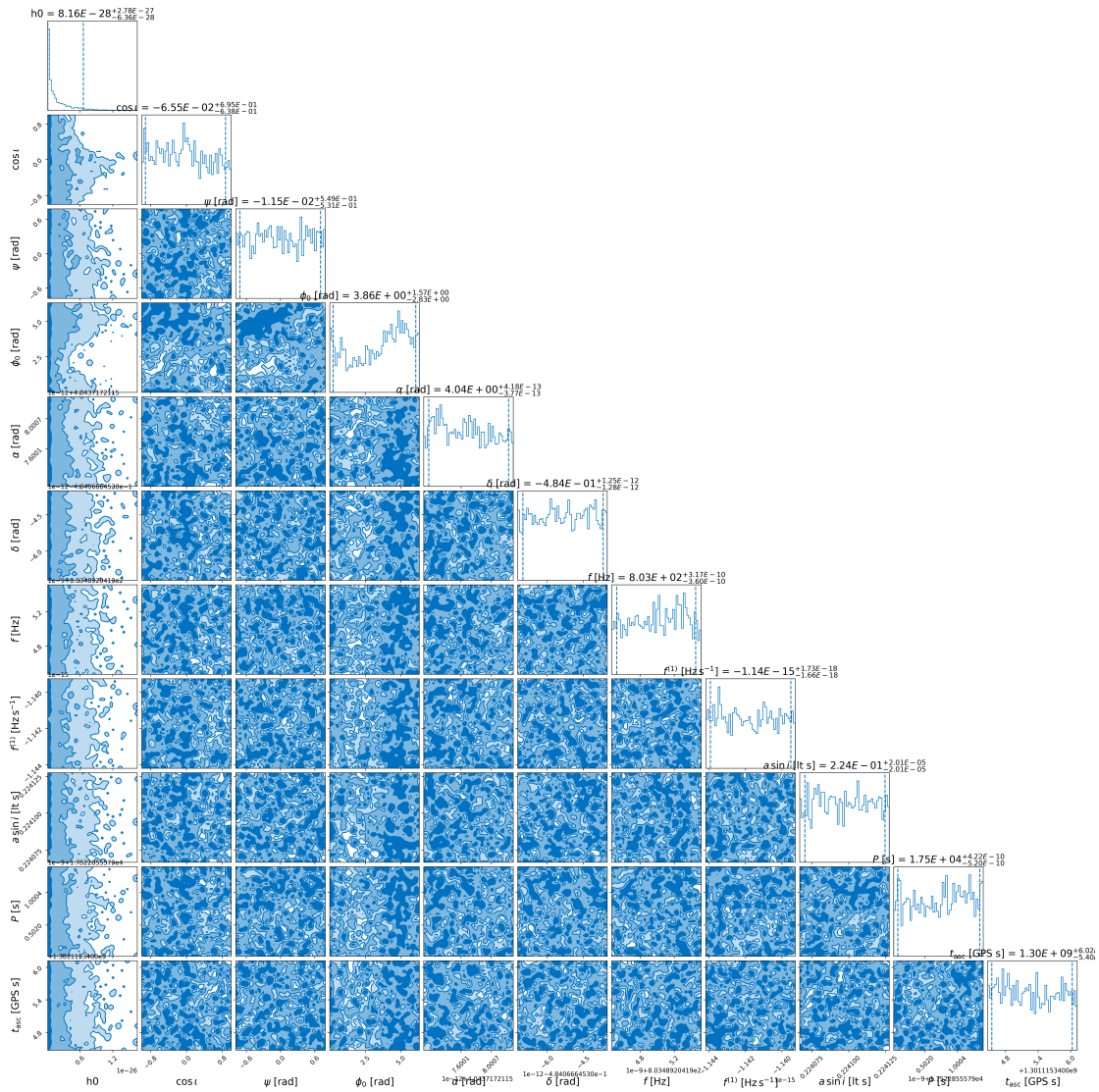


Figure 7.93: Bayesian posterior distributions of signal parameter for J1526-2744 .

The remaining results are from gamma-ray pulsars discovered and timed using the Fermi-LAT data by Colin Clark et.al. The continuous gravitational wave searches are based on preliminary timing solutions for them.

7.12 J1139-6247

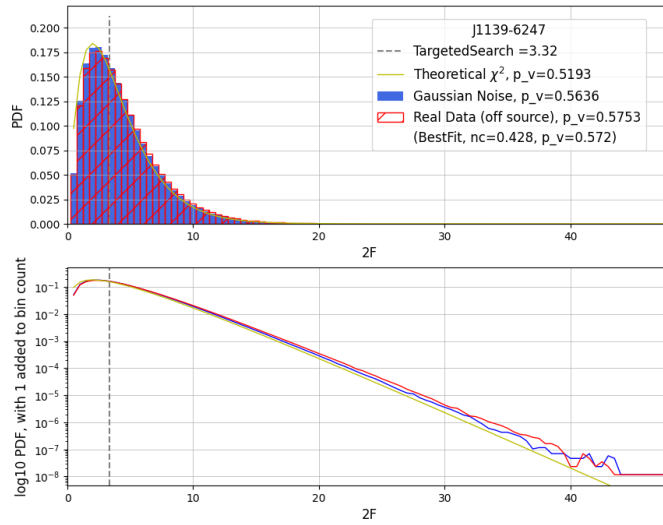


Figure 7.94: Distribution of $2\mathcal{F}$ in a 0.07 Hz region around the signal frequency of J1139-6247 in O1O2O3a data

For this pulsar, results from a preliminary search in a coherent combination of O1, O2 and O3A data sets are presented here. The targeted search returned a $2\mathcal{F}=3.3$ and has a p-value of 0.58 calculated with respect to off-source data as shown in figure 7.94.

The distribution of the loudest $2\mathcal{F}$ s from the band search is shown in figure 7.95. To compare, the results from searching in Gaussian noise are plotted as well. The figure shows that the search results are consistent with those from Gaussian noise.

The 95% upper limit based on a null detection in the targeted search is 7.8×10^{-25} . This h_0^{95} is a factor of 12 larger than the spin-down upper limit. The h_0 vs detection efficiency and the sigmoid fit is shown in figure 7.96.

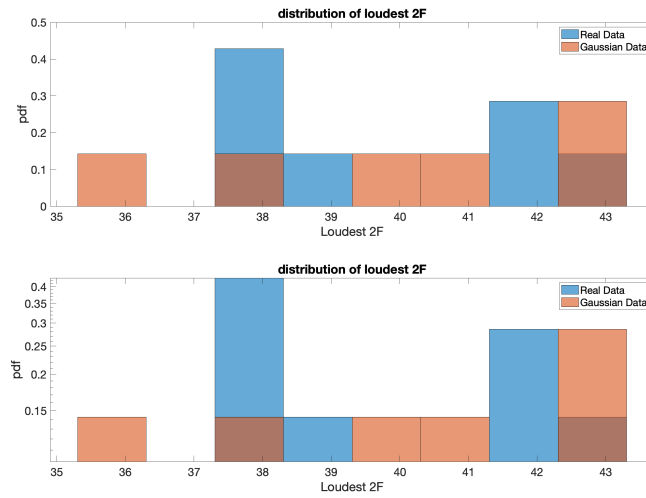


Figure 7.95: Distribution of loudest $2\mathcal{F}$ in 10mHz sub-bands in real O1O2O3a data and simulated Gaussian noise for J1139-6247. With a signal frequency of 16.6Hz, the frequency bandwidth probed is 0.07Hz. Hence there are only 7 points in this histogram.

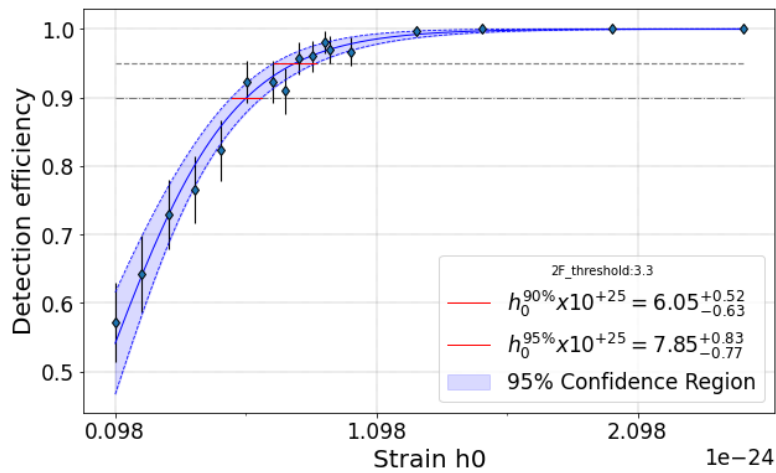


Figure 7.96: Upper limit sigmoid fit for J1139-6247 for O1O2O3a data

7.13 J0744-2525

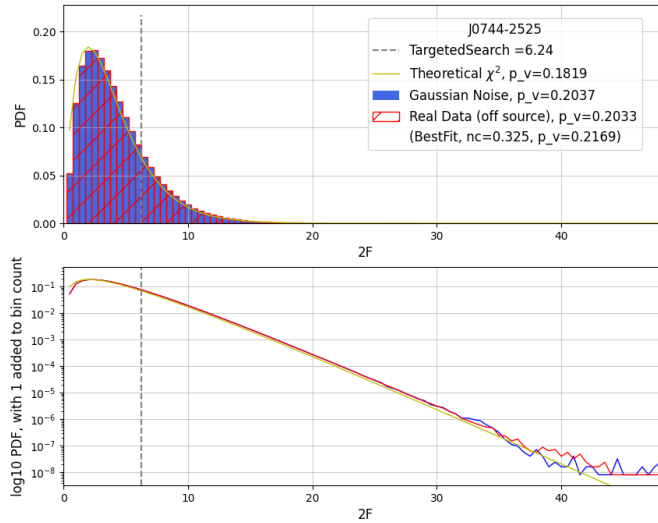


Figure 7.97: Distribution of $2\mathcal{F}$ in a 0.09Hz region around the signal frequency of J0744-2525 in $O_1O_2O_3$ data

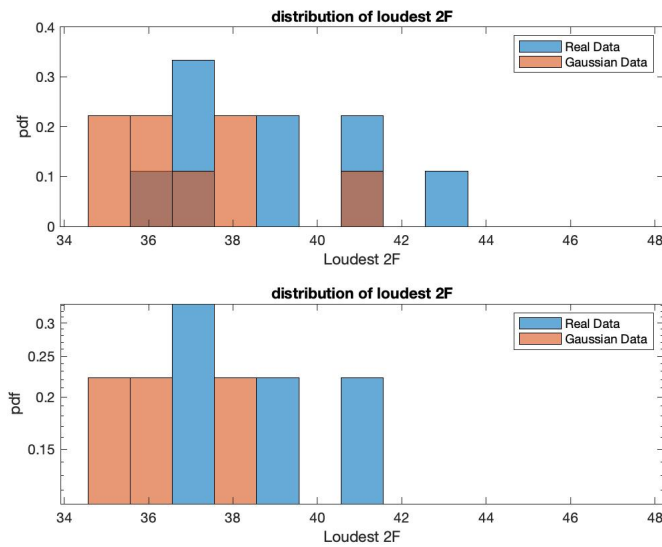


Figure 7.98: Distribution of loudest $2\mathcal{F}$ in 10mHz sub-bands in real $O_1O_2O_3$ data and simulated Gaussian noise for J0744-2525

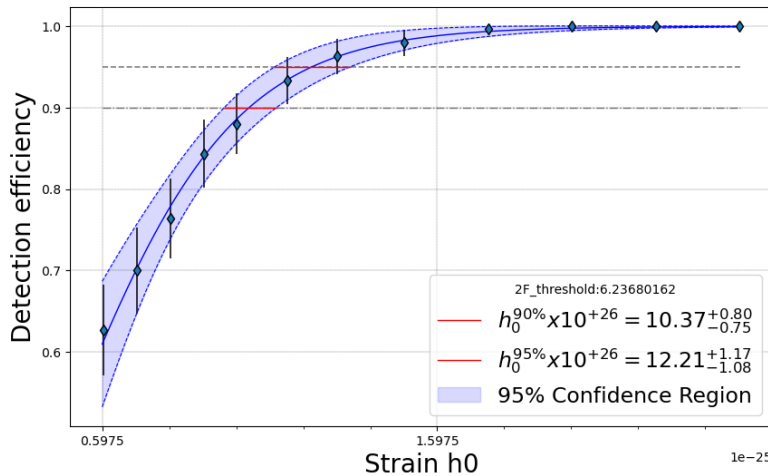


Figure 7.99: Upper limit sigmoid fit for J0744-2525 for O₁O₂O₃ data

The targeted search returned a $2\mathcal{F}=6.2$ and has a p-value of 0.2 calculated with respect to off-source data as shown in figure 7.97. The distribution of loudest $2\mathcal{F}$ s from the band search is shown in figure 7.98. To compare, the results from searching in Gaussian noise are plotted as well. The figure shows that the search results are consistent with those from Gaussian noise.

The 95% upper limit based on a null detection in the targeted search is 1.2×10^{-25} . This h_0^{95} is a factor of 4.5 times larger than the spin-down upper limit. The h_0 vs detection efficiency and the sigmoid fit is shown in figure 7.99.

7.14 J0418+6635

The targeted search returned a $2\mathcal{F}=7.1$ and has a p-value of 0.14 calculated with respect to off-source data as shown in figure 7.100.

The distribution of loudest $2\mathcal{F}$ s from the band search is shown in figure 7.101. To compare, the results from searching in Gaussian noise are plotted as well. The figure shows that the search results are consistent with those from Gaussian noise.

The 95% upper limit based on a null detection in the targeted search is 1.3×10^{-26} . This h_0^{95} is a factor of 22 larger than the spin-down upper limit. The h_0 vs detection efficiency and the sigmoid fit is shown in figure 7.102.

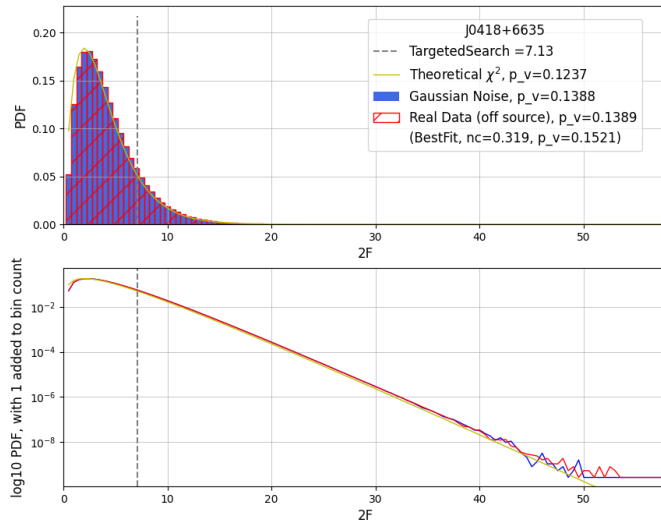


Figure 7.100: Distribution of $2\mathcal{F}$ in a 2.7Hz region around the signal frequency of J0418+6635 in O1O2O3 data

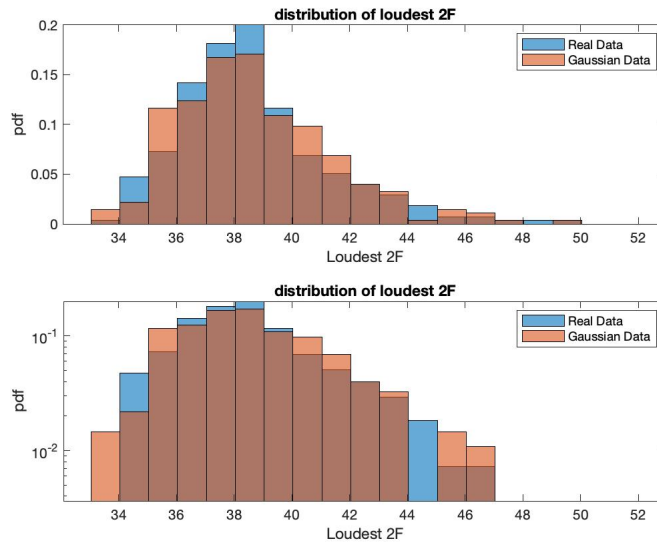


Figure 7.101: Distribution of loudest $2\mathcal{F}$ in 10mHz sub-bands in real O1O2O3 data and simulated Gaussian noise for J0418+6635

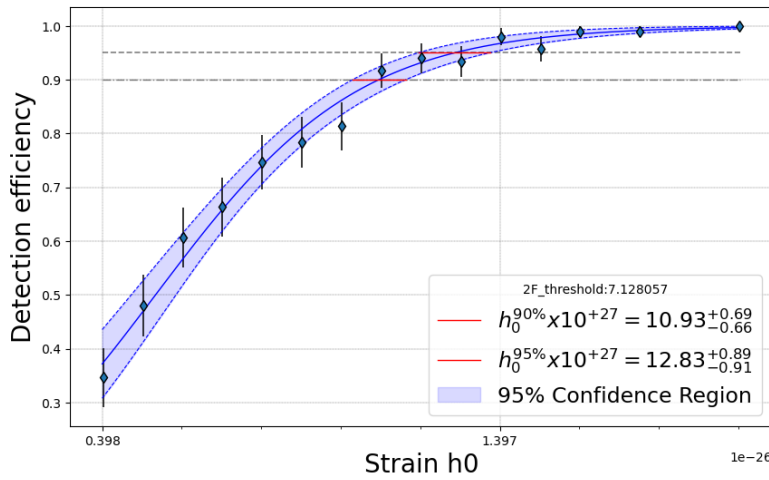


Figure 7.102: Upper limit sigmoid fit for J0418+6635 for O1O2O3 data

7.15 J1335-5656

The targeted search returned a $2\mathcal{F}=1.3$ and has a p-value of 0.91 calculated with respect to off-source data as shown in figure 7.103.

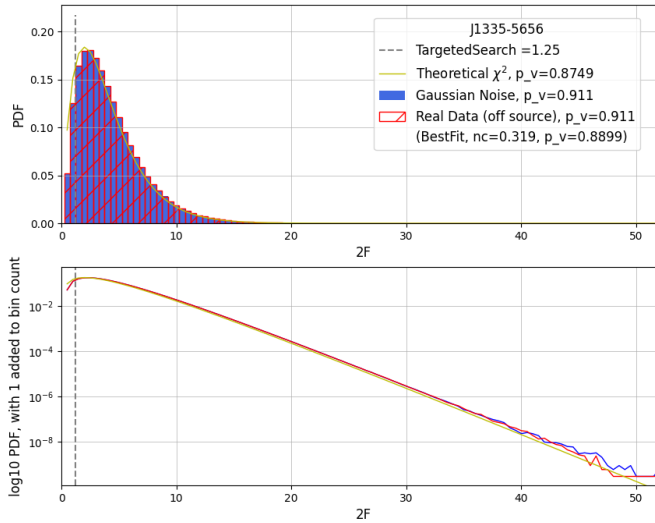


Figure 7.103: Distribution of $2\mathcal{F}$ in a 2.5Hz region around the signal frequency of J1335-5656 in O1O2O3 data

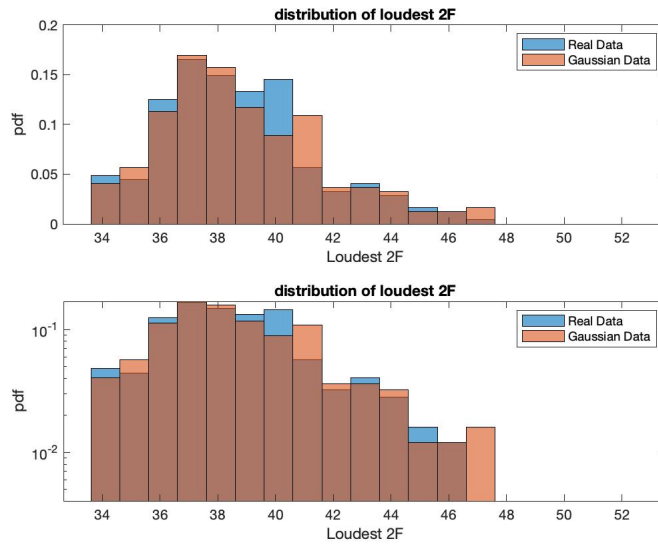


Figure 7.104: Distribution of loudest $2\mathcal{F}$ in 10mHz sub-bands in real O1O2O3 data and simulated Gaussian noise for J1335-5656

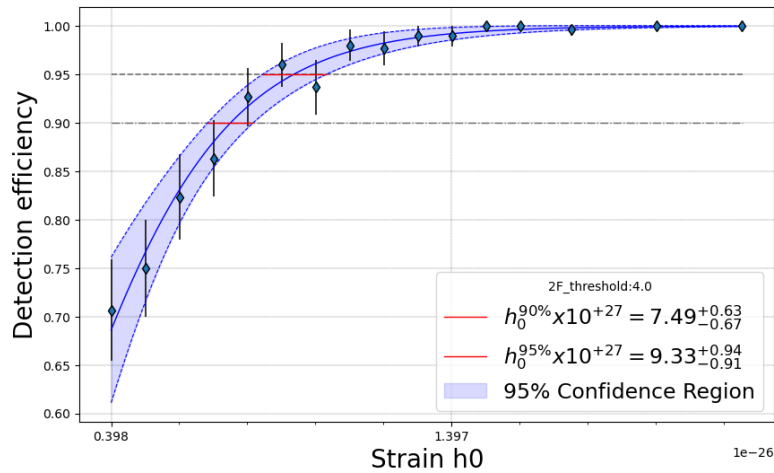


Figure 7.105: Upper limit sigmoid fit for J1335-5656 for O1O2O3 data

The distribution of loudest $2\mathcal{F}$ s from the band search is shown in figure 7.104. To compare, the results from searching in Gaussian noise are plotted as well. The figure shows that the search results are consistent with those from Gaussian noise. The 95% upper limit based on a null detection in the targeted search is 9.3×10^{-27} . This h_0^{95} is a factor of 18 larger than the spin-down upper limit. The h_0 vs detection efficiency and the sigmoid fit is shown in figure 7.105.

7.16 J2034+3632

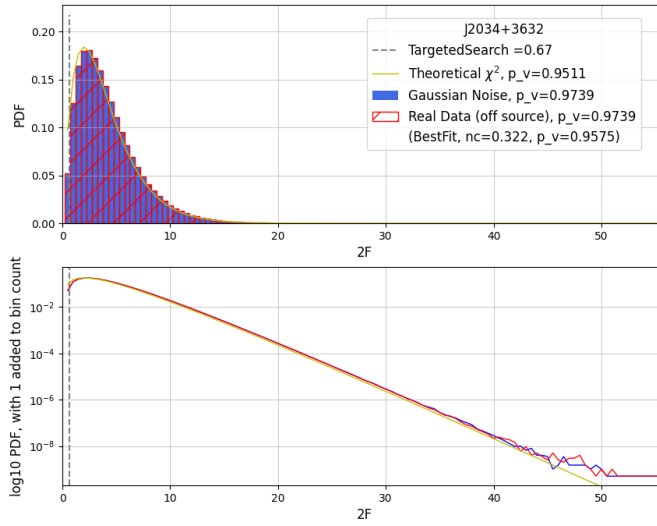


Figure 7.106: Distribution of $2\mathcal{F}$ in a 2.2Hz region around the signal frequency of J2034+3632 in O1O2O3 data

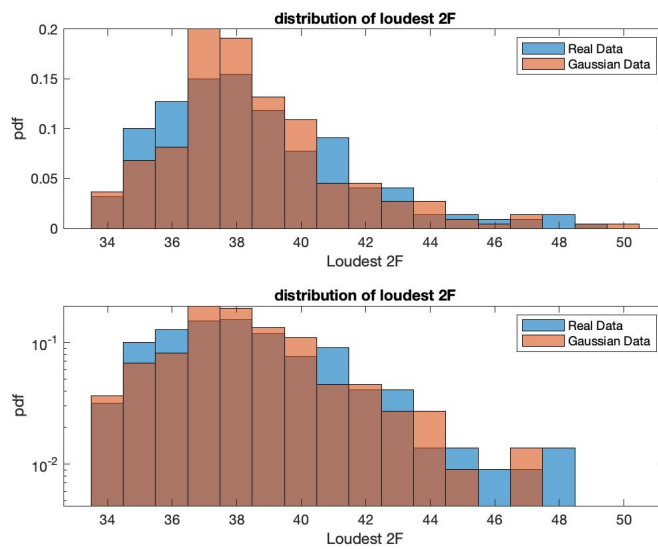


Figure 7.107: Distribution of loudest $2\mathcal{F}$ in 10mHz sub-bands in real O1O2O3 data and simulated Gaussian noise for J2034+3632

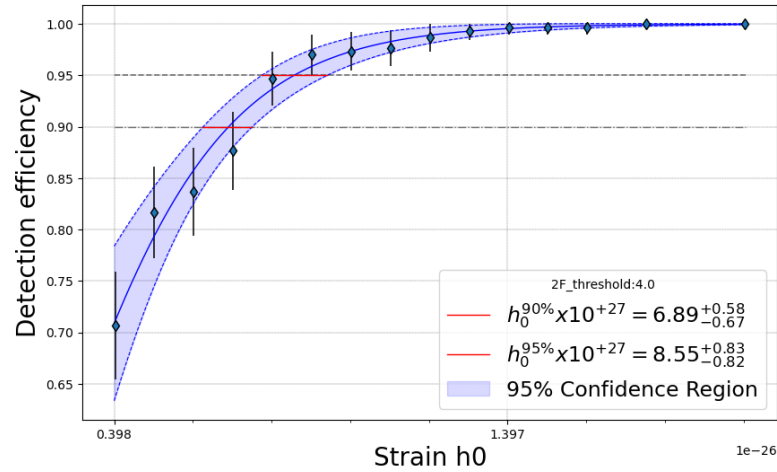


Figure 7.108: Upper limit sigmoid fit for J2034+3632 for O1O2O3 data

The targeted search returned a $2\mathcal{F}=0.67$ and has a p-value of 0.97 calculated with respect to off-source data as shown in figure 7.106. The distribution of loudest $2\mathcal{F}$ s from the band search is shown in figure 7.107. To compare, the results from searching in Gaussian noise are plotted as well. The figure shows that the search results are consistent with those from Gaussian noise. The 95% upper limit based on a null detection in the targeted search is 8.5×10^{-27} . This h_0^{95} is a factor of 46 larger than the spin-down upper limit. The h_0 vs detection efficiency and the sigmoid fit is shown in figure 7.108.

7.17 J1649-3012

For this pulsar, results from a preliminary search in a coherent combination of O1, O2 and O3A data sets are presented here. The targeted search returned a $2\mathcal{F}=3.7$ and has a p-value of 0.48 calculated with respect to off-source data as shown in figure 7.109.

The distribution of loudest $2\mathcal{F}$ s from the band search is shown in figure 7.110. To compare, the results from searching in Gaussian noise are plotted as well. The figure shows that the search results are consistent with those from Gaussian noise.

The 95% upper limit based on a null detection in the targeted search is 1.1×10^{-26} . This h_0^{95} is a factor of 21 larger than the spin-down upper limit. The h_0 vs detection efficiency and the sigmoid fit is shown in figure 7.111.

The results of the search for the remaining pulsars in this set will be published soon.

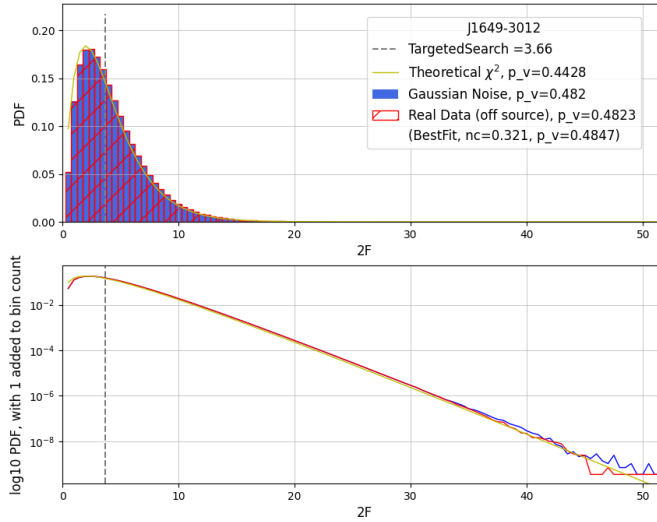


Figure 7.109: Distribution of $2\mathcal{F}$ in a 2.3Hz region around the signal frequency of J1649-3012 in O1O2O3a data

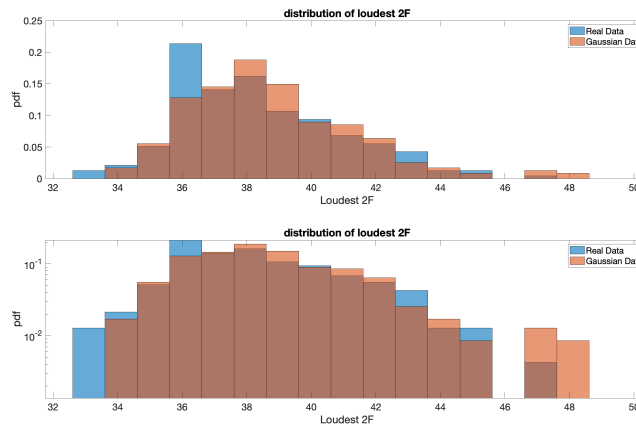


Figure 7.110: Distribution of loudest $2\mathcal{F}$ in 10mHz sub-bands in real O1O2O3a data and simulated Gaussian noise for J1649-3012

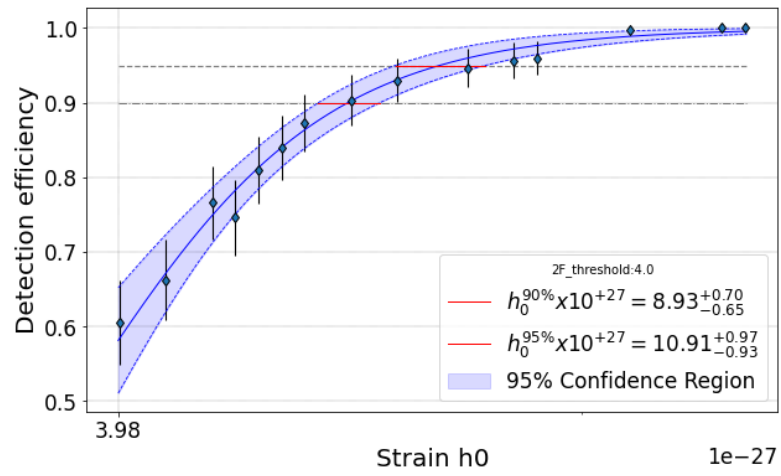


Figure 7.111: Upper limit sigmoid fit for J1649-3012 for O1O2O3a data

SUMMARY AND CONCLUSIONS

One never notices what has been done; one can only see what remains to be done.
– Marie Curie, Letter to her brother (1894)

The era of gravitational wave astronomy is here. Transient gravitational wave signals from ninety-four compact binary coalescences have been detected by the Advanced LIGO detectors (Abbott et al., 2021; Nitz et al.; Venumadhav et al., 2020; Olsen et al., 2022) to date. The physics of black holes and neutron stars, as well as fundamental physics, have already begun to benefit from observations using this new messenger. Large numbers of gravitational wave observations from binary black hole systems are helping to understand the formation and evolution channels of such systems in the universe (Farr et al., 2017), multi-messenger observations of binary neutron star mergers like GW170817 (Abbott et al., 2017) are addressing broader questions like the origin of heavy elements in the universe (Pian et al., 2017) and providing measurements of the Hubble constant (Abbott et al., 2017). The upcoming observation runs O4 and O5 are expected to be sensitive to transient signals from even further in the universe (Abbott et al., 2018).

At this juncture, it makes sense, in general, to search for other types of gravitational wave signals in Advanced LIGO data.

If we focus specifically on the motivations to search for continuous gravitational waves, firstly, there is an expected population of 10^8 to 10^9 neutron stars in the galaxy (Sartore et al., 2010), so there is no dearth of sources for continuous gravitational waves. This class of gravitational wave signals is present in the data persistently. The fact that the timespan of data from gravitational wave detectors is increasing with more observation runs and that the detector sensitivity is improving with each run combine according to equation 3.1, indicating that the signal-to-noise ratio builds up over time. This is an encouragement to search for these signals in the detector data. Speculating on what these signals could tell us, continuous gravitational waves can shed light on the properties of neutron stars, for example, on the degree of asymmetry in their mass distribution and potentially on what happens in their interiors. Owing to the difference in the emission mechanism, these signals can be treated like a new messenger of neutron star physics distinct from signals from binary neutron star mergers. Continuous gravitational waves could perhaps help understand exotic phenomena like that of axion clouds. Searching for continuous gravitational wave signals is thus a useful pursuit.

In this thesis, we approached this problem taking help from a well-established astrophysical messenger – electromagnetic waves. Using the timing solutions for pulsars, we searched for continuous gravitational wave signals they emit.

8.1 ON METHODS

In chapter 5 and 6, we described two methods for our search problem.

1. a templated search followed by a frequentist approach to inference. This search method is based on the well-established \mathcal{F} -statistic. We have set up a pipeline that carries out our standard procedure the LALSuite implementation of \mathcal{F} -statistic at its core. This pipeline starts with the timing solution of the pulsar we want to target and has six stages, namely
 - a) studying the noise in the data and choice of data for the search,
 - b) a targeted search,
 - c) quantifying the significance of the targeted search result,
 - d) setting upper limits on the strength of the continuous gravitational wave signal in the event of a non-detection,
 - e) a band search in frequency and spin down,
 - f) quantifying the significance of the results from band search,
 - g) setting upper limits in the band search for interesting/promising pulsars.

The single template search in step (b), when carried out in a coherent combination of all data from gravitational wave detectors, is the most sensitive search for a continuous gravitational wave signal. On top of that, it is also computationally the least expensive of the various search strategies. For every targeted pulsar, we also do a band search in frequency and its derivatives. The band search loses some sensitivity owing to the larger number of templates probed and costs more than a fully targeted search but allows for known and unknown effects that might cause the gravitational wave signal frequency parameters to deviate away from twice the rotational frequency parameters.

2. deriving Bayesian posterior distributions on the unknown amplitude parameters of the signal. This method was developed as an alternative approach to inferring from the data. At its core, this method is based on the calculation of \mathcal{F} -statistic itself, but we stop one step before the maximisation over amplitude parameters to obtain the likelihood function. This likelihood function (written in equation 6.38) is sampled in the amplitude parameter space, defined by prior beliefs on these parameters, to obtain their posterior distributions. Our method is also different from the one existing Bayesian tool for targeted continuous wave searches, Pitkin (2022), mainly in the sense that the former operates in the frequency domain and the latter in the time domain.

Having multiple search pipelines is always a good idea. One can cross-check results from the different pipelines. In the event of a detection, it becomes important to have

the same result show up consistently in more than one well-tested search pipeline. The two methods presented in this thesis differ in their philosophy of inferring from given data. Frequentist probability is understood as the fraction of occurrence over a large number of repeated trials. Bayesian probability is a ‘degree of plausibility.’ This difference manifests in the interpretation of upper limits on signal amplitude derived from the two methods. The two methods are asking different questions. The 95% confidence of the frequentist upper limit refers to the reliability of a procedure for finding an interval that contains the true value of h_0 . The Bayesian upper limit defines an interval in h_0 that includes the true value with 95% probability, given the data and the prior beliefs. Hence the two upper limits are not comparable, even though we would expect the two types of upper limits to have a *similar* value. This can be seen in the h_0 upper limits for PSR J1526-2744, the first pulsar which was targeted using both methods.

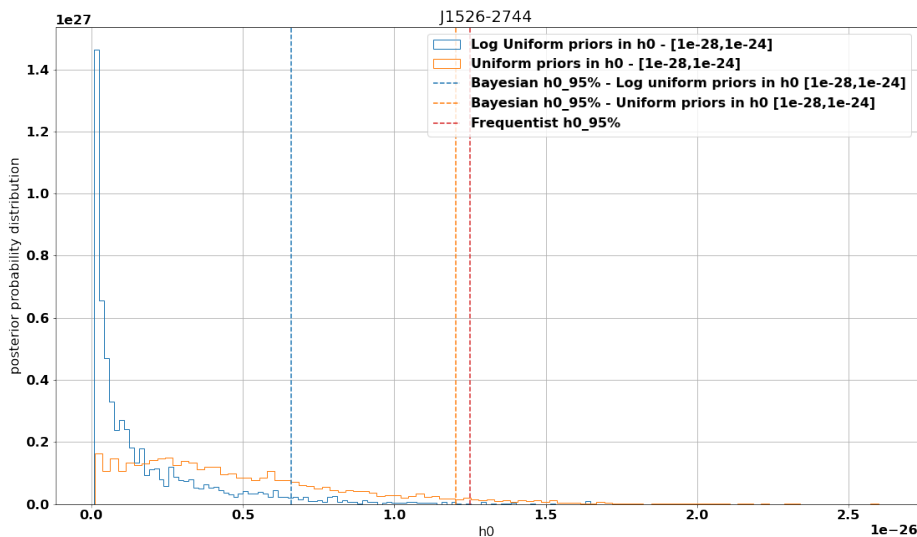


Figure 8.1: Comparison of continuous gravitational wave upper limits from frequentist and Bayesian pipelines for J1526-2744 which has been searched using both methods. The posterior distribution of h_0 is consistent with the noise-only hypothesis in both cases of the prior distribution function.

Figure 8.1 presents the results from both analyses together. The Bayesian 95% upper limit on h_0 of J1526-2744 is $\approx 7 \times 10^{-27}$, a factor of 2 smaller than the frequentist 95% upper limit.

8.2 ON RESULTS

We find no evidence of a continuous gravitational wave signal at twice the rotation frequency of the newly discovered pulsars PSR J1653-0158 , PSR J0154+1833, PSR J0824+0028, PSR J0509+0856, PSR J0709+0458, PSR J0732+2314, PSR J1411+2551, PSR J2204+2700, PSR J1526-2744, PSR J0418+6635, PSR J0744-2525, PSR J1139-6247, PSR J1335-5656, PSR J1649-3012, PSR J2034+3632 nor within 0.4% of twice their rotation frequency.

Quoting again from equation 3.27, the gravitational wave intrinsic amplitude expected from a triaxial star rotating around a principal axis z is

$$h_0 = \frac{16\pi^2 G}{c^4} \frac{I_{zz} \epsilon f_{rot}^2}{d}, \quad (8.1)$$

where I is the moment of inertia tensor and

$$\epsilon = \frac{I_{xx} - I_{yy}}{I_{zz}} \quad (8.2)$$

is the ellipticity of the star. Thus an upper limit on the strength of the gravitational wave emission can be translated into an upper limit on the ellipticity of the pulsar. Let us look at the constraints on these two quantities based on our null results for the pulsars.

8.2.1 Upper limits on gravitational wave emission

The 95% upper limits for the strength of gravitational wave emission from the targeted pulsars are best understood when compared against their spin-down upper limits, calculated according to equation 8.1, and the sensitivity of the data. Figure 8.2 shows such a comparison of spin-down upper limit, the strength of continuous gravitational wave signal we could detect given the data and the 95% upper limits we set for these pulsars. The spin-down upper limits were calculated assuming a canonical moment of inertia of 10^{38} kg m². The actual moment of inertia of the star may differ from the canonical one up by a factor of a few. Also, there could be uncertainties in distance measurements. Our 95% confidence upper limits did not beat the spin-down upper limits of any of these pulsars. For PSR J0824+0028, our upper limits using restricted priors on $\cos i$ were a factor of merely 3.8 times larger than its spin-down upper limit; this is the closest we came to the theoretical bounds for the pulsars in this thesis. This was possible thanks to the increased sensitivity of the detectors near 200 Hz where the signal frequency lies, and by the coherent combination of O1, O2, and O3a data, which were all the publicly available data at that time. The worst upper limits using O1,O2,O3a were derived for PSR J2204+2700, a factor of 166 times larger than the spin-down upper limit for the pulsar. This is not surprising because J2204 has a combination of large distance and low signal frequency.

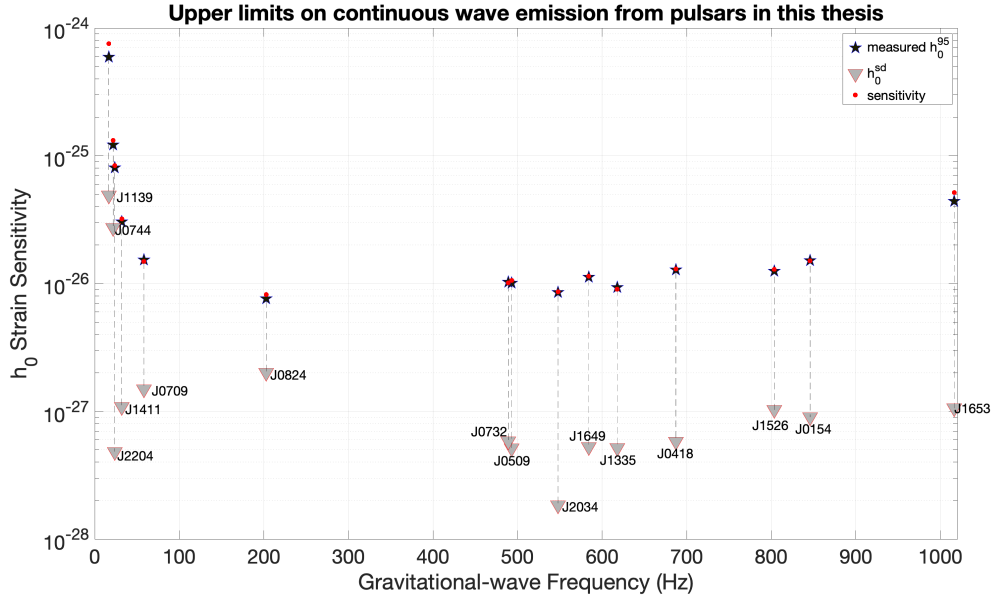


Figure 8.2: Comparison of the spin-down upper limit, measured upper limit and sensitivity of the data for all the pulsars in this thesis. In choosing to plot these quantities, we adhere to the convention of a typical known pulsar search paper (for example, Figure (2) in [Abbott et al. \(2022\)](#)). For ease of representation, the pulsar names are cut short. The spin-down upper limits are the grey triangles, the measured upper limits from our analysis of the Advanced LIGO data are the blue stars, and these reflect the sensitivity of the searches at that frequency using the data timespans available at the time of the search for the respective pulsar, shown in red circles.

8.2.2 Ellipticities

Our upper limits at twice the rotation frequency is translated in upper limits on the ellipticity of the pulsar, by

$$\varepsilon = 2.4 \times 10^{-7} \left(\frac{h_0}{1 \times 10^{-26}} \right) \times \left(\frac{D}{1 \text{ kpc}} \right) \left(\frac{200 \text{ Hz}}{f} \right)^2 \left(\frac{10^{38} \text{ kg m}^2}{I_{zz}} \right). \quad (8.3)$$

Ellipticity is a measure of distortion of the neutron star, and continuous gravitational wave signals provide, at the moment, the only way to constrain this property of the neutron star. Table 8.1 provides the ellipticity constraints for the targeted pulsars.

The most constraining upper limit on ellipticity is set for PSR J0154+1833, the pulsar with a high frequency of 845 Hz and at a close distance of 860 pc. For two-thirds of the pulsars we targeted we have probed ellipticities $\leq 3 \times 10^{-7}$, as shown in Table 8.1.

Pulsar	Ellipticity
J1653-0158	3.4×10^{-8}
J0154+1833	1.7×10^{-8}
J0509+0856	5.7×10^{-8}
J0709+0458	7.8×10^{-6}
J0732+2314	6.8×10^{-8}
J0824+0028	2.7×10^{-7}
J1411+2551	2.8×10^{-5}
J2204+2700	2.9×10^{-4}
J1526-2744	2.4×10^{-8}
J0418+6635	7.8×10^{-8}
J0744-2525	7.4×10^{-4}
J1139-6247	6.2×10^{-3}
J1335-5656	7.0×10^{-8}
J1649-3012	9.5×10^{-8}
J2034+3632	8.2×10^{-8}

Table 8.1: 95% ellipticity constraints on the pulsars.

These lie in the regime of ellipticity values sustainable by neutron star crusts (Morales and Horowitz, 2022). For distant and/or slow-spinning pulsars, the ellipticities are less constraining. Nevertheless, such low values of ellipticity can presently only be probed with the sensitivity of targeted searches. These values are also in the physically interesting ellipticity ranges (Woan et al., 2018). Such tight constraints on the ellipticity values for pulsars showcase the potential of targeted searches for continuous gravitational waves.

8.3 ON THE SCOPE OF TARGETED CONTINUOUS WAVE SEARCHES

In directed or all-sky searches, a null measurement could either mean that there were no sources emitting signals with the searched parameters or that the signals were too weak. In this sense, targeted searches (Ashok et al., 2021; Clark et al., 2023; Nieder et al., 2020) are distinct from the other types of searches because a source is guaranteed to be present. So a null measurement is directly informative about the gravitational wave emission. And the resulting ellipticity measurements are constraining an important astrophysical property of the pulsar. It should be noted that the ellipticity constraint on a pulsar becomes a physically interesting value when the measured gravitational wave upper limit is lower than the spin-down upper limit of the pulsar.

As mentioned before, targeted searches combine the best of both worlds – high sensitivity and low computational cost. Therefore it makes sense to carry out such searches for as many pulsars as possible. New surveys of the electromagnetic sky discover pulsars at a rate faster than ever before. The data from existing gravitational wave detectors are only getting better in sensitivity. And detectors in new locations are under construction. At such a time, looking forward, there is no reason to stop targeting pulsars for their gravitational wave emission.

If a pulsar has a spin frequency high enough that its continuous gravitational wave signal is within the sensitive frequency band of Advanced LIGO detectors, it should be targeted for continuous gravitational wave search. A timing solution that covers the Advanced LIGO data timespan is the ideal guide, but in case there is no such perfect overlap, it is still possible to adopt strategies as those presented in this thesis for the pulsars from ARECIBO survey (sections 7.3 to 7.9). The promise of a pulsar as a continuous gravitational wave candidate increases if it is

1. nearby,
2. is highly deformed,
3. has a continuous gravitational wave frequency in the high sensitivity regions of Advanced LIGO detectors.

This thesis focussed on newly-discovered pulsars, targeted for continuous wave emission for the first time. But when an updated timing solution is available for a high-value pulsar that was once targeted, it makes sense to re-do the search with the new timing solution.

Sometimes the continuous gravitational wave signal frequency of a promising pulsar is noise-infested, like in the case of J1653-0158 (Section 7.2). In such cases, we first thoroughly study the noise in the data and carefully choose the data that enters the search. But even then, a detection in such noise-infested frequencies would be hard to trust simply because of the possibility of unknown consequences of noise in data of such damage. The fact that one out of the fifteen pulsars in this thesis (and the very first search of the author) was a pulsar with frequency near a violin mode makes room for worrying if, in future, a pulsar of exceptional value for continuous gravitational wave search could be discovered with its expected frequency in a range beset by noise. Some noise sources, such as, for instance, the violin mode itself, are inevitable and are present in both H1 and L1 detectors. But they are well understood by experimental physicists who work closely with the detectors. Perhaps it is helpful to sit with an experimentalist and devise a strategy for data choices for the off-chance of a high-promise pulsar search in data with known noise.

New pulsar surveys also discover binary pulsars that are particularly interesting by virtue of their relationships with their companion, for example, PSR J1803-6707 in [Clark et al. \(2023\)](#). Such interactions could have repercussions on the degree of non-symmetry in their mass distribution, which in turn sources their continuous gravitational wave emission. A close look at each pulsar's features to decide the best search parameter ranges for the expected signal is a good idea. Some pulsars have measurements of higher derivatives of spin frequency. We have a few examples of such pulsars in our upcoming searches. Such specialities call for an update of existing search codes – eventually leading to the development of search software to handle a larger pool of possible scenarios for pulsars. Sometimes a whole different search method might be more suitable. For instance, a band search in the traditional sense described in this thesis may not be the best approach to allow deviations in higher spin derivatives from observed values. We work with the pulsar astronomers who understand the source best to come up with an ideal method in such cases.

8.4 CLOSING NOTE

Electromagnetic waves heralded new physics in the 20th century. Like every new scientific theory, the theory of electromagnetic waves put forth by James Clark Maxwell was treated with incredulity by his contemporaries. But soon, astronomy using light became the most commonplace tool to understand the universe. For the longest time, electromagnetic waves shed light, in the most literal manner, on various astrophysical phenomena like supernova explosions, gamma-ray bursts, distant stars, and pulsating

stars. Today, apart from their independent contributions to our observations of the universe, electromagnetic waves combine with gravitational waves and neutrinos to provide multiple perspectives of cosmic events like the binary neutron star merger GW₁₇₀₈₁₇ (Abbott et al., 2017). The era of multi-messenger astronomy is very much here. In this thesis, we saw an example of multi-messenger astronomy in action, where electromagnetic waves became guides in the hunt for gravitational waves.

APPENDIX

In this appendix, we include some algebraic details pertaining to Section 2.1, which were omitted in the body of the chapter to maintain focus on the flow of the main ideas.

A.1 CURVATURE IN LINEARISED GRAVITY

Here we explicitly work out the Riemann tensor, Ricci tensor and Ricci scalar in linearised gravity to plug into the Einstein equation given in 2.2. Since $|h_{\mu\nu}| \ll 1$, indices will be raised and lowered using the Minkowski metric. Starting at the expression for Riemann tensor, from equation 2.12,

$$R_{\mu\sigma\nu}^{\rho} = \partial_{\sigma}\Gamma_{\mu\nu}^{\rho} - \partial_{\nu}\Gamma_{\mu\sigma}^{\rho}. \quad (\text{A.1})$$

Expanding Christoffel connections in the weak field case, as in equation 2.11,

$$R_{\mu\sigma\nu}^{\rho} = \partial_{\sigma} \left[\frac{1}{2}\eta^{\rho\lambda} (\partial_{\mu}h_{\lambda\nu} + \partial_{\nu}h_{\lambda\mu} - \partial_{\lambda}h_{\mu\nu}) \right] - \partial_{\nu} \left[\frac{1}{2}\eta^{\rho\lambda} (\partial_{\mu}h_{\lambda\sigma} + \partial_{\sigma}h_{\lambda\mu} - \partial_{\lambda}h_{\mu\sigma}) \right]. \quad (\text{A.2})$$

Multiplying both sides by $\eta_{\lambda\rho}$ to simplify the calculation,

$$\begin{aligned} \eta_{\rho\lambda}R_{\mu\sigma\nu}^{\rho} &= R_{\lambda\mu\sigma\nu} \\ &= \frac{1}{2} [\partial_{\sigma}\partial_{\mu}h_{\lambda\nu} + \partial_{\sigma}\partial_{\nu}h_{\lambda\mu} - \partial_{\sigma}\partial_{\lambda}h_{\mu\nu} - \partial_{\nu}\partial_{\mu}h_{\lambda\sigma} - \partial_{\nu}\partial_{\sigma}h_{\lambda\mu} + \partial_{\nu}\partial_{\lambda}h_{\mu\sigma}] \\ &= \frac{1}{2} [\partial_{\sigma}\partial_{\mu}h_{\lambda\nu} - \partial_{\sigma}\partial_{\lambda}h_{\mu\nu} - \partial_{\nu}\partial_{\mu}h_{\lambda\sigma} + \partial_{\nu}\partial_{\lambda}h_{\mu\sigma}] \end{aligned} \quad (\text{A.3})$$

Raising the first index of $R_{\lambda\mu\sigma\nu}$ by multiplying with $\eta^{\lambda\beta}$

$$\begin{aligned} \eta^{\lambda\beta}R_{\lambda\mu\sigma\nu} &= R_{\mu\sigma\nu}^{\lambda} \\ &= \frac{1}{2} [\partial_{\sigma}\partial_{\mu}h_{\nu}^{\beta} - \partial_{\sigma}\partial^{\beta}h_{\mu\nu} - \partial_{\nu}\partial_{\mu}h^{\beta\sigma} + \partial_{\nu}\partial^{\beta}h_{\mu\sigma}] \end{aligned} \quad (\text{A.4})$$

From this, we construct the Ricci tensor $R_{\mu\nu} = R_{\mu\sigma\nu}^{\sigma}$,

$$R_{\mu\nu} = \frac{1}{2} [\partial_{\sigma}\partial_{\mu}h_{\nu}^{\sigma} - \partial_{\sigma}\partial^{\sigma}h_{\mu\nu} - \partial_{\nu}\partial_{\mu}h^{\sigma}_{\sigma} + \partial_{\nu}\partial^{\sigma}h_{\mu\sigma}]. \quad (\text{A.5})$$

Now, here we can identify,

$$\begin{aligned} h_{\sigma}^{\sigma} &\equiv h, \text{ the trace of the the tensor } h_{\mu\nu} \\ \partial_{\sigma}\partial^{\sigma} &\equiv \square = -\left(\frac{1}{c^2}\right)\partial_t^2 + \nabla^2. \end{aligned} \quad (\text{A.6})$$

So,

$$R_{\mu\nu} = \frac{1}{2} [\partial_\sigma \partial_\mu h_\nu^\sigma - \square h_{\mu\nu} - \partial_\nu \partial_\mu h + \partial_\nu \partial^\sigma h_{\mu\sigma}]. \quad (\text{A.7})$$

The Ricci scalar, R , is the trace of $R_{\mu\nu}$. First, raising μ by multiplying with $\eta^{\mu\lambda}$,

$$\eta^{\mu\lambda} R_{\mu\nu} = R_\nu^\lambda = \frac{1}{2} [\partial_\sigma \partial^\lambda h_\nu^\sigma - \square h_\nu^\lambda - \partial_\nu \partial^\lambda h + \partial_\nu \partial^\sigma h_\sigma^\lambda]. \quad (\text{A.8})$$

Now, with $\nu = \lambda$,

$$R = \frac{1}{2} [\partial_\sigma \partial^\lambda h_\lambda^\sigma - \square h_\lambda^\lambda - \partial_\lambda \partial^\lambda h + \partial_\lambda \partial^\sigma h_\sigma^\lambda], \quad (\text{A.9})$$

which using A.6 is

$$= \frac{1}{2} [2\partial_\sigma \partial^\lambda h_\lambda^\sigma - 2\square h].$$

Therefore,

$$R = \partial_\sigma \partial^\lambda h_\lambda^\sigma - \square h. \quad (\text{A.10})$$

A.2 TRACE OF $\bar{h}^{\mu\nu}$

This section is the proof for equation 2.16. We want to find the trace of the tensor

$$\bar{h}^{\mu\nu} = h^{\mu\nu} - \frac{1}{2} \eta^{\mu\nu} h. \quad (\text{A.11})$$

To lower the index ν , we multiply throughout by $\eta_{\lambda\nu}$,

$$\eta_{\lambda\nu} \bar{h}^{\mu\nu} = \eta_{\lambda\nu} h^{\mu\nu} - \frac{1}{2} \eta_{\lambda\nu} \eta^{\mu\nu} h \quad (\text{A.12})$$

Note that, $\eta^{\lambda\nu}$ is the inverse of $\eta_{\lambda\nu}$. So,

$$\eta_{\lambda\nu} \eta^{\mu\nu} = \delta_\lambda^\mu$$

where, δ_λ^μ is the Kronecker delta. So, equation A.12 is,

$$\bar{h}_\lambda^\mu = h_\lambda^\mu - \frac{1}{2} \delta_\lambda^\mu h. \quad (\text{A.13})$$

Trace of \bar{h}_λ^μ is then, with $\lambda = \mu$,

$$\bar{h}_\mu^\mu = h_\mu^\mu - \frac{1}{2} \delta_\mu^\mu h. \quad (\text{A.14})$$

Now,

$$\delta_{\mu\lambda} = \begin{bmatrix} 1 & 0 & 0 & 0 \\ 0 & 1 & 0 & 0 \\ 0 & 0 & 1 & 0 \\ 0 & 0 & 0 & 1 \end{bmatrix}$$

So,

$$\text{trace}(\delta_{\mu\lambda}) = \delta_{\mu}^{\mu} = 4. \quad (\text{A.15})$$

Using this in equation A.14,

$$\bar{h} = h - \frac{1}{2} \times 4 \times h = -h \quad (\text{A.16})$$

A.3 EINSTEIN'S EQUATION IN TERMS OF $\bar{h}_{\mu\nu}$

We start at the Einstein's equation in terms of $h_{\mu\nu}$, given in equation 2.13.

$$\partial_{\sigma}\partial_{\mu}h_{\nu}^{\sigma} - \square h_{\mu\nu} - \partial_{\nu}\partial_{\mu}h + \partial_{\nu}\partial^{\sigma}h_{\mu\sigma} - \eta_{\mu\nu}\partial_{\sigma}\partial^{\lambda}h_{\lambda}^{\sigma} + \eta_{\mu\nu}\square h = \frac{16\pi G}{c^4}T_{\mu\nu}, \quad (\text{A.17})$$

Let's focus on the left-hand side of this equation, the Einstein's tensor, and call it $G_{\mu\nu}$ –

$$G_{\mu\nu} = \partial_{\sigma}\partial_{\mu}h_{\nu}^{\sigma} - \square h_{\mu\nu} - \partial_{\nu}\partial_{\mu}h + \partial_{\nu}\partial^{\sigma}h_{\mu\sigma} - \eta_{\mu\nu}\partial_{\sigma}\partial^{\lambda}h_{\lambda}^{\sigma} + \eta_{\mu\nu}\square h. \quad (\text{A.18})$$

The trace-reverse metric is defined as (also in equation 2.14),

$$\bar{h}_{\mu\nu} = h_{\mu\nu} - \frac{1}{2}\eta_{\mu\nu}h. \quad (\text{A.19})$$

Then,

$$h_{\mu\nu} = \bar{h}_{\mu\nu} + \frac{1}{2}\eta_{\mu\nu}h, \quad (\text{A.20})$$

and,

$$\begin{aligned} \eta^{\mu\sigma}h_{\mu\nu} &= \eta^{\mu\sigma}\left[\bar{h}_{\mu\nu} + \frac{1}{2}\eta_{\mu\nu}h\right], \\ h_{\nu}^{\sigma} &= \bar{h}_{\nu}^{\sigma} + \frac{1}{2}\eta^{\mu\sigma}\eta_{\mu\nu}h. \end{aligned} \quad (\text{A.21})$$

We want to write $G_{\mu\nu}$ in terms of $\bar{h}^{\mu\nu}$. We first replace in equation A.18, $h_{\mu\nu}$ with equation A.20. Then,

$$\begin{aligned} G_{\mu\nu} &= \partial_{\sigma}\partial_{\mu}h_{\nu}^{\sigma} - \square\left[\bar{h}_{\mu\nu} + \frac{1}{2}\eta_{\mu\nu}h\right] \\ &\quad - \partial_{\nu}\partial_{\mu}h + \partial_{\nu}\partial^{\sigma}\left[\bar{h}_{\mu\sigma} + \frac{1}{2}\eta_{\mu\sigma}h\right] \\ &\quad - \eta_{\mu\nu}\partial_{\sigma}\partial^{\lambda}h_{\lambda}^{\sigma} + \eta_{\mu\nu}\square h. \\ &= \partial_{\sigma}\partial_{\mu}h_{\nu}^{\sigma} - \square\bar{h}_{\mu\nu} + \frac{1}{2}\eta_{\mu\nu}\square h \\ &\quad - \frac{1}{2}\partial_{\nu}\partial_{\mu}h + \partial_{\nu}\partial^{\sigma}\bar{h}_{\mu\sigma} - \eta_{\mu\nu}\partial_{\sigma}\partial^{\lambda}h_{\lambda}^{\sigma}. \end{aligned} \quad (\text{A.22})$$

Now replacing h_ν^σ with equation A.21,

$$\begin{aligned}
G_{\mu\nu} &= \partial_\sigma \partial_\mu \left[\bar{h}_\nu^\sigma + \frac{1}{2} \eta^{\mu\sigma} \eta_{\mu\nu} h \right] - \square \bar{h}_{\mu\nu} + \frac{1}{2} \eta_{\mu\nu} \square h \\
&\quad - \frac{1}{2} \partial_\nu \partial_\mu h + \partial_\nu \partial^\sigma \bar{h}_{\mu\sigma} - \eta_{\mu\nu} \partial_\sigma \partial^\lambda \left[\bar{h}_\lambda^\sigma + \frac{1}{2} \eta^{\mu\sigma} \eta_{\mu\lambda} h \right], \\
&= \partial_\sigma \partial_\mu \bar{h}_\nu^\sigma + \frac{1}{2} \eta^{\mu\sigma} \eta_{\mu\nu} \partial_\sigma \partial_\mu h - \square \bar{h}_{\mu\nu} + \frac{1}{2} \eta_{\mu\nu} \square h \\
&\quad - \frac{1}{2} \partial_\nu \partial_\mu h + \partial_\nu \partial^\sigma \bar{h}_{\mu\sigma} - \eta_{\mu\nu} \partial_\sigma \partial^\lambda \bar{h}_\lambda^\sigma - \frac{1}{2} \eta_{\mu\nu} \eta^{\mu\sigma} \eta_{\mu\lambda} \partial_\sigma \partial^\lambda h. \\
G_{\mu\nu} &= \partial_\sigma \partial_\mu \bar{h}_\nu^\sigma - \square \bar{h}_{\mu\nu} + \partial_\nu \partial^\sigma \bar{h}_{\mu\sigma} - \eta_{\mu\nu} \partial_\sigma \partial^\lambda \bar{h}_\lambda^\sigma. \tag{A.23}
\end{aligned}$$

Thus equation A.17 becomes,

$$\partial_\sigma \partial_\mu \bar{h}_\nu^\sigma - \square \bar{h}_{\mu\nu} + \partial_\nu \partial^\sigma \bar{h}_{\mu\sigma} - \eta_{\mu\nu} \partial_\sigma \partial^\lambda \bar{h}_\lambda^\sigma = \frac{16\pi G}{c^4} T_{\mu\nu}. \tag{A.24}$$

BIBLIOGRAPHY

- [1] Public list of lat-detected pulsars. <https://confluence.slac.stanford.edu/display/GLAMCOG/Public+List+of+LAT-Detected+Gamma-Ray+Pulsars>.
- [2] pycw. <https://gitlab.aei.uni-hannover.de/cw-group/cw-software/pycw>.
- [3] J. Aasi et al. Advanced LIGO. *Class. Quant. Grav.*, 32:074001, 2015. DOI: [10.1088/0264-9381/32/7/074001](https://doi.org/10.1088/0264-9381/32/7/074001).
- [4] B. Abbott et al. Setting upper limits on the strength of periodic gravitational waves using the first science data from the GEO 600 and LIGO detectors. *Phys. Rev. D*, 69:082004, 2004. DOI: [10.1103/PhysRevD.69.082004](https://doi.org/10.1103/PhysRevD.69.082004).
- [5] B. Abbott et al. Beating the spin-down limit on gravitational wave emission from the Crab pulsar. *Astrophys. J. Lett.*, 683:L45–L50, 2008. DOI: [10.1086/591526](https://doi.org/10.1086/591526). [Erratum: *Astrophys.J.Lett.* 706, L203–L204 (2009), Erratum: *Astrophys.J.* 706, L203–L204 (2009)].
- [6] B. P. Abbott et al. LIGO: The Laser interferometer gravitational-wave observatory. *Rept. Prog. Phys.*, 72:076901, 2009. DOI: [10.1088/0034-4885/72/7/076901](https://doi.org/10.1088/0034-4885/72/7/076901).
- [7] B. P. Abbott et al. Observation of Gravitational Waves from a Binary Black Hole Merger. *Phys. Rev. Lett.*, 116(6):061102, 2016. DOI: [10.1103/PhysRevLett.116.061102](https://doi.org/10.1103/PhysRevLett.116.061102).
- [8] B. P. Abbott et al. A gravitational-wave standard siren measurement of the Hubble constant. *Nature*, 551(7678):85–88, 2017. DOI: [10.1038/nature24471](https://doi.org/10.1038/nature24471).
- [9] B. P. Abbott et al. Gravitational Waves and Gamma-rays from a Binary Neutron Star Merger: GW170817 and GRB 170817A. *Astrophys. J. Lett.*, 848(2):L13, 2017. DOI: [10.3847/2041-8213/aa920c](https://doi.org/10.3847/2041-8213/aa920c).
- [10] B. P. Abbott et al. Prospects for observing and localizing gravitational-wave transients with Advanced LIGO, Advanced Virgo and KAGRA. *Living Rev. Rel.*, 21(1):3, 2018. DOI: [10.1007/s41114-020-00026-9](https://doi.org/10.1007/s41114-020-00026-9).
- [11] B. P. Abbott et al. GW170817: Measurements of neutron star radii and equation of state. *Phys. Rev. Lett.*, 121(16):161101, 2018. DOI: [10.1103/PhysRevLett.121.161101](https://doi.org/10.1103/PhysRevLett.121.161101).
- [12] B. P. Abbott et al. Narrow-band search for gravitational waves from known pulsars using the second LIGO observing run. *Phys. Rev. D*, 99(12):122002, 2019. DOI: [10.1103/PhysRevD.99.122002](https://doi.org/10.1103/PhysRevD.99.122002).

- [13] B. P. Abbott et al. Searches for Gravitational Waves from Known Pulsars at Two Harmonics in 2015-2017 LIGO Data. *Astrophys. J.*, 879(1):10, 2019. DOI: [10.3847/1538-4357/ab20cb](https://doi.org/10.3847/1538-4357/ab20cb). [Erratum: *Astrophys. J.* 899, 170 (2020)].
- [14] B. P. Abbott et al. A Gravitational-wave Measurement of the Hubble Constant Following the Second Observing Run of Advanced LIGO and Virgo. *Astrophys. J.*, 909(2):218, 2021. DOI: [10.3847/1538-4357/abdc7](https://doi.org/10.3847/1538-4357/abdc7).
- [15] R. Abbott et al. Gravitational-wave Constraints on the Equatorial Ellipticity of Millisecond Pulsars. *Astrophys. J. Lett.*, 902(1):L21, 2020. DOI: [10.3847/2041-8213/abb655](https://doi.org/10.3847/2041-8213/abb655).
- [16] R. Abbott et al. GWTC-3: Compact Binary Coalescences Observed by LIGO and Virgo During the Second Part of the Third Observing Run. 11 2021.
- [17] R. Abbott et al. The population of merging compact binaries inferred using gravitational waves through GWTC-3. 11 2021.
- [18] R. Abbott et al. All-sky, all-frequency directional search for persistent gravitational waves from Advanced LIGO's and Advanced Virgo's first three observing runs. *Phys. Rev. D*, 105(12):122001, 2022. DOI: [10.1103/PhysRevD.105.122001](https://doi.org/10.1103/PhysRevD.105.122001).
- [19] R. Abbott et al. Search for continuous gravitational wave emission from the Milky Way center in O3 LIGO-Virgo data. *Phys. Rev. D*, 106(4):042003, 2022. DOI: [10.1103/PhysRevD.106.042003](https://doi.org/10.1103/PhysRevD.106.042003).
- [20] R. Abbott et al. Searches for Gravitational Waves from Known Pulsars at Two Harmonics in the Second and Third LIGO-Virgo Observing Runs. *Astrophys. J.*, 935(1):1, 2022. DOI: [10.3847/1538-4357/ac6acf](https://doi.org/10.3847/1538-4357/ac6acf).
- [21] R. Abbott et al. Narrowband Searches for Continuous and Long-duration Transient Gravitational Waves from Known Pulsars in the LIGO-Virgo Third Observing Run. *Astrophys. J.*, 932(2):133, 2022. DOI: [10.3847/1538-4357/ac6ad0](https://doi.org/10.3847/1538-4357/ac6ad0).
- [22] R. Abbott et al. Model-based cross-correlation search for gravitational waves from the low-mass X-ray binary Scorpius X-1 in LIGO O3 data. 9 2022.
- [23] R. Abbott et al. All-sky search for continuous gravitational waves from isolated neutron stars using Advanced LIGO and Advanced Virgo O3 data. 1 2022.
- [24] B. Allen. Spherical ansatz for parameter-space metrics. *Phys. Rev. D*, 100(12):124004, 2019. DOI: [10.1103/PhysRevD.100.124004](https://doi.org/10.1103/PhysRevD.100.124004).
- [25] N. Andersson, K. D. Kokkotas, and B. F. Schutz. Gravitational radiation limit on the spin of young neutron stars. *Astrophys. J.*, 510:846, 1999. DOI: [10.1086/306625](https://doi.org/10.1086/306625).

- [26] N. Andersson, K. D. Kokkotas, and N. Stergioulas. On the relevance of the r mode instability for accreting neutron stars and white dwarfs. *Astrophys. J.*, 516: 307, 1999. DOI: [10.1086/307082](https://doi.org/10.1086/307082).
- [27] A. Arvanitaki and S. Dubovsky. Exploring the String Axiverse with Precision Black Hole Physics. *Phys. Rev. D*, 83:044026, 2011. DOI: [10.1103/PhysRevD.83.044026](https://doi.org/10.1103/PhysRevD.83.044026).
- [28] A. Arvanitaki, M. Baryakhtar, S. Dimopoulos, S. Dubovsky, and R. Lasenby. Black Hole Mergers and the QCD Axion at Advanced LIGO. *Phys. Rev. D*, 95(4):043001, 2017. DOI: [10.1103/PhysRevD.95.043001](https://doi.org/10.1103/PhysRevD.95.043001).
- [29] Z. Arzoumanian et al. The NANOGrav 12.5 yr Data Set: Search for an Isotropic Stochastic Gravitational-wave Background. *Astrophys. J. Lett.*, 905(2):L34, 2020. DOI: [10.3847/2041-8213/abd401](https://doi.org/10.3847/2041-8213/abd401).
- [30] A. Ashok, B. Beheshtipour, M. A. Papa, P. C. C. Freire, B. Steltner, B. Machenschalk, O. Behnke, B. Allen, and R. Prix. New Searches for Continuous Gravitational Waves from Seven Fast Pulsars. *Astrophys. J.*, 923(1):85, 2021. DOI: [10.3847/1538-4357/ac2582](https://doi.org/10.3847/1538-4357/ac2582).
- [31] G. Ashton et al. BILBY: A user-friendly Bayesian inference library for gravitational-wave astronomy. *Astrophys. J. Suppl.*, 241(2):27, 2019. DOI: [10.3847/1538-4365/ab06fc](https://doi.org/10.3847/1538-4365/ab06fc).
- [32] D. M. Beazley. Swig: An easy to use tool for integrating scripting languages with c and c++. In *Tcl/Tk Workshop*, 1996.
- [33] S. Chen et al. Common-red-signal analysis with 24-yr high-precision timing of the European Pulsar Timing Array: inferences in the stochastic gravitational-wave background search. *Mon. Not. Roy. Astron. Soc.*, 508(4):4970–4993, 2021. DOI: [10.1093/mnras/stab2833](https://doi.org/10.1093/mnras/stab2833).
- [34] C. J. Clark et al. The TRAPUM L-band survey for pulsars in Fermi-LAT gamma-ray sources. *Mon. Not. Roy. Astron. Soc.*, 519(4):5590–5606, 2023. DOI: [10.1093/mnras/stac3742](https://doi.org/10.1093/mnras/stac3742).
- [35] P. B. Covas et al. Identification and mitigation of narrow spectral artifacts that degrade searches for persistent gravitational waves in the first two observing runs of Advanced LIGO. *Phys. Rev. D*, 97(8):082002, 2018. DOI: [10.1103/PhysRevD.97.082002](https://doi.org/10.1103/PhysRevD.97.082002).
- [36] C. Cutler and B. F. Schutz. The Generalized F-statistic: Multiple detectors and multiple GW pulsars. *Phys. Rev. D*, 72:063006, 2005. DOI: [10.1103/PhysRevD.72.063006](https://doi.org/10.1103/PhysRevD.72.063006).

- [37] T. Damour and N. Deruelle. General relativistic celestial mechanics of binary systems. II. The post-Newtonian timing formula. *Ann. Inst. Henri Poincaré Phys. Théor*, 44(3):263–292, Jan. 1986.
- [38] K. Danzmann et al. Lisa: Unveiling a hidden universe.
- [39] M. M. Davis, J. H. Taylor, J. M. Weisberg, and D. C. Backer. HIGH PRECISION TIMING OBSERVATIONS OF THE MILLISECOND PULSAR PSR 1937 + 21. *Nature*, 315:547–550, 1985. DOI: [10.1038/315547a0](https://doi.org/10.1038/315547a0).
- [40] V. Dergachev, M. A. Papa, B. Steltner, and H.-B. Eggenstein. Loosely coherent search in LIGO O1 data for continuous gravitational waves from Terzan 5 and the galactic center. *Phys. Rev. D*, 99(8):084048, 2019. DOI: [10.1103/PhysRevD.99.084048](https://doi.org/10.1103/PhysRevD.99.084048).
- [41] S. V. Dhurandhar and B. S. Sathyaprakash. Choice of filters for the detection of gravitational waves from coalescing binaries. 2. Detection in colored noise. *Phys. Rev. D*, 49:1707–1722, 1994. DOI: [10.1103/PhysRevD.49.1707](https://doi.org/10.1103/PhysRevD.49.1707).
- [42] R. J. Dupuis and G. Woan. Bayesian estimation of pulsar parameters from gravitational wave data. *Phys. Rev. D*, 72:102002, 2005. DOI: [10.1103/PhysRevD.72.102002](https://doi.org/10.1103/PhysRevD.72.102002).
- [43] F. W. Dyson, A. S. Eddington, and C. Davidson. A Determination of the Deflection of Light by the Sun’s Gravitational Field, from Observations Made at the Total Eclipse of May 29, 1919. *Phil. Trans. Roy. Soc. Lond. A*, 220:291–333, 1920. DOI: [10.1098/rsta.1920.0009](https://doi.org/10.1098/rsta.1920.0009).
- [44] A. Einstein. Zur Allgemeinen Relativitätstheorie. *Sitzungsber. Preuss. Akad. Wiss. Berlin (Math. Phys.)*, 1915:778–786, 1915. [Addendum: *Sitzungsber. Preuss. Akad. Wiss. Berlin (Math. Phys.)* 1915, 799–801 (1915)].
- [45] A. Einstein. The Foundation of the General Theory of Relativity. *Annalen Phys.*, 49(7):769–822, 1916. DOI: [10.1002/andp.19163540702](https://doi.org/10.1002/andp.19163540702).
- [46] A. Einstein. Über Gravitationswellen. *Sitzungsber. Preuss. Akad. Wiss. Berlin (Math. Phys.)*, 1918:154–167, 1918.
- [47] W. M. Farr, S. Stevenson, M. Coleman Miller, I. Mandel, B. Farr, and A. Vecchio. Distinguishing Spin-Aligned and Isotropic Black Hole Populations With Gravitational Waves. *Nature*, 548:426, 2017. DOI: [10.1038/nature23453](https://doi.org/10.1038/nature23453).
- [48] A. S. Fruchter, D. R. Stinebring, and J. H. Taylor. A millisecond pulsar in an eclipsing binary. In H. Ögelman and E. P. J. van den Heuvel, editors, *Timing Neutron Stars*, volume 262 of *NATO Advanced Study Institute (ASI) Series C*, page 163, Jan. 1989.

- [49] H. G. Gale. Albert a. Michelson. *Astrophys. J.*, 74:1, 7 1931. DOI: [10.1086/143320](https://doi.org/10.1086/143320).
- [50] F. Gittins, N. Andersson, and D. I. Jones. Modelling neutron star mountains. *Mon. Not. Roy. Astron. Soc.*, 500(4):5570–5582, 2020. DOI: [10.1093/mnras/staa3635](https://doi.org/10.1093/mnras/staa3635).
- [51] B. Goncharov et al. Consistency of the Parkes Pulsar Timing Array Signal with a Nanohertz Gravitational- wave Background. *Astrophys. J.*, 932(2):L22, 2022. DOI: [10.3847/2041-8213/ac76bb](https://doi.org/10.3847/2041-8213/ac76bb).
- [52] J. S. Hazboun, J. D. Romano, and T. L. Smith. Realistic sensitivity curves for pulsar timing arrays. *Phys. Rev. D*, 100(10):104028, 2019. DOI: [10.1103/PhysRevD.100.104028](https://doi.org/10.1103/PhysRevD.100.104028).
- [53] R. w. Hellings and G. s. Downs. UPPER LIMITS ON THE ISOTROPIC GRAVITATIONAL RADIATION BACKGROUND FROM PULSAR TIMING ANALYSIS. *Astrophys. J. Lett.*, 265:L39–L42, 1983. DOI: [10.1086/183954](https://doi.org/10.1086/183954).
- [54] A. Hewish, S. J. Bell, J. D. H. Pilkington, P. F. Scott, and R. A. Collins. Observation of a rapidly pulsating radio source. *Nature*, 217:709–713, 1968. DOI: [10.1038/217709a0](https://doi.org/10.1038/217709a0).
- [55] G. Hobbs. Using the pulsar timing software package, TEMPO2. 5 2012.
- [56] R. A. Hulse and J. H. Taylor. Discovery of a pulsar in a binary system. *Astrophys. J. Lett.*, 195:L51–L53, 1975. DOI: [10.1086/181708](https://doi.org/10.1086/181708).
- [57] M. Isi, M. Pitkin, and A. J. Weinstein. Probing Dynamical Gravity with the Polarization of Continuous Gravitational Waves. *Phys. Rev. D*, 96(4):042001, 2017. DOI: [10.1103/PhysRevD.96.042001](https://doi.org/10.1103/PhysRevD.96.042001).
- [58] P. Jaranowski, A. Krolak, and B. F. Schutz. Data analysis of gravitational - wave signals from spinning neutron stars. 1. The Signal and its detection. *Phys. Rev.*, D58:063001, 1998. DOI: [10.1103/PhysRevD.58.063001](https://doi.org/10.1103/PhysRevD.58.063001).
- [59] D. I. Jones and N. Andersson. Gravitational waves from freely precessing neutron stars. *Mon. Not. Roy. Astron. Soc.*, 331:203, 2002. DOI: [10.1046/j.1365-8711.2002.05180.x](https://doi.org/10.1046/j.1365-8711.2002.05180.x).
- [60] V. Kalogera et al. The Next Generation Global Gravitational Wave Observatory: The Science Book. 11 2021.
- [61] D. Kasen, B. Metzger, J. Barnes, E. Quataert, and E. Ramirez-Ruiz. Origin of the heavy elements in binary neutron-star mergers from a gravitational wave event. *Nature*, 551:80, 2017. DOI: [10.1038/nature24453](https://doi.org/10.1038/nature24453).

- [62] C. Lange, F. Camilo, N. Wex, M. Kramer, D. C. Backer, A. G. Lyne, and O. Doroshenko. Precision timing measurements of psr j1012+5307. *Mon. Not. Roy. Astron. Soc.*, 326:274, 2001. DOI: [10.1046/j.1365-8711.2001.04606.x](https://doi.org/10.1046/j.1365-8711.2001.04606.x).
- [63] LIGO Scientific Collaboration. LIGO Algorithm Library - LALSuite. free software (GPL), 2018.
- [64] D. R. Lorimer. Binary and Millisecond Pulsars. *Living Rev. Rel.*, 11:8, 2008. DOI: [10.12942/lrr-2008-8](https://doi.org/10.12942/lrr-2008-8).
- [65] D. R. Lorimer and M. Kramer. *Handbook of Pulsar Astronomy*, volume 4. 2004.
- [66] M. Maggiore. *Gravitational Waves. Vol. 1: Theory and Experiments*. Oxford Master Series in Physics. Oxford University Press, 2007. ISBN 978-0-19-857074-5, 978-0-19-852074-0.
- [67] R. N. Manchester, G. B. Hobbs, A. Teoh, and M. Hobbs. The australia telescope national facility pulsar catalogue. *The Astronomical Journal*, 129(4):1993–2006, apr 2005. DOI: [10.1086/428488](https://doi.org/10.1086/428488). URL <https://doi.org/10.1086%2F428488>.
- [68] I. Mandel. The astrophysics of LIGO gravitational-wave observations. *PoS, INTEGRAL2016:002*, 2017. DOI: [10.22323/1.285.0002](https://doi.org/10.22323/1.285.0002).
- [69] J. G. Martinez, K. Stovall, P. C. C. Freire, J. S. Deneva, T. M. Tauris, A. Ridolfi, N. Wex, F. A. Jenet, M. A. McLaughlin, and M. Bagchi. Pulsar J1411+2551: A Low-mass Double Neutron Star System. *Astrophys. J. Lett.*, 851(2):L29, 2017. DOI: [10.3847/2041-8213/aa9d87](https://doi.org/10.3847/2041-8213/aa9d87).
- [70] J. G. Martinez, P. Gentile, P. C. C. Freire, K. Stovall, J. S. Deneva, G. Desvignes, F. A. Jenet, M. A. McLaughlin, M. Bagchi, and T. Devine. The Discovery of Six Recycled Pulsars from the Arecibo 327-MHz Drift-Scan Pulsar Survey. *Astrophys. J.*, 881:166, 2019. DOI: [10.3847/1538-4357/ab2877](https://doi.org/10.3847/1538-4357/ab2877).
- [71] J. Ming, M. A. Papa, B. Krishnan, R. Prix, C. Beer, S. J. Zhu, H.-B. Eggenstein, O. Bock, and B. Machenschalk. Optimally setting up directed searches for continuous gravitational waves in Advanced LIGO O1 data. *Phys. Rev. D*, 97(2):024051, 2018. DOI: [10.1103/PhysRevD.97.024051](https://doi.org/10.1103/PhysRevD.97.024051).
- [72] J. Ming, M. A. Papa, H.-B. Eggenstein, B. Machenschalk, B. Steltner, R. Prix, B. Allen, and O. Behnke. Results From an Einstein@Home Search for Continuous Gravitational Waves From G347.3 at Low Frequencies in LIGO O2 Data. *Astrophys. J.*, 925(1):8, 2022. DOI: [10.3847/1538-4357/ac35cb](https://doi.org/10.3847/1538-4357/ac35cb).
- [73] J. Ming et al. Results from an Einstein@Home search for continuous gravitational waves from Cassiopeia A, Vela Jr. and G347.3. *Phys. Rev. D*, 100(2):024063, 2019. DOI: [10.1103/PhysRevD.100.024063](https://doi.org/10.1103/PhysRevD.100.024063).

- [74] Miroslav Shaltev. Optimization and follow-up of semi-coherent searches for continuous gravitational waves. <http://opac.tib.eu/DB=1/XMLPRS=N/PPN?PPN=755483928>, 2013.
- [75] C. W. Misner, K. S. Thorne, and J. A. Wheeler. *Gravitation*. 1973.
- [76] C. J. Moore, R. H. Cole, and C. P. L. Berry. Gravitational-wave sensitivity curves. *Class. Quant. Grav.*, 32(1):015014, 2015. DOI: [10.1088/0264-9381/32/1/015014](https://doi.org/10.1088/0264-9381/32/1/015014).
- [77] J. A. Morales and C. J. Horowitz. Neutron star crust can support a large ellipticity. *Mon. Not. Roy. Astron. Soc.*, 517(4):5610–5616, 2022. DOI: [10.1093/mnras/stac3058](https://doi.org/10.1093/mnras/stac3058).
- [78] I. Newton. *Philosophiæ Naturalis Principia Mathematica*. England, 1687.
- [79] L. Nieder et al. Discovery of a Gamma-ray Black Widow Pulsar by GPU-accelerated Einstein@Home. *Astrophys. J. Lett.*, 902(2):L46, 2020. DOI: [10.3847/2041-8213/abb02](https://doi.org/10.3847/2041-8213/abb02).
- [80] A. H. Nitz, S. Kumar, Y.-F. Wang, S. Kastha, S. Wu, M. Schäfer, R. Dhurkunde, and C. D. Capano. 4-OGC: Catalog of gravitational waves from compact-binary mergers.
- [81] S. Olsen, T. Venumadhav, J. Mushkin, J. Roulet, B. Zackay, and M. Zaldarriaga. New binary black hole mergers in the LIGO-Virgo O3a data. *Phys. Rev. D*, 106(4):043009, 2022. DOI: [10.1103/PhysRevD.106.043009](https://doi.org/10.1103/PhysRevD.106.043009).
- [82] B. J. Owen. Search templates for gravitational waves from inspiraling binaries: Choice of template spacing. *Phys. Rev. D*, 53:6749–6761, 1996. DOI: [10.1103/PhysRevD.53.6749](https://doi.org/10.1103/PhysRevD.53.6749).
- [83] M. A. Papa. Gravity and gravitational waves.
- [84] M. A. Papa, J. Ming, E. V. Gotthelf, B. Allen, R. Prix, V. Dergachev, H.-B. Eggenstein, A. Singh, and S. J. Zhu. Search for Continuous Gravitational Waves from the Central Compact Objects in Supernova Remnants Cassiopeia A, Vela Jr., and G347.3–0.5. *Astrophys. J.*, 897(1):22, 2020. DOI: [10.3847/1538-4357/ab92a6](https://doi.org/10.3847/1538-4357/ab92a6).
- [85] E. Pian et al. Spectroscopic identification of r-process nucleosynthesis in a double neutron star merger. *Nature*, 551:67–70, 2017. DOI: [10.1038/nature24298](https://doi.org/10.1038/nature24298).
- [86] Pirani, Felix. Measurement of Classical Gravitation Fields. In: *The Role of Gravitation in Physics: Report from the 1957 Chapel Hill Conference*. Berlin: Max-Planck-Gesellschaft zur Förderung der Wissenschaften., 2011.
- [87] M. Pitkin. CWInPy: A Python package for inference with continuous gravitational-wave signals from pulsars. *J. Open Source Softw.*, 7(77):4568, 2022. DOI: [10.21105/joss.04568](https://doi.org/10.21105/joss.04568).

- [88] M. Pitkin, M. Isi, J. Veitch, and G. Woan. A nested sampling code for targeted searches for continuous gravitational waves from pulsars. 5 2017.
- [89] B. T. Reed, A. Deibel, and C. J. Horowitz. Modeling the Galactic Neutron Star Population for Use in Continuous Gravitational-wave Searches. *Astrophys. J.*, 921(1):89, 2021. DOI: [10.3847/1538-4357/ac1c04](https://doi.org/10.3847/1538-4357/ac1c04).
- [90] Rickles, Dean and DeWitt, Cécile M. An Expanded Version of the Remarks by R.P. Feynman on the Reality of Gravitational Waves. In: *The Role of Gravitation in Physics: Report from the 1957 Chapel Hill Conference*. Berlin: Max-Planck-Gesellschaft zur Förderung der Wissenschaften., 2011.
- [91] N. Sartore, E. Ripamonti, A. Treves, and R. Turolla. Galactic neutron stars I. Space and velocity distributions in the disk and in the halo. *Astron. Astrophys.*, 510:A23, 2010. DOI: [10.1051/0004-6361/200912222](https://doi.org/10.1051/0004-6361/200912222).
- [92] P. R. Saulson. Josh Goldberg and the physical reality of gravitational waves. *Gen. Rel. Grav.*, 43:3289–3299, 2011. DOI: [10.1007/s10714-011-1237-z](https://doi.org/10.1007/s10714-011-1237-z).
- [93] B. F. Schutz. *A FIRST COURSE IN GENERAL RELATIVITY*. Cambridge Univ. Pr., Cambridge, UK, 1985.
- [94] I. S. Shklovskii. Possible Causes of the Secular Increase in Pulsar Periods. *Soviet Astronomy*, 13:562, Feb. 1970.
- [95] R. Smits, M. Kramer, B. Stappers, D. R. Lorimer, J. Cordes, and A. Faulkner. Pulsar searches and timing with the square kilometre array. *Astron. Astrophys.*, 493:1161–1170, 2009. DOI: [10.1051/0004-6361:200810383](https://doi.org/10.1051/0004-6361:200810383).
- [96] J. S. Speagle. dynesty: a dynamic nested sampling package for estimating Bayesian posteriors and evidences. *Mon. Not. Roy. Astron. Soc.*, 493(3):3132–3158, 2020. DOI: [10.1093/mnras/staa278](https://doi.org/10.1093/mnras/staa278).
- [97] G. Srinivasan. Recycled pulsars. *New Astronomy Reviews*, 54(3):93–100, 2010. ISSN 1387-6473. DOI: <https://doi.org/10.1016/j.newar.2010.09.026>. URL <https://www.sciencedirect.com/science/article/pii/S1387647310000692>. Proceedings: A Life With Stars.
- [98] B. Steltner, M. A. Papa, and H.-B. Eggenstein. Identification and removal of non-Gaussian noise transients for gravitational-wave searches. *Phys. Rev. D*, 105(2):022005, 2022. DOI: [10.1103/PhysRevD.105.022005](https://doi.org/10.1103/PhysRevD.105.022005).
- [99] B. Steltner, M. A. Papa, H. B. Eggenstein, R. Prix, M. Bensch, and B. Machenschalk. Deep Einstein@Home all-sky search for continuous gravitational waves in LIGO O3 public data. 3 2023.

- [100] T. M. Tauris and R. J. Takens. Runaway velocities of stellar components originating from disrupted binaries via asymmetric supernova explosions. *Astron. Astrophys.*, 330:1047–1059, Feb. 1998.
- [101] J. H. Taylor, L. A. Fowler, and P. M. McCulloch. Measurements of general relativistic effects in the binary pulsar PSR 1913+16. *Nature*, 277:437–440, 1979. DOI: [10.1038/277437a0](https://doi.org/10.1038/277437a0).
- [102] G. Ushomirsky, C. Cutler, and L. Bildsten. Deformations of accreting neutron star crusts and gravitational wave emission. *Mon. Not. Roy. Astron. Soc.*, 319:902, 2000. DOI: [10.1046/j.1365-8711.2000.03938.x](https://doi.org/10.1046/j.1365-8711.2000.03938.x).
- [103] T. Venumadhav, B. Zackay, J. Roulet, L. Dai, and M. Zaldarriaga. New binary black hole mergers in the second observing run of Advanced LIGO and Advanced Virgo. *Phys. Rev. D*, 101(8):083030, 2020. DOI: [10.1103/PhysRevD.101.083030](https://doi.org/10.1103/PhysRevD.101.083030).
- [104] F. Verbunt and P. C. C. Freire. On the disruption of pulsar and X-ray binaries in globular clusters. *Astron. Astrophys.*, 561:A11, Jan. 2014. DOI: [10.1051/0004-6361/201321177](https://doi.org/10.1051/0004-6361/201321177).
- [105] K. Wette. SWIGLAL: Python and Octave interfaces to the LALSuite gravitational-wave data analysis libraries. *SoftwareX*, 12:100634, 2020. DOI: [10.1016/j.softx.2020.100634](https://doi.org/10.1016/j.softx.2020.100634).
- [106] G. Woan, M. D. Pitkin, B. Haskell, D. I. Jones, and P. D. Lasky. Evidence for a Minimum Ellipticity in Millisecond Pulsars. *Astrophys. J. Lett.*, 863(2):L40, 2018. DOI: [10.3847/2041-8213/aad86a](https://doi.org/10.3847/2041-8213/aad86a).
- [107] Y. Zhang, M. A. Papa, B. Krishnan, and A. L. Watts. Search for Continuous Gravitational Waves from Scorpius X-1 in LIGO O2 Data. *Astrophys. J. Lett.*, 906(2):L14, 2021. DOI: [10.3847/2041-8213/abd256](https://doi.org/10.3847/2041-8213/abd256).
- [108] M. Zimmermann and E. Szedenits. GRAVITATIONAL WAVES FROM ROTATING AND PRECESSING RIGID BODIES: SIMPLE MODELS AND APPLICATIONS TO PULSARS. *Phys. Rev. D*, 20:351–355, 1979. DOI: [10.1103/PhysRevD.20.351](https://doi.org/10.1103/PhysRevD.20.351).
- [109] M. Zucker. Getting an a+ : Enhancing advanced ligo, 7 2016.

PUBLICATIONS
AS FIRST AUTHOR OF THE GRAVITATIONAL WAVE ANALYSIS



New Searches for Continuous Gravitational Waves from Seven Fast Pulsars

A. Ashok^{1,2}, B. Beheshtipour^{1,2}, M. A. Papa^{1,2,3}, P. C. C. Freire⁴, B. Steltner^{1,2}, B. Machenschalk^{1,2}, O. Behnke^{1,2},
B. Allen^{1,2,3}, and R. Prix^{1,2}

¹ Max Planck Institute for Gravitational Physics (Albert Einstein Institute), Callinstrasse 38, D-30167 Hannover, Germany; anjana.ashok@aei.mpg.de,
maria.alessandra.papa@aei.mpg.de

² Leibniz Universität Hannover, D-30167 Hannover, Germany

³ University of Wisconsin Milwaukee, 3135 N Maryland Ave., Milwaukee, WI 53211, USA

⁴ Max-Planck-Institut für Radioastronomie, Auf dem Hügel 69, D-53121 Bonn, Germany

Received 2021 July 28; revised 2021 August 25; accepted 2021 September 1; published 2021 December 13

Abstract

We conduct searches for continuous gravitational waves from seven pulsars that have not been targeted in continuous wave searches of Advanced LIGO data before. We target emission at exactly twice the rotation frequency of the pulsars and in a small band around such a frequency. The former search assumes that the gravitational-wave quadrupole is changing in a phase-locked manner with the rotation of the pulsar. The latter search over a range of frequencies allows for differential rotation between the component emitting the radio signal and the component emitting the gravitational waves, for example the crust or magnetosphere versus the core. Timing solutions derived from the Arecibo 327 MHz Drift-Scan Pulsar Survey observations are used. No evidence of a signal is found and upper limits are set on the gravitational-wave amplitude. For one of the pulsars we probe gravitational-wave intrinsic amplitudes just a factor of 3.8 higher than the spin-down limit, assuming a canonical moment of inertia of 10^{38} kg m². Our tightest ellipticity constraint is 1.5×10^{-8} , which is a value well within the range of what a neutron star crust could support.

Unified Astronomy Thesaurus concepts: Gravitational waves (678); Pulsars (1306); LIGO (920); Neutron stars (1108)

Supporting material: machine-readable tables

1. Introduction

Continuous gravitational waves are expected from rotating neutron stars if these objects present a deviation from a perfectly axisymmetric configuration (Jaranowski et al. 1998; Lasky 2015). On the whole, the expected signal is simple, consisting of one or two harmonics at the rotation frequency of the star and at twice this frequency (Jones 2015).

The sensitivity of the LIGO instruments allows for the probing of continuous gravitational-wave emission from the Galactic population of neutron stars, for deformations of a few parts in a million and smaller, depending on the search, over a broad range of frequencies. Different types of searches are carried out: “blind” all-sky surveys (Abbott et al. 2021a; Steltner et al. 2021b; Covas & Sintes 2020; Dergachev & Papa 2021, 2020; Abbott et al. 2019a), searches directed at neutron star candidates like supernova remnants and low mass X-ray binaries (Zhang et al. 2021; Abbott et al. 2021b; Papa et al. 2020; Lindblom & Owen 2020; Jones & Sun 2021; Ming et al. 2019), and targeted searches aimed at known pulsars (Abbott et al. 2019b, 2019c; Nieder et al. 2020, 2019; Fesik & Papa 2020; Abbott et al. 2021c, 2021d).

Among the different searches, the ones that target pulsars have a special place. Pulsars are believed to be neutron stars, the distance is usually known and the rotation frequency and its derivatives are also known. This has important consequences: a null measurement is directly informative on the gravitational-wave emission—there is no question about whether a source is there in the first place. The search is simple because whatever the emission mechanism is, the gravitational frequency depends on the spin frequency, which is known. A detection would therefore immediately encode information on what is generating the gravitational waves. Because there is little to no uncertainty on

the gravitational waveform from a known pulsar, the number of templates that are searched is many orders of magnitude smaller than those investigated in surveys: the O2 data all-sky search of Steltner et al. (2021b) probed $\approx 10^{17}$ more templates than a targeted search. Fewer probed waveforms make targeted searches the most sensitive: the smallest detectable signal is a few times smaller than what the most sensitive broad survey could detect at the same frequency.

In this paper we present results from searches for emission from seven new pulsars using public data from all three Advanced LIGO observing runs (O1, O2 and O3; Abbott et al. 2021e and LIGO 2019a, 2019b, 2019c).

In this paper we introduce the signal model in Section 2, we detail the targeted objects in Section 3, the gravitational-wave searches are described in Section 4, and the results are presented and discussed in Section 5.

2. The Signal

The search described in this paper targets nearly monochromatic gravitational-wave signals of the form described, for example, in Section II of Jaranowski et al. (1998). In the calibrated strain data from a gravitational-wave detector the signal has the form

$$h(t) = F_+(\alpha, \delta, \psi; t)h_+(t) + F_\times(\alpha, \delta, \psi; t)h_\times(t), \quad (1)$$

with the “+” and “ \times ” indicating the two gravitational-wave polarizations. $F_+(\alpha, \delta, \psi; t)$ and $F_\times(\alpha, \delta, \psi; t)$ are the detector sensitivity pattern functions, which depend on relative orientation between the detector and the source, and hence on time t , on the position (α, δ) of the source, and on ψ , the polarization

angle. The waveforms $h_+(t)$ and $h_\times(t)$ are

$$\begin{aligned} h_+(t) &= A_+ \cos \Phi(t) \\ h_\times(t) &= A_\times \sin \Phi(t), \end{aligned} \quad (2)$$

with

$$\begin{aligned} A_+ &= \frac{1}{2} h_0 (1 + \cos^2 \iota) \\ A_\times &= h_0 \cos \iota. \end{aligned} \quad (3)$$

The angle between the total angular momentum of the star and the line of sight is $0 \leq \iota \leq \pi$ and $h_0 \geq 0$ is the intrinsic gravitational-wave amplitude. $\Phi(t)$ of Equation (2) is the phase of the gravitational-wave signal at time t . If τ_{SSB} is the arrival time of the wave with phase $\Phi(t)$ at the solar system barycenter, then $\Phi(t) = \Phi(\tau_{\text{SSB}}(t))$. The gravitational-wave phase as a function of τ_{SSB} is assumed to be

$$\begin{aligned} \Phi(\tau_{\text{SSB}}) &= \Phi_0 + 2\pi [f(\tau_{\text{SSB}} - \tau_{0\text{SSB}}) \\ &\quad + \frac{1}{2} \dot{f}(\tau_{\text{SSB}} - \tau_{0\text{SSB}})^2]. \end{aligned} \quad (4)$$

We take $\tau_{0\text{SSB}}$ consistently with the timing solution, and hence differently for every pulsar, as shown in Table 3.

3. The Pulsars

We target continuous gravitational-wave emission from seven recycled pulsars discovered and/or timed with data from the Arecibo 327 MHz Drift-Scan Pulsar Survey (AO327; Martinez et al. 2017, 2019): PSR J2204+2700, PSR J1411+2551, PSR J0709+0458, PSR J0824+0028, PSR J0732+2314, PSR J0509+0856, and PSR J0154+1833. For practicality we mostly use abbreviated forms of the names of the pulsars, omitting the ‘‘PSR’’ prefix and the part after the ‘‘+’’.

These pulsars have never been searched for before for gravitational-wave emission. They represent a relatively nearby sample, with distances smaller than 2 kpc, which is typical of all-sky surveys. This makes them particularly interesting for gravitational-wave searches, the only exception being 2204+2700, which is more distant, and also having an extremely low spin-down.

Our targets are all in binary systems except for J0154+1833, which is an isolated millisecond pulsar. Our set includes the radio pulsar in the notable double-neutron-star system PSR J1411+2551.

When available, we take the orbital inclination angle as estimate of the inclination angle ι for the determination of the constrained prior upper limit, see Section 5.1. We take the following values: $\iota_{\text{J1411}} = 0.83$ rad, $\iota_{\text{J0709}} = 1.30$ rad, $\iota_{\text{J0824}} = 1.32$ rad, $\iota_{\text{J0732}} = 0.93$ rad. For J0154, J0509, and J2204 we do not have an estimate of the inclination angle.

4. The Gravitational-wave Searches

We use LIGO public data from the Hanford (H1) and the Livingston (L1) detectors from the O1, O2, and the recently released first six months of the O3 science run (LIGO 2019a, 2019b, 2019c). The data is gated to remove loud glitches (Steltner et al. 2021a) and contiguous segments are Fourier transformed to produce the input to the search. After having excluded egregiously noisy segments in the band of each pulsar, we have ≈ 175 days of data from each detector

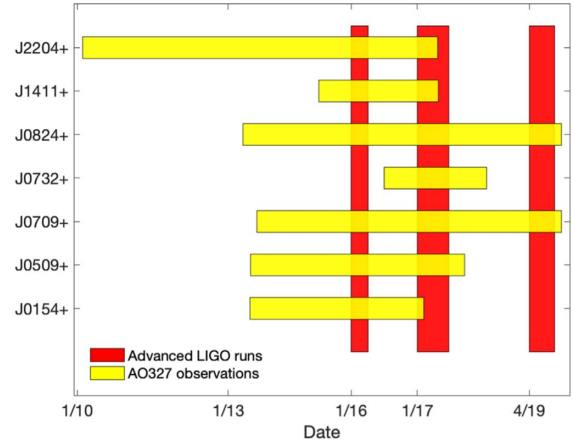


Figure 1. Time intervals corresponding to the O1, O2, and O3 LIGO runs are shown in red as vertical rectangles and the radio observation periods for each pulsar are shown in yellow as horizontal rectangles.

from the O1 and O2 runs combined, and ≈ 125 during the O3 run for H1 and ≈ 129 days for L1.

No glitch was recorded by the AO327 in any of the pulsars’ spins. As Figure 1 shows, these observations do not perfectly cover all the Advanced LIGO runs so we cannot exclude the possibility of a glitch. Even though our targets are very stable pulsars and a glitch is unlikely, we perform different searches and coherently combine the O1 and O2 data, the O3 data, and also all the data that we have, O1O2O3. We use the matched-filter detection statistic— \mathcal{F} -statistic (Cutler & Schutz 2005)—as our detection statistic. The \mathcal{F} -statistic is the maximum log-likelihood ratio of the signal hypothesis to the Gaussian-noise hypothesis. The signal is described by a frequency, spin-down, sky position, and orbital parameter values, which define the template waveform and are explicitly searched over. The signal amplitude parameters $\cos \iota$, ψ , Φ_0 , and h_0 are analytically maximized over.

In Gaussian noise the $2\mathcal{F}$ -statistic follows a noncentral chi-squared distribution with 4 degrees of freedom, $\chi_4^2(2\mathcal{F}, \rho^2)$. The noncentrality parameter ρ^2 is the expected squared signal-to-noise ratio and it is proportional to $h_0^2 T_{\text{data}}/S_h$, where T_{data} is the duration of time for which data is available and S_h is the strain power spectral density of the noise (Jaranowski et al. 1998).

For every pulsar and data set we conduct two searches: one with a single template with the gravitational-wave frequency f and spin-down \dot{f} being twice the spin frequency ν and spin-down $\dot{\nu}$, and one for a range of frequencies and spin-downs around these. The parameters of the targeted searches are given in Table 3 in the Appendix.

The search at $f = 2\nu$ is appropriate if the gravitational-wave frequency is exactly locked with the observed spin frequency. Mechanisms exist, however, that could produce a small difference between the gravitational-wave frequency and twice the spin frequency: a misalignment of the rotation axis with the symmetry axis of the star, causing free precession; or the component responsible for the gravitational-wave emission—for example a solid core—not spinning as the radio-emitting component. For such cases, it has been found that $f = 2\nu(1 \pm \delta_f)$ with $\delta_f \lesssim 10^{-4}$ (Jones & Andersson 2002; Abbott et al. 2008). With this in mind, we conservatively perform

searches over a band $\pm 2\nu \times 2 \times 10^{-3}$ of $f = 2\nu$, and consistently for \dot{f} .

For the band searches we set up a template grid in frequency and spin-down with spacings of 2.6×10^{-9} Hz and 1.9×10^{-17} Hz s $^{-1}$, respectively. These grids yield a maximum mismatch smaller than 1% for the O1O2 and O3 searches, and smaller than 8% for the O1O2O3 searches.

We also conduct the single-template searches using a Bayesian approach. We demodulate the data according to the expected signal, we heterodyne/downsample the data, and then search over the waveform amplitude parameters with a nested-sampling algorithm. The method is exactly the same as used by Abbott et al. (2019d), with the same uniform angular priors, namely $\Phi_0 \in [0, \pi]$, $\psi \in [0, \frac{\pi}{2}]$, $\cos \iota \in [-1, 1]$. For the intrinsic amplitude we adopt the same broad uniform prior for all sources with $h_0 \in [10^{-27}, 10^{-24}]$. The data used for this search is not gated. We report the results for the combined O1O2O3 data.

5. Results

In order to evaluate the significance of the search results we compute p -values. We do this because, based on insignificant p -values, we can exclude the presence of signals that we can confidently detect. We note, however, that a very low p -value in general is not enough to claim a confident detection.

The p -value associated with the realization $2\mathcal{F}'$ of a random variable is defined as

$$p(2\mathcal{F}') = \int_{2\mathcal{F}'}^{\infty} p_0(2\mathcal{F}) d2\mathcal{F}, \quad (5)$$

where p_0 is the distribution of $2\mathcal{F}$ in the presence of noise only.

If our data were Gaussian and our search pipelines were completely perfect implementations of the \mathcal{F} -statistic, $p_0 = \chi_4^2(2\mathcal{F}, 0)$. In reality the distribution of our search results may differ slightly from $\chi_4^2(2\mathcal{F}, 0)$, and for targeted searches we evaluate it on the actual data by running searches for fiducial sources at frequencies close to the target frequency.

None of the targeted searches yield a detection. Figure 2 shows the p -values for the targeted searches (blue circles): all the results for the targeted searches are consistent with the noise-only hypothesis. The most significant targeted-search result comes from PSR J0709 from the O3 data search, with a p -value of $\approx 23\%$. The product of the $\approx 55\%$ p -value of the O1O2 result and the O3 result is $\approx 12\%$, however the coherent O1O2O3 data search yields a totally insignificant p -value of $\approx 83\%$. The Bayesian posteriors of Figure 3 are consistent with the \mathcal{F} -stat results, with the only slightly off-zero posterior found for PSR J0709. Such a posterior is very broad, includes zero, and may happen just due to noise fluctuations. We also note that the target frequency for PSR J0709 is at ≈ 58 Hz, which is a highly contaminated region.

To evaluate the results from the band searches, for every pulsar we consider the most significant result in subbands that are 10 mHz wide, and compute the Gaussian-noise p -value associated with it. We do this by searching 10 mHz thousands of times, each time with a different Gaussian-noise realization. From each search we find the value of the loudest, $2\mathcal{F}_i$, and from the ensemble we estimate the $p_0(2\mathcal{F}_i)$, which we use to compute the p -value from Equation (5). Since we use Gaussian noise, this is a Gaussian-noise p -value and it is conservative (in the sense that we would not accidentally discard a potential signal) because in general it will overestimate the significance

of a result with respect to the p -value evaluated on real data. We do not use real data because each Monte Carlo realization covers 10 mHz; with thousands of independent realizations we would be considering target frequencies several hertz away from the original pulsar frequency, and at these distances there is no assurance that the noise is representative of the noise contributing to the original result. These p -values are the red circles shown in the left-hand-side plots in the first three rows of Figure 2.

We want to evaluate whether for any pulsar the band search yields a very significant result, so we consider the most significant (lowest) p -value found for each pulsar. One would then want to compare these lowest p -values but this cannot be done directly, because they do not come from the same distribution. In fact, simply due to the trials factor, the larger the band that has been searched, the lower the expected lowest p -value for that pulsar. To normalize the results and allow a direct comparison we estimate the trials factor to be equal to the number of independent 10 mHz subbands N^α searched for pulsar α , and introduce the following measure of significance for the most significant result for pulsar α :

$$s^\alpha = N^\alpha \min_{i \in [1, N^\alpha]} \{p_i^\alpha\}, \quad (6)$$

where p_i^α is the p -value associated with the i th subband: $p(2\mathcal{F}_i^\alpha)$. These quantities are shown in the right-hand-side plots of Figure 2.

A value of $s^\alpha < 1$ indicates that we would have to repeat the α -pulsar band search in random noise $1/s^\alpha$ times before we can expect a significant as the observed one. In this case s^α can be interpreted as a p -value. If $s^\alpha > 1$, it means that in a band search like the one conducted, in random noise, we expect that in s^α subbands the loudest values will be at least as significant as the observed result. For a detection we would need $s^\alpha \lll 1$.

The most significant result from the band searches comes again from PSR J0709 in the O1O2O3 coherent search and is at the level of $\approx 9\%$. However this significance is not confirmed in the O3 data where the lowest p -value (s^{J0709}) is 22% and it is at a different subband than the one that produced the O1O2O3 most significant result.

Figures 4 show the distributions of the most significant 10 mHz p -values and illustrate that they are consistent with the Gaussian-noise expectations for searches on all data.

5.1. Upper Limits

Based on the O1O2, O3, and O1O2O3 targeted-search results we place 95% confidence upper limits on the intrinsic gravitational-wave amplitude at the detector h_0 defined in Equation (3). We use a series of Monte Carlos where we simulate signals at a fixed amplitude in real data and measure the detection efficiency of our search. The detection criterion is that the obtained value of the detection statistic be equal or greater than the one found in the real search: if the measured detection statistic is high, a higher gravitational-wave amplitude will be needed in order for the signals to be detected. The amplitude for which 95% of the tested signals is detected is the upper limit value, $h_0^{95\%}$. With minor variations on the theme, this is the standard approach that we have taken for \mathcal{F} -statistic searches since the very first continuous waves search on LIGO data back in Abbott et al. (2004). The \mathcal{F} -stat upper limits are shown in Table 1.

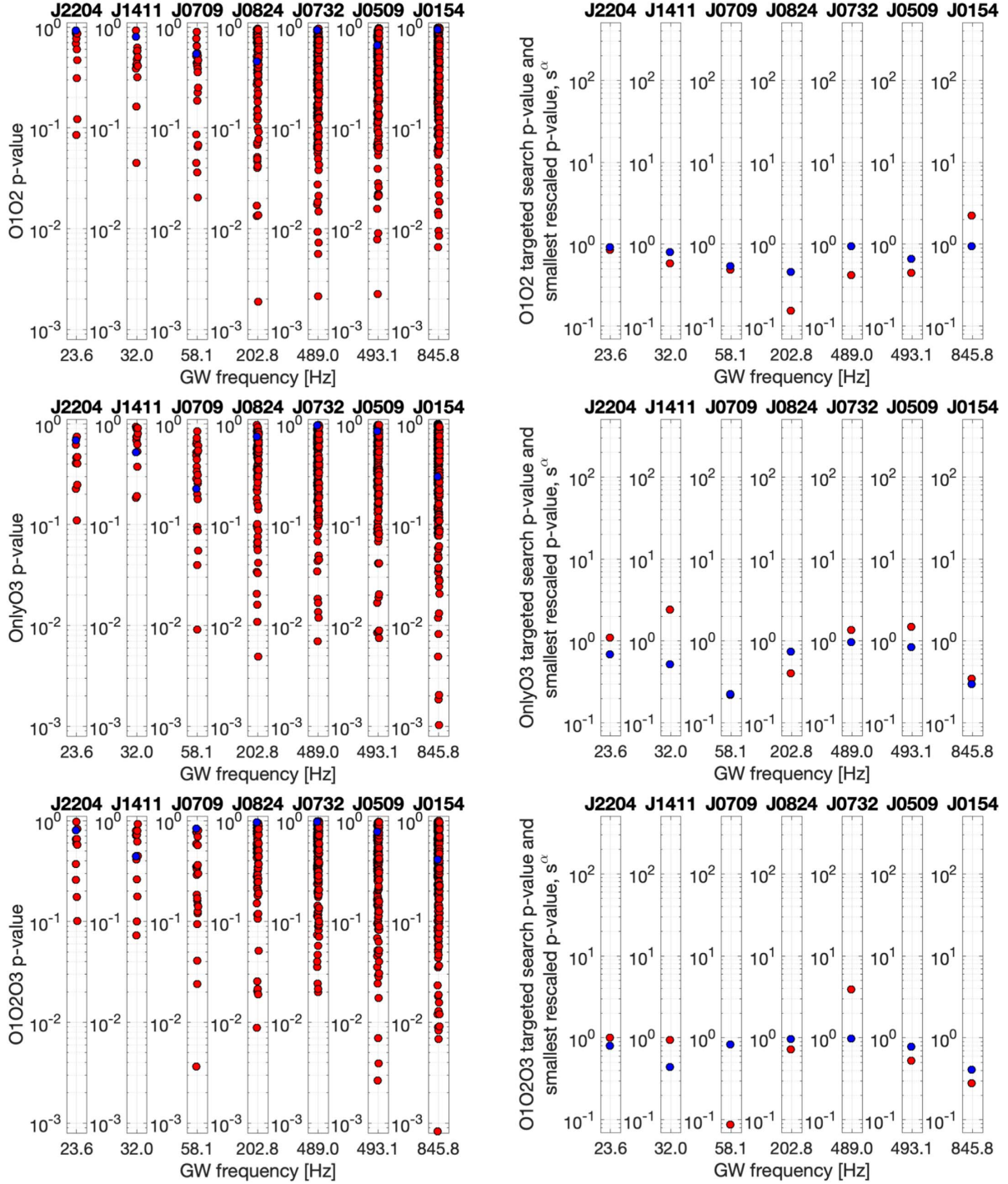


Figure 2. O1O2 (first row), O3 (second row), and O1O2O3 (third row) results. The blue circles show the p -values of the targeted searches. The red circles in the left-hand plots show the p -value of the most significant result in each 10 mHz subband of the band searches. These are generally higher than the targeted-search p -values because they are maxima over 10 mHz, whereas the targeted searches probe only a single waveform. The red circles in the right-hand plots show, for each pulsar, the lowest p -value among the subbands rescaled according to Equation (6), s^α . When $s^\alpha \leq 1$ it can be directly interpreted as a p -value. When $s^\alpha > 1$ it represents the number of 10 mHz subbands in which we would expect, in a band search of Gaussian-noise data such as that performed for pulsar α , to measure a result more significant than the most significant found in real data.

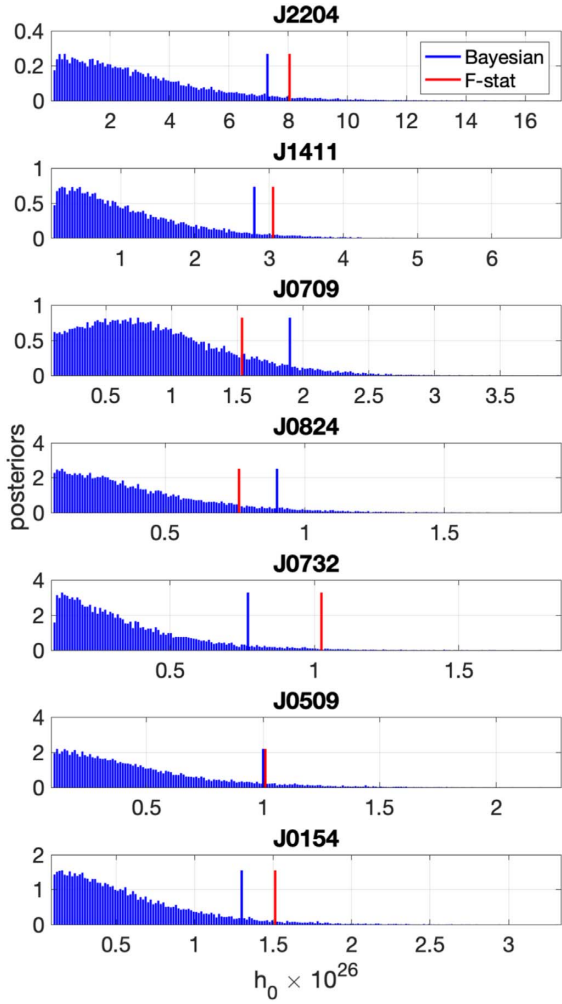


Figure 3. Bayesian posteriors for the combined O1O2O3 searches (blue) and associated 95% confidence upper limits. We also show (red) the \mathcal{F} -stat upper limits.

As discussed in the previous section the h_0 posteriors from the Bayesian analysis shown in Figure 3 are consistent with a null result. Because of this, the Bayesian upper limits are readily derived by integrating the posteriors up to a value such that the overall probability is the desired confidence level. Such value is the upper limit, and it represents the smallest extremum of the credible interval. The Bayesian upper limit values are shown in Table 2.

For the O1O2 band searches we divide the searched frequency range into 10 mHz subbands and take the most significant detection statistic value in that subband for our detection criteria. The subband searches probe numerous waveforms and so the loudest detection statistic value is going to be higher than for the targeted searches. Correspondingly the upper limits will also be higher, as shown in Figure 5 in the Appendix, typically by a factor of ≈ 2.7 . Since this is the most computationally intense part of this work, and we do not find evidence for a signal, we do not set upper limits based on the O3 data, or on the O1O2O3 data, but we

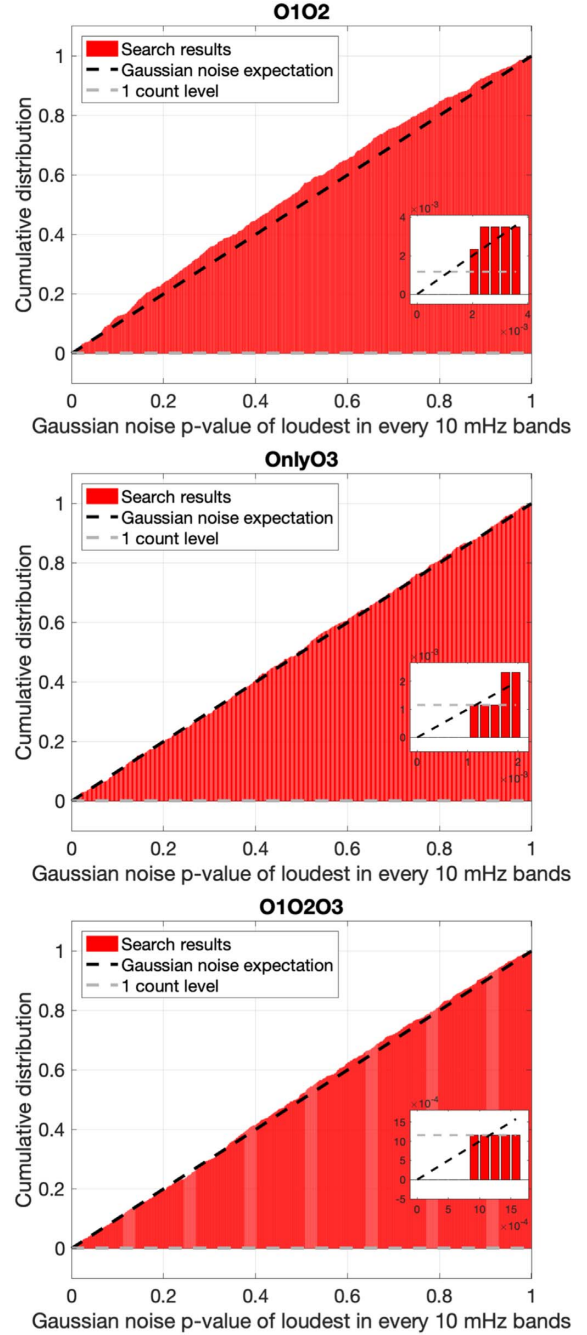


Figure 4. O1O2, O3, and O1O2O3 band-search results. For each 10 mHz frequency band searched, we show the cumulative distribution of the Gaussian p -value of the most significant result. If the data were Gaussian noise, the distribution would follow the dashed black line.

expect that these would also be higher than the corresponding targeted ones by a factor of a few.

The populations of fake signals used to determine the detection efficiencies have polarization angle ψ and initial

Table 1
95% Confidence Upper Limits on the Gravitational-wave Amplitude for the Targeted Searches Based on No Assumptions on the Inclination Angle (Unconstrained Prior) and if the Inclination Angle is the Same as the Estimated Value of the Orbital Inclination Angle (Constrained Prior), Using Different Data

Pulsar	f (Hz)	$h_0^{95\%}$	$h_0^{95\%}$	h_0^{spdown}	$\epsilon^{95\%}$	$\epsilon^{95\%}$	$h_0^{95\%}/h_0^{\text{spdown}}$	$h_0^{95\%}/h_0^{\text{spdown}}$
		Unconstrained Prior	Constrained Prior		Unconstrained Prior	Constrained Prior	Unconstrained Prior	Constrained Prior
O1 O2								
J0154	≈ 845.8	$2.7^{+0.5}_{-0.5} \times 10^{-26}$...	9.0×10^{-28}	3.1×10^{-08}	...	30.3	...
J0509	≈ 493.1	$1.9^{+0.5}_{-0.4} \times 10^{-26}$...	5.2×10^{-28}	1.1×10^{-07}	...	36.3	...
J0709	≈ 58.1	$3.3^{+0.5}_{-0.6} \times 10^{-26}$	$3.9^{+0.6}_{-0.7} \times 10^{-26}$	1.5×10^{-27}	1.6×10^{-05}	2.0×10^{-05}	21.9	26.5
J0732	≈ 489.0	$1.9^{+0.5}_{-0.4} \times 10^{-26}$	$1.4^{+0.4}_{-0.4} \times 10^{-26}$	5.8×10^{-28}	1.2×10^{-07}	9.2×10^{-08}	32.0	24.0
J0824	≈ 202.8	$1.4^{+0.3}_{-0.3} \times 10^{-26}$	$1.8^{+0.4}_{-0.4} \times 10^{-26}$	2.0×10^{-27}	4.9×10^{-07}	6.2×10^{-07}	6.9	8.8
J1411	≈ 32.0	$5.2^{+1.2}_{-1.4} \times 10^{-26}$	$3.6^{+0.9}_{-0.9} \times 10^{-26}$	1.1×10^{-27}	4.7×10^{-05}	3.2×10^{-05}	47.7	32.9
J2204	≈ 23.6	$1.5^{+0.4}_{-0.3} \times 10^{-25}$...	4.8×10^{-28}	5.6×10^{-04}	...	319.2	...
O3								
J0154	≈ 845.8	$1.9^{+0.4}_{-0.3} \times 10^{-26}$...	9.0×10^{-28}	2.2×10^{-08}	...	21.2	...
J0509	≈ 493.1	$1.2^{+0.2}_{-0.3} \times 10^{-26}$...	5.2×10^{-28}	6.9×10^{-08}	...	23.7	...
J0709	≈ 58.1	$2.2^{+0.3}_{-0.4} \times 10^{-26}$	$2.4^{+0.3}_{-0.1} \times 10^{-26}$	1.5×10^{-27}	1.1×10^{-05}	1.2×10^{-05}	14.6	16.1
J0732	≈ 489.0	$1.2^{+0.3}_{-0.3} \times 10^{-26}$	$10.0^{+2.5}_{-2.5} \times 10^{-27}$	5.8×10^{-28}	7.9×10^{-08}	6.6×10^{-08}	20.6	17.1
J0824	≈ 202.8	$9.9^{+1.5}_{-1.4} \times 10^{-27}$	$1.2^{+0.2}_{-0.3} \times 10^{-26}$	2.0×10^{-27}	3.5×10^{-07}	4.2×10^{-07}	5.0	5.9
J1411	≈ 32.0	$3.9^{+1.1}_{-1.1} \times 10^{-26}$	$2.7^{+0.7}_{-0.7} \times 10^{-26}$	1.1×10^{-27}	3.5×10^{-05}	2.5×10^{-05}	35.7	25.1
J2204	≈ 23.6	$9.9^{+2.6}_{-2.4} \times 10^{-26}$...	4.8×10^{-28}	3.6×10^{-04}	...	204.0	...
O1 O2 O3								
J0154	≈ 845.8	$1.5^{+0.3}_{-0.3} \times 10^{-26}$...	9.0×10^{-28}	1.7×10^{-08}	...	16.7	...
J0509	≈ 493.1	$1.0^{+0.2}_{-0.3} \times 10^{-26}$...	5.2×10^{-28}	5.7×10^{-08}	...	19.6	...
J0709	≈ 58.1	$1.5^{+0.3}_{-0.3} \times 10^{-26}$	$1.9^{+0.3}_{-0.4} \times 10^{-26}$	1.5×10^{-27}	7.7×10^{-06}	9.5×10^{-06}	10.3	12.7
J0732	≈ 489.0	$1.0^{+0.3}_{-0.3} \times 10^{-26}$	$7.8^{+2.5}_{-2.0} \times 10^{-27}$	5.8×10^{-28}	6.7×10^{-08}	5.1×10^{-08}	17.6	13.3
J0824	≈ 202.8	$7.6^{+1.6}_{-1.9} \times 10^{-27}$	$1.2^{+0.3}_{-0.2} \times 10^{-26}$	2.0×10^{-27}	2.7×10^{-07}	4.1×10^{-07}	3.8	5.8
J1411	≈ 32.0	$3.1^{+0.7}_{-0.7} \times 10^{-26}$	$2.2^{+0.4}_{-0.3} \times 10^{-26}$	1.1×10^{-27}	2.8×10^{-05}	2.0×10^{-05}	28.0	19.9
J2204	≈ 23.6	$8.1^{+2.0}_{-2.1} \times 10^{-26}$...	4.8×10^{-28}	2.9×10^{-04}	...	166.4	...

Note. We also show the spin-down upper limit calculated for a nominal value of the moment of inertia of 10^{38} kg m^2 , and the upper limits on the ellipticity of the star. The last two columns indicate how far our results are from being physically interesting: if $h_0^{95\%}/h_0^{\text{spdown}}$ is less than 1, then the upper limits are informative. (This table is available in machine-readable form.)

Table 2
Bayesian Upper Limits of O1–O2–O3 Targeted Searches (Unconstrained $\cos \iota$ Priors)

O1 O2 O3	$h_0^{95\%}$	$\epsilon^{95\%}$	$h_0^{95\%}/h_0^{\text{spdown}}$
Bayesian			
Pulsar			
J0154	1.3×10^{-26}	1.5×10^{-08}	14.9
J0509	1.0×10^{-26}	5.9×10^{-08}	20.1
J0709	1.9×10^{-26}	9.4×10^{-06}	12.5
J0732	7.7×10^{-27}	5.1×10^{-08}	13.2
J0824	9.0×10^{-27}	3.2×10^{-07}	4.5
J1411	2.8×10^{-26}	2.5×10^{-05}	25.9
J2204	7.3×10^{-26}	2.7×10^{-04}	151.4

(This table is available in machine-readable form.)

phase Φ_0 uniformly distributed as described in Section 4. For the orientation angle we consider two cases: $\cos \iota$ uniformly distributed in $[-1, 1]$ and fixed at the value of the orbital inclination, when available from the radio observations. We

refer to the resulting upper limits as *unconstrained* and *constrained*, respectively.

If we assume that the neutron star is a triaxial ellipsoid spinning around a principal moment of inertia axis I_{zz} , and that the continuous wave emission is due to an ellipticity

$$\epsilon = \frac{I_{xx} - I_{yy}}{I_{zz}}, \quad (7)$$

based on the intrinsic gravitational-wave amplitude upper limits $h_0^{95\%}$, we can exclude neutron star deformations above a $\epsilon^{95\%}$ level. The ellipticity needed for a neutron star at a distance D , spinning at $f/2$, to produce continuous gravitational waves with an intrinsic amplitude on Earth of h_0 is (Jaranowski et al. 1998; Gao et al. 2020):

$$\epsilon = 2.4 \times 10^{-7} \left(\frac{h_0}{1 \times 10^{-26}} \right) \times \left(\frac{D}{1 \text{ kpc}} \right) \left(\frac{200 \text{ Hz}}{f} \right)^2 \left(\frac{10^{38} \text{ kg m}^2}{I_{zz}} \right). \quad (8)$$

The ellipticity $\epsilon^{95\%}$ upper limits are given in Table 1.

5.2. Discussion

We have searched for continuous gravitational waves from seven pulsars that have not been targeted before. We use all the publicly available Advanced LIGO data, namely from the O1, O2, and O3 science runs.

We find no evidence of a gravitational-wave signal at a detectable level. The posterior probability distribution for PSR J0709 is peaked slightly off-zero, but this could well be a noise fluctuation as well as due to spectral contamination. At the lower frequencies in particular, it is not uncommon to find these posteriors, see for example Figure 3 of Abbott et al. (2020) showing the results for the Vela Pulsar from the search at ≈ 22 Hz. The \mathcal{F} -statistic results for the coherent O1O2O3 search are insignificant, which indicates that a coherent signal during all the observations is not detected. On the other hand PSR J0709 is one of the only two pulsars for which the radio observations overlap with all the LIGO runs, so we are most confident of the used template waveform.

For more than half of the pulsar sample, our searches probe ellipticities $\lesssim 3 \times 10^{-7}$, which could be sustained by neutron star crusts (Johnson-McDaniel & Owen 2013; Bhattacharyya 2020; Gittins et al. 2021). Our tightest ellipticity bound amounts to 1.7×10^{-8} (1.5×10^{-8} from the Bayesian analysis), for PSR J0154. The remaining four pulsars are more distant and/or spin slower, this yields less-constraining upper ellipticity limits. For the pulsar PSR J0824, assuming a canonical moment of inertia of 10^{38} kg m², our upper limits are within a factor of 3.8 (5.8) of the spin-down upper limit, for an unconstrained and constrained $\cos \iota$ prior, respectively. The actual moment of inertia of the star may differ from the canonical one up by a factor of a few. These are physically interesting ellipticity ranges (Woan et al. 2018), and showcase the potential for this type of search.

All the computational work for these searches was performed on the ATLAS cluster at AEI Hannover. We thank Carsten Aulbert and Henning Fehrmann for their support.

We would like to especially thank the instrument scientists and engineers of LIGO whose amazing work has produced detectors capable of probing gravitational waves that are so incredibly small.

This research has made use of data, software and/or web tools obtained from the Gravitational Wave Open Science Center (<https://www.gw-openscience.org/>), a service of LIGO Laboratory, the LIGO Scientific Collaboration, and the Virgo Collaboration. LIGO Laboratory and Advanced LIGO are funded by the United States National Science Foundation (NSF) as well as the Science and Technology Facilities Council (STFC) of the United Kingdom, the Max-Planck-Society (MPS), and the State of Niedersachsen/Germany for support of the construction of Advanced LIGO and construction and operation of the GEO600 detector. Additional support for Advanced LIGO was provided by the Australian Research Council. Virgo is funded, through the European Gravitational Observatory (EGO), by the French Centre National de Recherche Scientifique (CNRS), the Italian Istituto Nazionale di Fisica Nucleare (INFN), and the Dutch Nikhef, with contributions by institutions from Belgium, Germany, Greece, Hungary, Ireland, Japan, Monaco, Poland, Portugal, and Spain.

Appendix A Targeted Search Parameters

The parameters of the gravitational-wave templates for the pulsars in this search are provided in Table 3.

Table 3
Gravitational Waveform Parameters

Pulsar	GW Frequency f (Hz)	GW Freq. Derivative \dot{f} (Hz s ⁻¹)	R.A. (rad)	Decl. (rad)	Epoch T_{USSB} (MJD)	Proj. Semimajor Axis $a \sin i$ (lt-s)	Binary Period (s)	Eccentricity	Arg. of Periastron ω (rad)	Distance (pc)
J2204	≈ 23.6	-3.652×10^{-17}	5.7802112	0.4715040	56,805.0	210.680632593	70,437,206.11210689	0.00152	0.1118	2150
J1411	≈ 32.0	-4.904×10^{-17}	3.7145600	0.4512083	57,257.864168	9.204790917	226,010.02575114663	0.16993	1.4209	977
J0709	≈ 58.1	-6.418×10^{-16}	1.8724740	0.0869343	56,983.893691	15.716582025	377,281.1771422851	0.00023	5.6319	1790
J0824	≈ 202.8	-3.021×10^{-15}	2.2009213	0.0081476	56,600.0	18.988928488	2,005,081.527370442	0.00023	0.8084	1530
J0732	≈ 489.0	-7.344×10^{-16}	1.9749503	0.4057610	58,000.0	10.625842295	2,611,878.6842582175	0.00001	1.1879	1660
J0509	≈ 493.1	-5.366×10^{-16}	1.3498838	0.1560374	57,384.0	2.458025534	424,049.2036136159	0.00002	0.5642	1450
J0154	≈ 845.8	-1.046×10^{-15}	0.5001010	0.3240047	56,900.0	860

Appendix B
Band Search Upper Limit Plots

In this Appendix, in Figure 5, we show the O1O2 band search upper limit results and for reference we also plot the targeted-search upper limits.

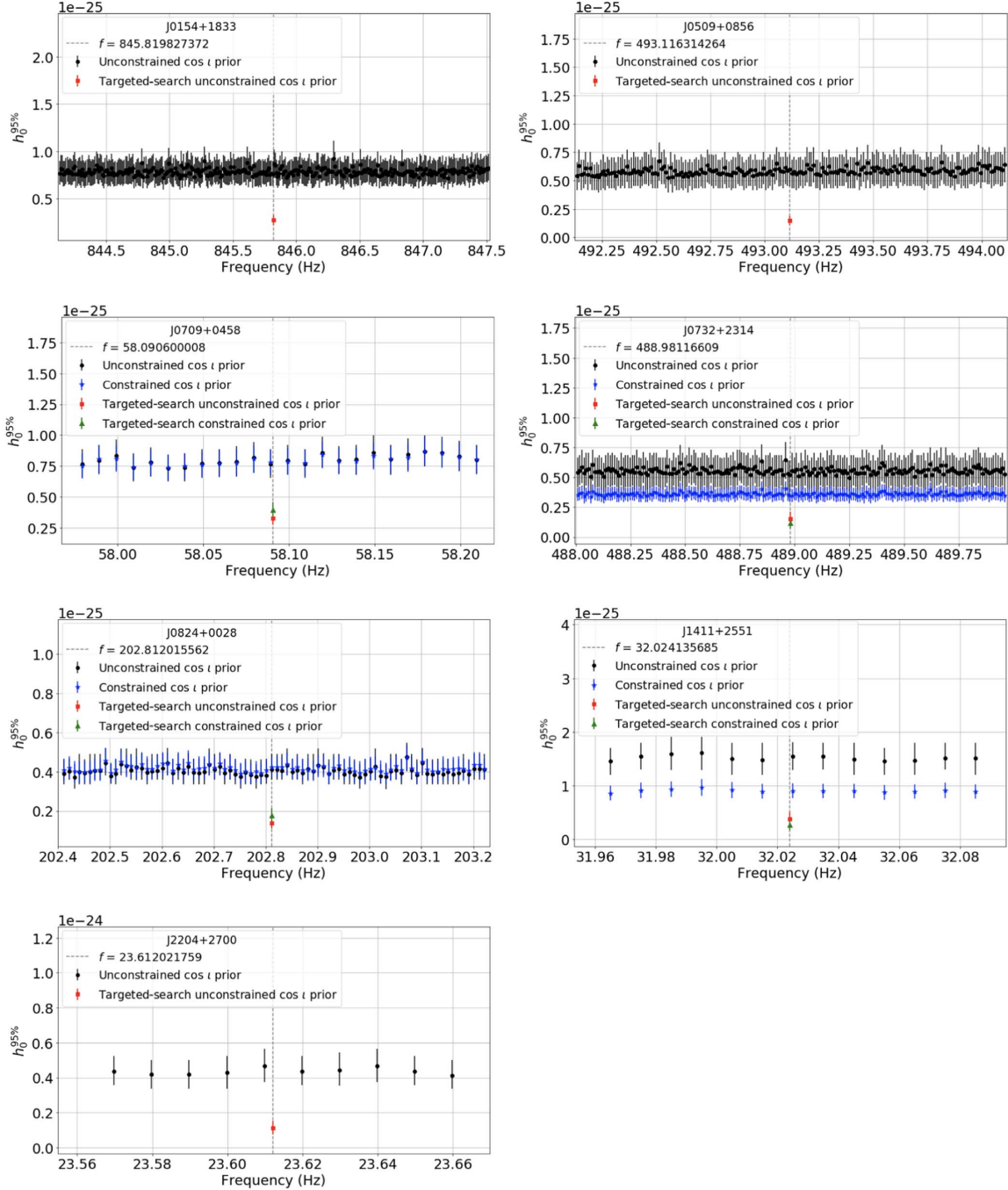


Figure 5. O1O2 data upper limits on the gravitational-wave amplitude in each 10 mHz frequency subband searched, based on the most significant result in that 10 mHz subband. We also show the targeted-search results, which are the lower points at the central frequency, which is twice the pulsar rotation frequency.

ORCID iDs

A. Ashok  <https://orcid.org/0000-0002-8395-957X>
 B. Beheshtipour  <https://orcid.org/0000-0002-8524-1537>
 M. A. Papa  <https://orcid.org/0000-0002-1007-5298>
 P. C. C. Freire  <https://orcid.org/0000-0003-1307-9435>
 B. Steltner  <https://orcid.org/0000-0003-1833-5493>
 O. Behnke  <https://orcid.org/0000-0003-0679-8562>
 B. Allen  <https://orcid.org/0000-0003-4285-6256>
 R. Prix  <https://orcid.org/0000-0002-3789-6424>

References

- Abbott, B., Abbott, R., Adhikari, R., et al. 2004, *PhRvD*, **69**, 082004
 Abbott, B., Abbott, R., Adhikari, R., et al. 2008, *ApJL*, **683**, L45
 Abbott, B. P., Abbott, R., Abbott, T. D., et al. 2019a, *PhRvD*, **100**, 024004
 Abbott, B. P., Abbott, R., Abbott, T. D., et al. 2019b, *ApJ*, **879**, 10
 Abbott, B. P., Abbott, R., Abbott, T. D., et al. 2019c, *PhRvD*, **99**, 122002
 Abbott, B. P., Abbott, R., Abbott, T. D., et al. 2019d, *ApJ*, **879**, 10
 Abbott, R., Abbott, T. D., Abraham, S., et al. 2020, *ApJL*, **902**, L21
 Abbott, R., Abbott, T. D., Abraham, S., et al. 2021a, *PhRvD*, **104**, 082004
 Abbott, R., Abbott, T. D., Abraham, S., et al. 2021b, *ApJ*, **921**, 80
 Abbott, R., Abbott, T. D., Abraham, S., et al. 2021c, *ApJ*, **913**, L27
 Abbott, R., Abbott, T. D., Abraham, S., et al. 2021d, arXiv:2104.14417
 Abbott, R., Abbott, T. D., Abraham, S., et al. 2021e, *SoftX*, **13**, 100658
 Bhattacharyya, S. 2020, *MNRAS*, **498**, 728
 Covas, P. B., & Sintes, A. M. 2020, *PhRvL*, **124**, 191102
 Cutler, C., & Schutz, B. F. 2005, *PhRvD*, **72**, 063006
 Dergachev, V., & Papa, M. A. 2020, *PhRvL*, **125**, 171101
 Dergachev, V., & Papa, M. A. 2021, *PhRvD*, **103**, 063019
 Fesik, L., & Papa, M. A. 2020, *ApJ*, **895**, 11
 Gao, Y., Shao, L., Xu, R., et al. 2020, *MNRAS*, **498**, 1826
 Gittins, F., Andersson, N., & Jones, D. 2021, *MNRAS*, **500**, 5570
 Jaranowski, P., Krolak, A., & Schutz, B. F. 1998, *PhRvD*, **58**, 063001
 Johnson-McDaniel, N. K., & Owen, B. J. 2013, *PhRvD*, **88**, 044004
 Jones, D., & Sun, L. 2021, *PhRvD*, **103**, 023020
 Jones, D. I. 2015, *MNRAS*, **453**, 53
 Jones, D. I., & Andersson, N. 2002, *MNRAS*, **331**, 203
 Lasky, P. D. 2015, *PASA*, **32**, e034
 LIGO 2019a, The O1 Data Release, <https://www.gw-openscience.org/O1/>
 LIGO 2019b, The O2 Data Release, <https://www.gw-openscience.org/O2/>
 LIGO 2019c, The O3 Data Release, <https://www.gw-openscience.org/O3/O3a/>
 Lindblom, L., & Owen, B. J. 2020, *PhRvD*, **101**, 083023
 Martinez, J. G., Gentile, P., Freire, P. C. C., et al. 2019, *ApJ*, **881**, 166
 Martinez, J. G., Stovall, K., Freire, P. C. C., et al. 2017, *ApJL*, **851**, L29
 Ming, J., Papa, M. A., Singh, A., et al. 2019, *PhRvD*, **100**, 024063
 Nieder, L., Clark, C. J., Bassa, C. G., et al. 2019, *ApJ*, **883**, 42
 Nieder, L., Clark, C. J., Kandel, D., et al. 2020, *ApJL*, **902**, L46
 Papa, M. A., Ming, J., Gotthelf, E. V., et al. 2020, *ApJ*, **897**, 22
 Steltner, B., Papa, M. A., & Eggenstein, H.-B. 2021a, arXiv:2105.09933
 Steltner, B., Papa, M. A., Eggenstein, H. B., et al. 2021b, *ApJ*, **909**, 79
 Woan, G., Pitkin, M., Haskell, B., Jones, D., & Lasky, P. 2018, *ApJL*, **863**, L40
 Zhang, Y., Papa, M. A., Krishnan, B., & Watts, A. L. 2021, *ApJL*, **906**, L14



The TRAPUM *L*-band survey for pulsars in *Fermi*-LAT gamma-ray sources

C. J. Clark^{1,2,3*}, R. P. Breton³, E. D. Barr⁴, M. Burgay⁵, T. Thongmeekom³, L. Nieder^{1,2}, S. Buchner⁶, B. Stappers³, M. Kramer^{4,3}, W. Becker^{7,4}, M. Mayer⁷, A. Phosrisom³, A. Ashok^{1,2}, M. C. Bezuidenhout³, F. Calore⁸, I. Cognard^{9,10}, P. C. C. Freire⁴, M. Geyer⁶, J.-M. Grießmeier^{9,10}, R. Karuppusamy⁴, L. Levin³, P. V. Padmanabh^{4,1,2}, A. Possenti⁵, S. Ransom¹¹, M. Serylak^{12,13}, V. Venkatraman Krishnan⁴, L. Vleeschower³, J. Behrend⁴, D. J. Champion⁴, W. Chen⁴, D. Horn⁶, E. F. Keane¹⁴, L. Küinkel¹⁵, Y. Men⁴, A. Ridolfi^{5,4}, V. S. Dhillon^{16,17}, T. R. Marsh¹⁸ and M. A. Papa^{1,2}

Affiliations are listed at the end of the paper

Accepted 2022 December 13. Received 2022 December 13; in original form 2022 October 14

ABSTRACT

More than 100 millisecond pulsars (MSPs) have been discovered in radio observations of gamma-ray sources detected by the *Fermi* Large Area Telescope (LAT), but hundreds of pulsar-like sources remain unidentified. Here, we present the first results from the targeted survey of *Fermi*-LAT sources being performed by the Transients and Pulsars with MeerKAT (TRAPUM) Large Survey Project. We observed 79 sources identified as possible gamma-ray pulsar candidates by a Random Forest classification of unassociated sources from the 4FGL catalogue. Each source was observed for 10 min on two separate epochs using MeerKAT's *L*-band receiver (856–1712 MHz), with typical pulsed flux density sensitivities of $\sim 100 \mu\text{Jy}$. Nine new MSPs were discovered, eight of which are in binary systems, including two eclipsing redbacks and one system, PSR J1526–2744, that appears to have a white dwarf companion in an unusually compact 5 h orbit. We obtained phase-connected timing solutions for two of these MSPs, enabling the detection of gamma-ray pulsations in the *Fermi*-LAT data. A follow-up search for continuous gravitational waves from PSR J1526–2744 in Advanced LIGO data using the resulting *Fermi*-LAT timing ephemeris yielded no detection, but sets an upper limit on the neutron star ellipticity of 2.45×10^{-8} . We also detected X-ray emission from the redback PSR J1803–6707 in data from the first eROSITA all-sky survey, likely due to emission from an intrabinary shock.

Key words: binaries: general – pulsars: general – pulsars: individual: J1036–4353, J1526–2744, J1803–6707 – gamma rays: stars.

1 INTRODUCTION

Observations by the Large Area Telescope (LAT; Atwood et al. 2009) onboard the *Fermi* Gamma-ray Space Telescope have led to the detection of gamma-ray pulsations from nearly 300 pulsars¹ (The *Fermi*-LAT Collaboration, in preparation). These fall into two main classes: canonical pulsars that are still rapidly spinning-down from their initial rotation periods; and millisecond pulsars (MSPs) that have been spun-up (or ‘recycled’ Bhattacharya & van den Heuvel 1991) to rates of hundreds of rotations per second by accretion from an orbiting star (Smarr & Blandford 1976; Alpar et al. 1982).

Both pulsar classes have characteristic gamma-ray emission properties (curved spectra and low flux variability over time) that are distinct from those of other gamma-ray emitting objects (e.g. Ackermann et al. 2012). These properties can be used to identify promising

pulsar-like gamma-ray sources, which can then be targeted with radio telescopes to detect pulsations and confirm their nature (Ray et al. 2012). The few-arcmin localization regions of unassociated *Fermi*-LAT sources enable targeted, long and repeated observations of promising sources, and a higher detection efficiency than can be achieved when surveying a broad region of the sky.

This method has proven highly successful at discovering new MSPs; more than a quarter of the 400 MSPs known in the Galactic field have been discovered in *Fermi*-LAT sources² (e.g. Cognard et al. 2011; Keith et al. 2011; Ransom et al. 2011; Kerr et al. 2012; Barr et al. 2013; Camilo et al. 2015; Cromartie et al. 2016) in a global effort coordinated by the *Fermi* Pulsar Search Consortium (Ray et al. 2012). These searches have been particularly effective in finding exotic but elusive ‘spider’ binary pulsars (‘black widows’ and ‘redbacks’, Roberts 2012) whose long radio eclipses due to diffuse intrabinary material make them easily missed in single-pass

* E-mail: colin.clark@aci.mpg.de

¹<http://tinyurl.com/fermipulsars>

²<http://astro.phys.wvu.edu/GalacticMSPs/>

untargeted surveys. Around two-thirds of the known spider binaries in the Galactic field were found by targeting *Fermi* sources².

Many new MSPs remain to be found amongst the LAT sources: pulsars make up around 6 per cent of the identified or associated³ sources in the recent 12-yr iteration (Abdollahi et al. 2022, hereafter 4FGL DR3) of the *Fermi*-LAT Fourth Source Catalog (Abdollahi et al. 2020, hereafter 4FGL), while over 2000 sources remain unassociated. Observed gamma-ray and radio fluxes from pulsars are not strongly correlated with one another (Abdo et al. 2013; The Fermi-LAT Collaboration, in preparation), and so prospects remain high for detecting radio pulsars even in faint new gamma-ray sources that have only recently been detected thanks to the exposure that has accumulated during *Fermi*'s ongoing all-sky survey. This also means that new radio MSPs discovered within faint new *Fermi*-LAT sources can still be bright enough to be valuable astrophysical tools, and indeed several new MSPs found using this method have been added to pulsar timing array (PTA) projects aiming to detect gravitational waves (e.g. Spiewak et al. 2022).

The potential importance of detecting new MSPs in *Fermi*-LAT sources is illustrated by the fact that several previous discoveries found in this manner now mark the extreme edges of the MSP population, and are therefore the best current probes for several fundamental astrophysics questions. These include: the fastest known Galactic MSP (PSR J0952–0607, Bassa et al. 2017); the pulsar binary system with the shortest known orbital period (PSR J1653–0158, Nieder et al. 2020b); and a group of massive black-widow MSPs that probe the maximum neutron star mass (Romani et al. 2022).

One crucial benefit of finding a new MSP within a gamma-ray source is that gamma-ray pulsations can often be detected and timed directly in the *Fermi*-LAT data. Initial timing solutions can be refined and extrapolated backwards to the start of the LAT data (which currently spans more than 14 yr), providing long and precise rotational ephemerides without the need for lengthy radio timing campaigns. Illustrating the potential scientific benefits of this capability, gamma-ray timing of the recently discovered black-widow PSR J1555–2908 (Ray et al. 2022) may have revealed a second, planetary mass object in a long period orbit around the inner binary system (Nieder et al. 2022). The LAT data have also even been recently exploited to build a gamma-ray PTA (The Fermi-LAT Collaboration 2022), whose sensitivity to a stochastic gravitational wave background may reach that of current radio PTAs within a decade. While searches for pulsations in the *Fermi*-LAT data itself can reveal new MSPs (e.g. Pletsch et al. 2012; Clark et al. 2018), trials factors and computational costs limit these searches to the brighter pulsars. The detection of gamma-ray pulsations from MSPs in binary systems (which most are) is also impossible without prior orbital constraints (Nieder et al. 2020a). Radio surveys and initial timing therefore remain critical for expanding the population of Galactic MSPs.

The efforts of searching for new MSPs in *Fermi*-LAT sources have recently been bolstered by new radio telescopes. These bring capabilities of observing in new parameter spaces (e.g. at low radio frequencies with LOFAR and GMRT, Bassa et al. 2017; Pleunis

et al. 2017; Bhattacharyya et al. 2021) or with greater sensitivity (e.g. FAST; Wang et al. 2021).

In this paper, we present the first results from one such new survey of unassociated *Fermi*-LAT sources, using the MeerKAT radio telescope (Jonas 2009; Jonas & MeerKAT Team 2016). The full MeerKAT array is around five times more sensitive than the Murriyang Parkes telescope (Bailes et al. 2020), the next most sensitive radio telescope in the Southern Hemisphere. The Transients and Pulsars with MeerKAT (TRAPUM) project is a large survey project using MeerKAT to search for new pulsars (Stappers & Kramer 2016). All TRAPUM observations target sky locations in which pulsars are particularly likely to lie: globular clusters (Ridolfi et al. 2021); nearby galaxies (Carli et al. 2022); supernova remnants, pulsar wind nebulae and other TeV sources; and GeV gamma-ray sources. A separate dedicated *L*-band survey of the Galactic plane (MMGPS-L) is also ongoing using the same instrumentation and processing infrastructure (Kramer et al. 2016, Padmanabh et al., in preparation). To date, the TRAPUM and MMGPS-L searches have discovered more than 150 new pulsars,⁴ the majority of which are MSPs. Here, we present the first results from TRAPUM's survey of unassociated *Fermi*-LAT sources, which led to 9 of these MSP discoveries.

The paper is organized as follows: Section 2 describes the survey setup (recording and processing infrastructure, target selection and observation strategy); Section 3 presents the new discoveries and subsequent investigation (localization, timing and multiwavelength follow-ups) and an estimate of the survey's sensitivity; and finally a brief discussion and conclusions follow in Sections 4 and 5.

2 SURVEY PROPERTIES

2.1 MeerKAT and the TRAPUM processing infrastructure

MeerKAT is a radio interferometer located in the Karoo, South Africa, consisting of 64 antennas with 13.5-m effective diameter. Here, we give a brief description of MeerKAT and the TRAPUM infrastructure used to perform our pulsar search observations. For a full technical description of the instrument, we refer the reader to Jonas & MeerKAT Team (2016). At the time of data taking (between 2020 June and 2021 February), two receivers were available: the *L*-band receiver operating between 856 and 1712 MHz and the Ultra High Frequency (UHF) receiver between 544 and 1088 MHz. This survey was conducted at *L* band, but follow-up observations of new pulsars were also made at UHF.

At the *L*-band centre frequency, a coherent tied-array beam produced using all 64 MeerKAT antennas has a typical full width at half-maximum of the order of a few arcseconds. Furthermore, the data rate of complex voltages from the antennas is too high to record while observing. Efficiently searching the several-arcmin localization region of an unassociated *Fermi*-LAT source in a single pointing therefore relies on the ability to form and record the Stokes intensities from a large number of coherent beams simultaneously. This capability is provided by the Filterbanking BeamFormer User Supplied Equipment (FBFUSE), a 32-node, GPU-based, software beamformer developed by the Max Planck Institute for Radio Astronomy (Barr 2018; Chen et al. 2021). FBFUSE coherently sums the channelized complex voltages in real time, using sky position-dependent complex weights computed by the purpose-built *Mosaic* software⁵ from a delay model provided by the MeerKAT

³Gamma-ray sources are only deemed 'identified' if they have pulsed gamma-ray emission, gamma-ray variability that correlates with that seen in other wavelengths, or are resolved and have an angular extent consistent with that of a known source seen at other wavelengths. If a known source is likely to be the source of the gamma-ray emission, but these conditions are not met, then the gamma-ray source is described as 'associated' but not identified.

⁴<http://trapum.org/discoveries/>

⁵<https://github.com/wchenastro/Mosaic>

Science Data Pipeline. FBFUSE can produce channelized time series for up to 864 coherent beams, as well as one incoherent beam produced by summing the (real-valued) Stokes intensities from each antenna. FBFUSE's beamforming algorithm requires a multiple of four antennas, and not all antennas are available for all observations. As such, we used either 56 or 60 antennas during our observations, depending on availability.

The channelized data from each coherent beam are then recorded on to a distributed 3.5-PiB file system accessible from the Accelerated Pulsar Search User Supplied Equipment (APSUSE) instrument, a second, 60-node computer cluster, with two NVIDIA GeForce GTX 1080 Ti GPUs per node, on which the pulsar search takes place. The number of beams that can be stored is limited by the data rate at which APSUSE can record, and so down-sampling in time from the native data rate is necessary for a large number of beams to be recorded. All of our observations used the 4096-channel MeerKAT F-engine channeliser mode, but beamformed spectra were down-sampled in time by a factor of 16 from the native time resolution (4096/856 MHz = 4.785 μ s) to give 76- μ s time resolution. With these time and frequency resolutions, up to 288 coherent beams could be formed and recorded. Additionally, downsampling in frequency by a factor of 2 allowed for 480 coherent beams with 2048 frequency channels. Both of these recording modes were used in our survey.

The full set of filterbank files for 480 coherent beams constitute 46 TiB of data per hour of observation, allowing at most 73 h of data in this format to be stored for processing on APSUSE. It was therefore necessary to process these data quickly, identify promising candidates for further follow-up, and delete the raw data to ensure there was sufficient storage space for other TRAPUM projects to continue observing. Only the filterbank files for beams in which promising candidates were identified were retained for later use.

2.2 Observing strategy

The very high gain and low system temperature of the MeerKAT array ($G = 2.8 \text{ K Jy}^{-1}$ for the full array and $T_{\text{sys}} = 18 \text{ K}$, Bailes et al. 2020) enable the detection of pulsars with low flux densities, even with short observation lengths. This motivated a strategy involving short pointings towards as many sources as possible. We chose 10-min observations, for which we still obtain flux density limit estimates of around $95 \mu\text{Jy}$ that compare favourably against previous surveys of Southern sources with longer observations (see Sections 3.4 and 4).

Previous surveys for MSPs within unidentified *Fermi*-LAT sources have revealed the importance of observing sources more than once to mitigate non-detections due to scintillation (Camilo et al. 2015) or unfavourable orbital phases (e.g. due to spider eclipses or 'jerk' effects Andersen & Ransom 2018). In this paper, we describe the first two passes of this survey, both performed at *L* band. At least two further passes are planned for each source at the UHF band, where the lower frequency will provide additional sensitivity to pulsars with steep spectra, but where propagation effects and dispersive smearing are larger.

During each observation, FBFUSE can be configured to form coherent beams that are distributed within the primary field of view either at pre-specified locations, or automatically using an optimal hexagonal tiling pattern. In this latter mode, used for all of our survey observations, the beam spacing is defined by an overlap parameter, which is the fractional sensitivity level of a 2D Gaussian function fit to the tied-array beam response, simulated by *Mosaic* (see Chen et al. 2021) at the centre of the frequency band, at the point mid-way between two neighbouring beams. The simple Gaussian model of

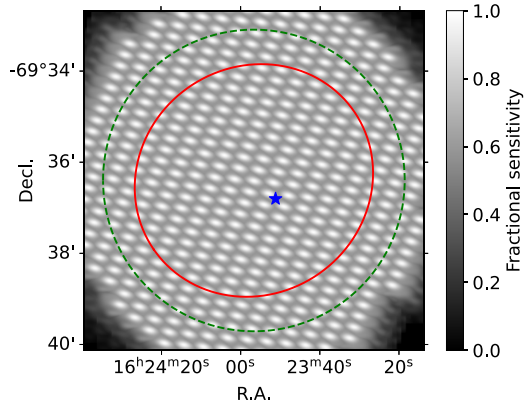


Figure 1. An example of the coherent beam tiling pattern, from the second observation of 4FGL J1623.9–6936. The greyscale image shows the fractional sensitivity according to the *Mosaic* beam simulation, maximized over neighbouring coherent tied-array beams, reaching 100 per cent at the centre of each beam. The solid red ellipse is the 95 per cent confidence region for the *Fermi*-LAT source. The dashed green circle shows the minimum region that we aimed to cover, and has a radius corresponding to the semimajor axis of an approximate 99 per cent confidence region. The blue star shows the location of PSR J1623–6936 discovered in this observation. The positional uncertainty (obtained in Section 3.2) is smaller than this marker.

the earlier versions of *Mosaic*, used for all our survey observations, tended to overestimate the true overlap when using the full MeerKAT array, and so e.g. points mid-way between beams in a tiling with an intended 50 per cent overlap actually only achieved ~ 40 per cent sensitivity.

In the first pass of all our targeted sources, we used the 4096-channel mode, with a maximum of 288 coherent beams. The beam tiling patterns for each source were configured with a desired overlap of 50 per cent. We prioritized observing sources with larger positional uncertainties when they were at lower elevations, where the coherent tied-array beams covered a larger solid angle, to ensure that the full localization region could be covered. For the sources with the largest uncertainty regions, observations were scheduled to ensure a sufficiently low elevation that the beam tiling covered a circle with a radius at least as large as the semimajor axis of the elliptical 95 per cent confidence region (hereafter r_{95}) from 4FGL. No significant sensitivity penalty due to ground spillover is incurred for elevations above 30° . For better-localized sources, the outer beams were well outside the *Fermi* source region.

Further development of FBFUSE after our survey began provided the capability to alter the tiling overlap between sources within one observing block. For 75 per cent of the observations in the second pass, we used the 2048-channel, 480-beam mode and adjusted the tiling overlaps for each source to maximize sensitivity while ensuring that the coherent beams covered a circular region with radius at least $r = \sqrt{\log(0.01)/\log(0.05)} r_{95}$, the semimajor axis of an approximate 99 per cent-confidence ellipse. An example of the resulting tiling pattern is shown in Fig. 1. All sources had $r_{95} < 5$ arcmin, such that the tiled region covered a very small patch around the centre of the ~ 1 deg primary beam, meaning no significant sensitivity loss occurs for coherent beams that are not located at the central pointing position.

2.3 Search pipeline

The filterbank data from all coherent tied-array beams and incoherent beams were searched by a dedicated pipeline built around the `peasoup`⁶ GPU-accelerated pulsar search code, which performs an FFT-based acceleration search via time-domain resampling with incoherent harmonic summing (Barr 2020, and described in detail in Morello et al. 2019).

The data were de-dispersed at trial dispersion measures (DMs) up to 300 pc cm^{-3} with spacing $\Delta\text{DM} = 0.06 \text{ pc cm}^{-3}$. This range covers the maximum DMs predicted by the Galactic electron density model of Yao, Manchester & Wang (2017, hereafter YMW16) in the direction of any of our target sources, and 70 of our 79 target sources have maximum predicted DMs that are less than half of this range (i.e. below 150 pc cm^{-3}).

The acceleration search covered a range of $a \pm 50 \text{ m s}^{-2}$, which is slightly less than twice as large as the maximum acceleration seen from any known fully recycled binary MSP (26.1 m s^{-2} from PSR J0024–7204V, Ridolfi et al. 2016) in the ATNF Pulsar Catalogue (v1.65, Manchester et al. 2005). Higher accelerations have been observed from relativistic binaries, such as pulsars with massive white dwarf companions or double neutron star systems, but these are all mildly recycled systems, which typically do not have sufficient spin-down power to emit gamma-ray pulsations, although the Double Pulsar is one notable exception (Guillemot et al. 2013). At each trial DM, the spacing between acceleration trials was chosen according to the scheme described in Morello et al. (2019), which ensures that signals lying between two acceleration trials suffer a total smearing that is not more than 10 per cent larger than the other (unavoidable) smearing effects due to intrachannel dispersion smearing and finite time resolution.

After performing the acceleration search, a clustering algorithm was used to search for clusters of candidates from neighbouring coherent beams with similar periods and DMs. Candidates with periods close to known radio-frequency interference (RFI) signals were excluded. This clustering step also aims to distinguish between astrophysical and terrestrial RFI signals, based on how the signal-to-noise ratio (S/N) drops off in neighbouring beams as a function of the angular offset from the beam in which the signal is detected most strongly. With the exception of side-lobe detections of very bright pulsars, signals from astrophysical point sources should only be detected in single beams, or in a small number of beams close to their sky positions. Candidates are therefore rejected if they are detected in many non-neighbouring coherent beams with S/N s that drop off too slowly with angular offset, as this is indicative of a terrestrial interference signal.

The data from the beam containing the strongest detection of each candidate cluster were then folded using the `PulsarX` software,⁷ and folded candidates were scored by the Pulsar Image-based Classification System (PICS) machine-learning classifier (Zhu et al. 2014). Candidates surpassing a conservatively low PICS-score threshold of 10 per cent, typically a few hundred per pointing, were then grouped for visual inspection. As mentioned previously, the full set of raw data could not be stored indefinitely, except for data from beams containing high-confidence pulsar candidates. Reduced data products, i.e. candidate lists, and folded data for every candidate, were retained from all observations.

⁶<https://github.com/ewanbarr/peasoup>

⁷<https://github.com/yymen/PulsarX>

2.4 Target selection

We built a list of observing targets by identifying pulsar-like unassociated *Fermi*-LAT gamma-ray sources within the 4FGL catalogue.

Several studies have had success in using machine-learning classification techniques to identify pulsar candidates from the population of unassociated sources detected by the *Fermi* LAT (Lee et al. 2012; Saz Parkinson et al. 2016; Luo et al. 2020; Finke, Krämer & Manconi 2021). These methods rely on the fact that gamma-ray pulsars have characteristic spectral properties that distinguish them from other gamma-ray emitting source classes: (1) gamma-ray pulsar spectra typically have significant curvature, in that they deviate from a simple power-law spectrum due to a sub-exponential cutoff at photon energies above a few GeV; and (2) gamma-ray pulsars are very stable emitters on long time-scales. The Random Forest algorithm (Breiman 2001) has been shown to perform well for the purpose of classifying *Fermi*-LAT sources (Saz Parkinson et al. 2016; Luo et al. 2020), and so we employed this method to rank sources from 4FGL.

We used five parameters from 4FGL for the classification: `PLEC.SigCurve`, the significance of the log-likelihood improvement when fitting the source spectrum with a (curved) sub-exponentially cutoff power-law spectrum typical of pulsars, compared to a simple power-law; `Variability2_Index`, the chi-squared value of the energy flux measured in 2-month time bins; `Signif_Avg`, the point-source significance (brighter sources can have higher curvature and variability significance, including this parameter in the ranking accounts for this); `PLEC.Index` and `PLEC.ExpFactor`, the photon index and the pre-factor a in the exponential cutoff term $\exp(-aE^b)$, where $b = 2/3$ was used for all unassociated sources and all but six bright pulsars in 4FGL. These final two parameters encode the energy at which the gamma-ray spectrum peaks, which for pulsars typically lies between 0.5 and 4 GeV, but which can be at much higher energies for active galactic nuclei (AGNs) with curved spectra.

We combined the gamma-ray source classes listed in 4FGL into three broad categories: AGNs, pulsars, or ‘other’ (which contains e.g. supernova remnants and pulsar wind nebulae). The classifier was trained to identify these classes using sources with highly likely or confirmed associations listed in 4FGL. To evaluate the classifier performance, we removed 33 per cent of the 4FGL sources, chosen at random, trained the classifier on the remaining population, and compared the classifier results to the known association classes. For identifying pulsars, the classifier had a precision of 82 per cent (i.e. 82 per cent of sources predicted to be pulsars were in fact pulsars) and a recall of 71 per cent (i.e. 71 per cent of pulsars in the sample were correctly identified as such).

For each unassociated source in 4FGL the Random Forest algorithm estimates the probability, $P(\text{psr})$, of this source being a pulsar. We used this list of unassociated sources, ranked by their predicted pulsar probability, and made further cuts to reduce the number of sources to observe. First, only sources with declinations below $+20^\circ$ were included. Next, we removed sources with Galactic latitudes within $|b| < 10^\circ$ of the Galactic plane. This is because gamma-ray pulsars close to the Galactic plane tend to be slowly spinning young pulsars, which have much narrower radio beams, and are therefore more likely to be radio-quiet gamma-ray pulsars undetectable to our survey. The Galactic plane is also being surveyed with MeerKAT with similar sensitivity as part of the MMGPS-L survey up to $|b| < 5^\circ$. Our survey was planned before the MMGPS-L survey region had been finalized, and hence our Galactic latitude cut aimed to avoid redundant observations. We then removed sources whose

4FGL 95 per cent confidence regions had semimajor axes larger than 5 arcmin, which is the largest region that could be covered in a single pointing using 288 coherent beams overlapping at 50 per cent sensitivity. This semimajor axis cut removes around 40 sources that pass our other cuts, but several of these will be covered in future UHF observations, where the coherent beams are wider.

Finally, we removed any sources with $P(\text{psr}) < 12$ per cent, which leaves 79 sources to search, while retaining 95 per cent of the total sum of all $P(\text{psr})$ values. Summing the classifier probabilities gives a (crude) prediction that 38 pulsars (not necessarily all detectable in radio surveys) should exist within these sources, with only 2 expected pulsars in the remaining sources that did not pass the probability threshold. The sources that were searched, along with the pulsar probabilities predicted by the classifier, are listed in Table 1.

3 RESULTS

From our two-pass survey, nine candidate signals were identified in the final visual inspection step as likely being new millisecond pulsars, and all of these were later confirmed by additional detections (see Section 3.1). The pulse profiles for the newly discovered MSPs are shown in Fig. 2.

Our survey also independently detected PSR J0312–0921, a black-widow MSP discovered recently in a GBT observation of 4FGL J0312.1–0921 (Tabassum et al., in preparation). Shortly after our first observations, another two target sources, 4FGL J0802.1–5612 and 4FGL J1231.6–5116, were identified as young gamma-ray pulsars by the direct detection of gamma-ray pulsations in the *Fermi*-LAT data by *Einstein@Home*.⁸ Neither pulsar was detected in our survey, but this is not surprising, as only a very small fraction of young pulsars discovered in gamma-ray pulsation searches have been detected in radio observations (Wu et al. 2018).

3.1 Follow-up observations

To confirm the pulsar nature of the detected candidates, we performed dedicated follow-up observations with MeerKAT at both L band and UHF, and checked for archival data from previous search observations of the *Fermi*-LAT sources in which they were found. Three pulsars (J1757–6032, J1803–6707, and J1823–3543) were re-detected in archival data from the Parkes radio telescope.

The five high-confidence pulsar candidates detected in the first pass were removed from the scheduled second survey pass, so that they could be observed in a dedicated set of confirmation observations along with candidates from the second pass. In these confirmation observations, we employed a very dense tiling (with 90 per cent overlap) with a smaller number of beams around the location of the coherent beam in which the candidate was detected most strongly in the initial survey observations. This dense tiling ensured high sensitivity for re-detecting these candidates, while also enabling us to more precisely localize each pulsar using the method described below (see Section 3.2).

Eight of the pulsar candidates (excluding PSR J1036–4353, discussed below) were re-detected in these confirmation observations. One pulsar, PSR J1709–033 was only seen in the UHF observation, most likely due to unfavourable scintillation that was seen during observations in which this pulsar was detected.

One pulsar, PSR J1036–4353 was not included in the confirmation observations, as it had not been immediately identified as a candidate due to a bug in the folding pipeline that caused it to be folded with the wrong acceleration sign. Instead, it was identified at a later date when the folded archives were corrected. It was confirmed in a later UHF observation as part of the next stage of this survey, which will be presented in a future paper.

3.2 Localization

Following the detection of a pulsar in our survey, the sky position could be estimated to a much higher precision than the size of a coherent beam by triangulation using the measured S/N s in neighbouring beams. The method with which we localized candidates from our survey is described in Bezuidenhout et al. (in preparation), based on the concept outlined in Obrocka, Stappers & Wilkinson (2015), which works as follows. Given the model of the coherent beam point spread function (PSF) provided by *Mosaic*, one can compute the expected ratio of the S/N s that would be recovered in two neighbouring beams for a pulsar at any given point nearby. This expected ratio will match the observed ratio, within uncertainties, for a strip of positions between the two beams. These strips can then be computed for each pair of beams, and the location of the candidate can be inferred from where these strips all cross one another.

This procedure is implemented by the *SeeKAT* package.⁹ We used *SeeKAT* on each of the confirmation observations, which had the most dense beam tilings. The best-fitting positions and uncertainties were in good agreement across the three observations (one at L band, two at UHF), and so we combined these results by summing together the log-likelihood surfaces from each observation.

The best-fitting positions and uncertainties for each pulsar are given in Table 2, and an example of the localization log-likelihood surface is illustrated in Fig. 3. The *SeeKAT* positional uncertainties for new pulsar candidates are typically of the order of a few arcseconds, sufficiently precise to enable the identification of potential counterparts in multiwavelength catalogues.

3.3 Timing

Follow-up timing campaigns have begun for all newly detected pulsars. Initially, all timing observations were performed at other telescopes. The pulsars visible from the Northern hemisphere are followed up mainly using the Nançay (for PSRs J1526–2744 and J1823–3543) and Effelsberg (for PSRs J1709–0333 and J1906–1754) telescopes at L band, while all other pulsars (and, initially, also those observed at other telescopes) are followed up at the Murriyang Parkes telescope, using the Ultra-wide-band Low (UWL) receiver (Hobbs et al. 2020), covering a frequency range from 0.7 to 4 GHz. Depending on the discovery S/N at MeerKAT or, when available, the S/N at the improved position, we follow-up the TRAPUM discoveries for 1–2 h. Observations are carried out in search mode. Whenever possible the pulsars have been observed with a pseudo-logarithmic cadence to help achieve phase coherence in our timing analysis. Phase-connected timing solutions for two MSPs, described in detail below, were obtained using the *Dracula* algorithm¹⁰ (Freire & Ridolfi 2018); this was necessary given the sparsity of the timing data in both cases.

⁸https://einsteinathome.org/gammaraypulsar/FGRP1_discoveries.html

⁹<https://github.com/BezuidenhoutMC/SeeKAT>

¹⁰<https://github.com/pfreire163/Dracula>

Table 1. List of survey observations of *Fermi*-LAT sources. $P(\text{psr})$ is the probability predicted by the Random Forest classifier of each source being a gamma-ray pulsar (see Section 2.4). S_{opt} , S_{50} , and S_{95} are sensitivity estimates (see Section 3.4) from the radiometer equation for a 500-Hz pulsar, with $\text{DM} = 100 \text{ pc cm}^{-3}$ and a 15 per cent duty cycle, based on optimistic (no losses due to finite frequency, acceleration, and DM trial spacings, and for a pulsar lying at the centre of a coherent beam), realistic (median losses), and conservative (95th centile losses) assumptions, respectively.

4FGL source	$P(\text{psr})$	Epoch 1	S_{opt} (μJy)	S_{50} (μJy)	S_{95} (μJy)	Epoch 2	S_{opt} (μJy)	S_{50} (μJy)	S_{95} (μJy)
J0048.6–6347	0.53	59034.2131	53	114	135	59196.6117	50	88	97
J0139.5–2228	0.29	59123.8042	53	110	142	59196.6191	50	94	112
J0251.1–1830	0.13	59034.206	52	112	136	59202.7276	49	78	89
J0312.1–0921 ^b	0.94	59034.1976	52	112	132	59202.7204	49	86	95
J0414.7–4300	0.45	59034.1435	52	113	136	59202.6874	49	92	106
J0529.9–0224	0.3	59065.4275	49	120	144	59188.1007	51	97	117
J0540.0–7552 ^c	0.19	59034.221	52	113	138	59188.1084	50	89	105
J0657.4–4658	0.26	59065.4594	50	121	142	59188.1538	50	96	115
J0712.0–6431	0.17	59065.5499	50	122	189	59188.161	49	99	118
J0802.1–5612 ^b	0.91	59065.444	52	128	148	59182.2759	54	94	108
J0940.3–7610 ^c	0.94	59065.4674	51	126	144	59188.1155	50	81	93
J0953.6–1509	0.89	59065.4514	49	118	137	59182.2831	53	94	112
J1036.6–4349 ^a	0.45	59065.4908	53	130	148	59182.3887	54	94	112
J1106.7–1742	0.57	59065.498	50	122	140	59182.3508	53	94	113
J1120.0–2204 ^c	0.75	59065.5058	52	126	143	59188.1761	49	64	74
J1126.0–5007	0.21	59065.4357	50	119	224	59182.412	54	95	111
J1204.5–5032	0.5	59020.8389	50	113	182	59188.0925	51	99	115
J1207.4–4536	0.7	59065.4835	52	127	152	59250.2806	54	103	126
J1213.9–4416	0.23	59065.5129	51	122	140	59188.1316	50	87	99
J1231.6–5116 ^b	0.96	59065.528	53	130	152	–	–	–	–
J1303.1–4714	0.15	59065.4207	67	159	248	59188.1244	51	103	121
J1345.9–2612	0.34	59065.4747	49	116	133	59188.1389	51	94	113
J1400.0–2415	0.91	59020.7561	50	117	134	59188.1461	51	87	100
J1416.7–5023	0.55	59020.7634	53	125	147	59188.1686	54	95	108
J1450.8–1424	0.14	59065.5427	52	130	158	59188.1981	51	96	111
J1458.8–2120	0.46	59065.5578	51	122	139	59188.1909	51	83	95
J1513.7–1519	0.19	59020.7276	51	120	143	59188.2053	52	91	103
J1517.7–4446	0.24	59065.5205	57	143	168	59188.1837	55	109	130
J1526.6–2743 ^a	0.68	59020.7346	51	120	140	–	–	–	–
J1526.6–3810	0.23	59065.5353	57	140	168	59188.2124	55	110	132
J1539.4–3323	0.9	59020.7418	52	116	140	59182.3427	57	100	116
J1543.6–0244	0.83	59182.3063	54	94	109	59250.3519	55	104	125
J1544.2–2554	0.59	59020.749	51	120	138	59196.4976	52	86	97
J1612.1+1407	0.84	59020.7713	52	123	144	59196.4842	66	114	129
J1622.2–7202	0.37	59065.5655	53	130	153	59182.2916	54	95	112
J1623.9–6936 ^a	0.17	59020.7123	51	119	137	59196.5798	51	83	94
J1630.1–1049	0.57	59020.8087	51	122	166	59182.2992	56	98	114
J1646.7–2154	0.17	59020.7198	53	127	175	59182.3136	58	102	270
J1656.4–0410	0.18	59123.674	134	271	337	59182.3591	55	97	112
J1659.0–0140	0.61	59123.7308	57	116	146	59182.3735	56	99	114
J1709.4–0328 ^a	0.13	59123.7082	57	117	147	59196.5426	53	98	112
J1711.9–1922	0.35	59020.8238	54	127	154	59196.5498	54	90	101
J1717.5–5804	0.66	59020.7791	54	126	147	59196.603	55	92	103
J1720.6+0708	0.6	59020.7944	53	124	144	59196.521	54	97	112
J1722.8–0418	0.29	59123.7452	58	118	147	59196.557	53	85	96
J1727.4+0326	0.13	59182.3663	57	99	115	59250.3446	57	119	138
J1730.4–0359	0.86	59123.738	58	118	150	59196.5641	54	82	95
J1735.3–0717	0.32	59123.7816	59	119	147	59196.5956	55	99	112
J1747.6–0324	0.46	59123.7673	59	121	152	59182.3969	59	103	122
J1749.8–0303	0.22	59020.8015	55	128	146	59196.5884	56	95	105
J1757.7–6032 ^a	0.84	59020.8314	52	121	140	59182.321	56	100	120
J1803.1–6708 ^a	0.23	59020.8161	51	118	138	–	–	–	–
J1813.7–6846	0.12	59123.6858	56	115	146	59182.3281	55	98	118
J1816.4–6405	0.47	59123.6931	57	116	148	59182.3353	56	99	120
J1816.7+1749	0.2	59123.7009	58	118	147	59196.5063	53	94	105
J1818.6+1316	0.77	59123.7601	57	118	147	59196.5282	53	92	104
J1822.9–4718	0.2	59123.7159	56	117	145	59202.6346	55	94	104
J1823.8–3544 ^a	0.13	59034.0991	58	125	150	–	–	–	–
J1824.2–5427	0.61	59123.6786	55	114	143	59182.3811	55	96	111
J1827.5+1141	0.96	59123.7744	59	121	151	59196.5354	55	92	103

Table 1 – continued

4FGL source	P (psr)	Epoch 1	S_{opt} (μJy)	S_{50} (μJy)	S_{95} (μJy)	Epoch 2	S_{opt} (μJy)	S_{50} (μJy)	S_{95} (μJy)
J1831.1–6503	0.67	59123.7231	55	114	143	59202.6716	52	73	85
J1845.8–2521	0.85	59123.8123	61	124	155	59202.6571	56	96	107
J1858.3–5424 ^a	0.71	59034.1361	54	118	140	–	–	–	–
J1906.0–1718	0.33	59034.1066	57	123	150	59182.4041	57	101	123
J1906.4–1757 ^a	0.14	59123.7962	58	120	151	–	–	–	–
J1913.4–1526	0.51	59123.789	58	120	150	59202.6428	54	95	105
J1916.8–3025	0.59	59123.7525	57	117	147	59202.6643	53	72	84
J1924.8–1035	0.78	59202.65	54	83	95	59250.31	59	102	128
J1947.6–1121	0.18	59034.1285	55	118	142	59202.6791	52	89	100
J2026.3+1431	0.19	59196.5136	51	90	100	59250.3282	55	110	130
J2043.9–4802	0.87	59034.1757	53	116	143	59202.7498	51	77	88
J2112.5–3043	0.96	59034.183	53	115	138	59202.6952	50	60	67
J2121.8–3412	0.23	59034.2283	53	114	141	59202.757	50	94	111
J2133.1–6432	0.77	59034.1903	53	115	137	59202.7354	50	81	91
J2201.0–6928	0.41	59034.1214	53	113	133	59202.7426	50	86	95
J2212.4+0708	0.92	59034.1595	53	113	133	59202.7041	50	87	99
J2219.7–6837	0.52	59034.1138	53	114	135	59196.4899	50	78	90
J2241.4–8327	0.33	59034.152	53	113	132	59202.7119	50	87	96
J2355.5–6614	0.24	59034.1679	53	115	137	59196.5724	50	91	104

^aNew MSP discovered in this work.

^bIdentified as a gamma-ray pulsar by other groups after this work began.

^cIdentified as a likely pulsar binary system through optical/X-ray observations, but without pulsation detections.

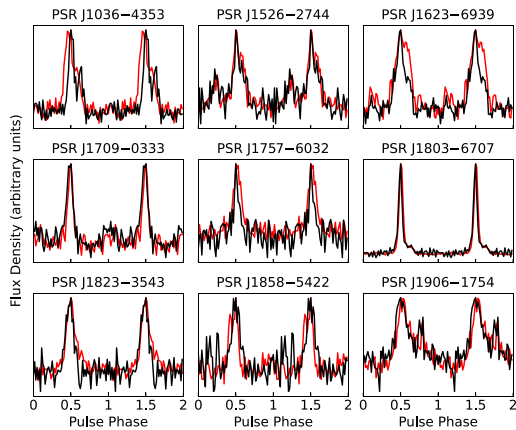


Figure 2. Pulse profiles of the newly discovered millisecond pulsars. Black and red curves show the profiles from L -band and UHF observations, respectively. For clarity, two identical pulses are shown, and pulses have been arbitrarily normalized and phase shifted to peak at phase 0.5.

Obtaining a phase-connected timing solution for the remaining seven pulsars has required a dedicated timing campaign using the Pulsar Timing User Supplied Equipment (PTUSE) system developed for the MeerTime project (Bailes et al. 2020), which additionally provides coherent de-dispersion and full Stokes polarization information. This MeerKAT timing campaign, along with follow-up searches for gamma-ray pulsations from these seven pulsars, will be presented in a dedicated paper (Burgay et al., in preparation). For these seven pulsars, we give a preliminary timing solution in Table 2, obtained using PRESTO’s `fit_circular_orbit.py` routine to fit a sinusoidal modulation to the observed barycentric spin periods from multiple observations without requiring phase-alignment across

observations. We also plot the orbital properties of the 8 newly detected binary MSPs (excluding PSR J1709–0333 which appears to be an isolated pulsar) according to these ephemerides, in comparison to the overall MSP population, in Fig. 4.

3.3.1 PSR J1526–2744

Using the *SeeKAT* position as a starting point, we obtained a phase-connected timing solution using TOAs produced from the original L -band observation, the two UHF observations, as well as several Nançay and Parkes observations taken in 2021 as part of our dedicated timing campaign. This timing solution provided precise constraints on the pulsar’s orbital semimajor axis and time of ascending node, as well as a refined position, but the spin-down rate was not significantly measurable and was highly correlated with the declination.

We used the radio timing solution to search for gamma-ray pulsations in the photon arrival times measured by the *Fermi* LAT. For this, we used *SOURCE*-class gamma-ray photons from within a 3° region-of-interest around the *SeeKAT* position, with energies greater than 100 MeV and with a zenith angle below 105° according to the ‘Pass 8’ `P8R3_SOURCE_V2` (Atwood et al. 2013; Bruel et al. 2018) instrument response functions.¹¹ To increase sensitivity to faint pulsations, we used `gtsrcprob` to compute photon probability weights (Kerr 2011), using the spectral and spatial parameters for nearby sources from the 4FGL DR2 catalogue, as well as the `gll_iem.v07.fits` Galactic and `iso_P8R3_SOURCE_V2.v1.txt` isotropic diffusion emission models.

Folding the gamma-ray data over the validity interval of the radio timing solution did not yield a significant detection. To search for gamma-ray pulsations in earlier data it was necessary to search over a 5D parameter space (α , δ , ν , $\dot{\nu}$, and P_{orb}). The pulsar’s orbital semimajor axis and time of ascending node were already constrained

¹¹See https://fermi.gsfc.nasa.gov/ssc/data/analysis/LAT_essentials.html

Table 2. Properties of newly discovered millisecond pulsars without phase-connected timing solutions. Initial orbital solutions are obtained from fitting sinusoids to observed barycentric spin periods as a function of time. These models are approximate, and so we only provide limited precision on orbital parameters and spin frequency. Positional parameters (RA and Dec.) are estimated from the measured S/N in neighbouring coherent beams using `SeeKAT` (see Section 3.2), except for J1036–4353 whose position is from *Gaia* DR3.

Parameter	PSR J1036–4353	PSR J1623–6939	PSR J1709–0333	PSR J1757–6032
RA, α (J2000)	10 ^h 36 ^m 30 ^s .21513(1)	16 ^h 23 ^m 51 ^s .41 ^{+0^s.33} _{-0^s.33}	17 ^h 09 ^m 32 ^s .79 ^{+0^s.18} _{-0^s.13}	17 ^h 57 ^m 45 ^s .53 ^{+0^s.22} _{-0^s.24}
Dec., δ (J2000)	–43°53′08″.7252(2)	–69°36′48″.3 ^{+2^s.2} _{-1^s.7}	–03°33′17″.7 ^{+6^s.0} _{-2^s.0}	–60°32′10″.7 ^{+2^s.6} _{-2^s.3}
Dispersion measure, DM (pc cm ^{–3})	61.1	46.4	35.7	62.9
Spin frequency, ν (Hz)	595.2	415.0	283.8	343.3
Orbital Period, P_{orb} (d)	0.259	11.01	–	6.28
Projected semimajor axis, x (lt-s)	0.665	6.73	–	9.62
Epoch of ascending node, T_{asc} (MJD)	59536.31	59192.91	–	59183.40
Minimum companion mass, $M_{\text{c,min}}$ (M_{\odot})	0.23	0.19	–	0.43
Distance (from YMW16), d (kpc)	0.40	1.3	0.21	3.5

Parameter	PSR J1823–3543	PSR J1858–5422	PSR J1906–1754	–
RA, α (J2000)	18 ^h 23 ^m 43 ^s .06 ^{+0^s.14} _{-0^s.13}	18 ^h 58 ^m 07 ^s .92 ^{+0^s.26} _{-0^s.23}	19 ^h 06 ^m 14 ^s .94 ^{+0^s.11} _{-0^s.15}	–
Dec., δ (J2000)	–35°43′40″.8 ^{+1^s.4} _{-2^s.2}	–54°22′14″.6 ^{+3^s.8} _{-2^s.7}	–17°54′33″.7 ^{+1^s.8} _{-3^s.2}	–
Dispersion measure, DM (pc cm ^{–3})	81.7	30.8	98.1	–
Spin frequency, ν (Hz)	421.4	424.5	347.7	–
Orbital period, P_{orb} (d)	144.5	2.58	6.49	–
Projected semimajor axis, x (lt-s)	51.8	1.68	1.35	–
Epoch of ascending node, T_{asc} (MJD)	59091.36	59564.98	59304.97	–
Minimum companion mass, $M_{\text{c,min}}$ (M_{\odot})	0.27	0.12	0.05	–
Distance (from YMW16), d (kpc)	3.7	1.2	6.8	–

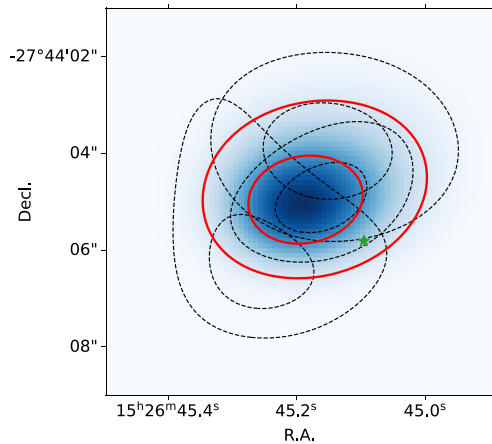


Figure 3. An example of pulsar localization using `SeeKAT`, from the three confirmation observations of PSR J1526–2744. The dashed black contours show the localization probabilities in three separate observations. The colour scale and the solid red contour lines show the joint likelihood (i.e. the product of the likelihoods from all three observations). Contour lines are at approximate 1 σ and 2 σ levels. The green star is at the *Fermi* timing position for this pulsar.

precisely enough by the initial radio ephemeris that only one trial was required in these dimensions. The search was performed using the weighted H -test (de Jager, Raubenheimer & Swanepoel 1989; Kerr 2011), a statistic that normally performs an optimal incoherent sum of the Fourier power in the first 20 harmonics. In this case,

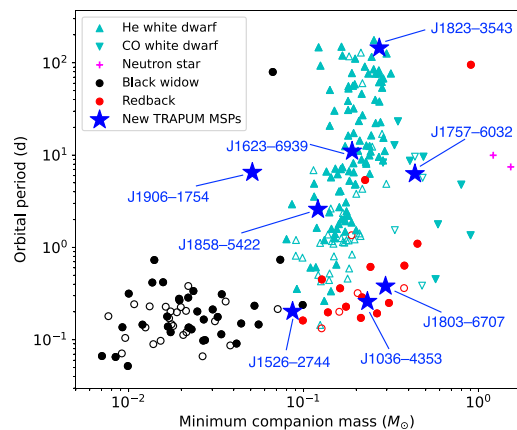


Figure 4. Orbital properties of known binary MSPs. Each companion type, according to the ATNF Pulsar Catalogue (Manchester et al. 2005), is denoted by a different marker as noted in the legend. We mark two pulsars categorized as having He white dwarf companions in the ATNF Pulsar Catalogue, PSRs J1518+0204C and J1653–0158, as black widows following Pallanca et al. (2014) and Nieder et al. (2020b), respectively. Filled markers show MSPs that were found by targeting an unidentified *Fermi*-LAT gamma-ray source. The new MSPs from this work are highlighted with blue stars and labelled.

we only summed over 3 harmonics, as detecting power in higher harmonics requires increased search grid density in each dimension, but gamma-ray pulsars have most power in lower harmonics. This search detected a significant pulsed signal with $H = 108.9$,

Table 3. Timing solution for PSR J1526–2744. Timing parameters are obtained from the gamma-ray timing analysis, with the exception of the DM measurement which is from the original MeerKAT discovery observation. Parameter values are in the Barycentric Dynamical Time (TDB) scale.

Parameter	Value
Timing parameters	
Data span (MJD)	54681–59476
Reference epoch (MJD)	59355.468037
RA, α (J2000)	15 ^h 26 ^m 45 ^s .103(2)
Dec., δ (J2000)	–27°44′05″.91(8)
Dispersion measure, DM (pc cm ^{–3})	30.95(3)
Spin frequency, ν (Hz)	401.7446020975(3)
Spin-down rate, $\dot{\nu}$ (Hz s ^{–1})	–5.71(1) $\times 10^{-16}$
Orbital period, P_{orb} (d)	0.2028108285(7)
Projected semi-major axis, x (lt s)	0.22410(3)
Epoch of ascending node, T_{asc} (MJD)	59303.20598(1)
Derived parameters	
Spin period, p (ms)	2.489143587192(2)
Spin period derivative, \dot{p}	3.537(6) $\times 10^{-21}$
Spin-down power, \dot{E} (erg s ^{–1})	9.1 $\times 10^{33}$
Surface magnetic field strength (G)	9.5 $\times 10^7$
Light-cylinder magnetic field strength (G)	5.7 $\times 10^4$
Minimum companion mass, M_{min} (M_{\odot})	0.083
Distance (from YMW16), d (kpc)	1.3

and with phase-connected pulsations visible from the start of the LAT data.

Following this detection, we derived a precise 13-yr gamma-ray timing solution by varying the timing parameters to maximize the unbinned Poisson log-likelihood of the weighted photon phases (Abdo et al. 2013) using a template pulse profile consisting of two wrapped Gaussian peaks whose parameters were also free to vary in the fit. The best-fitting parameter values and uncertainties are given in Table 3. The gamma-ray photon phases according to the best-fitting timing model and template pulse are shown in Fig. 5. We also tested for but did not significantly detect proper motion ($|\mu| < 49 \text{ mas yr}^{-1}$) or eccentricity ($e < 8 \times 10^{-4}$).

The nature of the companion star in this system is currently unclear. The short orbital period (4.9 h) and low minimum companion mass (0.08 M_{\odot}) suggest a heavy black-widow or light redback companion, but no radio eclipses typical of these systems have been seen. Many black-widow binaries have detectable optical counterparts, and so we searched for an optical counterpart to this system using the ULTRACAM (Dhillon et al. 2007) high-speed multiband imager on the 3.5-m New Technology Telescope (NTT) at ESO La Silla. The longest observation lasted 3.5 h, covering orbital phases between 0.1 and 0.8. We did not find any counterpart at the pulsar’s timing position, with 3σ magnitude upper limits of $i_s = 23.2$, $g_s = 24.0$, and $u_s = 23.0$ in the deepest 5-min stacked image, which was obtained close to the companion’s superior conjunction, where a heated black-widow companion would appear at its brightest. It therefore seems likely that the companion is a light-weight ($M_{\text{min}} = 0.083 M_{\odot}$) white dwarf. If confirmed, e.g. through the detection of a non-variable optical counterpart below our ULTRACAM detection threshold, this would be the shortest orbital period of any known fully recycled Galactic MSP–WD system, and the third shortest orbit of any Galactic PSR–WD binary system, after the relativistic binary PSRs J0348+0432 (Antoniadis et al. 2013) and J1141–6545 (Kaspi et al. 2000).

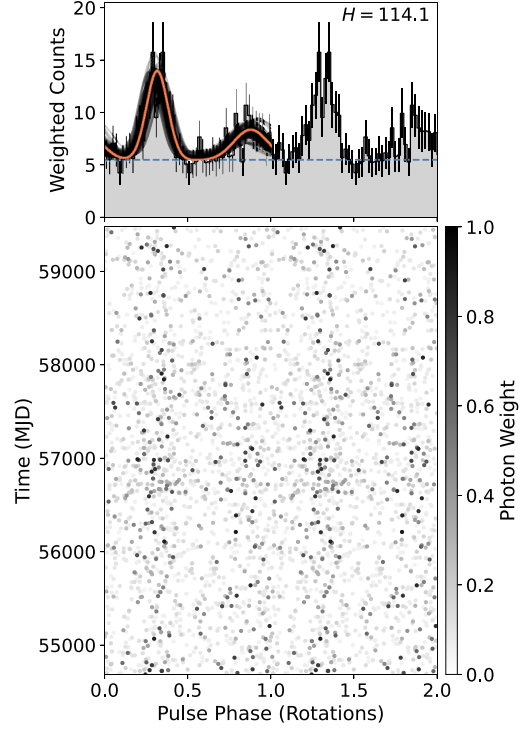


Figure 5. Gamma-ray pulsations from PSR J1526–2744 in *Fermi*-LAT data. The lower panel shows each photon’s phase according to the best-fitting timing solution. Each photon is assigned a weight, computed from its incidence angle and energy, and illustrated by greyscale representing the probability that it was emitted by the targeted source as opposed to a foreground or background source. The upper panel shows the integrated pulse profile, computed by summing the photon probability weights in each rotational phase bin. The dashed blue horizontal line shows the estimated background rate. In the upper panel, the opaque orange curve shows the best-fitting template pulse profile used to estimate the log-likelihood of the gamma-ray pulsations. The transparent black curves show templates with parameter values randomly drawn from our MCMC samples to illustrate the uncertainty on the pulse profile.

For the observed DM = 30.95(3) pc cm^{–3}, YMW16 predicts a distance of 1.3 kpc. The gamma-ray energy flux from this source above 100 MeV is $G_{100} = 2.5 \pm 0.4 \times 10^{-12} \text{ erg cm}^{-2} \text{ s}^{-1}$, corresponding to a gamma-ray luminosity of $L_{\gamma} = 5.3 \times 10^{32} \text{ erg s}^{-1}$. This can be compared to the pulsar’s spin-down power $\dot{E} = 4\pi^2 I \nu \dot{\nu} = 9.1 \times 10^{33} \text{ erg s}^{-1}$, for an assumed pulsar moment-of-inertia $I = 10^{45} \text{ g cm}^2$, corresponding to an efficiency $\eta = L_{\gamma} / \dot{E} \approx 0.06$, which is typical of gamma-ray MSPs (Abdo et al. 2013).

Using the timing solution obtained above, we carried out a search for continuous gravitational waves from this pulsar. Continuous gravitational wave emission is expected due to a non-axisymmetric deformation (ϵ) of the neutron star and the dominant signal frequency is twice its rotational frequency. Our search was therefore targeted at a frequency $f \approx 803.5 \text{ Hz}$ and spin-down $\dot{f} \approx -1.14 \times 10^{-15} \text{ Hz/s}$ and directed at the timing position.

An *a priori* estimate of the detectable strain amplitude using Advanced LIGO data yields a value about an order of magnitude larger than the spin-down upper limit amplitude (Aasi et al. 2014),

$$h_0^{sd} = \left(\frac{5 GI |\dot{\nu}|}{2 c^3 d^2 \nu} \right)^{1/2}, \quad (1)$$

where we again assume $I = 10^{45} \text{ g cm}^2$. This is the strain amplitude of the signal assuming that all the rotational kinetic energy lost by the pulsar (\dot{E}) was converted into gravitational waves. We therefore do not expect a detection, but, in the spirit of leaving no stones unturned (e.g. Abbott et al. 2018, 2019; Nieder et al. 2019, 2020b; Abbott et al. 2022a,b), we carried out the search.

We used all of the Advanced LIGO data from the Hanford and Livingston detectors collected during the O1, O2, and O3 runs (Abbott et al. 2021). The gamma-ray timing solution allows us to coherently combine these data sets using a single template, thus achieving the maximum possible sensitivity this search could have to date. Loud detector glitches in the data were removed through gating (Steltner, Papa & Eggenstein 2022). The frequency range relevant to this search is free of known lines in the detectors. The multidetector, matched-filtering \mathcal{F} -statistic (Cutler & Schutz 2005) was used for the analysis. Our search result has a p -value of 0.29, estimated using off-source data. This result implies a non-detection and based on it we set a 95 per cent confidence upper limit of 1.25×10^{-26} on the intrinsic gravitational wave amplitude. Our upper limit is a factor of ≈ 20 larger than the spin-down upper limit, and the uncertainty on this upper limit is not more than 8 per cent including calibration uncertainties. Translating the amplitude upper limit into an upper limit on the ellipticity of the source, we constrain the ellipticity of J1526–2744 to be $< 2.45 \times 10^{-8}$, which is close to the minimum ellipticity proposed for millisecond pulsars by Woan et al. (2018).

We also searched in a band of f and \dot{f} accounting for mismatches between the phase of the gravitational wave signal and the phase locked to the electromagnetic observations. Such mismatches could result from a differential rotation between the parts of the star emitting the gravitational wave and the electromagnetic pulsations or if the star was biaxial and consequently freely precessing. We searched in a bandwidth of 0.4 per cent of the spin parameter values following Abbott et al. (2020), and estimated the p values of the results as done in Ashok et al. (2021). The results from this band search were also consistent with expectations from Gaussian noise.

3.3.2 PSR J1803–6707

PSR J1803–6707 was the first pulsar to be found in our survey, and was quickly confirmed by a detection in 1 h of archival Parkes data from 2015. Detection of the pulsar in this observation required a significant jerk term, indicating that the pulsar was likely to be in a short-period binary system. Pulsations were only detected for ~ 30 min in one of two 1 h dedicated follow-up observations with Parkes in 2020 December, indicative of a wide eclipse typical of black-widow or redback systems.

Establishing an orbital timing solution (given in Table 4) revealed an ~ 9 h orbit and a minimum companion mass of $0.26 M_{\odot}$ (assuming a pulsar mass of $1.4 M_{\odot}$), as well as significant variations in the orbital period requiring several orbital frequency derivative terms to describe the orbital phase throughout the 1 yr of phase-connected timing data. These features are characteristic of redback binary systems (e.g. Deneva et al. 2016).

We used the UHF MeerKAT observations to estimate the sky position of this pulsar using SeeKAT. The refined position is

Table 4. Radio timing solution for PSR J1803–6707. Parameter values are in the TDB scale.

Parameter	Value
<i>Gaia</i> astrometry	
RA, α (J2000)	18 ^h 03 ^m 04 ^s .235339(9)
Dec., δ (J2000)	−67°07′36″.1576(2)
Proper motion in RA, $\mu_{\alpha} \cos \delta$ (mas yr ^{−1})	−8.4(2)
Proper motion in Dec. μ_{δ} (mas yr ^{−1})	−6.5(2)
Parallax, ϖ (mas)	0.18(17)
Position reference epoch (MJD)	57388.0
Timing parameters	
Data span (MJD)	59020–59583
Reference epoch (MJD)	59364.893677
Dispersion measure, DM (pc cm ^{−3})	38.382(3)
Spin frequency, ν (Hz)	468.46771214886(7)
Spin-down rate, $\dot{\nu}$ (Hz s ^{−1})	−4.01(2) $\times 10^{-15}$
Orbital period, P_{orb} (d)	0.38047324(8)
Projected semimajor axis, x (lt s)	1.061910(3)
Epoch of ascending node, T_{asc} (MJD)	59020.99710(1)
1st orbital frequency derivative, $f_{\text{orb}}^{(1)}$ (Hz s ^{−1})	1.05(9) $\times 10^{-19}$
2nd orbital frequency derivative, $f_{\text{orb}}^{(2)}$ (Hz s ^{−1})	−1.5(1) $\times 10^{-24}$
3rd orbital frequency derivative, $f_{\text{orb}}^{(3)}$ (Hz s ^{−1})	1.03(7) $\times 10^{-31}$
4th orbital frequency derivative, $f_{\text{orb}}^{(4)}$ (Hz s ^{−1})	−3.3(2) $\times 10^{-40}$
Derived parameters	
Spin period, p (ms)	2.1346188308539(3)
Spin period derivative, \dot{p}	1.828(7) $\times 10^{-20}$
Spin-down power, \dot{E} (erg s ^{−1})	7.4 $\times 10^{34}$
Surface magnetic field strength (G)	2 $\times 10^8$
Light-cylinder magnetic field strength (G)	1.9 $\times 10^5$
Minimum companion mass, M_{min} (M_{\odot})	0.26
Distance (from YMW16), d (kpc)	1.4

coincident with the location of a star in the *Gaia* DR3 catalogue (Gaia Collaboration 2016, 2022). We also observed this star with ULTRACAM, which revealed optical variability with the same 9-h periodicity, confirming that this is indeed the optical counterpart. The optical light curve, shown in Fig. 6, varies by around 1.5 mag, with a single peak indicative of significant heating via irradiation from the pulsar (similar to e.g. PSR J2215+5135, Schroeder & Halpern 2014) but the counterpart is detectable at all orbital phases, as is typical for nearby redback companions which tend to have hot surfaces ($T > 4000$ K) even on the non-irradiated side. Light-curve modelling to estimate properties of the companion such as its temperature, irradiation, radius, and the binary inclination angle will be performed in a dedicated follow-up project (Phosrisom et al., in preparation).

As with PSR J1526–2744, we folded the gamma-ray data using the radio ephemeris to check for gamma-ray pulsations. Significant pulsations are detected within the 1-yr interval in which the radio ephemeris is valid, with a weighted H -test of $H = 51$, corresponding to a 5.6σ detection using the false-alarm probability calibration from Bruel (2019). These pulsations are shown in Fig. 7. However, these pulsations quickly disappear when extrapolating to earlier data. This is not unexpected, as Taylor-series models for orbital period variations lack predictive power, and the spin-down rate is not measured precisely enough in the radio data to fold the 13 yr of *Fermi*-LAT data. We have not been successful in extending the ephemeris by timing the gamma-ray data, likely as a result of the pulsar's faint gamma-ray flux and the large amplitude of the orbital phase variations. A

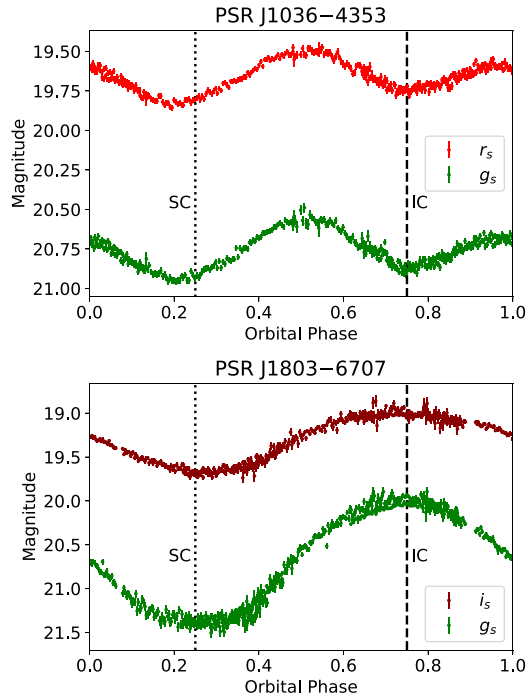


Figure 6. Optical light curves for PSRs J1036–4353 and J1803–6707 obtained using ULTRACAM+NTT. Observations are folded on the orbital period using the radio timing ephemerides. The pulsar’s superior and inferior conjunctions are marked with dotted and dashed vertical lines, and labelled SC and IC, respectively. The two peaks in the light curve for PSR J1036–4353 are due to ellipsoidal deformation of the companion star in the pulsar’s gravitational field, while the single peak in the light curve for PSR J1803–6707 indicates strong heating from the pulsar.

longer radio timing baseline will hopefully solve this problem by providing a more precise spin-down rate measurement, and a longer phase-connected radio ephemeris that will fold more *Fermi*-LAT data to provide better statistics with which to build a gamma-ray pulse profile template to search with. Nevertheless, this detection confirms the association between 4FGL J1803.1–6708 and PSR J1803–6707. The gamma-ray energy flux from this source above 100 MeV is $G_{100} = 5.0 \pm 0.5 \times 10^{-12} \text{ erg cm}^{-2} \text{ s}^{-1}$, corresponding to an efficiency $\eta = 0.017$ for the assumed YMW16 distance of 1.4 kpc (for $DM = 38.382 \text{ pc cm}^{-3}$), which is again fairly typical of gamma-ray MSPs (Abdo et al. 2013).

Using data from the first *eROSITA* all-sky survey (eRASS1; Predehl et al. 2021), the X-ray counterpart of PSR J1803–6707 was independently detected (positional match within ~ 5 arcsec) in a pilot search for likely X-ray counterparts of unassociated *Fermi*-LAT sources. Fig. 8 depicts the X-ray counterpart as seen in eRASS1. The formal detection significance in the 0.2–2.3 keV bandwidth is 4.6σ for a vignetting corrected exposure time of 167.63s and a count rate of $(7.2 \pm 2.4) \times 10^{-2} \text{ ct s}^{-1}$ obtained from all seven telescope modules. The source is not detected in the 2.3–8.0 keV bandpass. The detected X-ray photons do not support a detailed spectral analysis. *eROSITA*’s temporal resolution is 50 ms which prevents the detection of a periodicity at the millisecond level as well.

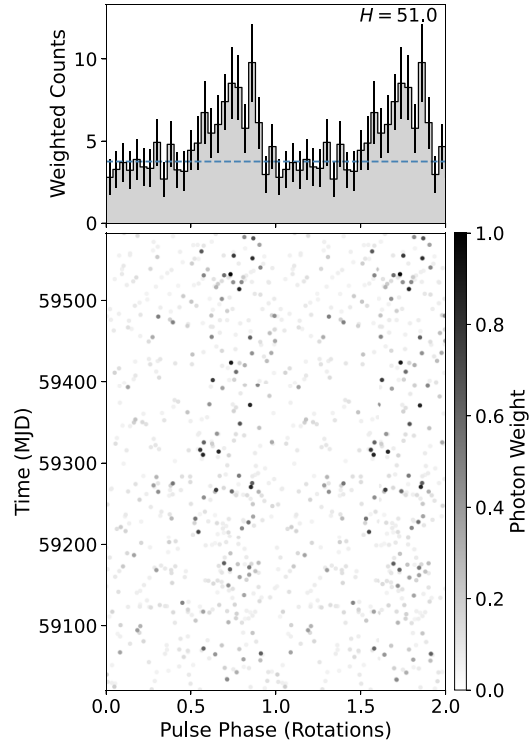


Figure 7. Gamma-ray pulsations from PSR J1803–6707 in *Fermi*-LAT data. The lower panel shows each photon arrival during the radio timing solution’s validity interval. Each photon is assigned a weight, computed from its incidence angle and energy, and illustrated by greyscale representing the probability that it was emitted by the targeted source as opposed to a foreground or background source. The upper panel shows the integrated pulse profile, computed by summing the photon probability weights in each rotational phase bin. The dashed blue horizontal line shows the estimated background rate.

Assuming a power-law spectrum with a photon index of 2.0 and an absorption column density of $6 \times 10^{20} \text{ cm}^{-2}$ (HI4PI Collaboration 2016), the *eROSITA* counting rate implies an unabsorbed X-ray flux of $F_X = (1.5 \pm 0.5) \times 10^{-13} \text{ erg s}^{-1} \text{ cm}^{-2}$ in the 0.2–10 keV band. For the Yao et al. (2017) distance, we obtain an X-ray luminosity of $L_X \sim 3.5 \times 10^{31} \text{ erg s}^{-1}$ and an X-ray efficiency of $L_X/\dot{E} \sim 4.7 \times 10^{-4}$, a typical value for X-ray detected MSPs (see e.g. Becker & Truemper 1997). A significant contribution by the $g \sim 20$ optical counterpart to the detected X-ray flux is not expected. The X-ray-to-optical flux ratio of the system is around 1, much greater than that expected for coronal X-ray emission from stars (Krautter et al. 1999).

It is interesting to note that, considering the γ -ray flux of the likely counterpart, the γ -ray to X-ray flux ratio of this source is comparatively small at $F_\gamma/F_X \sim 35$. This value is located at the lower end of the observed distribution for high-energy pulsars, which extends over a range of around 10 – 10^4 (Marelli, De Luca & Caraveo 2011; Bertheaud et al. 2021). It is therefore likely that the X-ray flux contains a contribution from, or is dominated by, an intrabinary shock, as is commonly seen in redback binary systems (e.g. Roberts

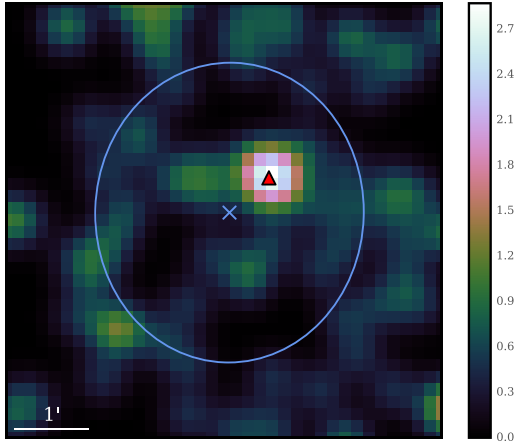


Figure 8. eRASS1 image in the 0.2–2.3 keV band, with the 95 percent positional error ellipse of 4FGL J1803.1–6708 indicated in blue, and the GAIA position overlaid on the eROSITA counterpart of PSR J1803–6707 marked in red. The image has been spatially binned to a pixel size of 10 arcsec and smoothed with a 15 arcsec kernel. The color bar indicates the count rate in units of $10^{-3} \text{ ct s}^{-1} \text{ pix}^{-1}$.

et al. 2015). Follow-up observations are planned to further investigate the X-ray emission from this system.

3.3.3 PSR J1036–4353

This pulsar is both the fastest-spinning (with $\nu \approx 595$ Hz), and the most highly-accelerated (with $a \approx 15 \text{ m s}^{-2}$) pulsar found by our survey. Follow-up observations have revealed this to also be a redback system. A preliminary orbital solution revealed an ~ 6.2 h orbit and a minimum companion mass of $0.23 M_{\odot}$. Several non-detections have occurred during our timing campaign in the half of the orbit in which the pulsar is behind its companion, likely due to eclipses by material from the redback companion. A single *Gaia* source lies within its SeeKAT localization region. Like PSR J1803–6707, we observed this source with ULTRACAM, revealing a double-peaked light curve, shown in Fig. 6, very typical of redback binary systems. Modelling of this data will also be presented in a future paper (Phosrisom et al., in preparation).

3.3.4 The other new MSPs

Of the remaining MSPs, one (PSR J1709–0333) appears to be isolated, while three (PSRs J1623–6939, J1823–3543, and J1858–5422) have companion masses and orbital periods that are consistent with helium white dwarf (He-WD) companions, but the remaining two warrant further mention. The first, PSR J1906–1754 lies at an unusual position in the orbital parameter space shown in Fig. 4, with a minimum companion mass ($M_c > 0.05 M_{\odot}$) much lower than that of typical white dwarf companions, but with an orbital period ($P_{\text{orb}} = 6.5$ d) much longer than a typical black-widow system. Of the MSP binaries with $P_{\text{orb}} > 1$ d, only PSR J1737–0811 has a similarly low minimum companion mass ($M_c > 0.06 M_{\odot}$, Boyles et al. 2013). The low minimum mass could indicate a very face-on binary inclination angle, with $i < 14.5$ deg required for $M_c = 0.2 M_{\odot}$. However, such orbits are *a priori* unlikely, as

only around 3 per cent of orbits should have a lower inclination, assuming a random distribution of viewing angles. The final pulsar, PSR J1757–6032, has a larger minimum companion mass ($M_c > 0.45 M_{\odot}$) that suggests it is perhaps more likely to have a CO-WD companion, similar to that of the relativistic binary PSR J1614–2230 (Demorest et al. 2010; Tauris, Langer & Kramer 2011).

3.4 Sensitivity

As our observations were not flux calibrated, we estimated the flux density thresholds (S) above which a pulsar should have been detectable to our survey. To estimate this, we used the pulsar radiometer equation (Lorimer & Kramer 2004),

$$S = \frac{\rho (T_{\text{sys}} + T_{\text{sky}})}{\beta G n_{\text{ant}} \sqrt{n_{\text{pol}} T_{\text{obs}} B}} \sqrt{\frac{w}{1-w}}, \quad (2)$$

where we have assumed: $G = 0.044 \text{ K Jy}^{-1}$ is the gain per antenna (Bailes et al. 2020); $\rho = 9$ was the S/N threshold required for a candidate to be folded for visual inspection; n_{ant} is the number of antennas; $n_{\text{pol}} = 2$ polarizations are summed; T_{obs} is the exposure time; $B = 700 \text{ MHz}$ is the estimated useable bandwidth after RFI excision; and $T_{\text{sys}} = 22.5 \text{ K}$ is the combination of the receiver temperature, atmospheric, and ground spillover contributions (Ridolfi et al. 2021). The sky temperature, T_{sky} , towards each source is taken from the 408 MHz all-sky map of Haslam et al. (1982), reprocessed by Remazeilles et al. (2015), and scaled to the central frequency of 1284 MHz according to an assumed spectral index of -2.6 . The resulting flux-density limits are given in Table 1. Estimated sensitivity also depends strongly on the assumed pulse duty cycle, w . For the new MSPs, this varies from 0.05 (PSR J1803–6707) to 0.35 (PSR J1906–1754); we have assumed $w = 0.15$ for our estimated sensitivities.

The remaining factor in equation (2), β , accounts for various losses incurred during observing and searching. This includes constant fractional losses due to the 8-bit voltage digitization (5 per cent) and beamforming efficiency (5 per cent); sensitivity losses due to using incoherent harmonic summing (15 per cent for our assumed 15 per cent duty cycle, Morello et al. 2020); finite time resolution and intrachannel dispersion smearing (both < 1 per cent). In addition to these fractional losses, there are random losses due to the location of a signal between FFT bins (averaging 8 per cent), DM trials and acceleration trials. We estimate these losses for an assumed $\nu = 500 \text{ Hz}$, $\text{DM} = 100 \text{ pc cm}^{-3}$ pulsar, via a Monte Carlo procedure – generating signals with random offsets from the nearest search trial and evaluating the S/N losses. The final loss factor to consider is that due to the angular offset between a pulsar and the centre of the nearest coherent beam. To evaluate this, for each source we drew random locations from the 4FGL localization probability densities and evaluated the sensitivity at that location of the nearest coherent beam according to the simulated PSF model from *Mosaic*. Combining all of these losses provided a Monte Carlo distribution for β .

For each source we quote three estimated sensitivities: S_{opt} is the optimum sensitivity, assuming only the constant losses described above, and therefore estimates a fundamental flux density limit for our survey; while S_{50} and S_{95} are the flux density limits obtained using equation (2) using the median and 95th centile values, respectively, of the β values obtained from our Monte Carlo estimates. Average sensitivities were $S_{\text{opt}} \approx 55 \mu\text{Jy}$, $S_{50} = 120$ (90) μJy , and $S_{95} = 150$ (110) μJy for the first (second) pass, respectively. The flux density threshold for the incoherent beam (for pulsars lying outside

the region tiled by coherent beams) is approximately $\sqrt{n_{\text{ant}}} \approx 8$ larger than that for a coherent beam.

4 DISCUSSION

In this paper, we have presented the first MeerKAT survey for new radio pulsars in unassociated *Fermi*-LAT sources. While our strategy of targeting pulsar-like gamma-ray sources is certainly not novel, the capabilities of this next-generation radio telescope do lead to significant advantages over previous surveys.

Foremost among these is the extremely high sensitivity of the full MeerKAT array, surpassed only by the Arecibo (Cromartie et al. 2016) and FAST (Wang et al. 2021) telescopes, but unprecedented in the Southern hemisphere. In Section 3.4, we estimated typical 95 per cent flux density upper limits of $\sim 100 \mu\text{Jy}$, which can be compared to the nominal $\sim 200 \mu\text{Jy}$ sensitivity (not including many of the loss terms that we consider) that was achieved with typical hour-long pointings in the similar survey of *Fermi*-LAT sources performed at Parkes by Camilo et al. (2015).

Of the newly discovered pulsars, only PSR J1803–6707 is bright enough that it could perhaps have been discovered in hour-long Parkes observations, but such a discovery would have been complicated by jerk effects from its short orbital period and high acceleration. All of the new pulsars have eventually been detected in dedicated Parkes observations, but with low S/Ns that would be hard to detect without prior knowledge of the DM and spin period.

A key factor for our survey, as Cromartie et al. (2016) also discussed for their survey of *Fermi*-LAT sources performed with the Arecibo telescope, is that these competitive flux-density thresholds are achieved with only short 10-min observations, bringing several benefits. Firstly, these short observation times allow for more sources to be observed within a given observing time budget, while MeerKAT’s rapid (~ 30 s) slew time ensures that costly overheads are not incurred by doing so. Secondly, short observations enable the search processing to be performed quickly (the computing cost of an acceleration search scales with at least $T^3 \log(T)$ for integration time T), allowing storage space to be freed quickly enough that observation scheduling is not limited by this factor, and allowing us to search up to high accelerations. Thirdly, short observation times enable the detection of very short-period binary MSPs. For very short orbits, the assumptions that go into an acceleration search (that the orbital motion within the observation can be approximated with a constant acceleration) break down as higher order ‘jerk’ terms become significant, with sensitivity to binary MSPs only maintained for observations lasting less than 10 per cent of an orbit (Johnston & Kulkarni 1991). Our short 10-min observation strategy mitigates the worst of the jerk effects, but still means that sensitivity is lost for binaries with periods shorter than ~ 100 min. Only three Galactic field MSPs with shorter orbital periods than this are known, although all three are gamma-ray MSPs (Pletsch et al. 2012; Stovall et al. 2014; Nieder et al. 2020b).

Additionally, short observations mean that multiple passes can be performed to minimize missed discoveries due to the time-varying effects that can contribute to a pulsar’s detectability in a given observation. Interstellar scintillation introduces time- and frequency-dependent variations in the observed spectrum, which can lead to a pulsar being undetectable over large frequency ranges (Camilo et al. 2015). Indeed PSR J1709–0333 remained undetected in our *L*-band confirmation observation, despite a dense beam tiling that covered its now-known position. Our UHF confirmation observations reveal the reason for this – in both observations, separated by 70 min, the pulsar was only detected in ~ 20 per cent (~ 100 MHz) of the bandwidth,

indicative of scintillation. Subsequent detections with the Parkes UWL and the Effelsberg *L*-band receivers revealed similar behaviour.

MSPs in black-widow and redback binaries can also be undetectable for large fractions of an orbit, usually (but not exclusively) around the pulsar’s superior conjunction, as a result of diffuse intra-binary plasma dispersing, scattering and absorbing radio pulsations. The jerk terms that limit the sensitivity of an acceleration search to short period binaries also have an orbital phase dependence (Johnston & Kulkarni 1991), and so sensitivity also depends on the orbital phase at which observations take place. Our short exposure, two-pass survey partially mitigates these effects. The case of PSR J1526–2744 further illustrates this: we were unable to detect this pulsar in dedicated follow-up observations with Parkes and Nançay prior to obtaining an orbital solution without performing jerk searches, a computationally expensive technique (Andersen & Ransom 2018) that has only recently started being employed in radio surveys of *Fermi* sources.

One additional time-dependent effect that is specific to this survey is the fact that the shape of a coherent tied-array beam on the sky depends on the elevation at which a source is observed, with beams being more elongated for sources at lower elevations due to the smaller projected baselines between antennas. The beam tiling pattern used to cover a given source region therefore depends on the exact sidereal time and array configuration.

Indeed, four of the nine pulsars discovered here were only detected in the second observation of their respective *Fermi* sources. This was partially due to the improved flexibility of FBFUSE’s tiling patterns that was developed between the first and second passes, and our use of a coarser frequency resolution but larger number of coherent beams, which allowed us to cover a larger solid angle around each source with a more sensitive tiling pattern. Two of these pulsars, PSRs J1709–0333 and J1036–4353, lay just outside the corresponding *Fermi*-LAT source 95 per cent localization regions that we aimed to tile with coherent beams in the first pass, but were detected in the second pass where we targeted a larger nominal 99 per cent confidence region. The other two pulsars that were only detected in the second pass, PSRs J1623–6936 and J1757–6032, lay in a less sensitive location in the coherent beam tiling pattern in their first observation, mid-way between three neighbouring beams, where sensitivity was ~ 50 per cent of that at the centre of a beam, but were at a more favourable location in the second observation.

One final advantage to our survey, over projects using single-dish telescopes, is the rapid and precise localization that can be obtained from a multibeam detection using SeeKAT. This has two significant scientific benefits: rapid localizations enable immediate multiwavelength follow-up and catalogue searches; and precise knowledge of a pulsar’s location greatly assists in obtaining a phase-connected timing solution to fully exploit the scientific potential of a new MSP discovery. In the absence of an interferometric localization, it often takes lengthy timing campaigns to reveal the location of a pulsar, as astrometric parameters can be highly degenerate with a pulsar’s spin-down rate (and sometimes orbital parameters) until a data set spanning several months has been obtained. The SeeKAT positions for PSRs J1803–6707 and J1036–4353, were precise enough to unambiguously link these pulsars to their *Gaia* counterparts, establishing these as redback binary systems, and providing sub-milliarcsecond astrometric uncertainties that are sufficiently precise that these parameters no longer needed to be fit for when building a timing solution. For PSR J1526–2744, the ~ 2 arcsec positional uncertainty represents a reduction of a factor of $\sim 10\,000$ in the number of sky positions that had to be searched to detect

gamma-ray pulsations, greatly decreasing the required computational effort.

With only two pointings towards our targeted sources there is still a high chance that some otherwise detectable pulsars among our targets may have been missed due to scintillation or eclipsing. We have therefore planned another two observations towards the sources observed here using the UHF receiver. All 9 pulsars discovered here were also detected at a higher S/N in our UHF observations, illustrating the sensitivity gains that can be made by observing at lower frequencies to exploit typical MSP spectra that decrease with frequency (Frail et al. 2016; Jankowski et al. 2018), and MeerKAT's extremely low RFI environment at UHF (Bailes et al. 2020).

It is important to consider what prospects remain for further detections among *Fermi*-LAT sources. To obtain a crude estimate for the number of pulsars remaining in this sample, we can simply sum the probabilities of each source being a gamma-ray pulsar that the Random Forest classifier computed in Section 2.4, obtaining $\sum P(\text{psr}) = 38.4$. Subtracting from this sum the 9 new pulsars discovered here, plus the 3 others mentioned in Section 3 that were recently discovered by other projects, gives ~ 26 pulsars remaining in this sample, and around 190 pulsars in the full 4FGL catalogue. However, this is certainly an overestimate, as many of these sources have been searched already with other telescopes, and therefore our target list represents the remainder from a larger, unbiased sample from which more easily detected pulsars have already been removed. There are hints of this effect in our results: five of the nine new pulsars had fairly low pulsar probabilities $P(\text{psr}) < 0.25$, perhaps because the more promising sources have already been surveyed extensively by other telescopes, while the lower probability targets tend to be fainter, newer sources many of which have not been searched before. This also suggests that further searches of a larger number of apparently less promising *Fermi*-LAT sources below the $P(\text{psr})$ threshold that we used here may yet bear fruit.

Furthermore, even if this is an accurate estimate of the number of gamma-ray pulsars in our sample, it does not mean that there are 26 detectable radio pulsars in this sample. A large fraction of the young gamma-ray pulsars detected by the *Fermi*-LAT remain undetected in radio observations (and indeed the two recently discovered young gamma-ray pulsars that were covered in our survey were not detected), presumably due to the viewing angle missing the radio beam. While we deliberately avoided sources at low Galactic latitudes in order to reduce the chance of young pulsars entering our sample, we note that there are 17 sources in our list at lower Galactic latitudes than 4FGL J0802.1–5612, one of the two recently discovered young pulsars in our sample. Although MSPs tend to have wider radio beams, and hence are less likely to be 'radio-quiet', a handful of gamma-ray MSPs have now been discovered in the *Fermi*-LAT data, but have remained undetected in deep radio follow-up searches (Clark et al. 2018; Nieder et al. 2020b), and similar objects may exist within our targets.

Nevertheless, it is certain that there are still several detectable MSPs lurking in our target list, and iterative 4FGL releases (Ballet et al. 2020; Abdollahi et al. 2022) bring new, albeit fainter, unassociated sources to target. Indeed, since our survey began, likely MSP binaries have been discovered in optical and X-ray searches of three of our target sources, 4FGL J0540.0–7552 (Strader et al. 2021), 4FGL J0940.3–7610 (Swihart et al. 2021), and 4FGL J1120.0–2204 (Swihart et al. 2022), while a fourth, 4FGL J1702.7–5655, has recently been identified through the detection of gamma-ray eclipses (Corbet et al. 2022). 4FGL J1120.0–2204 in particular appears to have a white dwarf companion in a fairly long (15 h) orbit, but has remained undetected in many previous long radio observations,

as well as in our 10-min pointings. Its non-detection is therefore unlikely to be explained by orbital or eclipsing effects, suggesting that deeper searches, in addition to our continuing 'shallow' survey, may be necessary to uncover the nature of many of the remaining unidentified but pulsar-like *Fermi*-LAT sources.

5 CONCLUSIONS AND FUTURE WORK

We have presented the first results from TRAPUM's survey for new pulsars in unassociated *Fermi*-LAT sources using the MeerKAT radio telescope, discovering nine new MSPs, of which eight are in binary systems. Our results continue the trend of short-period binaries being discovered at a far higher rate within *Fermi*-LAT sources than in untargeted surveys, with the discovery of two new redback binaries (PSRs J1036–4353 and J1803–6707) with optically bright companion stars and radio eclipses, and a third (PSR J1526–2744) that is possibly the most compact known MSP–WD binary system in the Galactic field. Two other MSPs have preliminary orbital solutions that mark their companions as outliers among the known MSP–binary population, PSR J1757–6032 appears to have a less typical CO–WD companion, while PSR J1906–1754 has a much longer orbital period than any known black widow, but a minimum companion mass that is far lighter than that of a typical WD companion.

We obtained phase-connected timing solutions for two of the new MSPs, PSRs J1526–2744 and J1803–6707, using timing observations at Parkes and Nançay, that enabled us to detect gamma-ray pulsations in the *Fermi*-LAT data. Orbital period variations in PSR J1803–6707 precluded further extrapolation of the timing solution, but for PSR J1526–2744, gamma-ray timing provides a full 14-yr timing solution. This in turn enabled us to search for continuous gravitational waves from this pulsar in the Advanced LIGO O1, O2, and O3 data, although none were detected and the strain upper limit remains well above the pulsar's spin-down luminosity budget. A dedicated timing campaign is underway at MeerKAT to obtain phase-connected timing solutions, and afterwards gamma-ray pulsations, from the remaining seven discoveries (Burgay et al., in preparation), as are optical follow-up observations and modelling of the new redback binaries (Phosrisom et al., in preparation).

Our results also emphasize the promise of continued radio surveys of *Fermi*-LAT sources: several high-confidence pulsar candidates still remain within our target list but have eluded detection in ours and earlier surveys, perhaps due to scintillation, eclipses, or simple intrinsic faintness. Indeed, our TRAPUM survey continues to make discoveries beyond the first results presented here. Two further passes of the sources surveyed here are currently underway using MeerKAT's UHF receiver, from which we have discovered 8 additional MSPs already.¹² We have also performed several hour-long observations of a group of high confidence redback candidates that were previously identified in optical observations, detecting a further three new MSPs that will be presented in a dedicated paper (Thongmeekarkom et al., in preparation). We will continue our initial survey strategy of observing a large number of sources with short (10-min) observations, expanding our target list to include more sources from the most recent 4FGL DR3 catalogue, but deeper observations may be required to fully explore the most promising gamma-ray sources.

¹²<http://trapum.org/discoveries/>

ACKNOWLEDGEMENTS

The MeerKAT telescope is operated by the South African Radio Astronomy Observatory, which is a facility of the National Research Foundation, an agency of the Department of Science and Innovation. We thank staff at SARAO for their help with observations and commissioning. TRAPUM observations used the FBFUSE and AP-SUSE computing clusters for data acquisition, storage and analysis. These clusters were funded and installed by the Max-Planck-Institut für Radioastronomie (MPIfR) and the Max-Planck-Gesellschaft. The National Radio Astronomy Observatory is a facility of the National Science Foundation operated under cooperative agreement by Associated Universities, Inc. The Parkes radio telescope is part of the Australia Telescope National Facility (<https://ror.org/05qajvd42>) which is funded by the Australian Government for operation as a National Facility managed by CSIRO. We acknowledge the Wiradjuri people as the traditional owners of the Observatory site. The Nançay Radio Observatory is operated by the Paris Observatory, associated with the French Centre National de la Recherche Scientifique (CNRS) and Université d'Orléans. It is partially supported by the Region Centre Val de Loire in France. Partly based on observations with the 100-m telescope of the MPIfR at Effelsberg.

The Fermi LAT Collaboration acknowledges generous ongoing support from a number of agencies and institutes that have supported both the development and the operation of the LAT as well as scientific data analysis. These include the National Aeronautics and Space Administration and the Department of Energy in the United States, the Commissariat à l'Énergie Atomique and the Centre National de la Recherche Scientifique/Institut National de Physique Nucléaire et de Physique des Particules in France, the Agenzia Spaziale Italiana and the Istituto Nazionale di Fisica Nucleare in Italy, the Ministry of Education, Culture, Sports, Science and Technology (MEXT), High Energy Accelerator Research Organization (KEK) and Japan Aerospace Exploration Agency (JAXA) in Japan, and the K. A. Wallenberg Foundation, the Swedish Research Council and the Swedish National Space Board in Sweden.

Additional support for science analysis during the operations phase is gratefully acknowledged from the Istituto Nazionale di Astrofisica in Italy and the Centre National d'Études Spatiales in France. This work performed in part under DOE Contract DE-AC02-76SF00515.

eROSITA is the primary instrument aboard SRG, a joint Russian-German science mission supported by the Russian Space Agency (Roskosmos), in the interests of the Russian Academy of Sciences represented by its Space Research Institute (IKI), and the Deutsches Zentrum für Luft- und Raumfahrt (DLR). The SRG spacecraft was built by Lavochkin Association (NPOL) and its subcontractors, and is operated by NPOL with support from IKI and the Max Planck Institute for Extraterrestrial Physics (MPE). The development and construction of the eROSITA X-ray instrument was led by MPE, with contributions from the Dr. Karl Remeis Observatory Bamberg & ECAP (FAU Erlangen-Nürnberg), the University of Hamburg Observatory, the Leibniz Institute for Astrophysics Potsdam (AIP), and the Institute for Astronomy and Astrophysics of the University of Tübingen, with the support of DLR and the Max Planck Society. The Argelander Institute for Astronomy of the University of Bonn and the Ludwig Maximilians Universität Munich also participated in the science preparation for eROSITA. The eROSITA data shown here were processed using the eSASS/NRTA software system developed by the German eROSITA consortium.

This research has made use of data or software obtained from the Gravitational Wave Open Science Center (gw-openscience.org), a service of LIGO Laboratory, the LIGO Scientific Collaboration, the Virgo Collaboration, and KAGRA. LIGO Laboratory and Advanced

LIGO are funded by the United States National Science Foundation (NSF) as well as the Science and Technology Facilities Council (STFC) of the United Kingdom, the Max-Planck-Society (MPS), and the State of Niedersachsen/Germany for support of the construction of Advanced LIGO and construction and operation of the GEO600 detector. Additional support for Advanced LIGO was provided by the Australian Research Council. Virgo is funded, through the European Gravitational Observatory (EGO), by the French Centre National de Recherche Scientifique (CNRS), the Italian Istituto Nazionale di Fisica Nucleare (INFN) and the Dutch Nikhef, with contributions by institutions from Belgium, Germany, Greece, Hungary, Ireland, Japan, Monaco, Poland, Portugal, Spain. The construction and operation of KAGRA are funded by Ministry of Education, Culture, Sports, Science and Technology (MEXT), and Japan Society for the Promotion of Science (JSPS), National Research Foundation (NRF) and Ministry of Science and ICT (MSIT) in Korea, Academia Sinica (AS) and the Ministry of Science and Technology (MoST) in Taiwan.

This work has made use of data from the European Space Agency (ESA) mission *Gaia* (<https://www.cosmos.esa.int/gaia>), processed by the *Gaia* Data Processing and Analysis Consortium (DPAC, <https://www.cosmos.esa.int/web/gaia/dpac/consortium>). Funding for the DPAC has been provided by national institutions, in particular the institutions participating in the *Gaia* Multilateral Agreement.

Based on observations collected at the European Southern Observatory under ESO programmes 105.20RJ.001 and 105.20RJ.002.

CJC and RPB acknowledge support from the European Research Council (ERC) under the European Union's Horizon 2020 research and innovation programme (grant agreement no. 715051; Spiders). BWS and MCB acknowledge funding from the ERC under the European Union's Horizon 2020 research and innovation programme (grant agreement no. 694745). MB, AP, and AR gratefully acknowledge financial support by the research grant 'iPeska' (P.I. Andrea Possenti) funded under the INAF national call Prin-SKA/CTA approved with the Presidential Decree 70/2016. EDB, CJC, DJC, WC, MK, VVK, LN, PVP, and AR acknowledge continuing valuable support from the Max-Planck Society. LV acknowledges financial support from the Dean's Doctoral Scholar Award from the University of Manchester. VSD, TRM, and ULTRACAM acknowledge the support of the STFC. SMR is a CIFAR Fellow and is supported by the NSF Physics Frontiers Center awards 1430284 and 2020265.

We would like to thank Matthew Kerr, Guillem Martí-Devesa, and David Smith for reviewing this paper on behalf of the *Fermi*-LAT collaboration.

DATA AVAILABILITY

TRAPUM data products are available upon reasonable request to the TRAPUM collaboration. The *Fermi*-LAT data are available from the *Fermi* Science Support Center (<http://fermi.gsfc.nasa.gov/ssc>).

REFERENCES

- Aasi J. et al., 2014, *ApJ*, 785, 119
 Abbott B. P. et al., 2018, *Phys. Rev. Lett.*, 120, 031104
 Abbott B. P. et al., 2019, *Phys. Rev. D*, 99, 122002
 Abbott R. et al., 2020, *ApJ*, 902, L21
 Abbott R. et al., 2021, *SoftwareX*, 13, 100658
 Abbott R. et al., 2022a, *ApJ*, 932, 133
 Abbott R. et al., 2022b, *ApJ*, 935, 1
 Abdo A. A. et al., 2013, *ApJS*, 208, 17
 Abdollahi S. et al., 2020, *ApJS*, 247, 33
 Abdollahi S. et al., 2022, *ApJS*, 260, 53

- Ackermann M. et al., 2012, *ApJ*, 753, 83
- Alpar M. A., Cheng A. F., Ruderman M. A., Shaham J., 1982, *Nature*, 300, 728
- Andersen B. C., Ransom S. M., 2018, *ApJ*, 863, L13
- Antoniadis J. et al., 2013, *Science*, 340, 448
- Ashok A. et al., 2021, *ApJ*, 923, 85
- Atwood W. B. et al., 2009, *ApJ*, 697, 1071
- Atwood W. et al., 2013, in Brandt T. J., Omodei N., Wilson-Hodge C., eds, Proc. 4th Fermi Symposium 2012. eConf C121028. Monterey, California, p. 8
- Bailes M. et al., 2020, *PASA*, 37, e028
- Ballet J., Burnett T. H., Digel S. W., Lott B., 2020, preprint (arXiv:2005.11208)
- Barr E. D., 2018, in Weltevrede P., Perera B. B. P., Preston L. L., Sanidas S., eds, Pulsar Astrophysics the Next Fifty Years, Vol. 337. Jodrell Bank Observatory, UK, p. 175
- Barr E., 2020, Astrophysics Source Code Library, record ascl:2001.014
- Barr E. D. et al., 2013, *MNRAS*, 429, 1633
- Bassa C. G. et al., 2017, *ApJ*, 846, L20
- Becker W., Truemper J., 1997, *A&A*, 326, 682
- Berteaud J., Calore F., Clavel M., Serpico P. D., Dubus G., Petrucci P.-O., 2021, *Phys. Rev. D*, 104, 043007
- Bhattacharya D., van den Heuvel E. P. J., 1991, *Phys. Rep.*, 203, 1
- Bhattacharyya B. et al., 2021, *ApJ*, 910, 160
- Boyles J. et al., 2013, *ApJ*, 763, 80
- Breiman L., 2001, *Mach. Learn.*, 45, 5
- Bruel P., 2019, *A&A*, 622, A108
- Bruel P., Burnett T. H., Digel S. W., Johannesson G., Omodei N., Wood M., 2018, preprint (arXiv:1810.11394)
- Camilo F. et al., 2015, *ApJ*, 810, 85
- Carli E. et al., 2022, *MNRAS*, 517, 5406
- Chen W., Barr E., Karuppusamy R., Kramer M., Stappers B., 2021, *J. Astron. Instrum.*, 10, 2150013
- Clark C. J. et al., 2018, *Sci. Adv.*, 4, eaao7228
- Cognard I. et al., 2011, *ApJ*, 732, 47
- Corbet R. H. D. et al., 2022, *ApJ*, 935, 2
- Cromartie H. T. et al., 2016, *ApJ*, 819, 34
- Cutler C., Schutz B. F., 2005, *Phys. Rev. D*, 72, 063006
- Demorest P. B., Pennucci T., Ransom S. M., Roberts M. S. E., Hessels J. W. T., 2010, *Nature*, 467, 1081
- Deneva J. S. et al., 2016, *ApJ*, 823, 105
- de Jager O. C., Raubenheimer B. C., Swanepoel J. W. H., 1989, *A&A*, 221, 180
- Dhillon V. S. et al., 2007, *MNRAS*, 378, 825
- Finke T., Krämer M., Manconi S., 2021, *MNRAS*, 507, 4061
- Frail D. A., Jagannathan P., Mooley K. P., Intema H. T., 2016, *ApJ*, 829, 119
- Freire P. C. C., Ridolfi A., 2018, *MNRAS*, 476, 4794
- Gaia Collaboration, 2016, *A&A*, 595, A1
- Gaia Collaboration, 2022, preprint (arXiv:2208.00211)
- Guillemot L. et al., 2013, *ApJ*, 768, 169
- Haslam C. G. T., Salter C. J., Stoffel H., Wilson W. E., 1982, *A&AS*, 47, 1
- HI4PI Collaboration, 2016, *A&A*, 594, A116
- Hobbs G. et al., 2020, *PASA*, 37, e012
- Jankowski F., van Straten W., Keane E. F., Bailes M., Barr E. D., Johnston S., Kerr M., 2018, *MNRAS*, 473, 4436
- Johnston H. M., Kulkarni S. R., 1991, *ApJ*, 368, 504
- Jonas J. L., 2009, *IEEE Proc.*, 97, 1522
- Jonas J., MeerKAT Team, 2016, in Taylor R., Camilo F., Leeuw L., Moodley K., eds, Proc. MeerKAT Science: On the Pathway to the SKA – PoS(MeerKAT2016). SISSA, Trieste, PoS#1
- Kaspi V. et al., 2000, *ApJ*, 543, 321
- Keith M. J. et al., 2011, *MNRAS*, 414, 1292
- Kerr M., 2011, *ApJ*, 732, 38
- Kerr M. et al., 2012, *ApJ*, 748, L2
- Kramer M. et al., 2016, in Taylor R., Camilo F., Leeuw L., Moodley K., eds, Proc. MeerKAT Science: On the Pathway to the SKA – PoS(MeerKAT2016). SISSA, Trieste, PoS#3
- Krautter J. et al., 1999, *A&A*, 350, 743
- Lee K. J., Guillemot L., Yue Y. L., Kramer M., Champion D. J., 2012, *MNRAS*, 424, 2832
- Lorimer D. R., Kramer M., 2004, Handbook of Pulsar Astronomy, Vol. 4. Cambridge Univ. Press, Cambridge
- Luo S., Leung A. P., Hui C. Y., Li K. L., 2020, *MNRAS*, 492, 5377
- Manchester R. N., Hobbs G. B., Teoh A., Hobbs M., 2005, *AJ*, 129, 1993
- Marelli M., De Luca A., Caraveo P. A., 2011, *ApJ*, 733, 82
- Morello V. et al., 2019, *MNRAS*, 483, 3673
- Morello V., Barr E. D., Stappers B. W., Keane E. F., Lyne A. G., 2020, *MNRAS*, 497, 4654
- Nieder L. et al., 2019, *ApJ*, 883, 42
- Nieder L., Allen B., Clark C. J., Pletsch H. J., 2020a, *ApJ*, 901, 156
- Nieder L. et al., 2020b, *ApJ*, 902, L46
- Nieder L., Kerr M., Clark C. J., Bruel P., Cromartie H. T., Ransom S. M., Ray P. S., 2022, *ApJ*, 931, L3
- Obrocka M., Stappers B., Wilkinson P., 2015, *A&A*, 579, A69
- Pallanca C., Ransom S. M., Ferraro F. R., Dalessandro E., Lanzoni B., Hessels J. W. T., Stairs I., Freire P. C. C., 2014, *ApJ*, 795, 29
- Pletsch H. J. et al., 2012, *Science*, 338, 1314
- Pleunis Z. et al., 2017, *ApJ*, 846, L19
- Predehl P. et al., 2021, *A&A*, 647, A1
- Ransom S. M. et al., 2011, *ApJ*, 727, L16
- Ray P. S. et al., 2012, in Morselli A., ed., Proc. 2011 Fermi Symposium, eConf C110509
- Ray P. S. et al., 2022, *ApJ*, 927, 216
- Remazeilles M., Dickinson C., Bandy A. J., Bigot-Sazy M. A., Ghosh T., 2015, *MNRAS*, 451, 4311
- Ridolfi A. et al., 2016, *MNRAS*, 462, 2918
- Ridolfi A. et al., 2021, *MNRAS*, 504, 1407
- Roberts M. S. E., 2012, in van Leeuwen J., ed., Proc. IAU Symp. S291: Neutron Stars and Pulsars: Challenges and Opportunities After 80 Years. Cambridge Univ. Press, Cambridge, p. 127
- Roberts M. S. E., McLaughlin M. A., Gentile P. A., Ray P. S., Ransom S. M., Hessels J. W. T., 2015, in Fukazawa Y., Tanaka Y., Itoh R., eds, Proc. 5th Fermi Symposium, eConf C14102.1. p. 62
- Romani R. W., Kandel D., Filippenko A. V., Brink T. G., Zheng W., 2022, *ApJ*, 934, L17
- Saz Parkinson P. M., Xu H., Yu P. L. H., Salvetti D., Marelli M., Falcone A. D., 2016, *ApJ*, 820, 8
- Schroeder J., Halpern J., 2014, *ApJ*, 793, 78
- Smarr L. L., Blandford R., 1976, *ApJ*, 207, 574
- Spiewak R. et al., 2022, *PASA*, 39, e027
- Stappers B., Kramer M., 2016, in Taylor R., Camilo F., Leeuw L., Moodley K., eds, Proc. MeerKAT Science: On the Pathway to the SKA – PoS(MeerKAT 2016). SISSA, Trieste, PoS#9
- Steltner B., Papa M. A., Eggenstein H.-B., 2022, *Phys. Rev. D*, 105, 022005
- Stovall K. et al., 2014, *ApJ*, 791, 67
- Strader J. et al., 2021, *ApJ*, 917, 69
- Swihart S. J., Strader J., Aydi E., Chomiuk L., Dage K. C., Shishkovsky L., 2021, *ApJ*, 909, 185
- Swihart S. J., Strader J., Aydi E., Chomiuk L., Dage K. C., Kawash A., Sokolovsky K. V., Ferrara E. C., 2022, *ApJ*, 926, 201
- Tauris T. M., Langer N., Kramer M., 2011, *MNRAS*, 416, 2130
- The Fermi-LAT Collaboration, 2022, *Science*, 376, 521
- Wang P. et al., 2021, *Sci. China Phys. Mech. Astron.*, 64, 129562
- Woan G., Pitkin M. D., Haskell B., Jones D. I., Lasky P. D., 2018, *ApJ*, 863, L40
- Wu J. et al., 2018, *ApJ*, 854, 99
- Yao J. M., Manchester R. N., Wang N., 2017, *ApJ*, 835, 29
- Zhu W. W. et al., 2014, *ApJ*, 781, 117

¹Max Planck Institute for Gravitational Physics (Albert Einstein Institute), D-30167 Hannover, Germany

²Leibniz Universität Hannover, D-30167 Hannover, Germany

³Jodrell Bank Centre for Astrophysics, Department of Physics and Astronomy, The University of Manchester, Manchester M13 9PL, UK

⁴Max-Planck-Institut für Radioastronomie, Auf dem Hügel 69, D-53121 Bonn, Germany

⁵INAF – Osservatorio Astronomico di Cagliari, Via della Scienza 5, I-09047 Selargius, CA, Italy

⁶South African Radio Astronomy Observatory, 2 Fir Street, Black River Park, Observatory 7925, South Africa

⁷Max-Planck-Institut für Extraterrestrische Physik, Giessenbachstraße, D-85748 Garching, Germany

⁸Laboratoire d'Annecy-le-Vieux de Physique Théorique (LAPTh), CNRS, USMB, F-74940 Annecy, France

⁹LPC2E – Université d'Orléans / CNRS, F-45071 Orléans cedex 2, France

¹⁰Observatoire Radioastronomique de Nançay (ORN), Observatoire de Paris, Université PSL, Univ Orléans, CNRS, F-18330 Nançay, France

¹¹National Radio Astronomy Observatory, 520 Edgemont Road, Charlottesville, VA 22903, USA

¹²SKA Observatory, Jodrell Bank, Lower Withington, Macclesfield SK11 9FT, UK

¹³Department of Physics and Astronomy, University of the Western Cape, Bellville, Cape Town 7535, South Africa

¹⁴School of Physics, Trinity College Dublin, College Green, Dublin 2, D02 E8C0, Ireland

¹⁵Fakultät für Physik, Universität Bielefeld, Postfach 100131, D-33501 Bielefeld, Germany

¹⁶Department of Physics and Astronomy, University of Sheffield, Sheffield S3 7RH, UK

¹⁷Instituto de Astrofísica de Canarias, E-38205 La Laguna, Tenerife, Spain

¹⁸Department of Physics, University of Warwick, Coventry CV4 7AL, UK

This paper has been typeset from a $\text{\TeX}/\text{\LaTeX}$ file prepared by the author.

**Discovery of a Gamma-Ray Black Widow Pulsar by GPU-accelerated Einstein@Home**

L. Nieder^{1,2}, C. J. Clark³, D. Kandel⁴, R. W. Romani⁴, C. G. Bassa⁵, B. Allen^{1,6,2}, A. Ashok^{1,2}, I. Cognard^{7,8}, H. Fehrmann^{1,2}, P. Freire⁹, R. Karuppusamy⁹, M. Kramer^{9,3}, D. Li^{10,11}, B. Machenschalk^{1,2}, Z. Pan¹⁰, M. A. Papa^{1,6,2}, S. M. Ransom¹², P. S. Ray¹³, J. Roy¹⁴, P. Wang¹⁰, J. Wu⁹, C. Aulbert^{1,2}, E. D. Barr⁹, B. Beheshtipour^{1,2}, O. Behnke^{1,2}, B. Bhattacharyya¹⁴, R. P. Breton³, F. Camilo¹⁵, C. Choquet¹⁶, V. S. Dhillon^{17,18}, E. C. Ferrara^{19,20}, L. Guillemot^{7,8}, J. W. T. Hessels^{5,21}, M. Kerr¹³, S. A. Kwang⁶, T. R. Marsh²², M. B. Mickaliger³, Z. Pleunis^{23,24}, H. J. Pletsch¹, M. S. E. Roberts^{25,26}, S. Sanpa-arsa²⁷, and B. Steltner^{1,2}

¹Max-Planck-Institut für Gravitationsphysik (Albert-Einstein-Institut), 30167 Hannover, Germany; lars.nieder@aei.mpg.de

²Leibniz Universität Hannover, 30167 Hannover, Germany

³Jodrell Bank Centre for Astrophysics, Department of Physics and Astronomy, The University of Manchester, Manchester M13 9PL, UK

⁴KIPAC/Dept. of Physics, Stanford University, Stanford, CA 94305, USA

⁵ASTRON, The Netherlands Institute for Radio Astronomy, Oude Hoogeveensedijk 4, 7991 PD Dwingeloo, The Netherlands

⁶Department of Physics, University of Wisconsin–Milwaukee, P.O. Box 413, Milwaukee, WI 53201, USA

⁷Laboratoire de Physique et Chimie de l'Environnement et de l'Espace, Université d'Orléans/CNRS, F-45071 Orléans Cedex 02, France

⁸Station de radioastronomie de Nançay, Observatoire de Paris, CNRS/INSU, F-18330 Nançay, France

⁹Max-Planck-Institut für Radioastronomie, auf dem Hügel 69, 53121 Bonn, Germany

¹⁰National Astronomical Observatories, Chinese Academy of Sciences, Beijing 100101, People's Republic of China

¹¹NAOC-UKZN Computational Astrophysics Centre, University of KwaZulu-Natal, Durban 4000, South Africa

¹²National Radio Astronomy Observatory, 520 Edgemont Road, Charlottesville, VA, 22903, USA

¹³Space Science Division, Naval Research Laboratory, Washington, DC 20375-5352, USA

¹⁴National Centre for Radio Astrophysics, Tata Institute of Fundamental Research, Pune 411 007, India

¹⁵South African Radio Astronomy Observatory, 2 Fir Street, Black River Park, Observatory 7925, South Africa

¹⁶Résidence Le Dauphiné, rue Jean Bleuzen, Vanves, France

¹⁷Department of Physics and Astronomy, University of Sheffield, Sheffield S3 7RH, UK

¹⁸Instituto de Astrofísica de Canarias, E-38205 La Laguna, Tenerife, Spain

¹⁹NASA Goddard Space Flight Center, Greenbelt, MD 20771, USA

²⁰Department of Astronomy, University of Maryland, College Park, MD 20742, USA

²¹Anton Pannekoek Institute for Astronomy, University of Amsterdam, Science Park 904, 1098 XH Amsterdam, The Netherlands

²²Astronomy and Astrophysics Group, Department of Physics, University of Warwick, Coventry CV4 7AL, UK

²³Department of Physics, McGill University, 3600 rue University, Montréal, QC H3A 2T8, Canada

²⁴McGill Space Institute, McGill University, 3550 rue University, Montréal, QC H3A 2A7, Canada

²⁵New York University Abu Dhabi, P.O. Box 129188, Abu Dhabi, UAE

²⁶Eureka Scientific, Inc., 2452 Delmer Street, Suite 100, Oakland, CA 94602-3017, USA

²⁷National Astronomical Research Institute of Thailand (Public Organization), 260 Moo 4, T. Donkaew, A. Maerim, Chiang Mai, 50180, Thailand

Received 2020 September 1; revised 2020 September 22; accepted 2020 September 23; published 2020 October 22

Abstract

We report the discovery of 1.97 ms period gamma-ray pulsations from the 75 minute orbital-period binary pulsar now named PSR J1653–0158. The associated Fermi Large Area Telescope gamma-ray source 4FGL J1653.6–0158 has long been expected to harbor a binary millisecond pulsar. Despite the pulsar-like gamma-ray spectrum and candidate optical/X-ray associations—whose periodic brightness modulations suggested an orbit—no radio pulsations had been found in many searches. The pulsar was discovered by directly searching the gamma-ray data using the GPU-accelerated Einstein@Home distributed volunteer computing system. The multidimensional parameter space was bounded by positional and orbital constraints obtained from the optical counterpart. More sensitive analyses of archival and new radio data using knowledge of the pulsar timing solution yield very stringent upper limits on radio emission. Any radio emission is thus either exceptionally weak, or eclipsed for a large fraction of the time. The pulsar has one of the three lowest inferred surface magnetic-field strengths of any known pulsar with $B_{\text{surf}} \approx 4 \times 10^7$ G. The resulting mass function, combined with models of the companion star's optical light curve and spectra, suggests a pulsar mass $\gtrsim 2 M_{\odot}$. The companion is lightweight with mass $\sim 0.01 M_{\odot}$, and the orbital period is the shortest known for any rotation-powered binary pulsar. This discovery demonstrates the Fermi Large Area Telescope's potential to discover extreme pulsars that would otherwise remain undetected.

Unified Astronomy Thesaurus concepts: [Gamma-ray sources \(633\)](#); [Millisecond pulsars \(1062\)](#); [Neutron stars \(1108\)](#); [Binary pulsars \(153\)](#)

Supporting material: data behind figure



Original content from this work may be used under the terms of the [Creative Commons Attribution 4.0 licence](#). Any further distribution of this work must maintain attribution to the author(s) and the title of the work, journal citation and DOI.

1. Introduction

The Fermi Large Area Telescope (LAT) source 4FGL J1653.6–0158 is a bright gamma-ray source, and the brightest remaining unassociated source (Saz Parkinson et al. 2016). It was first seen by the Energetic Gamma Ray Experiment Telescope (EGRET; Hartman et al. 1999), and was also listed in the LAT Bright Gamma-ray source list (Abdo et al. 2009) more than a decade ago. While pulsars were discovered in several other sources from this list (see, e.g., Ransom et al. 2011), the origin of 4FGL J1653.6–0158 remained unidentified. The detection of a variable X-ray and optical candidate counterpart with 75 minute period consistent with the gamma-ray position of 4FGL J1653.6–0158 provided strong evidence of it being a binary gamma-ray pulsar (Kong et al. 2014; Romani et al. 2014).

To identify the neutron star in 4FGL J1653.6–0158, we carried out a binary-pulsar search of the gamma-rays, using the powerful GPU-accelerated distributed volunteer computing system Einstein@Home. Such searches are very computationally demanding, and would take decades to centuries on a single computer while still taking weeks or months on Einstein@Home. Thus, the search methods are specifically designed to ensure efficiency (Nieder et al. 2020). One key element is the use of constraints derived from optical observations. The companion’s pulsar-facing side is heated by the pulsar wind, leading to a periodically varying optical light curve. This permits the orbital period P_{orb} and other orbital parameters to be tightly constrained (for a feasible search the uncertainty ΔP_{orb} needs to be less than a few milliseconds). In addition, because the sky position of the optical source is typically known to high precision (sub-milliarcsecond level), a search over position parameters is not needed.

Here we present the discovery and analysis of gamma-ray pulsations from PSR J1653–0158 in 4FGL J1653.6–0158. The pulsar is spinning very rapidly, at a rotational frequency of 508 Hz. The inferred surface magnetic-field strength is one of the lowest of all known pulsars. The discovery also confirms the 75 minute orbital period. This very short orbital period raises interesting questions about the evolutionary path which created the system.

This Letter is organized as follows. In Section 2, we describe the gamma-ray search, detection, and analysis within LAT data. The optical analysis of the pulsar’s companion, radio pulsation searches, and a continuous gravitational-wave follow-up search are presented in Section 3. We discuss the results and conclude in Section 4.

2. Gamma-Ray Pulsations

2.1. Data Preparation

We searched for gamma-ray pulsations in the arrival times of photons observed by the Fermi-LAT (Atwood et al. 2009) between 2008 August 3 and 2018 April 16 (MJDs 54,681 and 58,224). We included SOURCE-class photons according to the P8R2_SOURCE_V6 (Atwood et al. 2012) instrument response functions (IRFs),²⁸ with reconstructed incidence angles within a 5° region of interest (RoI) around the putative pulsar position, energies above 100 MeV, and zenith angles below 90°. Here, we used the presumptive companion’s position as reported in

the Gaia DR2 Catalog (hereafter Gaia catalog; Gaia Collaboration et al. 2018). The celestial parameters (J2000.0) are $\alpha = 16^{\text{h}}53^{\text{m}}38^{\text{s}}.05381(5)$ and $\delta = -01^{\circ}58'36''.8930(5)$, with 1σ uncertainties on the last digits reported in parentheses.

Using the photon incidence angles and energies, we constructed a probability or weight for each photon, $w_j \in [0, 1]$, where j labels the photon: w_j is the probability that the j th photon originated from the posited source, as opposed to a foreground source. These weights were computed by `gtsrcprob`, using the preliminary Fermi-LAT 8 yr source catalog²⁹ as a model for the flux within the RoI without performing a full spectral fit. Weighting the contribution of each photon to a detection statistic in this way greatly increases the search sensitivity (Kerr 2011), and the distribution of weights can be used to predict expected signal-to-noise ratios (Nieder et al. 2020).

The data set used here consisted of $N = 354,009$ photons, collected over a period of 3542 days. The properties of the detection statistics (semicoherent power S_1 , coherent power P_1 , and H statistic) depend upon the lowest moments of the weights, which are

$$\sum_{j=1}^N w_j \approx 10266, \quad \sum_{j=1}^N w_j^2 \approx 2464, \quad \text{and} \quad \sum_{j=1}^N w_j^4 \approx 931.$$

These moments determine the ultimate sensitivity to a particular pulse profile and pulsed fraction, as given in Equation (11) in Nieder et al. (2020).

Following the pulsar discovery, we extended this data set to 2020 February 23 (MJD 58,902), using the latest P8R3_SOURCE_V2 IRFs (Bruehl et al. 2018), a larger maximum zenith angle of 105°, and using the Fermi-LAT Fourth Source Catalog (hereafter 4FGL; Abdollahi et al. 2020) as the RoI model for the photon probability weight computations.

2.2. Search

The binary-pulsar search methods are described by Nieder et al. (2020), which are a generalization and extension of the isolated-pulsar search methods from Pletsch & Clark (2014).

The searched ranges are guided by the known millisecond pulsar (MSP) population in the Australia Telescope National Facility (ATNF) Pulsar Catalogue³⁰ (Manchester et al. 2005). For the spin frequency, we searched $f \in [0, 1500]$ Hz.³¹ The spin-frequency derivative was expected to be in the range $\dot{f} \in [-10^{-13}, 0]$ Hz s⁻¹.

The sky position of the candidate optical counterpart is constrained to high precision in the Gaia catalog, so no astrometric search is required. The proper motion measured by Gaia for the optical counterpart was ignored for the search.

2.2.1. Orbital Constraints from Optical Observations

The orbital-period estimate of Romani et al. (2014) was derived from Southern Astrophysical Research (SOAR), WIYN, and Catalina Sky Survey (CSS) observations. These were augmented by new 350 s SOAR Goodman High Throughput

²⁹ <https://fermi.gsfc.nasa.gov/ssc/data/access/lat/f8y/>

³⁰ <http://www.atnf.csiro.au/research/pulsar/psrcat>

³¹ The upper limit has been chosen to be sensitive to pulsars spinning at up to 750 Hz, which have two-peaked pulse profiles where the peaks are half a rotation apart (see also Pletsch & Clark 2014). Note that the current record spin frequency is 716 Hz (Hessels et al. 2006).

²⁸ See https://fermi.gsfc.nasa.gov/ssc/data/analysis/LAT_essentials.html.

Spectrograph (GHTS) g' , r' , i' exposures (63 g' , 75 r' , 42 i') from MJD 56,514.074–56,516.184, and with the 300 s g' , r' , and i' exposures obtained by Kong et al. (2014) using the Wide Field camera (WFC) on the 2.5 m Isaac Newton Telescope (INT) on La Palma. For these two data sets, the scatter about the light-curve trends was appreciably larger than the very small statistical errors; we thus add 0.03 mag in quadrature to account for unmodeled fast variability and/or photometry systematics. To further refine the orbital-period uncertainty, we obtained additional observations in u' , g' , and i' using the high-speed multiband imager ULTRACAM (Dhillon et al. 2007) on the 4.2 m William Herschel Telescope (WHT) on two nights (MJDs 57,170 and 57,195), covering six and three orbits of the binary system, respectively, with a series of 20 s exposures. Conditions were very poor on the first night with seeing $>5''$, particularly at the beginning of the observation. We therefore only used the second night’s data for the optical light-curve modeling in Section 3.1, adding the latter half of the first night’s observations for orbital-period estimation. Finally, we obtained further INT+WFC exposures (23 g' , 151 r' , 45 i') on MJD 57,988–57,991. The g' , r' , i' filter fluxes were referenced to in-field PanSTARRS catalog sources, and then converted to the Sloan Digital Sky Survey (SDSS) scale. The u' photometry was calibrated against an SDSS standard star observed on MJD 57,170. We estimate ~ 0.05 mag systematic uncertainties in g' , r' , and i' , with uncertainties as large as ~ 0.1 mag in u' .

We constrained the orbital period using the multiband Lomb–Scargle periodogram method (VanderPlas & Ivezić 2015, excluding the u' ULTRACAM data, as the modulation has very low signal-to-noise ratio in this band). To infer reasonable statistical uncertainties, we fit for and removed constant magnitude offsets, consistent with our estimated calibration uncertainties, between each night’s observations in each band, and additionally rescaled the magnitude uncertainties to obtain a reduced chi-square of unity. This constrained the orbital period to $P_{\text{orb}} = 0.0519447518 \pm 6.0 \times 10^{-9}$ days, where the quoted uncertainty is the 1σ statistical uncertainty. For the pulsation search, we chose to search the 3σ range around this value.

In Romani et al. (2014), the time of the pulsar’s ascending node, T_{asc} , was estimated from the photometric light curve. However, the optical maximum is distinctly asymmetric (see Section 3.1), which can bias orbital phase estimates. We therefore used the spectroscopic radial-velocity measurements from Romani et al. (2014), folded at the orbital period obtained above, and fit the phase of a sinusoidal radial-velocity curve, finding $T_{\text{asc}} = \text{MJD } 56,513.47981 \pm 2.1 \times 10^{-4}$. However, as radial velocities may still be slightly biased by asymmetric heating, we elected to search a wide range around this value, corresponding to $\pm 8\sigma$.

For the projected semimajor-axis parameter $x = a_1 \sin i/c$, we decided to start searching $x \in [0, 0.1]$ s, with the intention to go to larger values in the case of no detection. For a pulsar mass of $1.6 M_{\odot}$, this would cover the companion mass range up to $0.2 M_{\odot}$ and would include companion masses of all known “black-widow” systems as well as some of the lower-mass “redback” systems (Roberts 2013; Strader et al. 2019). Here, a_1 is the pulsar’s semimajor axis, i denotes the inclination angle, and c is the speed of light. As described in Nieder et al. (2020), we expected $x \in [0, 0.2]$ s based on the companion’s velocity amplitude reported by Romani et al. (2014) and the masses

expected for “spider” companions, i.e., black-widow or redback companions.

2.2.2. Search Grids

To cover the relevant orbital-parameter space in $\{x, P_{\text{orb}}, T_{\text{asc}}\}$, we use *optimized grids* (Fehrmann & Pletsch 2014). These grids use as few points as possible still ensuring that a signal within the relevant space should be detected. Furthermore, they are able to cover the orbital-parameter space efficiently even though the required density depends on one of the orbital parameters, x .

Key to building an optimized grid is to know how the signal-to-noise ratio drops due to offsets from the true pulsar parameters. This is estimated using a *distance metric* on the orbital-parameter space (Nieder et al. 2020). In our case, the three-dimensional grid was designed to have a worst-case mismatch $\bar{m} = 0.2$, i.e., not more than 20% of the (semicoherent or coherent) signal power should be lost due to orbital-parameter offsets. Of most relevance is that 99% of randomly injected orbital-parameter points have a mismatch below $\bar{m} = 0.04$ to the closest grid point.

Due to the f -dependency of the required grid-point density, we search f in steps, and build the corresponding orbital grids prior to the start of the search on the computing cluster ATLAS in Hannover (Aulbert & Fehrmann 2008).

2.2.3. Einstein@Home

Searching the five-dimensional parameter space $\{f, \dot{f}, x, P_{\text{orb}}, T_{\text{asc}}\}$ is a huge computational task with over 10^{17} trials. Thus, the first (computing-intensive) search stages were performed on Einstein@Home, a distributed volunteer computing system (Allen et al. 2013). As done for radio pulsar searches previously, the search code utilizes the approximately 10,000 GPUs active on Einstein@Home for a computing speedup of ~ 10 , comparing the runtimes on CPUs and GPUs.

The parameter space is divided into more than one million regions. Searching one of these is called a “work unit.” These work units are sent to computers participating in Einstein@Home, and are searched when the computer is otherwise idle. Depending on the system, searching a work unit takes between half an hour and up to a few hours of computational time. In total, the search would have taken more than 50 years on a single computer, but using Einstein@Home it took less than 2 weeks.

2.2.4. Gamma-Ray Detection

The search process involves multiple stages in which semicoherent statistics are constructed, and the most significant candidates are passed on to fully coherent follow-up stages (for full details of the search pipeline and signal-to-noise ratio definitions, see Nieder et al. 2020). In the last semicoherent stage, a candidate found at a frequency of 1016 Hz had signal-to-noise ratio $S_1 = 8.6$, which we now associate with PSR J1653–0158. This was not the strongest candidate or far above the background of noise, but was among the 10 most significant candidates in its work unit, and therefore passed on to the coherent stage. In the coherent stage, it was very significant, with a signal-to-noise ratio $P_1/2 = 94$.

The search follow-ups confirmed significant pulsations with period $P \approx 1.97$ ms (or $f \approx 508$ Hz), while the actual search revealed an alias at twice the pulsar frequency. This may be

Table 1
Timing Solution for PSR J1653–0158

Parameter	Value
Range of observational data (MJD)	54682–58902
Reference epoch (MJD)	56100.0
Celestial Parameters from Gaia Catalog	
R.A., α (J2000.0)	16 ^h 53 ^m 38 ^s .05381(5)
Decl., δ (J2000.0)	−01°58′36″.8930(5)
Positional epoch (MJD)	57205.875
Proper motion in R.A., $\mu_\alpha \cos \delta$ (mas yr ^{−1})	−19.62 ± 1.86
Proper motion in decl., μ_δ (mas yr ^{−1})	−3.74 ± 1.12
Parallax ^a , ϖ (mas)	1.88 ± 1.01
Timing Parameters	
Spin frequency, f (Hz)	508.21219457426(6)
Spin-frequency derivative, \dot{f} (Hz s ^{−1})	−6.204(8) × 10 ^{−16}
Spin period, P (ms)	1.9676820247057(2)
Spin-period derivative, \dot{P} (s s ^{−1})	2.402(3) × 10 ^{−21}
Proj. semimajor axis, x (s)	0.01071(1)
Orbital period, P_{orb} (days)	0.0519447575(4)
Epoch of ascending node, T_{asc} (MJD)	56513.479171(8)
Derived Parameters for Distance $d = 840$ pc	
Shklovskii spin-down, \dot{P}_{Shk} (s s ^{−1})	1.6 × 10 ^{−21}
Galactic acceleration spin-down, \dot{P}_{Gal} (s s ^{−1})	−4.8 × 10 ^{−23}
Spin-down power, \dot{E} (erg s ^{−1})	4.4 × 10 ³³
Surface B -field, B_{surf} (G)	4.1 × 10 ⁷
Light-cylinder B -field, B_{LC} (G)	5.0 × 10 ⁴
Characteristic age, τ_c (Gyr)	37
Gamma-ray luminosity ^b , L_γ (erg s ^{−1})	2.9 × 10 ³³
Gamma-ray efficiency, $n_\gamma = L_\gamma / \dot{E}$	0.66

Notes. The JPL DE405 solar system ephemeris has been used, and times refer to TDB.

^a Corresponds to a model-independent distance $d = 533_{-187}^{+625}$ pc, but for the derived parameters the consistent distance $d = 840_{-40}^{+40}$ pc derived from optical modeling is used (see Table 2).

^b Taken from 4FGL Source Catalog (Abdollahi et al. 2020).

because the signal has significant power in the second harmonic.

Note that the signal was found outside the 3σ range in T_{asc} from the constraints reported in this work, and outside the 3σ range given by Romani et al. (2014). This can be caused by asymmetric heating (see Section 2.2.1).

2.3. Timing

The parameters used in the phase model to describe the pulsar’s rotation are measured in a timing analysis. We use the timing methods as explained in Clark et al. (2017), which are an extension of the methods by Kerr et al. (2015). The basic principle is that the parameter space around the discovery parameters is explored using a Monte Carlo sampling algorithm with a template pulse profile.

To marginalize over the pulse-profile template, we vary the template parameters as described in Nieder et al. (2019). In the case of PSR J1653–0158, we used a template consisting of two symmetrical, wrapped Gaussian peaks. We used constraints on the peaks’ FWHM, such that the peaks must be broader than 5% of a rotation, and narrower than half a rotation.

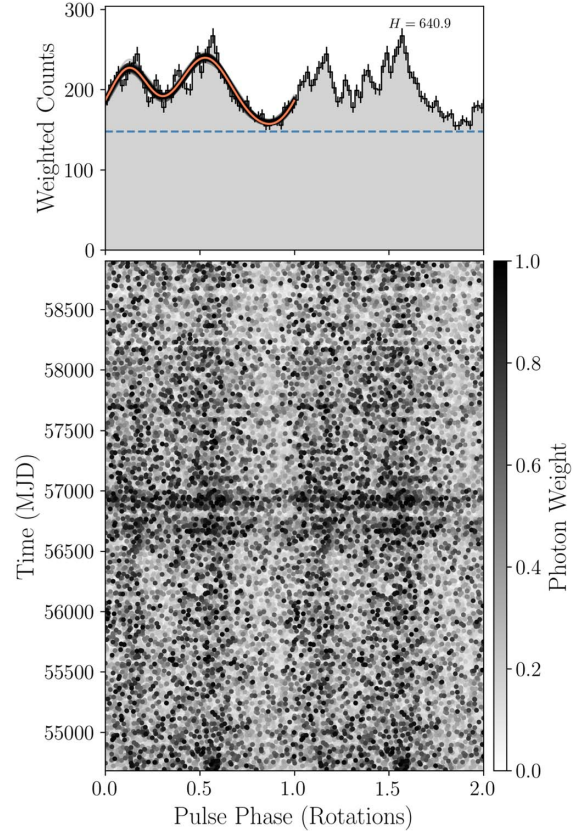


Figure 1. Integrated pulse-profile and phase-time diagram of PSR J1653–0158, showing two identical rotations. Top: the histogram shows the weighted counts for 50 bins. The orange curve indicates the pulse-profile template with the highest signal power, and the transparent black curves represent 100 templates randomly selected from the Monte Carlo samples after the chain stabilized, to indicate the uncertainty on the profile. The dashed blue line denotes the source background. Bottom: each point represents the pulsar’s rotational phase at emission of a photon, with the intensity indicating the photon’s probability weight. Note that PSR J1653–0158 received more exposure between MJDs 56,600 and 57,000 when the LAT pointed more often toward the Galactic center.

Our timing solution over 11 yr of LAT data is shown in Table 1. The folded gamma-ray data and the pulse profile are portrayed in Figure 1.

The observed spin-down \dot{P} is one of the lowest of all known pulsars. To estimate the intrinsic \dot{P} we account for the Shklovskii effect (Shklovskii 1970), and the Galactic acceleration (see, e.g., Damour & Taylor 1991). The results are summarized in Table 1. The observed contribution due to the difference in Galactic acceleration of the Sun and the pulsar is computed with $R_{\text{Sun}} = 8.21$ kpc, $z_{\text{Sun}} = 14$ pc, and the Galactic potential model `PJM17_best.Tpot` (McMillan 2017), as implemented in their code.³² For PSR J1653–0158, we used $R_{\text{J1653}} = 7.48$ kpc, and $z_{\text{J1653}} = 367$ pc, assuming $d = 840$ pc (see Table 2). The contributions parallel and perpendicular to the Galactic disk nearly cancel each other, so that the choice of the potential and its relevant parameters have a seemingly large

³² <https://github.com/PaulMcMillan-Astro/GalPot>

Table 2
Light-curve Fit Results for PSR J1653–0158

Parameters	Veiled	Veiled+HS
Inclination, i (deg)	$79.4^{+5.7}_{-6.8}$	$72.3^{+5.0}_{-4.9}$
Filling factor, f_c	$0.97^{+0.02}_{-0.02}$	$0.88^{+0.03}_{-0.03}$
Heating luminosity, L_P (10^{33} erg s $^{-1}$)	$3.33^{+0.39}_{-0.34}$	$3.15^{+0.26}_{-0.27}$
Night-side temperature, T_N (K)	3250^{+243}_{-331}	3295^{+227}_{-300}
V-band extinction, A_V	$1.06^{+0.08}_{-0.10}$	$1.06^{+0.07}_{-0.09}$
Distance, d (pc)	830^{+50}_{-50}	840^{+40}_{-40}
Veiling flux norm, f_A (μ Jy)	$101.7^{+11.4}_{-11.1}$	$99.9^{+11.7}_{-11.4}$
Veiling flux index, p	$0.50^{+0.05}_{-0.03}$	$0.49^{+0.03}_{-0.03}$
Spot azimuth, θ_c (deg)	...	$286.8^{+5.8}_{-6.9}$
Spot co-latitude, ϕ_c (deg)	...	$-50.5^{+9.2}_{-8.4}$
Gaussian spot width, σ_c (deg)	...	$25.2^{+5.0}_{-4.9}$
Spot temperature increase, A_c	...	$0.66^{+0.21}_{-0.21}$
Neutron star mass, M_{NS} (M_\odot)	$1.99^{+0.18}_{-0.08}$	$2.17^{+0.21}_{-0.15}$
Companion mass, M_c (M_\odot)	$0.013^{+0.001}_{-0.001}$	$0.014^{+0.001}_{-0.001}$
χ^2/DoF	1.72	1.38

Note. Parameters from the best-fit light-curve/radial-velocity models, with and without a surface hot spot, including MCMC errors.

effect on the actual small value of \dot{P}_{Gal} , and can even change the sign. However, the overall kinematic contribution to the observed \dot{P} is dominated by the Shklovskii term, and its uncertainty by the uncertainty in the distance estimate. The estimated intrinsic spin-down is $\dot{P}_{\text{int}} = 8.5 \times 10^{-22}$ s s $^{-1}$ for distance $d = 840$ pc.

3. Multiwavelength and Multimessenger

3.1. Optical Light-curve Modeling and System Masses

By modeling the optical light curves and radial velocities we can constrain the binary mass and distance and the system viewing angle. Comparing the individual filters between nights suggest small $\delta m \approx 0.05$ shifts in zero-points, consistent with the systematic estimates above. Correcting to match the individual filters, we then rebinned the light curve, placing the photometry on a regular grid with points spaced by $\delta\phi = 0.004$, using the Python package `Lightkurve`; after excision of a few obviously discrepant points, we retain 248 u' , 239 g' , 220 r' , and 245 i' points for light-curve fitting (Figure 2). This fitting is done with a version of the `Icarus` code of Breton et al. (2013) modified to include the effect of hot spots on the companion surface, likely generated by precipitation of particles from the intrabinary shock (IBS) to companion magnetic poles (Sanchez & Romani 2017). All parameter values and errors are determined by Markov Chain Monte Carlo (MCMC) modeling.

The very shallow modulation of these light curves might normally be interpreted as indicating a small inclination i . However given the large companion radial-velocity amplitude $K = 666.9 \pm 7.5$ km s $^{-1}$, implying a mass function $f(M) = 1.60 \pm 0.05 M_\odot$, measured by Romani et al. (2014), a small inclination would give an unphysical, large neutron star mass. As noted in that paper, the light curves and spectra show that a strong blue nonthermal veiling flux dominates at orbital minimum. With increasingly shallow modulation for the bluer colors, this is also evident in the present photometry. Thus, the minimal model for this pulsar must include a nonthermal veiling flux. Although this is likely associated with the IBS, we

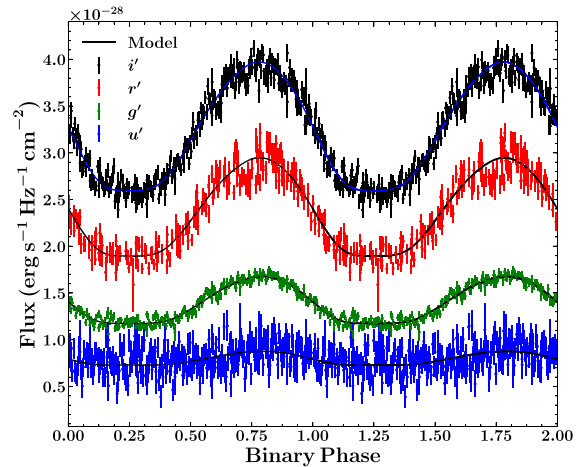


Figure 2. u' , g' , r' , and i' light curves for PSR J1653–0158, with the best-fit model curves. Note the flat minima and decreasing modulation for bluer colors, a consequence of the hard spectrum veiling flux. Two identical cycles are shown for clarity.

model it here as a simple power law with form $f_\nu = f_A (\nu/10^{14} \text{ Hz})^{-p}$. This flux is nearly constant through the orbit, although there are hints of phase structure, e.g., in r' and i' at $\phi_B = 0.72$ (see Figure 2). Any model without such a power-law component is completely unacceptable. These fits prefer an A_V slightly higher than, but consistent with, the maximum in this direction (obtained by ~ 300 pc; Green et al. 2019).³³

In Figure 2, one notices that the orbital maximum is slightly delayed from $\phi_B = 0.75$, especially in the bluer colors. Such asymmetric heating is most easily modeled adding a polar hot spot with location (θ_c, ϕ_c) and local temperature increase A_c in a Gaussian pattern of width σ_c ; when we include such a component, the fit improves greatly, with $\Delta\chi^2/\text{DoF} = -0.34$. The Akaike information criterion comparison of the two models indicates that the model with a hot spot is preferred at the 10^{-18} level, despite the extra degrees of freedom. We give the fit parameters for both models in Table 2. Note that with the fine structure near maximum, the model is not yet fully acceptable ($\chi^2/\text{DoF} \sim 1.4$). More detailed models, including direct emission from the IBS or possibly the effects of companion global winds (Kandel & Romani 2020), may be needed to fully model the light curves. Such modeling would be greatly helped by light curves over an even broader spectral range, with IBS effects increasingly dominant in the UV, and low-temperature companion emission better constrained in the IR. With many cycles we could also assess the reality (and stability) of the apparent fine structure and test for hot-spot motion.

Our fit distance may be cross-checked with two other quantities. (1) With the 4FGL energy flux $f_\gamma = 3.5 \times 10^{-11}$ erg cm $^{-2}$ s $^{-1}$ between 100 MeV and 100 GeV, our fit distance gives an isotropic gamma-ray luminosity $L_\gamma = 3 \times 10^{33}$ erg s $^{-1}$, in good agreement with the $L_\gamma \approx (10^{33} \text{ erg s}^{-1} \dot{E})^{1/2}$ heuristic luminosity law (Abdo et al. 2013), as a function of the spin-down power \dot{E} . This luminosity is consistent with the model for direct radiative heating of the companion. (2) Our fit distance is also consistent with the model-independent, but lower-accuracy, distance from the Gaia

³³ <https://doi.org/10.7910/DVN/2EJ9TX>

Table 3
Summary of Radio Searches for PSR J1653–0158

Telescope	Frequency (MHz)	Data Start (UTC)	Data Span (s)	Orbital Phase	Limit (μ Jy)	Reference/Survey
Effelsberg	1210–1510	2010 May 26, 21:33	1920	0.88–1.31	63	Barr et al. (2013)
Effelsberg	1210–1510	2014 Aug 26, 20:27	4600	0.15–1.17	41	
Effelsberg	4608–5108	2014 Aug 29, 18:52	4600	0.62–1.65	33	
Effelsberg	4608–5108	2020 Jun 18, 22:09	11820	0.85–3.48	20	
FAST	1050–1450	2020 Jun 04, 16:30	2036	0.80–1.25	8	Li et al. (2018)
GBT	720–920	2009 Sep 20, 00:49	3200	0.93–1.65	51	
GBT	720–920	2010 Dec 13, 21:04	1300	0.91–1.20	80	
GBT	720–920	2011 Dec 22, 12:11	2400	0.74–1.27	59	Sanpa-arsa (2016)
GBT	305–395	2012 Feb 22, 14:31	1700	0.27–0.65	301	
GBT	1700–2300	2014 Nov 18, 14:28	1200	0.36–0.63	43	
GBT	1700–2300	2014 Nov 20, 13:56	2400	0.44–0.98	30	
GBT	1700–2300	2014 Nov 21, 22:38	1800	0.66–1.07	35	
GBT	720–920	2017 Jan 28, 13:20	1200	0.97–1.24	83	
GMRT	591–623	2011 Feb 02, 02:32	1800	0.94–1.34	730	Bhattacharyya et al.
GMRT	306–338	2012 May 15, 22:31	1800	0.54–1.06	990	(2013, 2020, in preparation)
GMRT	306–338	2012 Jun 11, 17:49	1800	0.55–0.95	990	"
GMRT	591–623	2014 Aug 19, 13:44	1800	0.00–0.54	270	"
GMRT	591–623	2014 Aug 30, 11:17	1800	0.80–1.38	270	"
GMRT	591–623	2015 Dec 28, 03:55	1800	0.73–1.13	270	"
LOFAR	110–180	2017 Mar 15, 04:18	15 × 320	Full orbit	6,200	Bassa et al. (2017)
LOFAR	110–180	2017 Apr 15, 02:20	15 × 320	Full orbit	6,200	"
Lovell	1332–1732	2019 Mar 15, 01:34	5400	0.57–1.77	82	
Lovell	1332–1732	2019 Mar 16, 02:53	5400	0.87–2.08	82	
Lovell	1332–1732	2019 Mar 17, 01:47	5400	0.25–1.45	82	
Nançay	1230–1742	2014 Aug 20, 18:33	1850	0.12–0.53	77	Desvignes et al. (2013)
Parkes	1241–1497	2016 Nov 05, 06:17	3586	0.26–1.06	178	Camilo et al. (2016)

Note. The columns show the telescope used, the observed frequency range, the start time and data span, the range of orbital phases covered, the resulting limit on a pulsed component, and a reference with relevant details. The orbital phase is given in orbits, and ranges >1 indicate that more than one orbit has been observed. The considered maximum dispersion measure varies with the observing frequency from $DM = 80 \text{ pc cm}^{-3}$ at the lowest frequencies to $DM = 350 \text{ pc cm}^{-3}$ at the highest frequencies. To estimate the limit on the pulsed component, we used Equation (6) from Ray et al. (2011) assuming a pulse width of $0.25 P$, and a threshold signal-to-noise ratio $S/N_{\min} = 7$.

parallax. Thus, the 840 pc distance seems reliable, although systematic effects probably dominate over the rather small ~ 50 pc statistical errors.

Armed with the fits, we can estimate the companion masses, correcting the observed radial-velocity amplitude (fit with a K-star template) for the temperature-dependent weighting of the absorption lines across the companion face as in Kandel & Romani (2020). The results indicate substantial mass accretion, as expected for these ultrashort-period systems. With the preferred Veiled+HS model the mass significantly exceeds $2.0 M_{\odot}$, adding to the growing list of spider binaries in this mass range. Note that the inclination i uncertainty dominates the error in this mass determination. Broader range photometric studies, with better constraint on the heating pattern, can reduce the i uncertainty.

3.2. Radio Pulsation Searches

The pulsar position has been observed in radio multiple times. Several searches were performed before the gamma-ray pulsation discovery, and a few very sensitive follow-up searches afterward. Despite the more than 20 observations with eight of the most sensitive radio telescopes, no radio pulsations have been found.

The results of the radio searches are given in Table 3. Observations are spread over 11 yr, with observing frequencies ranging from 100 MHz up to 5 GHz. All orbital phases have been covered by most of the telescopes. Since there was no detection, the table also gives upper limits derived from the

observations. For all but LOFAR, the data (both archival and recent) were folded with the gamma-ray-derived ephemeris, and searched only over dispersion measure.

The strictest upper limits on pulsed radio emission are $8 \mu\text{Jy}$ at 1.4 GHz, and $20 \mu\text{Jy}$ at 4.9 GHz. This is fainter than the threshold of $30 \mu\text{Jy}$ that Abdo et al. (2013) use to define a pulsar to be “radio-quiet.” Note, that for the calculation of the limits we included the parts of the orbit where eclipses might be expected for spider pulsars. Thus, the limit constrains the maximum emission of the system, and not the maximum emission from the pulsar alone.

3.3. Continuous Gravitational Waves

We search for nearly monochromatic, continuous gravitational waves (GWs) from PSR J1653–0158, using data from the first³⁴ and second³⁵ observing runs of the Advanced LIGO detectors (The LIGO Scientific Collaboration et al. 2019). We assume that GWs are emitted at the first and second harmonic of the neutron star’s rotational frequency, as would occur if the spin axis is misaligned with the principal axes of the moment of inertia tensor (Jones 2010, 2015).

We employ two different analysis procedures, which yield consistent results. The first is frequentist, based on the multi-detector maximum-likelihood \mathcal{F} -statistic introduced by Cutler & Schutz (2005). The second is the Bayesian time-domain method

³⁴ <https://doi.org/10.7935/K57P8W9D>

³⁵ <https://doi.org/10.7935/CA75-FM95>

(Dupuis & Woan 2005) as detailed by Pitkin et al. (2017), with triaxial nonaligned priors (Pitkin et al. 2015). Both methods coherently combine data from the two detectors, taking into account their antenna patterns and the GW polarization. The \mathcal{F} -statistic search excludes data taken during times when the relevant frequency bands are excessively noisy.

The results are consistent with no GW emission. At twice the rotation frequency, the \mathcal{F} -statistic 95% confidence upper limit on the intrinsic GW amplitude h_0 is 4.4×10^{-26} . The 95% credible interval upper limit from the Bayesian analysis on $h_0 = 2C_{22}$ is 3.0×10^{-26} . At the rotation frequency (only checked with the Bayesian method) the 95% confidence upper limit on the amplitude C_{21} is 6.6×10^{-26} .

Since the dominant GW frequency might be mismatched from twice the rotation frequency (Abbott et al. 2019a), we performed an \mathcal{F} -statistic search in a ± 1 Hz band around this, with an extended \dot{f} -range. This yields larger upper limits on h_0 , with a mean value of 1.3×10^{-25} in 10 mHz-wide bands. Full details are given in the supplementary materials.

Our upper limits on h_0 at twice the rotation frequency may also be expressed as upper limits on the ellipticity ϵ of the pulsar (Abbott et al. 2019b). This is $\epsilon = 3.9 \times 10^{-8} \times (h_0/5 \times 10^{-26}) \times (10^{45} \text{ g cm}^3/I_{zz}) \times (840 \text{ pc}/d)$, where I_{zz} is the moment of inertia about the spin axis, and d is the distance.

As is the case for most known pulsars, it is unlikely that our searches would have detected a GW signal. In fact, suppose that all of the rotational kinetic-energy losses associated with the intrinsic spin-down are via GW emission. Then assuming the canonical $I_{zz} = 10^{45} \text{ g cm}^3$, this would imply a “spin-down” ellipticity $\epsilon^{\text{sd}} = 4.7 \times 10^{-10}$, which is a factor ~ 80 below our upper limit.

4. Discussion and Conclusions

PSR J1653–0158 is the second binary pulsar (Pletsch et al. 2012) and the fourth MSP (Clark et al. 2018) to be discovered through periodicity searches of gamma-rays. This pulsar is remarkable in many ways. It is only the second rotationally powered MSP from which no radio pulsations have been detected. It is among the fastest-rotating known pulsars with spin frequency $f = 508$ Hz. The 75 minute orbital period is shorter than for any other known rotation-powered pulsar, with the previous record being PSR J1311–3430 with a 93 minute orbit (Pletsch et al. 2012). The inferred surface magnetic field is possibly the weakest, depending on the Shklovskii correction.

The discovery was enabled by constraints on the sky position and orbital parameters from optical observations, together with efficient search techniques and the large computing power of the distributed volunteer computing system Einstein@Home. The detection proves that the optically variable candidate counterpart (Kong et al. 2014; Romani et al. 2014) is indeed the black-widow-type binary companion to PSR J1653–0158, and it conclusively resolves the nature of the brightest remaining unidentified gamma-ray source, first found more than 2 decades ago (Hartman et al. 1999).

The distance to PSR J1653–0158 and its proper motion are well constrained. Gaia measurements of the parallax, $\varpi = 1.88 \pm 1.01$ mas, imply a distance $d = 530_{-200}^{+470}$ pc. A consistent, but tighter constraint is given by our optical modeling with $d = 840_{-40}^{+40}$ pc. The proper motion (see Table 1) is also measured with good precision (Gaia and our timing are in agreement).

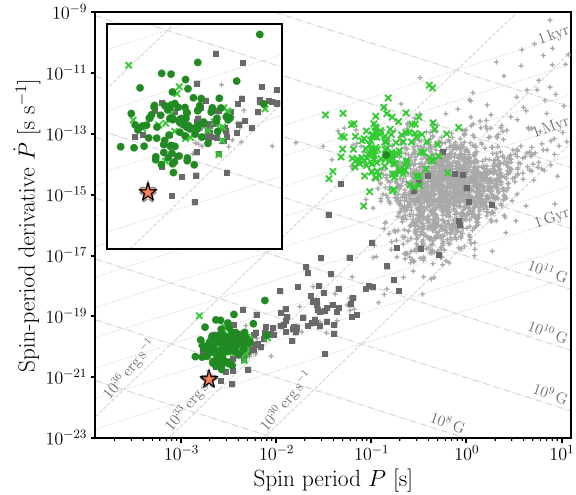


Figure 3. Newly detected PSR J1653–0158 on a P – \dot{P} diagram of the known pulsar population outside of globular clusters. The MSP population is shown magnified in the inset. LAT pulsars are marked in green (isolated by a cross and binary by a circle). Non-LAT pulsars in the ATNF are marked in gray (isolated by a plus and binary by a square). The lines show constant surface magnetic-field strength (dashed–dotted), characteristic age (dotted), and spin-down power (dashed). The spin period and intrinsic spin-period derivative of PSR J1653–0158 are marked by the orange star. The transparent stars indicate the (distance-dependent) maximum and minimum intrinsic spin-period derivatives according to the distance estimated from our optical models.

PSR J1653–0158 has one of the lowest observed spin-period derivatives of all known pulsars ($\dot{P} = 2.4 \times 10^{-21} \text{ s s}^{-1}$). The intrinsic $\dot{P} = 8.5 \times 10^{-22} \text{ s s}^{-1}$ (accounting for Galactic acceleration and Shklovskii effects) is even smaller. In Figure 3, PSR J1653–0158 is shown in a P – \dot{P} diagram, alongside the known radio and gamma-ray pulsar population outside of globular clusters.

The intrinsic \dot{P} can be used to estimate the pulsar’s spin-down power \dot{E} , surface magnetic-field strength B_{surf} , magnetic-field strength at the light cylinder B_{LC} , and characteristic age τ_c . These are given in Table 1 for $d = 840$ pc. Constant lines of \dot{E} , B_{surf} , and τ_c are displayed in Figure 3 to show the distance-dependent ranges.

Spider pulsars in very-short-period orbits are difficult to discover with traditional radio searches. Even though we can now fold the radio data with the exact parameters, PSR J1653–0158 is still not visible. There are two simple explanations for the nondetection of radio pulsations. (1) Radio emission is blocked by material produced by the pulsar evaporating its companion. Eclipses for large fractions of the orbit would be expected, since they have been seen for many spider pulsars (see, e.g., Fruchter et al. 1988; Archibald et al. 2009; Polzin et al. 2020). This is further supported by the observed extremely compact orbit and the strong IBS. Radio imaging observations could be used to check whether there is any continuum radio flux at the sky position of PSR J1653–0158, but previous experience is not encouraging. The eclipses of a few other spider systems have been imaged at low frequencies, showing that, during the eclipse, the continuum flux from the pulsar disappears in tandem with the pulsed flux (Broderick et al. 2016; Polzin et al. 2018). (2) PSR J1653–0158 is intrinsically radio-quiet, in that its radio beam does not cross the line of sight, or it has a very low luminosity. There is one other radio-quiet MSP known (Clark et al. 2018).

The minimum average density of the companion 64 g cm^{-3} is very high, assuming a filled Roche lobe (Eggleton 1983). Using the filling factor from optical modeling, the average companion density 73 g cm^{-3} is even higher. The high density and the compact orbit suggest that the companion may be a helium white-dwarf remnant, and that the system may have evolved from an ultracompact X-ray binary (Sengar et al. 2017; Kaplan et al. 2018). In addition, simulations predict evolved ultracompact X-ray binaries to have orbital periods of around 70–80 minutes (van Haften et al. 2012), consistent with the 75 minute orbital period from PSR J1653–0158. Future analysis of optical spectroscopic data may give additional insight into the evolution and composition of the companion.

The discovery of PSR J1653–0158 is the result of a multiwavelength campaign. The pulsar-like gamma-ray spectrum, and the nondetection of radio pulsations, motivated the search for a visible companion. This was subsequently discovered in optical and X-ray observations. Further optical observations provided constraints on the orbital parameters that were precise enough to enable a successful gamma-ray pulsation search.

We are deeply grateful to the thousands of volunteers who donated their computing time to Einstein@Home, and to those whose computers first detected PSR J1653–0158: Yi-Sheng Wu of Taoyuan, Taiwan; and Daniel Scott of Ankeny, Iowa, USA.

This work was supported by the Max-Planck-Gesellschaft (MPG), by the Deutsche Forschungsgemeinschaft (DFG) through an Emmy Noether Research grant, No. PL 710/1-1 (PI: Holger J. Pletsch) and by National Science Foundation grants 1104902 and 1816904. L.N. was supported by an STSM Grant from COST Action CA16214. C.J.C. and R.P.B. acknowledge support from the ERC under the European Union’s Horizon 2020 research and innovation program (grant agreement No. 715051; Spiders). V.S.D. and ULTRACAM are supported by the STFC. R.W.R. and D.K. were supported in part by NASA grant 80NSSC17K0024. S.M.R. is a CIFAR Fellow and is supported by the NSF Physics Frontiers Center award 1430284 and the NASA Fermi GO Award NNX16AR55G. Fermi research at NRL is funded by NASA. J.W.T.H. is an NWO Vici fellow.

The ULTRACAM photometry was obtained as part of program WHT/2015A/35. The William Herschel Telescope is operated on the island of La Palma by the Isaac Newton Group of Telescopes in the Spanish Observatorio del Roque de los Muchachos of the Instituto de Astrofísica de Canarias. Based on observations made with the Isaac Newton Telescope (program I17BN005) operated on the island of La Palma by the Isaac Newton Group of Telescopes in the Spanish Observatorio del Roque de los Muchachos of the Instituto de Astrofísica de Canarias. This paper makes use of data obtained from the Isaac Newton Group of Telescopes Archive which is maintained as part of the CASU Astronomical Data Centre at the Institute of Astronomy, Cambridge.

We acknowledge support of the Department of Atomic Energy, Government of India, under project No. 12-R&D-TFR-5.02-0700 for the GMRT observations. The GMRT is run by the National Centre for Radio Astrophysics of the Tata Institute of Fundamental Research, India. The Nançay Radio Observatory is operated by the Paris Observatory, associated with the French Centre National de la Recherche Scientifique (CNRS). We acknowledge financial support from the “Programme National Hautes Energies” (PNHE) of CNRS/INSU, France. This Letter is based (in part) on data obtained with the International LOFAR Telescope (ILT) under

project code LC7_018. LOFAR (van Haarlem et al. 2013) is the Low Frequency Array designed and constructed by ASTRON. The National Radio Astronomy Observatory is a facility of the National Science Foundation operated under cooperative agreement by Associated Universities, Inc. The Green Bank Observatory is a facility of the National Science Foundation operated under cooperative agreement by Associated Universities, Inc. FAST is a Chinese national mega-science facility, built and operated by NAOC. Partly based on observations with the 100 m telescope of the MPIfR (Max-Planck-Institut für Radioastronomie) at Effelsberg.

The Fermi-LAT Collaboration acknowledges generous ongoing support from a number of agencies and institutes that have supported both the development and the operation of the LAT as well as scientific data analysis. These include the National Aeronautics and Space Administration and the Department of Energy in the United States, the Commissariat à l’Energie Atomique and the Centre National de la Recherche Scientifique/ Institut National de Physique Nucléaire et de Physique des Particules in France, the Agenzia Spaziale Italiana and the Istituto Nazionale di Fisica Nucleare in Italy, the Ministry of Education, Culture, Sports, Science and Technology (MEXT), High Energy Accelerator Research Organization (KEK) and Japan Aerospace Exploration Agency (JAXA) in Japan, and the K. A. Wallenberg Foundation, the Swedish Research Council, and the Swedish National Space Board in Sweden.

Additional support for science analysis during the operations phase is gratefully acknowledged from the Istituto Nazionale di Astrofisica in Italy and the Centre National d’Études Spatiales in France. This work performed in part under DOE Contract DE-AC02-76SF00515.

The authors thank the LIGO Scientific Collaboration for access to the data and gratefully acknowledge the support of the United States National Science Foundation (NSF) for the construction and operation of the LIGO Laboratory and Advanced LIGO as well as the Science and Technology Facilities Council (STFC) of the United Kingdom, and the Max-Planck-Society (MPS) for support of the construction of Advanced LIGO. Additional support for Advanced LIGO was provided by the Australian Research Council. This research has made use of data, software, and/or web tools obtained from the LIGO Open Science Center (<https://losc.ligo.org>), a service of LIGO Laboratory, the LIGO Scientific Collaboration and the Virgo Collaboration, to which the authors have also contributed. LIGO is funded by the U.S. National Science Foundation. Virgo is funded by the French Centre National de Recherche Scientifique (CNRS), the Italian Istituto Nazionale della Fisica Nucleare (INFN), and the Dutch Nikhef, with contributions by Polish and Hungarian institutes.

Software: Fermi Science Tools, MultiNest (Feroz et al. 2019), ULTRACAM software pipelines, Icarus (Breton et al. 2012), psrqpy (Manchester et al. 2005; Pitkin 2018), Astropy (Astropy Collaboration et al. 2013, 2018), matplotlib (Hunter 2007), NumPy (Oliphant 2006; van der Walt et al. 2011), GalPot (McMillan 2017), Lightkurve (Lightkurve Collaboration et al. 2018), PRESTO (Ransom et al. 2002), LALSuite (LIGO Scientific Collaboration 2018).

Appendix Continuous Gravitational Waves

Acknowledging the possibility of mismatches between the pulsar rotation frequency and the gravitational-wave frequency,

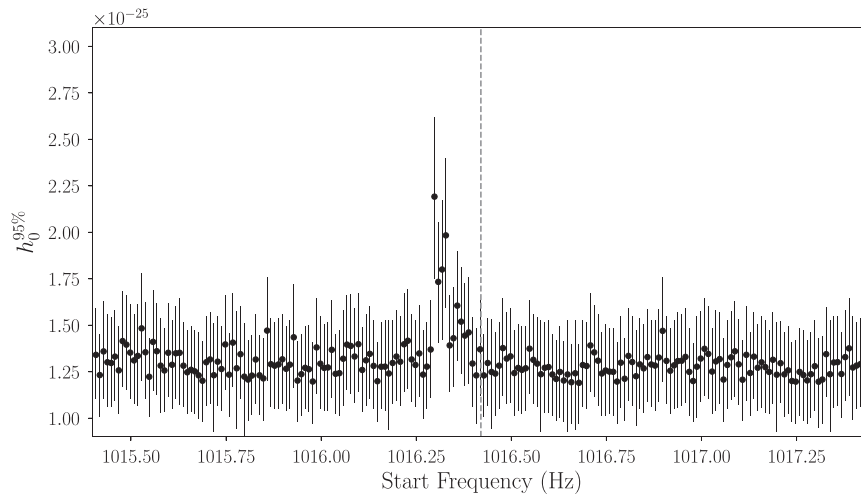


Figure 4. 95% confidence upper limits on the gravitational-wave amplitude in 10 mHz bands around twice the rotation frequency of PSR J1653–0158, which is indicated by the gray dashed line. The bars indicate a conservative estimate of the uncertainty on the upper limit values. The “spike” does not indicate a detection: it is due to a disturbance in L1 around ≈ 1016.32 Hz. The upper limit values are available as data behind the figure.

(The data used to create this figure are available.)

we perform an \mathcal{F} -statistic search in a ~ 2 Hz band around twice the rotation frequency, a factor of 10^{-3} of the gravitational-wave frequency, similarly to what was done in Abbott et al. (2019a) and also extend the spin-down search to the range $2\dot{f} \in (-1.260, -1.2216) \times 10^{-15} \text{ Hz s}^{-1}$. Overall, we use 2.4×10^9 templates resulting in an average mismatch of 1%. We examine the results in 10 mHz-wide bands. The most significant $2\mathcal{F}$ values from each band are consistent with the noise-only expectation, apart from six outliers that can be ascribed to a disturbance in L1 around ≈ 1016.32 Hz. We set upper limits in each band. The values are plotted in Figure 4 and are provided as data behind the figure. The mean value is 1.3×10^{-25} and it is higher than the targeted search upper limit, consistently with the larger volume of searched wave shapes.

ORCID iDs

L. Nieder <https://orcid.org/0000-0002-5775-8977>
 C. J. Clark <https://orcid.org/0000-0003-4355-3572>
 D. Kandel <https://orcid.org/0000-0002-5402-3107>
 R. W. Romani <https://orcid.org/0000-0001-6711-3286>
 C. G. Bassa <https://orcid.org/0000-0002-1429-9010>
 B. Allen <https://orcid.org/0000-0003-4285-6256>
 A. Ashok <https://orcid.org/0000-0002-8395-957X>
 I. Cognard <https://orcid.org/0000-0002-1775-9692>
 H. Fehrmann <https://orcid.org/0000-0001-8036-1882>
 P. Freire <https://orcid.org/0000-0003-1307-9435>
 R. Karuppusamy <https://orcid.org/0000-0002-5307-2919>
 M. Kramer <https://orcid.org/0000-0002-4175-2271>
 D. Li <https://orcid.org/0000-0003-3010-7661>
 B. Machenschalk <https://orcid.org/0000-0002-2332-0459>
 Z. Pan <https://orcid.org/0000-0001-7771-2864>
 M. A. Papa <https://orcid.org/0000-0002-1007-5298>
 S. M. Ransom <https://orcid.org/0000-0001-5799-9714>
 P. S. Ray <https://orcid.org/0000-0002-5297-5278>
 J. Roy <https://orcid.org/0000-0002-2892-8025>

P. Wang <https://orcid.org/0000-0002-3386-7159>
 J. Wu <https://orcid.org/0000-0003-3536-4368>
 C. Aulbert <https://orcid.org/0000-0002-1481-8319>
 E. D. Barr <https://orcid.org/0000-0001-8715-9628>
 B. Beheshtipour <https://orcid.org/0000-0002-8524-1537>
 O. Behnke <https://orcid.org/0000-0003-0679-8562>
 B. Bhattacharyya <https://orcid.org/0000-0002-6287-6900>
 R. P. Breton <https://orcid.org/0000-0001-8522-4983>
 F. Camilo <https://orcid.org/0000-0002-1873-3718>
 C. Choquet <https://orcid.org/0000-0001-6900-1851>
 V. S. Dhillon <https://orcid.org/0000-0003-4236-9642>
 E. C. Ferrara <https://orcid.org/0000-0001-7828-7708>
 L. Guillemot <https://orcid.org/0000-0002-9049-8716>
 J. W. T. Hessels <https://orcid.org/0000-0003-2317-1446>
 M. Kerr <https://orcid.org/0000-0002-0893-4073>
 T. R. Marsh <https://orcid.org/0000-0002-2498-7589>
 Z. Pleunis <https://orcid.org/0000-0002-4795-697X>
 H. J. Pletsch <https://orcid.org/0000-0002-1164-4755>
 M. S. E. Roberts <https://orcid.org/0000-0002-9396-9720>
 B. Steltner <https://orcid.org/0000-0003-1833-5493>

References

Abbott, B. P., Abbott, R., Abbott, T. D., et al. 2019a, *PhRvD*, **99**, 122002
 Abbott, B. P., Abbott, R., Abbott, T. D., et al. 2019b, *ApJ*, **879**, 10
 Abdo, A. A., Ackermann, M., Ajello, M., et al. 2009, *ApJS*, **183**, 46
 Abdo, A. A., Ajello, M., Allafort, A., et al. 2013, *ApJS*, **208**, 17
 Abdollahi, S., Acero, F., Ackermann, M., et al. 2020, *ApJS*, **247**, 33
 Allen, B., Knispel, B., Cordes, J. M., et al. 2013, *ApJ*, **773**, 91
 Archibald, A. M., Stairs, I. H., Ransom, S. M., et al. 2009, *Sci*, **324**, 1411
 Astropy Collaboration, Price-Whelan, A. M., Sipőcz, B. M., et al. 2018, *AJ*, **156**, 123
 Astropy Collaboration, Robitaille, T. P., Tollerud, E. J., et al. 2013, *A&A*, **558**, A33
 Atwood, W., Albert, A., Baldini, L., et al. 2012, arXiv:1303.3514
 Atwood, W. B., Abdo, A. A., Ackermann, M., et al. 2009, *ApJ*, **697**, 1071
 Aulbert, C., & Fehrmann, H. 2008, Forschungsbericht 2008—Max-Planck-Institut für Gravitationsphysik, Teilinstitut Hannover, <https://www.mpg.de/308429/forschungsschwerpunkt>
 Barr, E. D., Guillemot, L., Champion, D. J., et al. 2013, *MNRAS*, **429**, 1633

- Bassa, C. G., Pleunis, Z., Hessels, J. W. T., et al. 2017, *ApJL*, **846**, L20
- Bhattacharyya, B., Roy, J., Ray, P. S., et al. 2013, *ApJL*, **773**, L12
- Breton, R. P., Rappaport, S. A., van Kerkwijk, M. H., & Carter, J. A. 2012, *ApJ*, **748**, 115
- Breton, R. P., van Kerkwijk, M. H., Roberts, M. S. E., et al. 2013, *ApJ*, **769**, 108
- Broderick, J. W., Fender, R. P., Breton, R. P., et al. 2016, *MNRAS*, **459**, 2681
- Bruel, P., Burnett, T. H., Digel, S. W., et al. 2018, arXiv:1810.11394
- Camilo, F., Reynolds, J. E., Ransom, S. M., et al. 2016, *ApJ*, **820**, 6
- Clark, C. J., Pletsch, H. J., Wu, J., et al. 2018, *SciA*, **4**, eaao7228
- Clark, C. J., Wu, J., Pletsch, H. J., et al. 2017, *ApJ*, **834**, 106
- Cutler, C., & Schutz, B. F. 2005, *PhRvD*, **72**, 063006
- Damour, T., & Taylor, J. H. 1991, *ApJ*, **366**, 501
- Desvignes, G., Cognard, I., Champion, D., et al. 2013, in IAU Symposium, Vol. 291, Neutron Stars and Pulsars: Challenges and Opportunities after 80 years, ed. J. van Leeuwen (Cambridge: Cambridge Univ. Press), 375
- Dhillon, V. S., Marsh, T. R., Stevenson, M. J., et al. 2007, *MNRAS*, **378**, 825
- Dupuis, R. J., & Woan, G. 2005, *PhRvD*, **72**, 102002
- Eggleton, P. P. 1983, *ApJ*, **268**, 368
- Fehrmann, H., & Pletsch, H. J. 2014, *PhRvD*, **90**, 124049
- Feroz, F., Hobson, M. P., Cameron, E., & Pettitt, A. N. 2019, *OJAp*, **2**, 10
- Fruchter, A. S., Stinebring, D. R., & Taylor, J. H. 1988, *Natur*, **333**, 237
- Gaia Collaboration, Brown, A. G. A., Vallenari, A., et al. 2018, *A&A*, **616**, A1
- Green, G. M., Schlafly, E., Zucker, C., Speagle, J. S., & Finkbeiner, D. 2019, *ApJ*, **887**, 93
- Hartman, R. C., Bertsch, D. L., Bloom, S. D., et al. 1999, *ApJS*, **123**, 79
- Hessels, J. W. T., Ransom, S. M., Stairs, I. H., et al. 2006, *Sci*, **311**, 1901
- Hunter, J. D. 2007, *CSE*, **9**, 90
- Jones, D. I. 2010, *MNRAS*, **402**, 2503
- Jones, D. I. 2015, *MNRAS*, **453**, 53
- Kandel, D., & Romani, R. W. 2020, *ApJ*, **892**, 101
- Kaplan, D. L., Stovall, K., van Kerkwijk, M. H., Fremling, C., & Istrate, A. G. 2018, *ApJ*, **864**, 15
- Kerr, M. 2011, *ApJ*, **732**, 38
- Kerr, M., Ray, P. S., Johnston, S., Shannon, R. M., & Camilo, F. 2015, *ApJ*, **814**, 128
- Kong, A. K. H., Jin, R., Yen, T. C., et al. 2014, *ApJL*, **794**, L22
- Li, D., Wang, P., Qian, L., et al. 2018, *IMMag*, **19**, 112
- Lightkurve Collaboration, Cardoso, J. V. d. M. a., Hedges, C., et al. 2018, Lightkurve: Kepler and TESS Time Series Analysis in Python, Astrophysics Source Code Library, ascl:1812.013
- LIGO Scientific Collaboration 2018, LIGO Algorithm Library—LALSuite, free software (GPL), doi:10.7935/GT1W-FZ16
- Manchester, R. N., Hobbs, G. B., Teoh, A., & Hobbs, M. 2005, *AJ*, **129**, 1993
- McMillan, P. J. 2017, *MNRAS*, **465**, 76
- Nieder, L., Allen, B., Clark, C. J., & Pletsch, H. J. 2020, *ApJ*, **901**, 156
- Nieder, L., Clark, C. J., Bassa, C. G., et al. 2019, *ApJ*, **883**, 42
- Oliphant, T. E. 2006, A Guide to NumPy, Vol. 1 (USA: Trelgol Publishing)
- Pitkin, M. 2018, *JOSS*, **3**, 538
- Pitkin, M., Gill, C., Jones, D. I., Woan, G., & Davies, G. S. 2015, *MNRAS*, **453**, 4399
- Pitkin, M., Isi, M., Veitch, J., & Woan, G. 2017, arXiv:1705.08978
- Pletsch, H. J., & Clark, C. J. 2014, *ApJ*, **795**, 75
- Pletsch, H. J., Guillemot, L., Fehrmann, H., et al. 2012, *Sci*, **338**, 1314
- Polzin, E. J., Breton, R. P., Bhattacharyya, B., et al. 2020, *MNRAS*, **494**, 2948
- Polzin, E. J., Breton, R. P., Clarke, A. O., et al. 2018, *MNRAS*, **476**, 1968
- Ransom, S. M., Eikenberry, S. S., & Middleditch, J. 2002, *AJ*, **124**, 1788
- Ransom, S. M., Ray, P. S., Camilo, F., et al. 2011, *ApJL*, **727**, L16
- Ray, P. S., Kerr, M., Parent, D., et al. 2011, *ApJS*, **194**, 17
- Roberts, M. S. E. 2013, in IAU Symposium, Vol. 291, Neutron Stars and Pulsars: Challenges and Opportunities after 80 Years, ed. J. van Leeuwen (Cambridge: Cambridge Univ. Press), 127
- Romani, R. W., Filippenko, A. V., & Cenko, S. B. 2014, *ApJL*, **793**, L20
- Sanchez, N., & Romani, R. W. 2017, *ApJ*, **845**, 42
- Sanpa-arsa, S. 2016, PhD Thesis, Graduate School of Arts and Sciences, University of Virginia
- Saz Parkinson, P. M., Xu, H., Yu, P. L. H., et al. 2016, *ApJ*, **820**, 8
- Sengar, R., Tauris, T. M., Langer, N., & Istrate, A. G. 2017, *MNRAS*, **470**, L6
- Shklovskii, I. S. 1970, *SvA*, **13**, 562
- Strader, J., Swihart, S., Chomiuk, L., et al. 2019, *ApJ*, **872**, 42
- The LIGO Scientific Collaborationthe Virgo Collaboration, Abbott, R., et al. 2019, arXiv:1912.11716
- van der Walt, S., Colbert, S. C., & Varoquaux, G. 2011, *CSE*, **13**, 22
- van Haften, L. M., Nelemans, G., Voss, R., Wood, M. A., & Kuijpers, J. 2012, *A&A*, **537**, A104
- van Haarlem, M. P., Wise, M. W., Gunst, A. W., et al. 2013, *A&A*, **556**, A2
- VanderPlas, J. T., & Ivezić, Ž. 2015, *ApJ*, **812**, 18

Curriculum Vitae

Personal Details

Name Anjana Ashok
Date of Birth 29.06.1994
Place of Birth Calicut, Kerala, India

Education

10-2018 – 3-2023

PhD studies at Max Planck Institute for Gravitational Physics (Albert Einstein Institute) Hannover, Germany,

Doctoral thesis: 'Targeted Searches for Continuous Gravitational Waves', under the supervision of Prof. Dr. Maria Alessandra Papa.

1-2018 – 6-2018

Junior Research Fellow at Indian Institute of Space Science and Technology, Trivandrum, Kerala, India,

Project: 'Study of Gamma-Ray Bursts with a focus on their radio afterglows', under the supervision of Assoc. Prof. Dr. Resmi Lekshmi.

8-2017 – 10-2017

Research Internship at Inter University Center for Astronomy and Astrophysics, Pune, India,

Project: ' χ^2 discriminator for glitches in LIGO data', under the supervision of Emeritus Prof. Sanjeev Dhurandhar.

2015 – 2017

Master studies in Physics at National Institute of Technology, Karnataka India,

Master thesis: 'Einstein's Gravity, sources of Gravitational Waves and an introduction to Post-Newtonian approximation', under the supervision of Assoc. Prof. Dr. Ajith K.M.

2012 – 2015

Bachelor studies in Physics at University of Calicut, Kerala India,

Government Arts And Science College, Calicut, Bachelor thesis (at Saha Institute of Nuclear Physics, Kolkata, India): 'Superheated Drop Detectors and PICO dark matter search experiment' under the supervision of Prof. Dr. Mala Das, Minor subjects: Mathematics, Chemistry.

2010 – 2012

Senior School, Central Board of Secondary Education,

Veda Vyasa Vidyalayam, Calicut, Kerala, India. Physics, Mathematics, Chemistry, Computer Science, English

2010

Secondary School, Central Board of Secondary Education,

Bharatiya Vidya Bhavan, Calicut, Kerala, India. Science, Mathematics, Social Science, English, Sanskrit

ACKNOWLEDGMENTS

I thank Maria Alessandra Papa (MAP), my supervisor, for, first and foremost, giving me the opportunity to do my PhD in the world's leading Continuous Gravitational Wave group. She has been a generous supervisor, patient and consistent in providing her own guidance as well as putting me in the right collaborations that I needed in order to learn and grow. Depending on what the situation demanded, she has been immensely kind, as well as tough and unrelenting with me. I am glad for her training at this early stage of my scientific career. I am also grateful for her detailed comments on every chapter of this thesis.

I am grateful to Pep Covas and Reinhard Prix for everything I learnt (which was a lot) and for all the inspiration while working on the Bayesian pipeline with them. I acknowledge that I learnt the details underlying the practical implementation of a CW search from Reinhard's notes 'CFSv2.pdf'; the times that I (finally) understood how something is actually computed in LALSuite, have been some of my most joyous ones.

The Continuous Wave team at AEI-Hannover has some awesome people in it. When software threw problems that I could not solve on my own, Heinz-Bernd Eggenstein (HBE) and Max Bensch were only a Rocket-chat away from providing support. The resources of the group and of the AEI, especially the ATLAS computing cluster, made it possible to work with efficiency and peace of mind. I thank Carsten Aulbert and Henning Fehrmann for their commendable work in managing the cluster. I thank Bruce Allen for leading this brilliant research institute and being an exemplary scientist. I thank Gabi and the International Officers over the years who have made life in the institute and in Germany easy for me.

My PhD work was possible because of newly discovered pulsars. I thank Lars Nieder, Paulo Freire and Colin Clark for the pulsars we already worked on and those in the queue. I acknowledge the contributions of Banafsheh Beheshtipour, Oliver Behnke and every other collaborator from both the gravitational wave and the pulsar astronomy world towards the work in this thesis. I especially thank Banafsheh for also being a patient sounding board while the \mathcal{F} -stat based search pipeline was being built.

I'm grateful for the wonderful friendships I made here at the AEI – officemates over the years, fellow PhD-students and post-docs in the building, experimental physicists from across the bridge, I shall not attempt to name each of you, but you know who you are – Thank you for being my friend, I cherish you! Many thanks to Daniel Steinmeyer, Benjamin Steltner and Lars Nieder for their efforts in proofreading and providing insightful feedback on different chapters.

I thank Extrakt, Nordstadt, for becoming something like a home.

I thank my family back in Calicut, for believing in me. Especially my grandfather, who is keenly interested in what I do and routinely enquires after my pulsars. Achan, Amma and Nandu – Thank you.

I have wanted to be an astronomer ever since I pored into a book filled with pictures of outer space as an eight year old. I thank my aunt for bringing me that book. Approximately twenty years later, I thank everybody who has contributed to my journey up to this last sentence in my PhD thesis in Gravitational Wave Astronomy.